UNIVERSITÉ DE NANTES
FACULTÉ DES SCIENCES ET DES TECHNIQUES

———

ECOLE DOCTORALE Sciences Pour l'Ingénieur, Géosciences, Architecture (SPIGA)

Année 2015

Dynamique des satellites de glace avec une phase liquide

———————

THÈSE DE DOCTORAT
Discipline : Sciences de la Terre et de l'Univers
Spécialité :

Présentée
et soutenue publiquement par

Klára KALOUSOVÁ

Le 28 janvier 2015, devant le jury ci-dessous

Président	
Rapporteurs	Yanick RICARD, Directeur de recherche CNRS, ENS Lyon – UCB Lyon 1
	Hauke HUSSMANN, Physicien, DLR Berlin
Examinateurs	Hana ČÍŽKOVÁ, Professeur associé, U Charles Prague
	Josef MÁLEK, Professeur, U Charles Prague
	Olivier GRASSET, Professeur, U Nantes

Directeurs de thèse : Ondřej Čadek, Gaël Choblet, Gabriel Tobie

First of all, I would like to thank all three my supervisors, Dr. Ondřej Čadek, Dr. Gaël Choblet and Dr. Gabriel Tobie, for their help and guidance, plenty of very inspiring scientific discussions and loads of necessary encouragement during these beautiful four years. Thank you also for this great experience that was my stay in Nantes.

My dearest, Dr. Ondřej Souček, deserves my deepest gratitude for these never-ending anytime discussions of equations, boundary conditions, and numerical schemes. Thank you for your bottomless patience and understanding, especially during the last few months.

My special thank belongs to the Karlin guys, Jan Blechta and Dr. Jaroslav Hron, for their help with all the traps and guiles of FEniCS. I also thank all the teachers and students at the Department of Geophysics in Prague for creating friendly and inspiring atmosphere. All these years at the department have been a great pleasure.

Un grand merci à toutes et à tous au Laboratoire de Planétologie et Géodynamique de Nantes. Même si je n'ai passé que 18 mois à Nantes, je me sentirai comme chez moi chaque fois que je reviens.

Last but not least, I am very grateful to my family, especially my parents, for their long-lasting support and their belief in me even in times when I was giving up. Thank you.

This research received funding from the European Research Council under the European Community's Seventh Framework Programme FP7/2007-2013 grant agreement 259285. Support from Charles University through projects SVV-2012-265308, SVV-2013-267308, and SVV-2014-260096 is thankfully acknowledged. This work was also supported by the IT4Innovations Centre of Excellence project (CZ.1.05/1.1.00/02.0070), funded by the European Regional Development Fund and the national budget of the Czech Republic via the Research and Development for Innovations Operational Programme, as well as Czech Ministry of Education, Youth and Sports via the project Large Research, Development and Innovations Infrastructures (LM2011033).

I declare that I carried out this doctoral thesis independently, and only with the cited sources, literature and other professional sources.

I understand that my work relates to the rights and obligations under the Act No. 121/2000 Coll., the Copyright Act, as amended, in particular the fact that the Charles University in Prague has the right to conclude a license agreement on the use of this work as a school work pursuant to Section 60 paragraph 1 of the Copyright Act.

In Prague 29.9.2014 Klára Kalousová

Název práce: Modelování dynamiky ledových měsíců s kapalnou fází

Autor: Klára Kalousová

Katedra: Katedra geofyziky
Laboratoire de Planétologie et Géodynamique de Nantes

Vedoucí disertační práce: Doc. RNDr. Ondřej Čadek, CSc.
Dr. Gaël Choblet

Abstrakt: Povrch Jupiterova měsíce Europa vykazuje velmi nízký věk, který spolu s množstvím unikátních terénů svědčí o nedávné vnitřní aktivitě. Morfologické studie a spektrální pozorování naznačují existenci podpovrchového oceánu a mělkých vodních kapes ve vnější ledové slupce. Přítomnost kapalné vody v chemicky bohatém prostředí a dlouhodobý zdroj energie zajištěný slapovým zahříváním činí z Europy jednoho z hlavních kandidátů na možnou existenci života, pro nějž je nezbytná materiálová výměna mezi povrchem a vnitřním oceánem. V této práci se zabýváme táním uvnitř ledové slupky Europy a následnou evolucí natáté vody za použití rovnic pro dvoufázovou směs odvozených pro tento účel. Výsledky parametrické studie pro případ slupky tvořené temperovaným ledem naznačují, že rychlost průtoku vody porézním prostředím je řízena permeabilitou ledu, zatímco viskozita ledu ovlivňuje vlnovou délku řešení. Následně uvažujeme polytermální ledovou slupku ve dvou scénářích umožňujících tání: (i) V případě slapově zahřívané konvektující ledové slupky dochází k tání především v její dolní polovině a všechna natátá voda okamžitě odtéká do podpovrchového oceánu. (ii) Smykové pohyby na slapově aktivovaném zlomu mohou naopak vést k tání v hloubce pouze 3 kilometry pod povrchem. Takto vzniknuvší vodní kapsa může zůstat gravitačně stabilní alespoň 600 tisíc let, pokud pod ní ležící materiál není vnitřně zahříván.

Klíčová slova: Europa, slapové zahřívání, tání ledu, směs vody a ledu, dvoufázové tečení

Title: Dynamics of icy satellites with a liquid phase

Author: Klára Kalousová

Department: Department of Geophysics
Laboratoire de Planétologie et Géodynamique de Nantes

Supervisors: Doc. RNDr. Ondřej Čadek, CSc.
Dr. Gaël Choblet

Abstract: Jupiter's moon Europa has a young surface with a plethora of unique terrains that indicate recent endogenic activity. Morphological models and spectral observations suggest that it possesses an internal ocean as well as shallow pockets of liquid water within its outer ice shell. Presence of water in a chemically rich environment and a longterm energy source ensured by tidal heating, make Europa one of the best candidates for habitability, for which the material exchange between the surface and the ocean is critical. In this thesis, we investigate internal melting and subsequent meltwater evolution within Europa's ice shell by using a two-phase formalism developed for this context. Results of a parametric study for a temperate ice shell indicate that the time scale of water transport by porous flow is governed by the ice permeability, while the ice viscosity affects the solution wavelength. We then consider a polythermal ice shell with two melting scenarios: (i) In a tidally-heated convecting ice shell, melting occurs mainly in its lower half and all the meltwater is immediately transported to the underlying ocean. (ii) Contrarily, shear motions on a tidally-activated fault can induce melting as shallow as three kilometers below the surface. This meltwater pocket can remain gravitationally stable for at least 600 kyr if the underlying ice layer is not volumetrically heated.

Keywords: Europa, tidal heating, ice melting, water-ice mixture, two-phase flow

Contents

Introduction

With its dearth of large impact craters that indicates a young surface (<100 Myr), and the abundance of various tectonic and cryovolcanic features that points to a relatively recent endogenic activity, Europa is one of the most exciting planetary bodies within our Solar System. Magnetic induction signals (*Khurana et al.*, 1998; *Zimmer al.*, 2000) and detection of salts on Europa's icy surface (*McCord et al.*, 1998) indicate that the moon probably possesses a salty ocean a few tens of kilometers below its surface. Morphological studies (*Schmidt et al.*, 2011; *Dombard et al.*, 2013) moreover suggest the presence of shallow water reservoirs, perched only a few kilometers below Europa's cold brittle surface. Recent detection of water vapor over Europa's south pole (*Roth et al.*, 2014) suggests the existence of an ongoing plume activity similar to that observed at Enceladus (e.g. *Hansen et al.*, 2006; *Porco et al.*, 2006; *Waite et al.*, 2006). Powered by tides, this endogenic activity in a chemically rich environment together with an expected ocean-mantle contact may provide the key ingredients for life (i.e. the presence of liquid water, a suite of biologically essential elements, and a source of energy, cf. *Hand et al.*, 2009), which makes Europa one of the best candidates for habitability and places it atop the interest of astrobiologists. The material exchange between the surface and the ocean, critical for potential habitability, is thus of primary interest.

In this context it is crucial to understand (i) How can meltwater be generated at shallow depth and what is its lifetime? and (ii) What processes control the water and chemical transport between the surface and the ocean? In order to address these major questions, we numerically model the mechanisms of water transport through the ice shell using two-phase flow formalism. The goal of this thesis is to investigate whether melting can initiate at shallow depths as a result of enhanced tidal heating in different geodynamical contexts, and to address the gravitational stability of these potential meltwater reservoirs with the consequences for recent morphological models.

This thesis is divided into four parts, each of which contains two chapters. In the first part, after introducing Europa in more details (Chapter 1), we focus on the evidences for liquid water within its icy shell in the form of lenses or sills. We also discuss the heating sources due to tidal friction and their distribution within the ice shell. On Europa, due to its eccentric orbit around Jupiter, the tidal dissipation has a strong impact on the thermal structure of the ice shell. We consider two different geodynamical contexts - convective hot plumes and strike-slip faults - where enhanced tidal heating is expected to induce ice melting at shallow depths. In Chapter 2, we describe different meltwater transport mechanisms known in Earth's glaciers context, and discuss their plausibility for the conditions within Europa's ice shell.

The second part deals with the development of numerical tools that are used throughout this thesis. Chapter 3 contains a detailed derivation of two-phase flow equations - after writing down the general single-phase equations and the corresponding jump conditions, the multi-phase equations are obtained through the use of an averaging procedure. Restricting ourselves only to two phases, water ice and liquid water, we formulate the governing equations for this two-phase

mixture together with the appropriate constitutive relations. In order to neglect terms of minor importance, a scale analysis is performed. In the following chapter (4), we proceed with the description of the numerical methods used throughout this thesis together with their thorough testing.

The third part contains parametric studies of water transport through the temperate ice shells by two-phase flow - we perform a one-dimensional parametric study in Chapter 5 and a similar two-dimensional study in Chapter 6. We investigate the role of various material parameters (such as permeability, viscosity, or surface tension) on the transport process, and we also address the question of mechanical coupling between the two phases. In these two chapters, the ice shell is assumed to be at the melting temperature during the whole simulation. However, such an assumption is not valid when dealing with Europa's ice shell.

That is why, in the last part of this thesis, we consider polythermal shells, that comprise regions of temperate (i.e. at the melting temperature) as well as cold (i.e. below the melting temperature) ice. A one-dimensional study of meltwater production and transport in polythermal ice shell of Europa is performed in Chapter 7. As already mentioned, we consider two different geophysical contexts in which melting can occur - hot plumes and strike-slip faults. The subsequent transport of meltwater is enabled by porous two-phase flow in those parts that are sufficiently warm and permeable (i.e. temperate). This one-dimensional approach however cannot account for lateral flows and possible gravitational destabilization by the formation of Rayleigh-Taylor-like instabilities. Therefore, we proceed with a two-dimensional study in the last chapter (8), where we assume that water can be transported only by the formation of these gravitational instabilities, while we neglect porous flow. The results of this thesis as well as the outline of potential next steps are briefly summarized and discussed in Conclusions and perspectives.

Part I

Liquid water in Europa's ice shell: Observations and models

1. Europa

1.1 Discovery and further exploration

In January 1610, Galileo Galilei first observed his 'three little stars' near Jupiter. Subsequent observations showed that the three stars were indeed four satellites that orbited around Jupiter in the prograde fashion. Even though Galileo proposed to call them the Medician satellites, to honor his Medici patrons, the term 'Galilean satellites', in honor of their discoverer, prevailed over time. The individual satellites, Io, Europa, Ganymede, and Callisto, bear the names of mythic Jupiter's lovers, given to them by Simon Marius. They were the first celestial bodies discovered by telescope and, more importantly, their discovery provided an argument for the (then controversial) heliocentric theory of Copernic by showing an example of celestial bodies orbiting something other than the Earth.

The basic characteristics of the Galilean satellites, such as mass, diameter, shape, or albedo, have been mainly inferred from observations in the nineteenth and at the beginning of the twentieth century. The first published suggestion that they could be made of ice comes from *Jeffreys* (1923) and during the following fifty years, this notion was further explored and supported by both, observations (mainly spectroscopic, e.g. *Pilcher et al.*, 1972; *Greene et al.*, 1975) and modeling (e.g. *Lewis*, 1971; *Consolmagno & Lewis*, 1976).

With the fast development of spatial exploration program and the first successful mission to another planet (Mariner 2 to Venus in 1962), the plans for the ambitious mission to the outer Solar System first appeared. In 1972, Pioneer 10 was launched and was followed by Pioneer 11 a year later. These spacecrafts became the first to fly beyond Mars' orbit and through the asteroid belt. Both Pioneers provided the first spacecraft views of the Galilean moons, as well as improved values of satellites' masses. The 1979 flybys of Voyager 1 and 2 (both launched in 1977) revealed evidence of substantial geological activity (e.g. *Smith et al.*, 1979a,b) and further improved the satellites' diameter (and hence density) values. Voyager images of volcanic flows and gas plumes also confirmed Io's volcanic activity, predicted a few months earlier by *Peale et al.* (1979), and indicated the key role of heating that results from tidal forces.

More than a decade after the success of both Voyagers, the Galileo spacecraft was launched to Jupiter, which it reached in 1996 after a seven-year journey, and provided the first high resolution-images of the Galilean moons' surfaces as well as crucial geophysical informations on their interior structure. In the course of its twelve Europa-targetted flybys, it discovered several geological features unique to Europa (for more details cf. Sections 1.4 and 1.5) that indicated some amount of sub-ice activity at the time of their formation. Among its most important discoveries is the evidence for a liquid water ocean under Europa's surface (*Khurana et al.*, 1998; *Kivelson et al.*, 2000), the extensive resurfacing of Io's surface due to continuing volcanic activity since the Voyagers flew by in 1979 (*McEwen et al.*, 1998; *Lopes-Gautier et al.*, 1999) or the discovery of the first internal magnetic field of a moon (Ganymede, cf. *Kivelson et al.*, 1996).

Europa is also a primary target for future explorations. Determination of surface composition and detection of possible near-surface liquid will be among

the primary objectives of the recently approved ESA mission JUICE with two dedicated flybys (*Grasset et al.*, 2013). A Europa targetted flagship mission (Europa Clipper mission, *Pappalardo et al.*, 2013) is presently also under study by NASA.

1.2 Interior structure and dynamics

Among the Galilean satellites, Europa is the smallest and second in distance from Jupiter. The first three satellites, Io, Europa, and Ganymede, are locked together in the Laplace resonance with a mean motion ratio of 4:2:1 - in the time it takes Ganymede to orbit Jupiter once, Europa has gone around twice, and Io four times (e.g. *Alexander et al.*, 2009). This resonance prevents circularization of the satellites' orbits and maintains their eccentricity non-zero which leads to significant tidal deformations within the interior of these bodies (e.g. *Greenberg*, 1987; *Showman & Malhotra*, 1997; *Peale*, 1999). The associated tidal heating, mostly located within the ice shell, may be several times larger than radiogenic heating in the rocky core and might prevent Europa's ocean from freezing completely (*Tobie et al.*, 2003; *Sotin et al.*, 2009).

With a radius of 1562 km, Europa is slightly smaller than the Moon. Gravitational data collected by the Galileo spacecraft indicate that the satellite's interior is fully differentiated into a metallic core, a silicate mantle and an outer water ice/liquid shell approximately 80–170 km thick (*Anderson et al.*, 1998; *Schubert et al.*, 2009, cf. Figure 1.1). However, due to small density difference between liquid water and solid ice, these data provide no information on the thicknesses of the ocean and the outer ice shell. The existence of a subsurface liquid water ocean has been proposed based mainly on the results of geological studies of several surface features - cycloidal ridges, for example, provide an indirect evidence in favor of Europa's ocean (*Hoppa et al.*, 1999a). Nonetheless, the most compelling evidence for the ocean's existence was the detection of an induced magnetic field by the Galileo magnetometer - the measured data are consistent with an electri-

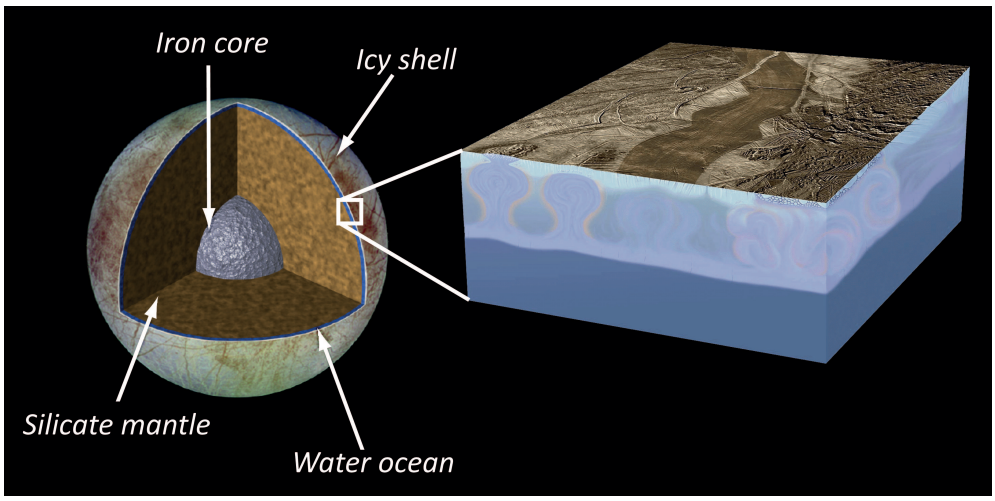

Figure 1.1: Model of Europa's subsurface structure. Courtesy NASA/JPL-Caltech.

cally conducting layer lying within 200 km from the surface with the electrical conductivity comparable with that of seawater on the Earth (*Khurana et al.*, 1998; *Kivelson et al.*, 2000).

Even though the interest in Europa (and icy satellites in general) increased during the last few decades and the associated research efforts intensified, several basic characteristics, such as the current thickness of the ice shell or its thermal state, remain still unconstrained. Many circular features identified on Europa's surface suggest that the ice shell was convecting at the time of their formation (*Pappalardo et al.*, 1998), however, it is not clear whether the ice shell is still convecting at present (*Barr & Showman*, 2009). The state of the ice shell (convective or conductive) depends mostly on the shell thickness and viscosity (*McKinnon*, 1999; *Barr & Pappalardo*, 2005). Unfortunately, no observations that would allow a robust assessment of the viscosity structure are available and the thickness estimates vary from a few kilometers to more than 40 km (e.g. *Ojakangas & Stevenson*, 1989; *Golombek & Banerdt*, 1990; *Williams & Greeley*, 1998; *McKinnon*, 1999; *Hussmann et al.*, 2002; *Nimmo et al.*, 2003; *Billings & Kattenhorn*, 2005). Various features observed at the surface may be compatible with a brittle-elastic lithosphere (1–2 km thick) above a ductile and possibly convecting layer at the time of formation (*Pappalardo et al.*, 1999), but it is again not clear whether the ice shell has remained in this state until now. *Mitri & Showman* (2005) have shown that slight (bottom) heat flux variations in thermal convection models with a near-critical Rayleigh number can induce a switch between a thin conductive ice shell (∼10 km) and a thick convective shell (∼30 km) at time scales of $\sim 10^7$ yr. Moreover, the model of coupled thermal-orbital evolution of Europa, tidally-locked together with its neighbor Io, predicts variations in the ice shell thickness over several tens of kilometers during Europa's evolution (*Hussmann & Spohn*, 2004) which might be compatible with the formation of different surface features on Europa.

1.3 Surface composition and age

While the surface of Europa appears smooth on a large scale with a relatively high geometric albedo of ∼0.67 (average of leading and trailing hemisphere values, cf. *Buratti & Veverka*, 1983), higher resolution images reveal extensive surface alteration caused by cracking of the cold (brittle) ice and possibly also by convective motions within the ductile portion of the icy shell.

The predominant material observed on Europa's surface is water ice (*Carlson et al.*, 2009), with pure ice present particularly on the leading hemisphere, while on the trailing hemisphere the distorted H_2O absorption spectra suggest presence of hydrated salts (*McCord et al.*, 1998) or hydrated sulfuric acid (*Carlson et al.*, 1999). Sulfur material may come from Europa's ocean (*Kargel et al.*, 2000) or be of exogenic origin and delivered from Io (and possibly other satellites), the jovian magnetosphere, and comet and meteorite impacts (*Carlson et al.*, 2009). Recently, *Brown & Hand* (2013) found a new absorption band which they associated with magnesium sulfate and predicted the dominance of chloride salts among the non-ice components of the leading hemisphere. Other species that might be present on Europa's surface include sulfur dioxide, polymeric sulfur, molecular oxygen, hydrogen peroxide, carbon dioxide, sodium, potassium and

others (*Carlson et al.*, 2009).

Chemical and physical processes that modify Europa's surface composition include impact gardening and micrometeoric deposition predominant on the leading hemisphere (cf. *Zahnle et al.*, 1998) and plasma implantation and high-energy electrons bombardment that prevails on the trailing hemisphere (*Tiscareno & Geissler*, 2003). These processes can lead to the observed hemispheric albedo differences, producing the 'white' and 'red' hemispheres (*Carlson et al.*, 2009).

When compared to the heavilly cratered terrains of her neighbors Ganymede and Callisto, Europa's surface displays a notable dearth of large impact craters (*Bierhaus et al.*, 2009). Their size frequency distributions lead to surface age estimates that range between 40 and 90 Myr, indicating a strikingly young surface (w.r.t. the solar system time scales), consistent with current geological activity and presence of an interior ocean (*Bierhaus et al.*, 2009; *Doggett et al.*, 2009).

1.4 Main tectonic features

While impact craters are scarce, there is an abundance of diverse tectonic and cryovolcanic surface features unique for Europa. The prevalence of global tension, along with the ice weakness, resulted in supremacy of extensional tectonics whereas crustal convergence features are less obvious (*Kattenhorn & Hurford*, 2009). Diurnal tidal stresses due to Europa's eccentric orbit are the most important source of stress that could account for the observed deformation on Europa's surface, together with non-synchronous rotation, shell thicknening, and possibly true polar wander (*Nimmo & Manga*, 2009; *Kattenhorn & Hurford*, 2009).

1.4.1 Extensional tectonics

The ubiquitous **double ridges** consist of a central crack or trough flanked by two raised edifices (Figure 1.2, left). They are the most common lineaments on

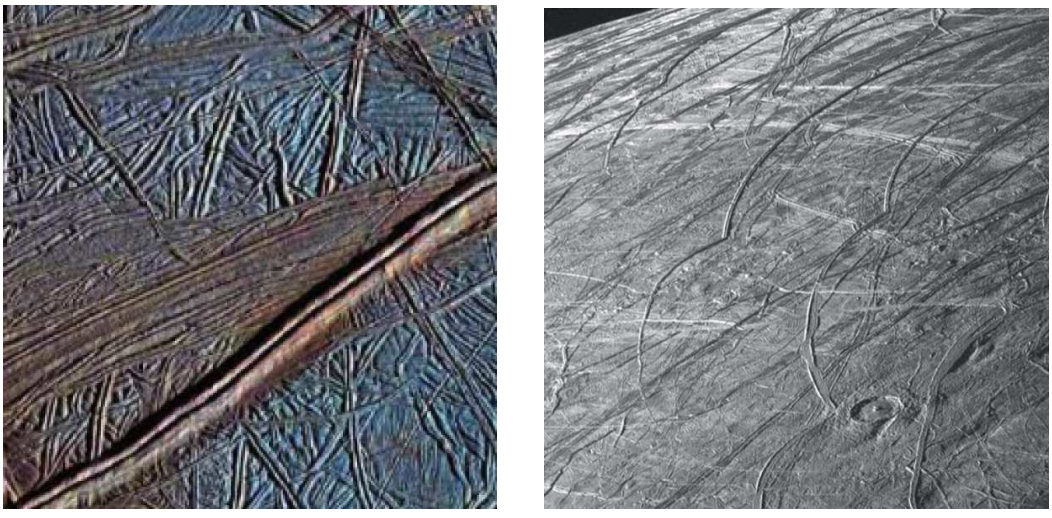

Figure 1.2: Example of double ridges (left) and cycloids (right). Courtesy NASA/JPL-Caltech.

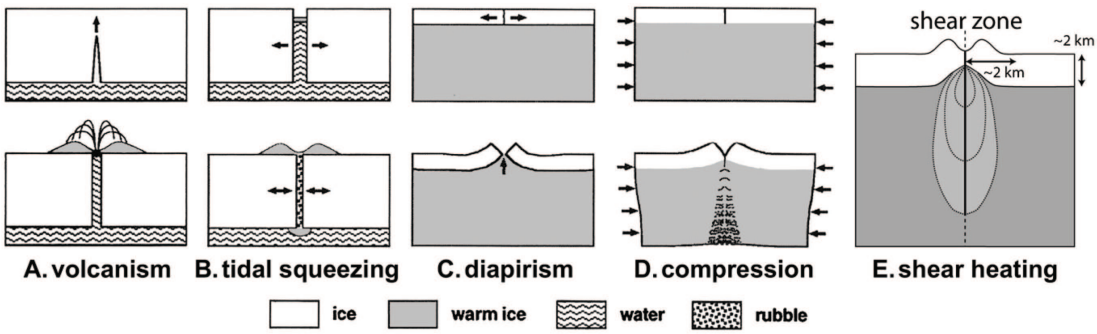

Figure 1.3: Various models for double-ridge formation on Europa. From *Aydin* (2006), which was adapted from *Pappalardo et al.* (1999) and *Nimmo & Gaidos* (2002).

Europa and may extend from a few kilometers to more than 1000 km across the surface. Double ridges make up the primary component of the oldest ridged plains and they comprise also some of the youngest geological features, indicating that they are the most persistent structures on Europa's surface (*Doggett et al.*, 2009; *Kattenhorn & Hurford*, 2009). Numerous models were proposed in order to explain their formation, such as cryovolcanism (where a pre-existing crack provides pathway for eruptions that build the ridge, cf. *Kadel et al.*, 1998, and Figure 1.3, panel a), tidal squeezing (with daily tidal forces opening and closing the crack and thus squeezing the material onto the surface, cf. *Greenberg et al.*, 1998, and Figure 1.3, panel b), diapirism (where the crack leads to a formation of a warm ice diapir that uplifts the ridge, cf. *Head et al.*, 1999, and Figure 1.3, panel c), compression (with the ridge representing the buckled lithosphere that borders the crack under a compressive stress, cf. *Sullivan et al.*, 1998, and Figure 1.3, panel d) or shear heating (where periodic shear motions on a crack dissipate heat that results in the warm, buoyant ice uplifting the ridge, cf. *Nimmo & Gaidos*, 2002, and Figure 1.3, panel e). Recently, based on observations of fractures on the double ridge flanks, *Dombard et al.* (2013) proposed a cryovolcanic sill model (cf. Figure 1.4) in which the growing ridge is underlain by a cryomagmatic sill that locally heats and thins the lithosphere, consistently with the observation of flanking fractures running parallel to double ridges. However, they do not provide

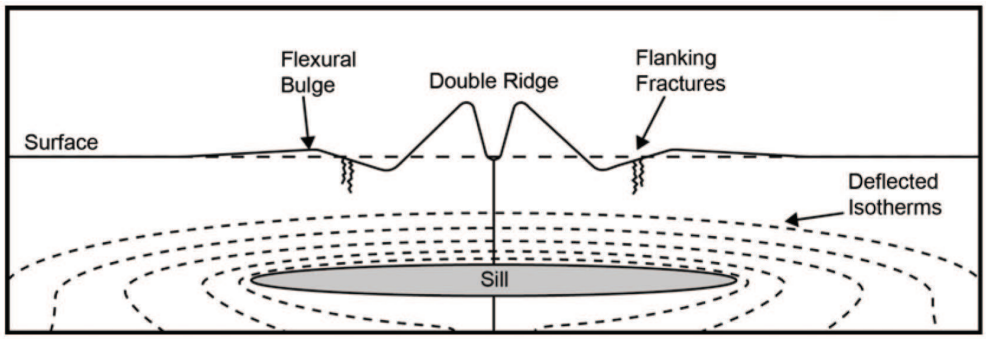

Figure 1.4: Cryovolcanic sill model. From *Dombard et al.* (2013).

a mechanism for the formation of such a sill.

Morphologically similar to ridges are **cycloids** (sometimes referred to as cycloidal ridges). These are curved cracks that form chains extending from hundreds to thousands of kilometers across Europa's surface (Figure 1.2, right) with each segment of typical length of tens of kilometers linked to the adjacent one at a cusp (*Kattenhorn & Hurford*, 2009). Tensile cracking in response to diurnally varying tidal stresses was proposed as a suitable mechanism for their formation (*Hoppa et al.*, 1999a).

Dilational bands composed of zones of new crustal material that intruded between the dilating walls of a tension fracture (Figure 1.5, left) represent an evidence of dilation in the icy shell and indicate a resurfacing process on the icy satellite (*Kattenhorn & Hurford*, 2009).

Relatively common are also **troughs** which lack the raised edifices and represent probably tension fractures that never developed into a more evolved landform (Figure 1.5, right). Based on crosscutting relationships, they constitute the youngest tectonic features on Europa thus providing the most promising indicator of recent to current activity (*Doggett et al.*, 2009; *Kattenhorn & Hurford*, 2009).

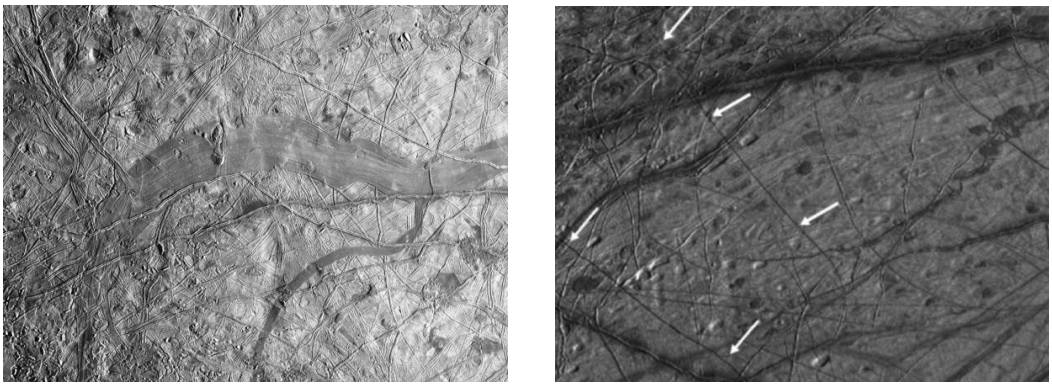

Figure 1.5: Example of dilational band (left) and troughs (right). Courtesy NASA/JPL-Caltech.

1.4.2 Compressive tectonics

Despite being less prominent, some contractional features must be present on Europa's surface to compensate for surface extension. The first discovered candidate features were parallel **folds** present within a dilational band (*Prockter & Pappalardo*, 2000), however these are scarce and insufficient to balance out the extension (*Kattenhorn & Hurford*, 2009). **Convergence bands**, across which a tectonic reconstruction reveals a zone of 'missing' crust (Figure 1.6, left), constitute another evidence for contraction on Europa. They form broad zones many kilometers wide and tens of kilometers long that appear to disrupt the surrounding terrain (*Greenberg*, 2004). *Mével & Mercier* (2005) also identified crustal disappereance in the Astypalaea Linea extensive region and proposed pressure melting to be responsible for the mobilization of surface material and its **collapse down** through the icy crust. Part of the contraction may also be accomodated by the ubiquitous **double ridges** as suggested by some authors (e.g. *Sullivan et al.*,

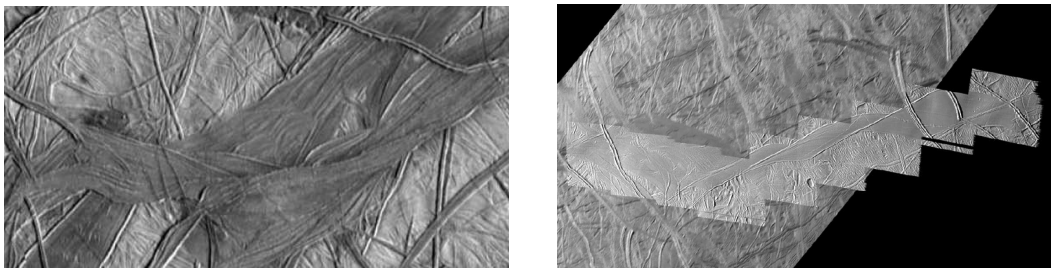

Figure 1.6: Example of convergence band (left) and band-like strike-slip fault (right). Courtesy NASA/JPL-Caltech.

1997; *Culha et al.*, 2014). Recently, *Kattenhorn & Prockter* (2014) proposed that **subduction** may be recycling surface material into the interior of Europa's ice shell, which would make Europa the only solar system body other than the Earth to exhibit a system of **plate tectonics**.

1.4.3 Lateral shearing

Lateral shearing occurs on Europa predominantly through reactivation of the existing structures (faults and fractures) in response to changes in the stress field due to temporal variations in the tidal forcing during each orbit (*Kattenhorn & Hurford*, 2009). Lateral offsets large enough to be recognized in satellite images arise along ridges and dilational bands - accordingly, ridge-like and band-like **strike-slip faults** (Figure 1.6, right) are distinguished (*Kattenhorn*, 2004). Typical lateral offsets of the former are in the range of hundreds of meters to several kilometers (*Hoppa et al.*, 2000), while the latter have lateral offsets of tens of kilometers (*Kattenhorn*, 2004). In the case of ridge-like strike-slip faults, frictional shearing may contribute to the ridge development (*Nimmo & Gaidos*, 2002). Constantly changing diurnal tidal stresses were suggested to drive the strike-slip motions along faults through a process of **tidal walking** (*Hoppa et al.*, 1999b).

1.5 Chaotic terrain

Approximately one quarter of Europa's surface is covered by **chaotic terrains**, that appear to be unique to Europa (*Collins & Nimmo*, 2009). This widespread type of terrain is formed by disruption of the preexisting surface into isolated plates and formation of lumpy matrix material between these plates (e.g. *Carr et al.*, 1998, Figure 1.7, left). While some chaos areas consist of densely packed fractured blocks and narrow strips of matrix between them, others are made up of almost all matrix and no blocks (*Collins et al.*, 2000, e.g. Murias Chaos on Figure 1.7, right). The most intensely studied chaos area, Conamara Chaos (Figure 1.8, left), lies in the middle of this range with ∼60% of its area composed of matrix and the remainder of blocks (*Spaun et al.*, 1998). Chaotic terrains were also identified in the interiors of **lenticulae** (Figure 1.8, right), small features that can be further categorised into three major classes (cf. *Spaun et al.*, 1999): **domes** (upraised domical features which commonly do not affect the texture

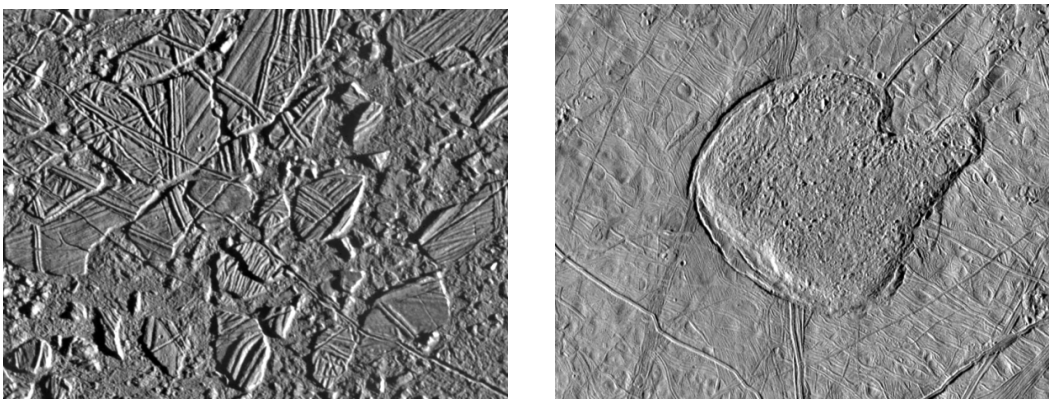

Figure 1.7: Example of chaos terrain (left) and Murias Chaos (right). Courtesy NASA/JPL-Caltech.

of preexisting terrain), **spots** (smooth low albedo areas which subdue or conceal preexisting terrain), and **pits** (lenticulae that have disrupted the preexisting terrain and sometimes contain a chaos-like matrix material).

The plates of disrupted terrains within chaos regions range in size from approximately 1 km to 20 km across and are usually topographically higher than the surrounding matrix (*Collins & Nimmo*, 2009). Many of them have moved from their original positions - for Conamara Chaos, *Spaun et al.* (1998) reported that at least 78% of the blocks shifted by an average of 2 km of lateral translation. In addition, some plates were found to have rotated around their vertical axes and several plates have tilted (*Spaun et al.*, 1998; *Collins & Nimmo*, 2009). The adjacent matrix is formed from irregular material that appears to be a jumbled collection of ice chunks of all sizes, from a kilometer to tens of meters acros (*Collins et al.*, 2000) and usually lies topographically higher than the background terrain (*Collins & Nimmo*, 2009).

Several models were designed to explain chaotic terrains formation. In the melting through the icy shell model (*Greenberg et al.*, 1999; *Thomson & Delaney*, 2001, cf. Figure 1.9, panel a), the surface exposure of the underlying ocean is

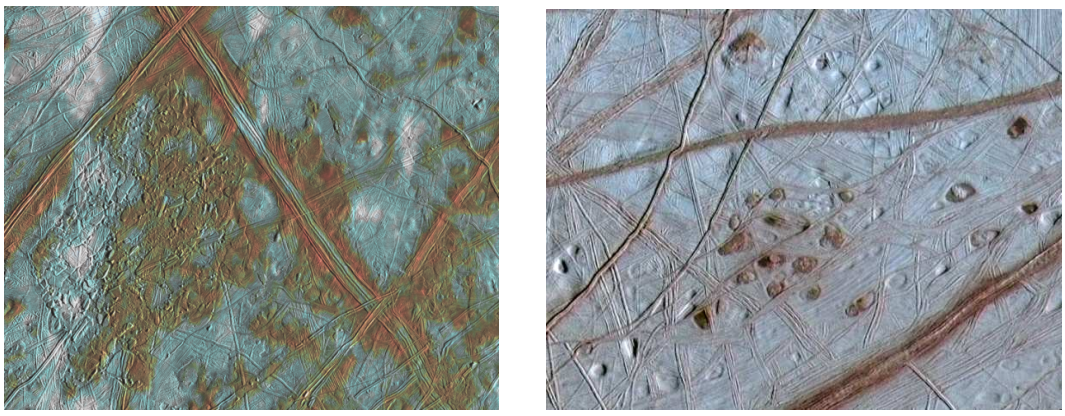

Figure 1.8: Conamara Chaos (left) and example of lenticulae (right). Courtesy NASA/JPL-Caltech.

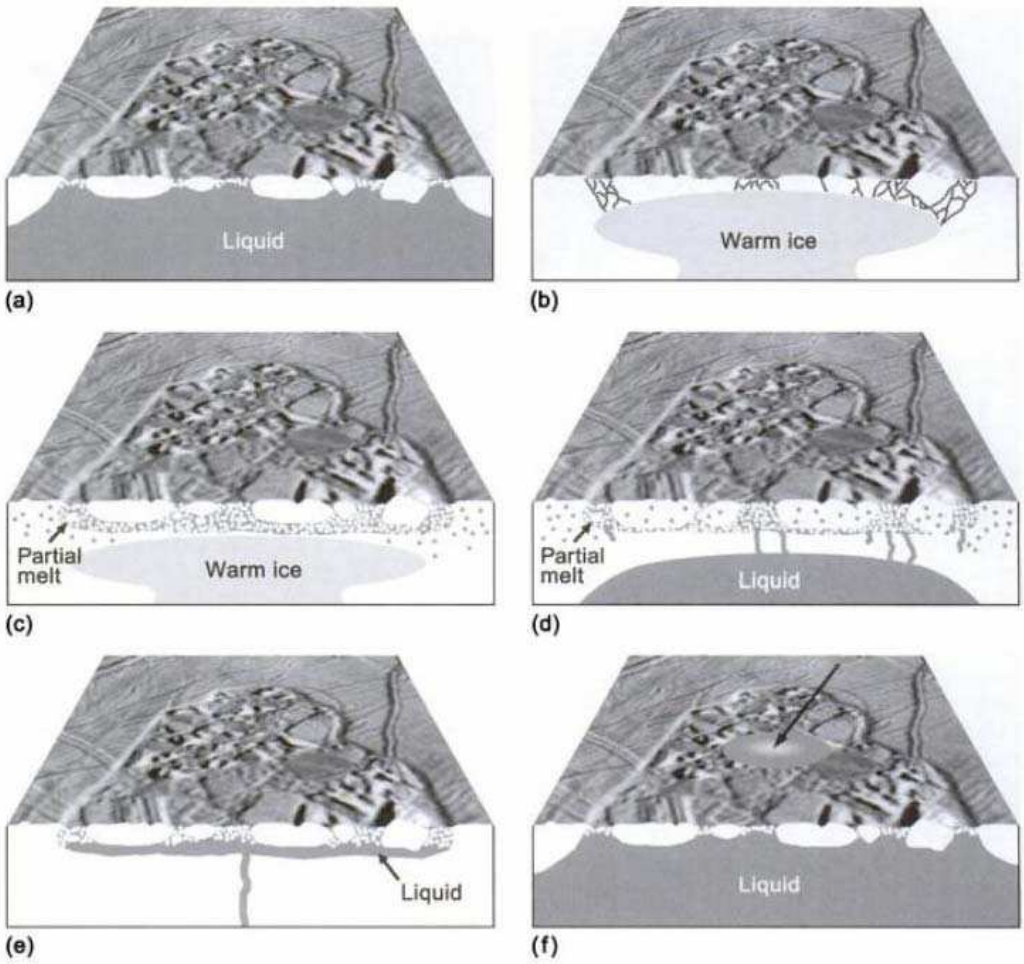

Figure 1.9: Various models for chaos formation on Europa: (a) melt-through, (b) diapirism, (c) brine mobilization driven by diapirism, (d) brine mobilization driven by partial melt-through, (e) sill formation, and (f) impact. From *Collins & Nimmo* (2009).

envisioned as a result of a strong heat source at the base of the icy shell that melted through it - the plates can then float in the ocean and the matrix is formed as the top of this ocean freezes. Thermally or compositionally buoyant diapirs were proposed in order to explain formation of both, small and large domical features (*Rathbun et al.*, 1998; *Figueredo et al.*, 2002; *Mével & Mercier*, 2007, cf. Figure 1.9, panel b). Diapir-driven brine mobilization where rising diapir of clean ice mobilizes lower-melting-temperature brines in the upper part of the ice shell leading to disintegration of surface and providing a detachment layer necessary for plate motions was proposed by *Head & Pappalardo* (1999) and *Collins et al.* (2000) (cf. Figure 1.9, panel c). A hybrid model, that would combine the melt-through model with a brine mobilization might overcome problems of these two individual models and thus represents a promising base for further investigation (*Collins & Nimmo*, 2009, cf. Figure 1.9, panel d). Water necessary for the chaos blocks to move and tilt might be delivered below Europa's surface also directly from the ocean by injection due to pressure build up in the ocean (as a result

of the ice shell thickenning, cf. *Manga & Wang*, 2007; *Collins & Nimmo*, 2009, and Figure 1.9, panel e). Contrary to the previous endogenic heating models, an exogenic impact was proposed by *Billings & Kattenhorn* (2003) on the basis of similar morphologies between Europa's chaos terrains and terrestrial explosion craters on floating ice (cf. Figure 1.9, panel f). Finally, in their recent study, *Schmidt et al.* (2011) proposed a lense collapse model in which chaos terrains originate as a result of ice blocks movement in water lenses that formed due to eutectic melting as shallow as 3 kilometers below the surface and refreezed (cf. Figure 1.10).

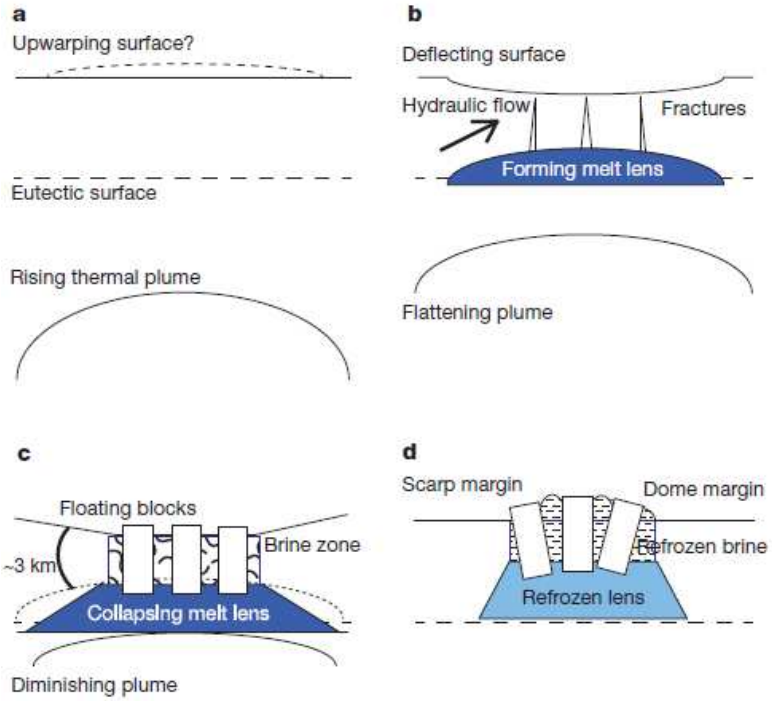

Figure 1.10: Lense collapse model. From *Schmidt et al.* (2011).

1.6 Ice shell - mechanical properties and heat sources

1.6.1 Viscous rheology

As already mentioned above (Section 1.2), the state of Europa's ice shell strongly depends on its viscosity structure, which unfortunatelly is not well constrained. At the surface and at shallow depths, where temperatures are very low, the ice is expected to behave in a brittle manner and to undergo a brittle failure along preexisting cracks (e.g. *Nimmo & Manga*, 2009). In numerical simulations, this behavior is often parametrized by the use of plastic rheology (e.g. *Showman & Han*, 2005) which is however not considered in the present work.

At greater depths, the temperatures increase thus allowing ductile deformation. Ice is known to have a highly nonlinear rheology, with at least four known deformational mechanisms (diffusion creep, dislocation creep, grain boundary

	T K	A_i $\mathrm{m}^m\ \mathrm{Pa}^{-n}\ \mathrm{s}^{-1}$	n_i	m_i	E_i $\mathrm{kJ\ mol}^{-1}$	V_i $\mathrm{m}^3\ \mathrm{mol}^{-1}$
μ_{diff}	—	3.3×10^{-10}	1.0	2.0	59	-13×10^{-6}
μ_{disl}	≤ 258	4.0×10^{-19}	4.0	0.0	60	-13×10^{-6}
	> 258	6.0×10^{4}	4.0	0.0	180	-13×10^{-6}
μ_{bs}	—	2.2×10^{-7}	2.4	0.0	60	-13×10^{-6}
μ_{gbs}	≤ 255	6.2×10^{-14}	1.8	1.4	49	-13×10^{-6}
	> 255	4.8×10^{15}	1.8	1.4	192	-13×10^{-6}

Table 1.1: Creep parameters of ice (after *Goldsby & Kohlstedt*, 2001; *Durham et al.*, 2001). Value of prefactor A_i in the case of diffusion creep is computed by taking into account only the volume (Nabarro-Herring) diffusion creep, neglecting grain boundary (Coble) diffusion creep and using T=T_0 (cf. *Goldsby & Kohlstedt*, 2001), thus reducing the temperature dependence of diffusion creep only to the exponential decrease.

sliding and basal slip, cf. *Durham et al.*, 2001; *Goldsby & Kohlstedt*, 2001), each characterized by a respective viscosity μ_{diff}, μ_{disl}, μ_{gbs} and μ_{bs}. Viscosity of each mechanism depends in general on temperature T, pressure P, grain size d, and the second invariant of the deviatoric stress σ_{II} as:

$$\mu_{\mathrm{i}} = \frac{1}{2} \frac{d^{m_{\mathrm{i}}}}{A_{\mathrm{i}} \sigma_{\mathrm{II}}^{n_i - 1}} \exp\left(\frac{E_{\mathrm{i}} + P\, V_{\mathrm{i}}}{RT}\right) , \tag{1.1}$$

where exponents m_{i} and n_{i}, prefactor A_{i} and activation parameters E_{i} and V_{i} are specific to each creep mechanism and given in Table 1.1, $\sigma_{\mathrm{II}} = (\frac{1}{2} \sum_{\mathrm{kl}} \sigma_{\mathrm{mkl}} \sigma_{\mathrm{mkl}})^{\frac{1}{2}}$ and σ_{mkl} are the components of deviatoric stress tensor of the ice matrix[1]. Considering the composite creep as in *Goldsby & Kohlstedt* (2001), we approximate the effective viscosity μ_{m} of the ice matrix as follows

$$\frac{1}{\mu_{\mathrm{m}}} = \frac{1}{\mu_{\mathrm{diff}}} + \frac{1}{\mu_{\mathrm{disl}}} + \frac{1}{\mu_{\mathrm{gbs}} + \mu_{\mathrm{bs}}} . \tag{1.2}$$

In numerical simulations, it is often convenient to simplify the complex ice rheology by assuming a certain grain-size and stress regime - ice viscosity in that regime is then represented by a reference value modulated only by a temperature-dependent rate factor. An example of such simplification is the Arrhenius-like temperature dependence used e.g. by *Běhounková et al.* (2012):

$$\mu_{\mathrm{m}} = \mu_{\mathrm{m}}^{\mathrm{ref}} \exp\left(\frac{E_{\mathrm{a}}}{RT_{\mathrm{ref}}}\left(\frac{T_{\mathrm{ref}}}{T} - 1\right)\right) , \tag{1.3}$$

with $\mu_{\mathrm{m}}^{\mathrm{ref}}$ the reference viscosity (typically of the order of 10^{15} Pa s), T_{ref}=255 K the reference temperature, $R \doteq 8.314\ \mathrm{J\ K}^{-1}\ \mathrm{mol}^{-1}$ the universal gas constant, and E_{a} the activation energy that accounts for the premelting effect at temperatures

[1]The subscript m denotes the matrix, i.e. the dominant phase in the two-phase description, cf. Chapter 3.

close to the melting point (cf. *Durham et al.*, 2001; *Goldsby & Kohlstedt*, 2001):

$$E_{\mathrm{a}} = \begin{cases} 50 & \text{kJ mol}^{-1} \quad T<T_{\mathrm{ref}} \\ 190 & \text{kJ mol}^{-1} \quad T\geq T_{\mathrm{ref}} \end{cases} \quad . \tag{1.4}$$

Finally, the presence of meltwater significantly reduces the viscosity of the matrix by attenuating the internal stress field in the ice crystals and thus promoting basal slip (*De La Chapelle et al.*, 1999). Following *Tobie et al.* (2003), we include this effect by introducing into the above formulae also a porosity-dependent factor

$$\mu_{\mathrm{m}} = \mu_{\mathrm{m}}^{\mathrm{pure}} \exp(-\gamma_{\mathrm{m}}\phi) \ , \tag{1.5}$$

where $\mu_{\mathrm{m}}^{\mathrm{pure}}$ is the viscosity of pure (meltwater free) ice, given by either eq. (1.2) or eq. (1.3), and parameter $\gamma_{\mathrm{m}}\doteq 45$ roughly corresponds to one order of magnitude reduction in viscosity as a result of 5% porosity increase found by *De La Chapelle et al.* (1999).

1.6.2 Heat distribution within the ice shell

The presence of meltwater at shallow depth, a necessary ingredient of some morphological models of surface features formation (e.g. *Schmidt et al.*, 2011; *Dombard et al.*, 2013) is largely complicated by the very low surface temperature of Europa (∼100 K, e.g. *Ojakangas & Stevenson*, 1989). The production of meltwater within Europa's ice shell is considered to be the consequence of tidal heating expected presently in two main scenarios.

First of them is melting within thermal hot plumes, first suggested by *Sotin et al.* (2002) and further investigated by *Tobie et al.* (2003) and *Mitri & Showman* (2008). In this context, melting is a result of tidal heating enhanced due to thermally-reduced viscosity. *Tobie et al.* (2003) proposed this heat source could be parametrized as

$$H_{\mathrm{t}} = \frac{2H_{\mathrm{t}}^{\max}}{\mu_{\mathrm{m}}/\mu_{\mathrm{m}}^{\max} + \mu_{\mathrm{m}}^{\max}/\mu_{\mathrm{m}}} \ , \tag{1.6}$$

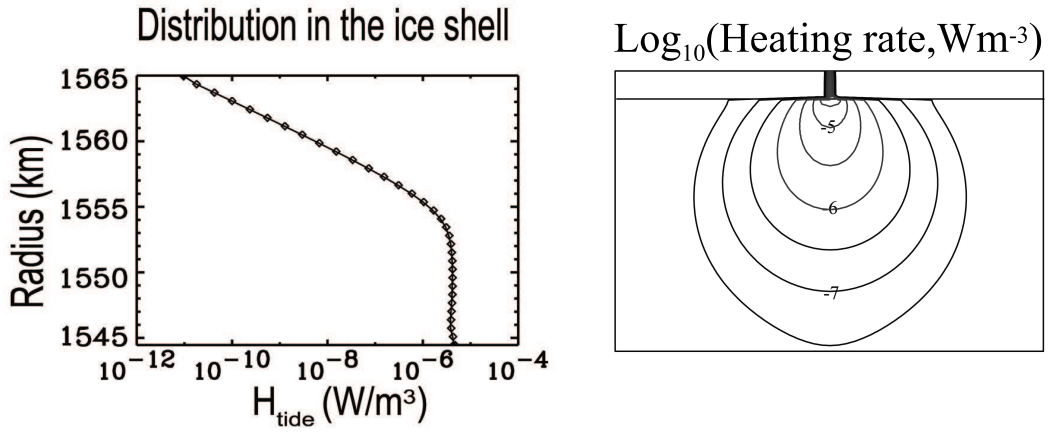

Figure 1.11: Heat distribution in the ice shell for the two considered contexts: hot plume (left, from *Tobie et al.*, 2003) and strike-slip fault (right, from *Nimmo & Gaidos*, 2002). Thickness of the shell is 20 km in both cases and the brittle layer in the case of strike-slip fault (right panel) is 2 km thick.

where $H_{\mathrm{t}}^{\mathrm{max}}$ is the maximum heating rate of the order of 10^{-6} W m^{-3} that occurs for viscosity $\mu_{\mathrm{m}}^{\mathrm{max}} \sim 1.5 \times 10^{14}$ Pa s. For ice viscosities close to the melting point ($\sim 10^{13}$–10^{15} Pa s), the Maxwell time (i.e. $\tau_{\mathrm{M}} = \mu_{\mathrm{m}}/G$, with G the shear modulus) is close to Europa's orbital period and the tidal heating might be strong enough to initiate melting within the warm convecting ice (cf. left panel of Figure 1.11).

Shear motions along tidally-activated strike-slip faults result in very strong, localized heating that might also intiate melting, as first suggested by *Gaidos & Nimmo* (2000) and further studied by *Nimmo & Gaidos* (2002). They found that for shear velocities of the order of 10^{-6} m s^{-1}, appropriate for Europa's diurnal tides, the heating amplitudes may be as high as 10^{-4} W m^{-3} and may promote melting as shallow as few kilometers (cf. right panel of Figure 1.11).

While the former mechanism requires the ice shell to be in a convective regime, the latter is rather insensitive to the thermal state since it is localized in the coldest (brittle) part of the layer along the faults and at the transition between the brittle and the ductile layer (*Nimmo & Gaidos*, 2002). While the melting processes responsible for water generation inside the ice shell appear to be relatively well studied, only little attention has so far been paid to meltwater propagation, which we discuss in the next chapter.

2. Water transport mechanisms in ice

In the previous chapter, we have discussed possible mechanisms of melt generation at shallow depths within Europa's ice shell. Regardless of the source of heating, a major issue concerns the thermal and gravitational stability of potential water reservoirs - due to the higher density of water relative to the surrounding ice, these perched reservoirs should be drained rather rapidly (*Nimmo & Giese*, 2005). In numerical simulations of thermal convection within icy satellites' shells the dynamic effect of melt generation and accumulation is often completely neglected (e.g. *Sotin et al.*, 2002; *Han & Showman*, 2005; *Mitri & Showman*, 2005; *Han & Showman*, 2010) or highly simplified (*Běhounková et al.*, 2012, 2013). The goal of this chapter is to give an overview of possible mechanisms that would assure the transport of liquid water through the ice shell.

To gain some insight, it is tempting to investigate liquid water transport through a closer analogue, the terrestrial glaciers. The hydrological configuration of a glacier is significantly influenced by its thermal structure (*Irvine-Fynn et al.*, 2011) and since the thermal conditions that can occur in glaciers vary substantially, a special terminology was proposed to better distinguish between particular cases. **Temperate** ice is at the pressure melting point with some amount of interstitial liquid water of up to few percents (*Pettersson et al.*, 2004) coexisting within the ice. Contrastingly, **cold** ice is below the pressure melting point and exhibits negligible interstitial water (*Irvine-Fynn et al.*, 2011). **Polythermal** glaciers are then defined as ice masses where temperate and cold ice are simultaneously present with various configurations of these distinct thermal structures possible (e.g. *Blatter & Hutter*, 1991; *Irvine-Fynn et al.*, 2011).

Extensive reviews of glacial hydrology for temperate and polythermal glaciers can be found e.g. in *Fountain & Walder* (1998) and *Irvine-Fynn et al.* (2011), respectively. Here, we only summarise basic characteristics. The glacier hydrological system comprises surface (**supraglacial**), internal (**englacial**), and basal (**subglacial**) components, with their roles and their mutual coupling varying over space and time (*Irvine-Fynn et al.*, 2011, cf. also schematic Figure 2.1). After the onset of melting season, the enhanced solar radiation provides an increasing amount of meltwater, leading to gradual development of a supraglacial hydrological system (*Fountain & Walder*, 1998). Since the ice permeability near the glacier surface is lower than within the glacier body (*Lliboutry*, 1996), the intergranular drainage (**primary permeability**) is probably negligible and the water flowing to lower altitudes gets eventually captured in surface-reaching crevasses and/or moulins. It is thus this **secondary permeability** that represents the most efficient way of draining meltwater from the glacier surface (*Irvine-Fynn et al.*, 2011). The distribution of crevasses therefore controls the extent to which supraglacial meltwater is routed across the glacier surface before entering the englacial system (*Nienow & Hubbard*, 2006) and the dearth of water-filled crevasses indicates that the supraglacial meltwater is directed into the glacier interior quite efficiently (*Fountain & Walder*, 1998).

Within the glacier, there are two distinct permeable pathways. At the largest

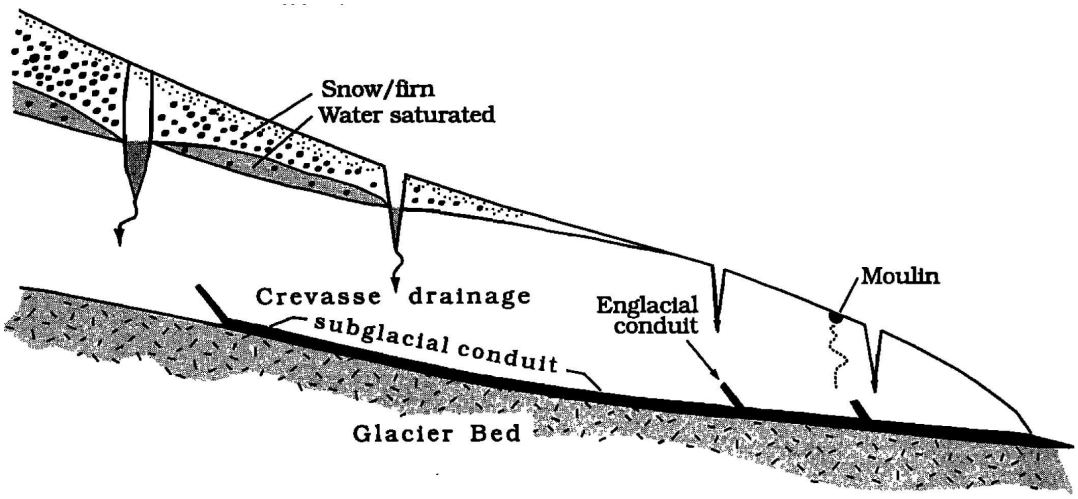

Figure 2.1: The main components of the glacier hydrological system. From *Fountain & Walder* (1998).

scale, this pathway is provided by surface crevasses (*Nienow & Hubbard*, 2006) which tend to propagate downwards by a combination of hydrofracturing and/or frictional downcutting. If sufficiently supplied by meltwater, the crevasses can penetrate all the way to the glacier base and establish an efficient hydrological connection between the surface and the basal drainage system. This **macroscopic water system** (MWS) can route significant volumes of water to the bed of the glacier (*Gusmeroli et al.*, 2010). Polycrystalline ice is permeable also at the microscale through a network of water-filled veins that are formed at the three-grain intersections joining together in fours at the four-grain intersections (*Nye & Frank*, 1973; *Nye*, 1989, cf. also Figure 2.2) and creating the **microscopic water system** (mWS). This system is primarily controlled by ice temperature

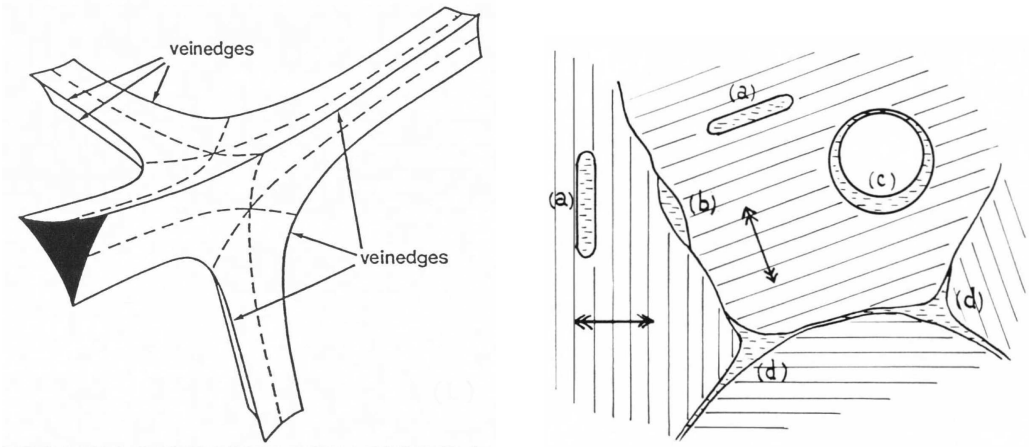

Figure 2.2: Left: Node of a vein system. From *Nye* (1989). Right: Water inclusions in polycrystalline ice - (a) intracrystalline, (b) on two-grain intersection, (c) air bubbles, and (d) three-grain intersection inclusions (that correspond to these in left panel). From *Lliboutry* (1971).

and is only present in temperate parts of glaciers (*Gusmeroli et al.*, 2010). In both cases, the water propagation through a glacier is usually described by Darcy law, thus neglecting the interaction forces between water and ice (e.g. *Greve*, 1997; *Aschwanden & Blatter*, 2009).

At the glacier base, the hydrological network interacts in a very complicated manner with both the overlying glacier and the underlying till (or bedrock), and operates basically in two regimes, the high-pressure linked cavity network or the low-pressure channels (e.g. *Paterson*, 1981; *Fountain & Walder*, 1998).

Application of the knowledge gained at the Earth conditions to the icy satellites' shells is not straightforward. The understanding of water transport through the ice shells is largely complicated by the fact that the precise conditions within are far from certain despite the intense research efforts during the last few decades. In the following text, we consider three main physical mechanisms to be potentially able to destabilize the water reservoirs and be responsible for downward water drainage. Where necessary, we take Europa as an example, but our findings should be valid for shells of icy satellites in general.

2.1 Crevasse hydrofracturing

Hydrofracturing is a process of crack propagation within the brittle ice structure promoted by meltwater supply. This mechanism is dominant on the Earth and typically allows for very rapid water drainage (*Krawczynski et al.*, 2009). However, reliable estimates of the efficiency of this drainage process require rather detailed knowledge of the hydrological network within the layer.

Theoretical formulation of the problem of fracture propagation through the ice layer can be based on the linear elastic fracture mechanics (LEFM, cf. *Weertman*, 1996). Crack propagation in a medium subjected to background tensional/compressional stress is in this framework controlled by the evaluation of stress intensity factor at the tip of a crack and by its comparison with the critical value that represents the fracture toughness. The additional pressure resulting from partial filling of the crack by water can greatly promote its propagation (*Weertman*, 1971), or even lead to fracture pinch-off followed by its gravity-driven descent in analogy with rising magma-filled chambers (*Weertman*, 1973). Weertman's theory predicts also the crevasse equilibrium shape for given stress conditions, elastic properties and water column height, however, it does not provide any time scale for the crevasse propagation. This complicates any attempts to provide quantitative estimate of hydrofracture transport efficiency.

In their early study, *Crawford & Stevenson* (1988) applied LEFM to investigate the possibility of downward water-free crack propagation, or conversely, upward propagation of water-filled cracks. They excluded the possibility of water-free cracks extending across the whole ice shell, on the other hand, they argued that water-filled cracks propagating upwards might reach Europa's surface provided they contain enough exsolved gas. Recently, *Lee et al.* (2005) and *Rudolph & Manga* (2009) revisited the subject of ice shell cracking under the applied tensional stresses (e.g. due to tides, non-synchronous rotation, or ice shell thickening). While the former study found that surface cracks may penetrate through the entire outer brittle layer, the results of the latter indicate that the entire shell would be completely cracked only when sufficiently thin ($\lesssim$2.5 km). Both studies

assume only water-free cracks originating at the surface.

Irrespective of the uncertainties on the ice shell structure and tectonic context, one would be tempted to use an analogy with the processes in terrestrial glaciers when addressing the possible water transport mechanisms through icy satellites' shells. It is nevertheless crucial not to overlook several important differences between the physical setting within the ice shell of Europa and that within the Earth's glaciers. Since the outer ice shell is underlain by a global water ocean, the subglacial drainage system at the interface between the ice and the underlying bedrock, so typical and perhaps the most complex part of the hydrological network in terrestrial glaciers, is completely missing. In addition, the very low surface temperature (∼100 K, cf. *Ojakangas & Stevenson*, 1989) probably eliminates any supraglacial system of crevasses and moulins, thus making the hydrological network effectively closed from above. With the possible exception of surface-reaching strike-slip faults (*Nimmo & Gaidos*, 2002), all the meltwater would be generated in the bulk by viscous tidal heating, often several kilometers below the surface (*Sotin et al.*, 2002; *Tobie et al.*, 2003). In the interior of the shell, hydrofracturing is less likely since the overburden pressure probably maintains the ice in compressional regime and thus limits crack initiation (cf. *Weertman*, 1996). Even if cracks developed, the estimated meltwater production rates are smaller by few orders of magnitude compared to the terrestrial supply during the melting season. For frictional heat generation rate at the fault of 10^{-4} W m^{-3} (*Nimmo & Gaidos*, 2002) and for the fault thickness of the order of 10^3 m, the estimated heat flux is $\sim 10^{-1}$ W m^{-2}, which is significantly smaller than typical values obtained for Alpine glaciers ($\sim 10^1$–10^2 W m^{-2}, cf. *Hock*, 2005). The resulting meltwater supply might thus be insufficient to feed the crevasses by the appropriate amount required for hydrofracturing across the whole ice layer, particularly if refreezing is efficient. Besides, the thickness of Europa's ice shell (at least a few tens of kilometers, e.g. *Schubert et al.*, 2009) is one order of magnitude larger than that of the biggest terrestrial glaciers which does not exceed a few kilometers.

2.2 Two-phase flow

If we neglect hydrofracturing for reasons mentioned above and rule out voids (that are unlikely due to large overburden pressure), then any meltwater flow through the ice shell must be compensated by an accompanying flow of the viscously-deforming ice. The mechanical coupling between the two phases is thus much stronger than in the glaciers on the Earth and must be taken into account. The problem of ice melting and subsequent meltwater propagation within the shells of icy satellites is then rather similar to the problem of silicate magma generation and transport through the Earth's mantle and thus requires the adoption of a two-phase formalism (developed originally for magma generation and transport, e.g. *McKenzie*, 1984; *Scott & Stevenson*, 1984, 1986; *Spiegelman*, 1993a; *Bercovici et al.*, 2001; *Šrámek et al.*, 2007) in order to capture the complex thermomechanical coupling between the viscously deforming matrix and the melt flow. As the problem is rather complicated per se, several approximations have been introduced, such as 'small porosity approximation' (e.g. *Connolly & Podladchikov*, 2007) or 'zero compaction length approximation' (e.g. *Scott & Stevenson*, 1989;

Spiegelman, 1993a,b), with the latter neglecting the effect of matrix deformation on melt flow. Typical feature of two-phase systems is the formation of nonlinear porosity waves (cf. *Scott et al.*, 1986; *Olson & Christensen*, 1986; *Spiegelman*, 1993a). While numerical modeling of two-phase flow is well established among the mantle flow community, no study has yet, to our best knowledge, attempted to apply this formalism for ice shells despite the potentially important impact on the ice shell dynamics.

Considering the ice shell as a two-phase mixture of water ice and liquid water, then water, as the less viscous phase (melt), would be transported through the more viscous phase (ice matrix) by a system of interconnected channels, in glaciological literature well known as a microscopic water system (e.g. *Gusmeroli et al.*, 2010, cf. above). For low dihedral angle measured for the ice-water system (with typical values around 30°, e.g. *Mader*, 1992a; *Walford et al.*, 1987; *Walford & Nye*, 1991), the melt phase is interconnected even at small porosities (volume fractions of water in the water-ice mixture, e.g. *Nye & Frank*, 1973; *Mader*, 1992b). The meltwater transport by this mechanism is expected to be predominant in sufficiently large regions of partially molten material, such as within the hot plumes. We provide a more detailed mathematical description of flow of liquid water through the viscously deforming ice matrix in Chapter 3.

The key parameter in two-phase flow modeling is **permeability**, i.e. the ability of a material to transmit fluids. In many applications, a simple power-law function of porosity ϕ with the exponent typically between 2 and 3 is assumed (e.g. *McKenzie*, 1984; *Scott & Stevenson*, 1984; *Spiegelman*, 1993b; *Rabinowicz et al.*, 2002; *Šrámek et al.*, 2007). Ice permeability generally depends on numerous state and material parameters, such as the geometric properties of the pore system (pore diameter and tortuosity of the path), pressure in the liquid, temperature and composition (salinity, presence of ammonia), deformation history etc. (cf. *Lliboutry*, 1996; *Petrich et al.*, 2006; *Golden et al.*, 2006, 2007; *Petrich & Eicken*, 2009). Depending on the physical context and growth mechanisms of ice crystals, ice permeability may also exhibit anisotropy (*Freitag & Eicken*, 2003) and it may abruptly decrease for very small porosities (below a certain porosity, the 'percolation threshold' ϕ_c). This decrease corresponds to the closure of the net of veins and microchannels in the matrix and subsequent drop in its connectivity (*Golden et al.*, 1998). Measurements of ice permeability reveal variations over several orders of magnitude (e.g. *Freitag*, 1999; *Eicken et al.*, 2002; *Freitag & Eicken*, 2003; *Kawamura et al.*, 2006; *Golden et al.*, 2007). In this work, we consider scalar (isotropic) permeability in the standard form

$$k(\phi) = k_0 \phi^n \ , \tag{2.1}$$

with n=2 and 3 and we include the uncertainty in magnitude by varying k_0 accordingly, in order to capture the whole range of admissible situations. To mimic the abrupt permeability decrease below percolation threshold, we also employ the following expression in the parametric studies in Sections 5.2.2 and 6.3.2:

$$k(\phi) = k_0 \begin{cases} ((\phi - \phi_c)^2 + k_0^c) & \phi \geq \phi_c \\ k_0^c \left(\frac{\phi}{\phi_c}\right)^4 & \phi < \phi_c \end{cases} . \tag{2.2}$$

Figure 2.3 compares the measured values of ice permeability with the theoretical

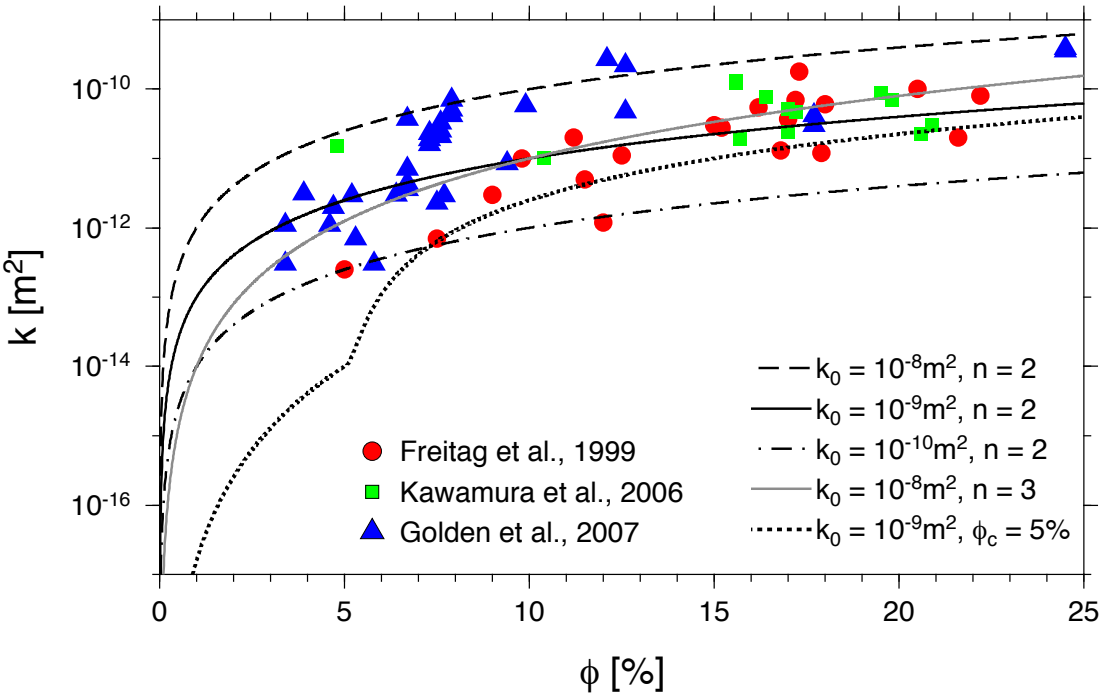

Figure 2.3: Comparison of measured values of ice permeability (colored symbols) with the theoretical curves considered in this work (black and gray lines). Measured values have been read from figures in *Freitag* (1999), *Kawamura et al.* (2006) and *Golden et al.* (2007).

curves obtained for different permeability laws considered in this work. The curve for the smallest value of k_0 (10^{-10} m^2) and n=2 (dot-dashed in Figure 2.3) is used in Chapter 7, where it provides the lower bound on permeability and thus the upper bound on the extraction time scale.

2.3 Rayleigh-Taylor instabilities

In case of totally impermeable ice (with no cracks or pores), a third mechanism involves gravitational destabilization of large liquid water reservoirs by Rayleigh-Taylor (R-T) instabilities in the water-ice system. This instability develops at the interface between two viscous fluids of different densities. If the interface is slightly distorted, a small pressure gradient evolves that (in viscous fluids) initiates a slow flow even for very small pressures (*Whitehead & Luther*, 1975). Several factors influence the development of R-T instability, such as the density ratio between the two fluids, surface tension, viscosity ratio etc. (e.g. *Sharp*, 1984).

Gravitational destabilization of liquid water reservoir by R-T instability would probably require accumulation of substantial volume of meltwater underlain by sufficiently impermeable (cold) ice - otherwise, the liquid water would rather be drained by microscopic two-phase flow. This may be possible only in the vicinity of localized frictional heat sources at strike-slip faults, or in the zones with reduced melting temperature (e.g. due to presence of salts) heated from below by ascending plumes. According to the analytical description of *Whitehead*

& Luther (1975), the time required to destabilize a dense water reservoir (of a few meters thickness) above a half-space ice layer is longer than 10 kyr only for ice viscosities of at least 10^{22} Pa s - such high viscosity values are possible only for temperatures $\leq$150 K, which implies that destabilization by R-T instability would be quite efficient, except in the case of an extremely cold conductive layer subjected very locally to intense heating.

As shown by *Tobie et al.* (2003), a small fraction (<2%) of interstitial melt is sufficient to create a negative density buoyancy that overcomes the thermal buoyancy and leads to rapid downwelling with the residence time of partially molten ice in the head of a hot plume around few tens of thousands of years.

Summary of Part I

Apart from the global subsurface ocean, the existence of which is now generally accepted, liquid water might be present also within Europa's ice shell. Recent morphological analyses of chaos terrains (*Schmidt et al.*, 2011) and double ridges (*Dombard et al.*, 2013) as well as the UV spectra observations consistent with water vapor eruptions (*Roth et al.*, 2014), support the hypothesis of presence of liquid water within the ice shell in the form of lenses or sills located a few kilometers below the surface. However, these interpretations are still subject to debate and it is not clear whether liquid water can accumulate in the upper part of Europa's ice shell. The question of long-term stability of such subsurface water reservoirs is challenging and cannot be answered without considering meltwater generation and its subsequent propagation through the ice shell.

The production of meltwater at shallow depth is considered to be the consequence of enhanced tidal heating expected presently in two main scenarios - either in thermal hot plumes as a result of thermally-reduced viscosity (*Sotin et al.*, 2002; *Tobie et al.*, 2003) or along the faults due to tidally-activated strike-slip motions (*Nimmo & Gaidos*, 2002). While the melting processes within the ice shell are relatively well studied, only little attention has so far been paid to meltwater propagation.

Hydrofracturing, the drainage mechanism dominant on the Earth, seems unlikely to prevail in the conditions within Europa's ice shell (cf. Table 2.1 for a comparison of the two hydrological systems). Even though we cannot fully rule it out, we decided not to consider hydrofracturing in this study, mainly due to lack

Earth	**Europa**
extensive supraglacial system (supraglacial lakes, surface reaching crevasses/moulins)	**network closed from above** (low surface temperatures)
complex englacial system (enough meltwater supply)	**limited crack initiation** (overburden pressure in the ice shell)
complicated subglacial system (channels/cavities at the ice-bedrock interface)	**no subglacial drainage system** (ice shell underlain by a water ocean)
large meltwater supply (heatfluxes during the melting season $\sim 10^1$–10^2 W m^{-2})	**insufficient meltwater supply** (heat generation rate at the fault 10^{-4} W m^{-3} $\times$ fault thickness $\sim 10^3$ m $\rightarrow$ heatflux $\sim 10^{-1}$ W m^{-2})
few kilometers (typical thickness of terrestrial glaciers)	**few tens of kilometers** (estimates of Europa's ice shell thickness)

Table 2.1: Differences between the hydrological systems in Earth's glaciers and Europa's ice shell.

of observations that would help to constrain the drainage system within the ice shell. Instead, we concentrate on two other mechanisms, microporous two-phase flow and gravitational destabilization by Rayleigh-Taylor instability, and leave the investigation of the water transport by hydrofracturing for future study.

Part II

Theoretical model and numerical implementation

3. Two-phase model

The two-phase (or generally multi-phase) flow has been intensively studied in geophysics, especially in connection with magma generation and lava flows (e.g. *McKenzie*, 1984; *Scott & Stevenson*, 1986; *Spiegelman & McKenzie*, 1987; *Ghods & Arkani-Hamed*, 2000; *Schmeling*, 2006; *Katz*, 2010), planetary core formation and segregation (e.g. *Ricard et al.*, 2009; *Šrámek et al.*, 2010), soil mechanics (e.g. *Birchwood & Turcotte*, 1994), or closer to our application, in glaciology (e.g. *Hutter*, 1982; *Fowler*, 1984; *Blatter & Hutter*, 1991; *Hutter*, 1993; *Greve*, 1997).

Despite the obvious multiscale (both temporal and spatial) nature of the above phenomena, we are often interested only in physical processes at macroscopic (or mesoscopic) scale. A substantial theoretical simplification can then be achieved by employing the framework of continuum mechanics and thermodynamics. Two main branches exist within these theories concerning multi-component processes and phenomena: (i) the mixture theory and (ii) the multi-phase theory.

In the first case, the underlying theoretical framework is the continuum theory of mixtures - an approach that ignores the internal material structure and describes all the components of the mixture as omnipresent. A typical feature of continuum mixture theories is the use of concentration (mass fraction) as a weighting function to express contribution of a particular component. The mixture theory framework is developed by postulating mixture equivalents of the traditional balance laws and by supplementing them with the additional thermodynamic principles that constrain the constitutive theory. A number of mixture theories exist that differ mainly in the applied thermodynamic approach, e.g. the rational thermodynamics (*Truesdell*, 1984), the Liu-Müller theory (*Müller*, 1968), the classical or extended irreversible thermodynamics (*de Groot & Mazur*, 1984; *Jou et al.*, 2010), etc.

A possible alternative to the mixture theory is the theory of multi-phase materials. This approach is connected with the work of *Drew* (1971, 1983) and *Drew & Passman* (1999), and relies on a better insight into the geometrical structure of the material. The space-temporal distribution of the phases at a sufficiently fine mesoscale is assumed to be known and the traditional single-component continuum theory is assumed to be valid in the regions occupied by each phase. After the identification of suitable boundary conditions at the interfaces between the phases, the multi-component description is obtained by performing an averaging procedure (over a representative volume or statistical ensemble) which eliminates the microscale details. Such averaging typically leads to a formally similar system of balance equations as in the continuum mixture theory - the main difference lies in the use of a different phase-weighting function. In contrast to the mass fraction (concentration) in the first case, the multi-phase theory favors the volume fraction (often called porosity in two-phase systems), that is the volumetric 'occupancy' of the point by a particular component (phase).

In this work, we choose the second approach, i.e. the multi-phase theory. Even though the system of governing equations have been derived several times we go through this derivation for the sake of clarity and manuscript completeness. We start with a derivation of the single-phase continuum balance laws and the appropriate jump conditions at possible interfaces (Section 3.1). Then, folowing

Drew (1983) and *Drew & Passman* (1999), we proceed with the averaging procedure and write the general multi-phase equations (Section 3.2). Employing the jump conditions on the phase interface and following *Drew* (1983), *Drew & Passman* (1999), *Bercovici et al.* (2001), *Bercovici & Ricard* (2003), and *Šrámek et al.* (2007), we derive the full equations for a compressible mixture of two incompressible components (phases), water ice and liquid water, and we write down the relevant constitutive equations (Section 3.3). Finaly, in Section 3.4, we perform a scale analysis using the appropriate physical parameters and present the final reduced model.

3.1 Balance laws and jump conditions for single-phase continuum

The balance of quantity Ψ in a material body of volume Ω that is separated by a singular surface Γ can be in general written as (e.g. *Müller*, 1985):

$$\begin{aligned}\frac{\mathrm{D}}{\mathrm{D}t}\left(\int_\Omega \psi_\mathrm{v}\mathrm{d}v + \int_\Gamma \psi_\mathrm{s}\mathrm{d}s\right) &= -\int_{\partial\Omega} \Phi_\mathrm{v}^\Psi \cdot \boldsymbol{n}\mathrm{d}s - \int_{\partial\Gamma} \Phi_\mathrm{s}^\Psi \cdot \boldsymbol{\nu}\mathrm{d}l \\ &+ \int_\Omega (\pi_\mathrm{v}^\Psi + \varsigma_\mathrm{v}^\Psi)\mathrm{d}v + \int_\Gamma (\pi_\mathrm{s}^\Psi + \varsigma_\mathrm{s}^\Psi)\mathrm{d}s\ , \end{aligned} \tag{3.1}$$

with ψ_v and ψ_s the volume and surface densities of Ψ, respectively, Φ_v^Ψ and Φ_s^Ψ the volume and surface flux densities of Ψ, respectively, $\boldsymbol{n}$ and $\boldsymbol{\nu}$ the outer normals of $\partial\Omega$ and $\partial\Gamma$, respectively, π_v^Ψ and π_s^Ψ the volume and surface production densities of Ψ, respectively, and $\varsigma_\mathrm{v}^\Psi$ and $\varsigma_\mathrm{s}^\Psi$ the volume and surface densities of supply of Ψ, respectively (supply, in contrast to production, may be controlled from the exterior of Ω).

The singular surface Γ divides the body Ω in two parts, let us say Ω_{γ^+} and Ω_{γ^-}, each of which can be distinguished by a characteristic (phase) function $\chi(\boldsymbol{x}, t)$ of the form (e.g. *Drew*, 1983):

$$\chi_{\gamma^\pm}(\boldsymbol{x}, t) = \begin{cases} 1 & \text{if } \boldsymbol{x} \in \Omega_{\gamma^\pm} \text{ at time } t \\ 0 & \text{otherwise} \end{cases}\ . \tag{3.2}$$

This function 'picks out' domain $\Omega_{\gamma^\pm}$ (or component $\gamma^\pm$), and ignores all other domains (components) and interfaces - that is why it is very important in the theoretical description of multi-component materials. The characteristic function $\chi_{\gamma^\pm}$ is treated as a generalized function, especially with respect to derivatives - its gradient behaves as a δ-function, i.e. it is zero, except at the interface:

$$\nabla\chi_{\gamma^\pm} = \frac{\partial\chi_{\gamma^\pm}}{\partial n}\boldsymbol{n} = |\nabla\chi_{\gamma^\pm}|\boldsymbol{n}\ . \tag{3.3}$$

Thus, for φ_s, a surface density of quantity Φ, we can rewrite the surface integral into volume integral as[1]:

$$\int_\Gamma \varphi_\mathrm{s}\mathrm{d}s = \int_\Omega |\nabla\chi_\gamma|\varphi_\mathrm{s}\mathrm{d}v\ . \tag{3.4}$$

[1] In the following text, we will omit the $\pm$ index in the interface description, since $|\nabla\chi_{\gamma^+}| = |\nabla\chi_{\gamma^-}| = |\nabla\chi_\gamma|$.

With the use of modified Reynolds transport theorem for a volume with discontinuity (e.g. *Martinec*, 2011), the first term on the left-hand side of eq. (3.1) can be rewritten as:

$$\begin{aligned}\frac{\mathrm{D_v}}{\mathrm{D}t}\int_\Omega \psi_\mathrm{v}\mathrm{d}v &= \int_{\tilde\Omega}\left(\frac{\partial\psi_\mathrm{v}}{\partial t}+\nabla\cdot(\psi_\mathrm{v}\boldsymbol{v})\right)\mathrm{d}v+\int_\Gamma[\![\psi_\mathrm{v}(\boldsymbol{v}-\boldsymbol{v}_\mathrm{i})]\!]^+_-\cdot\boldsymbol{n}\mathrm{d}s \qquad (3.5)\\ &= \int_{\tilde\Omega}\left(\frac{\partial\psi_\mathrm{v}}{\partial t}+\nabla\cdot(\psi_\mathrm{v}\boldsymbol{v})\right)\mathrm{d}v+\int_\Omega|\nabla\chi_\gamma|[\![\psi_\mathrm{v}(\boldsymbol{v}-\boldsymbol{v}_\mathrm{i})]\!]^+_-\cdot\boldsymbol{n}\mathrm{d}v\ ,\end{aligned}$$

with $\boldsymbol{v}$ the velocity of a material within the domain Ω, $\boldsymbol{v}_\mathrm{i}$ the velocity of the interface Γ, $\tilde\Omega{=}\Omega_{\gamma^+}{\cup}\Omega_{\gamma^-}$, and $[\![\ ]\!]^+_-$ the jump across the interface Γ from Ω_{γ^+} to Ω_{γ^-}. The second equality is due to eq. (3.4) and the convective time derivative is defined as

$$\frac{\mathrm{D_v}\bullet}{\mathrm{D}t}=\frac{\partial\bullet}{\partial t}+\boldsymbol{v}\cdot\nabla\bullet\ . \qquad (3.6)$$

Since we consider no discontinuity of the interface, we can rewrite the second term on the left-hand side of eq. (3.1) using eq. (3.4) and a standard Reynolds transport theorem (e.g. *Martinec*, 2011):

$$\begin{aligned}\frac{\mathrm{D_s}}{\mathrm{D}t}\int_\Gamma\psi_\mathrm{s}\mathrm{d}s &= \frac{\mathrm{D_s}}{\mathrm{D}t}\int_\Omega|\nabla\chi_\gamma|\psi_\mathrm{s}\mathrm{d}v\\ &= \int_\Omega|\nabla\chi_\gamma|\left(\frac{\partial\psi_\mathrm{s}}{\partial t}+\nabla\cdot(\psi_\mathrm{s}\boldsymbol{v}_\mathrm{s})\right)\mathrm{d}v+\int_\Omega\psi_\mathrm{s}\frac{\mathrm{D_s}|\nabla\chi_\gamma|}{\mathrm{D}t}\mathrm{d}v\ , \qquad (3.7)\end{aligned}$$

with $\boldsymbol{v}_\mathrm{s}$ the velocity of a material at the interface Γ and the convective time derivative defined as

$$\frac{\mathrm{D_s}\bullet}{\mathrm{D}t}=\frac{\partial\bullet}{\partial t}+\boldsymbol{v}_\mathrm{s}\cdot\nabla\bullet\ . \qquad (3.8)$$

Similarly, the first term on the right-hand side of eq. (3.1) can be rewritten using the Gauss theorem for a volume with discontinuity (e.g. *Martinec*, 2011):

$$\begin{aligned}-\int_{\partial\Omega}\Phi^\Psi_\mathrm{v}\cdot\boldsymbol{n}\mathrm{d}s &= -\int_{\tilde\Omega}\nabla\cdot\Phi^\Psi_\mathrm{v}\mathrm{d}v-\int_\Gamma[\![\Phi^\Psi_\mathrm{v}]\!]^+_-\cdot\boldsymbol{n}\mathrm{d}s\\ &= -\int_{\tilde\Omega}\nabla\cdot\Phi^\Psi_\mathrm{v}\mathrm{d}v-\int_\Omega|\nabla\chi_\gamma|[\![\Phi^\Psi_\mathrm{v}]\!]^+_-\cdot\boldsymbol{n}\mathrm{d}v\ , \qquad (3.9)\end{aligned}$$

where again the second equality is due to eq. (3.4), while the second term on the right-hand side of eq. (3.1) is modified in a similar way as the second term on the left-hand side of the same equation:

$$-\int_{\partial\Gamma}\Phi^\Psi_\mathrm{s}\cdot\boldsymbol{\nu}\mathrm{d}l=-\int_\Gamma\nabla_\mathrm{s}\cdot\Phi^\Psi_\mathrm{s}\mathrm{d}s=-\int_\Omega|\nabla\chi_\gamma|\nabla\cdot\Phi^\Psi_\mathrm{s}\mathrm{d}v\ . \qquad (3.10)$$

The third term on the right-hand side of eq. (3.1) remains unchanged and the last term is again modified using eq. (3.4). Finally, the whole balance equation reads

$$\begin{aligned}&\int_{\tilde\Omega}\left(\frac{\partial\psi_\mathrm{v}}{\partial t}+\nabla\cdot(\psi_\mathrm{v}\boldsymbol{v})+\nabla\cdot\Phi^\Psi_\mathrm{v}-\pi^\Psi_\mathrm{v}-\varsigma^\Psi_\mathrm{v}\right)\mathrm{d}v\\ +\ &\int_\Omega|\nabla\chi_\gamma|\Bigg(\frac{\partial\psi_\mathrm{s}}{\partial t}+\nabla\cdot(\psi_\mathrm{s}\boldsymbol{v}_\mathrm{s})+\nabla\cdot\phi^\Psi_\mathrm{s}-\pi^\Psi_\mathrm{s}-\varsigma^\Psi_\mathrm{s}\\ +\ &\frac{\psi_\mathrm{s}}{|\nabla\chi_\gamma|}\frac{\mathrm{D_s}|\nabla\chi_\gamma|}{\mathrm{D}t}+[\![\psi_\mathrm{v}(\boldsymbol{v}-\boldsymbol{v}_\mathrm{i})+\Phi^\Psi_\mathrm{v}]\!]^+_-\cdot\boldsymbol{n}\Bigg)\mathrm{d}v=0\ , \qquad (3.11)\end{aligned}$$

indicating the form of local balance laws:

$$\frac{\partial \psi_{\mathrm{v}}}{\partial t} + \nabla \cdot (\psi_{\mathrm{v}} \boldsymbol{v}) + \nabla \cdot \Phi_{\mathrm{v}}^{\Psi} - \pi_{\mathrm{v}}^{\Psi} - \varsigma_{\mathrm{v}}^{\Psi} = 0 \qquad \text{in } \tilde{\Omega} \ , \tag{3.12a}$$

$$\frac{\partial \psi_{\mathrm{s}}}{\partial t} + \nabla_{\mathrm{s}} \cdot (\psi_{\mathrm{s}} \boldsymbol{v}_{\mathrm{s}}) + \nabla_{\mathrm{s}} \cdot \Phi_{\mathrm{s}}^{\Psi} - \pi_{\mathrm{s}}^{\Psi} - \varsigma_{\mathrm{s}}^{\Psi} + \frac{\psi_{\mathrm{s}}}{|\nabla \chi_\gamma|} \frac{\mathrm{D}_{\mathrm{s}} |\nabla \chi_\gamma|}{\mathrm{D}t} = -[\![\psi_{\mathrm{v}} (\boldsymbol{v} - \boldsymbol{v}_{\mathrm{i}}) + \Phi_{\mathrm{v}}^{\Psi}]\!]_{-}^{+} \cdot \boldsymbol{n} \qquad \text{at } \Gamma \ , \tag{3.12b}$$

where the novel term $\frac{\psi_{\mathrm{s}}}{|\nabla \chi_\gamma|} \frac{\mathrm{D}_{\mathrm{s}} |\nabla \chi_\gamma|}{\mathrm{D}t}$ describes the evolution of the interface Γ and even enables to depict the formation of the new and/or the extinction of the old interface.[2] The balance laws and interface jump conditions for single-component continuum can now be deduced by substituting the appropriate quantities into general balances (3.12):

Balance of mass

When investigating the balance of mass, the balanced quantity is the material density, $\psi_{\mathrm{v}}{=}\rho$. We consider neither any fluxes, production and sources of mass, nor any interface quantities. The balance law for mass in volume $\tilde{\Omega}$ and the corressponding jump condition at the interface Γ thus read:

$$\frac{\partial \rho}{\partial t} + \nabla \cdot (\rho \boldsymbol{v}) = 0 \qquad \text{in } \tilde{\Omega} \ , \tag{3.13a}$$

$$[\![\rho (\boldsymbol{v} - \boldsymbol{v}_{\mathrm{i}})]\!]_{-}^{+} \cdot \boldsymbol{n} = 0 \qquad \text{at } \Gamma \ . \tag{3.13b}$$

Balance of linear momentum

The balanced quantity is now the volume density of linear momentum, $\psi_{\mathrm{v}}{=}\rho\boldsymbol{v}$. We also consider the volume flux of linear momentum, i.e. the stress tensor, $\Phi_{\mathrm{v}}^{\Psi}{=}{-}\boldsymbol{\tau}$, the supply of linear momentum through the outer volume forces, $\zeta_{\mathrm{v}}^{\Psi}{=}\rho\boldsymbol{b}$, and the surface flux of linear momentum due to surface tension, $\Phi_{\mathrm{s}}^{\Psi}{=}{-}\sigma\boldsymbol{I}_{\mathrm{s}}$ with $\boldsymbol{I}_{\mathrm{s}}{=}\boldsymbol{I}{-}\boldsymbol{n}{\otimes}\boldsymbol{n}$. The linear momentum balance and the appropriate jump condition then read:

$$\frac{\partial (\rho \boldsymbol{v})}{\partial t} + \nabla \cdot (\rho \boldsymbol{v} \otimes \boldsymbol{v}) = \nabla \cdot \boldsymbol{\tau} + \rho \boldsymbol{b} \qquad \text{in } \tilde{\Omega} \ , \tag{3.14a}$$

$$[\![\rho \boldsymbol{v} \otimes (\boldsymbol{v} - \boldsymbol{v}_{\mathrm{i}}) - \boldsymbol{\tau}]\!]_{-}^{+} \cdot \boldsymbol{n} = \nabla_{\mathrm{s}} \cdot (\sigma \boldsymbol{I}_{\mathrm{s}}) \qquad \text{at } \Gamma \ . \tag{3.14b}$$

In the following, the stress tensor $\boldsymbol{\tau}$ is considered as

$$\boldsymbol{\tau} = -P\boldsymbol{I} + \boldsymbol{\sigma} \ , \tag{3.15}$$

with $P{=}{-}\frac{1}{3}\mathrm{tr}(\boldsymbol{\tau})$ the pressure and $\boldsymbol{\sigma}$ the deviatoric stress. We also assume only non-polar materials (i.e. materials without the intrinsic angular momentum), for which the balance of angular momentum implies

$$\boldsymbol{\tau} = \boldsymbol{\tau}^{\mathrm{T}} \ . \tag{3.16}$$

[2] When new interface is not created, this term takes the classical form $-2\psi_{\mathrm{s}}\kappa v_{\mathrm{s}}^{\mathrm{n}}$ with κ the mean surface curvature and $v_{\mathrm{s}}^{\mathrm{n}}$ the size of the velocity normal to the interface Γ (cf. *Müller*, 1985). Since we want to describe the creation of the new interface, we keep it in this more general form.

Balance of energy

Here, the balanced quantity is the volume density of energy, consisting of two terms, the internal energy with density ε and the kinetic energy, $\psi_{\mathrm{v}}{=}\rho(\varepsilon{+}\frac{1}{2}|\boldsymbol{v}|^2)$. The volume flux is also composed of two contributions, the heat flux $\boldsymbol{q}$ and the power exerted by stresses, $\Phi_{\mathrm{v}}^{\Psi}{=}\boldsymbol{q}{-}\boldsymbol{\tau}\cdot\boldsymbol{v}$. The volume production is represented by a general heat source, $\pi_{\mathrm{v}}^{\Psi}{=}Q$, while the volume supply is due to power exerted by body forces, $\varsigma_{\mathrm{v}}^{\Psi}{=}\rho\boldsymbol{b}{\cdot}\boldsymbol{v}$. In contrast to the previous balances, we also consider the surface specific energy, $\psi_{\mathrm{s}}{=}\xi$, and the surface flux corresponding to power exerted by surface forces, $\Phi_{\mathrm{s}}^{\Psi}{=}{-}\sigma\boldsymbol{v}_{\mathrm{s}}$. The volume and surface balances can then be written as:

$$\frac{\partial}{\partial t}\left(\rho(\varepsilon{+}\frac{1}{2}|\boldsymbol{v}|^2)\right)+\nabla\cdot\left(\rho(\varepsilon{+}\frac{1}{2}|\boldsymbol{v}|^2)\boldsymbol{v}\right) \tag{3.17a}$$

$$=\nabla\cdot(\boldsymbol{\tau}\cdot\boldsymbol{v}{-}\boldsymbol{q})+\rho\boldsymbol{b}\cdot\boldsymbol{v}+Q \qquad \text{in}\,\tilde{\Omega}\ ,$$

$$\left[\!\!\left[\rho\left(\varepsilon{+}\frac{1}{2}|\boldsymbol{v}|^2\right)(\boldsymbol{v}{-}\boldsymbol{v}_{\mathrm{i}})-\boldsymbol{\tau}\cdot\boldsymbol{v}+\boldsymbol{q}\right]\!\!\right]_{-}^{+}\cdot\boldsymbol{n}$$

$$=-\frac{\partial\xi}{\partial t}-\nabla_{\mathrm{s}}\cdot(\xi\boldsymbol{v}_{\mathrm{s}})+\nabla_{\mathrm{s}}\cdot(\sigma\boldsymbol{v}_{\mathrm{s}})-\frac{\xi}{|\nabla\chi_\gamma|}\frac{\mathrm{D}_{\mathrm{s}}|\nabla\chi_\gamma|}{\mathrm{D}t} \qquad \text{at}\,\Gamma\ . \tag{3.17b}$$

Balance of entropy

Finally, we balance the entropy with density s, i.e. $\psi_{\mathrm{v}}{=}\rho s$. The volume flux is represented by the non-convective entropy flux, $\Phi_{\mathrm{v}}^{\Psi}{=}\boldsymbol{J}$, and the volume source is given by the internal entropy production rate, $\pi_{\mathrm{v}}^{\Psi}{=}\mathcal{S}$. As in the balance of energy above, we also consider the surface specific entropy, $\psi_{\mathrm{s}}{=}\eta$. The entropy balances in the volume $\tilde{\Omega}$ and on the interface Γ then read:

$$\frac{\partial(\rho s)}{\partial t}+\nabla\cdot(\rho s\boldsymbol{v})=-\nabla\cdot\boldsymbol{J}+\mathcal{S} \qquad \text{in}\,\tilde{\Omega}\ , \tag{3.18a}$$

$$[\![\rho s(\boldsymbol{v}{-}\boldsymbol{v}_{\mathrm{i}})+\boldsymbol{J}]\!]_{-}^{+}\cdot\boldsymbol{n}=-\frac{\partial\eta}{\partial t}-\nabla_{\mathrm{s}}\cdot(\eta\boldsymbol{v}_{\mathrm{s}})-\frac{\eta}{|\nabla\chi_\gamma|}\frac{\mathrm{D}_{\mathrm{s}}|\nabla\chi_\gamma|}{\mathrm{D}t} \qquad \text{at}\,\Gamma\ . \tag{3.18b}$$

3.2 Averaged multi-phase balance laws

In order to obtain equations that do not contain the microscopic details of the flow, we will apply the volumetric averaging process which is appropriate for flows that are statistically spatially uniform, or homogeneous. Let $\langle\ \rangle$ denote an averaging process so that if $f(\boldsymbol{x},t)$ is an exact microscopic field, then $\langle f\rangle(\boldsymbol{x},t)$ is the corresponding averaged field. The volume average can be defined as (cf. *Drew*, 1983):

$$\langle f\rangle(\boldsymbol{x},t)=\frac{1}{V}\int_V f(\boldsymbol{x},t)\mathrm{d}v\ , \tag{3.19}$$

where V is some sufficiently large volume. The average is assumed to satisfy the following conditions (for field quantities f, f_1, f_2 and constants c_1, c_2):

$$\langle c_1 f_1 + c_2 f_2 \rangle = c_1 \langle f_1 \rangle + c_2 \langle f_2 \rangle \ , \tag{3.20a}$$

$$\langle \langle f_1 \rangle f_2 \rangle = \langle f_1 \rangle \langle f_2 \rangle \ , \tag{3.20b}$$

$$\left\langle \frac{\partial f}{\partial t} \right\rangle = \frac{\partial}{\partial t} \langle f \rangle \ , \tag{3.20c}$$

$$\left\langle \frac{\partial f}{\partial x_\mathrm{i}} \right\rangle = \frac{\partial}{\partial x_\mathrm{i}} \langle f \rangle \ . \tag{3.20d}$$

The first two conditions are called Reynolds' rules, the third is called Leibniz' rule, and the fourth is called Gauss' rule (*Drew*, 1983).

For the purpose of averaging of balance equations for each component, the phase function $\chi_\gamma(\boldsymbol{x}, t)$ defined by eq. (3.2) is used. The average interfacial area per unit volume can be defined as (*Drew*, 1983):

$$\alpha = \left\langle \frac{\partial \chi_\gamma}{\partial n} \right\rangle = \langle |\nabla \chi_\gamma| \rangle \ , \tag{3.21}$$

and the derivative of the product of a field quantity f with the phase function χ_γ reads:

$$\frac{\partial}{\partial \zeta}(\chi_\gamma f) = \chi_\gamma \frac{\partial}{\partial \zeta} f + f_\gamma^\mathrm{i} \frac{\partial}{\partial \zeta} \chi_\gamma \ , \tag{3.22}$$

with ζ denoting the space coordinate x_j or time t and f_γ^i the value of quantity f evaluated on the component γ side of the interface. It can be further shown that (cf. *Drew*, 1983)

$$\frac{\partial \chi_\gamma}{\partial t} + \boldsymbol{v}_\mathrm{i} \cdot \nabla \chi_\gamma = 0 \ , \tag{3.23}$$

which is the topological equation that describes the material derivative of χ_γ that follows the interface. Using the above definitions, we can write:

$$\begin{aligned}
& \left\langle \chi_\gamma \left(\frac{\partial f}{\partial t} + \nabla \cdot (f \boldsymbol{v}) \right) \right\rangle \\
= \ & \left\langle \frac{\partial}{\partial t}(\chi_\gamma f) \right\rangle - \left\langle f_\gamma^\mathrm{i} \frac{\partial \chi_\gamma}{\partial t} \right\rangle + \langle \nabla \cdot (\chi_\gamma f \boldsymbol{v}) \rangle - \left\langle f_\gamma^\mathrm{i} \boldsymbol{v}_\gamma^\mathrm{i} \cdot \nabla \chi_\gamma \right\rangle \\
= \ & \frac{\partial}{\partial t} \langle \chi_\gamma f \rangle + \nabla \cdot \langle \chi_\gamma f \boldsymbol{v} \rangle - \left\langle f_\gamma^\mathrm{i} \left(\frac{\partial \chi_\gamma}{\partial t} + \boldsymbol{v}_\mathrm{i} \cdot \nabla \chi_\gamma \right) \right\rangle - \left\langle f_\gamma^\mathrm{i} (\boldsymbol{v}_\gamma^\mathrm{i} - \boldsymbol{v}_\mathrm{i}) \cdot \nabla \chi_\gamma \right\rangle \\
= \ & \frac{\partial}{\partial t} \langle \chi_\gamma f \rangle + \nabla \cdot \langle \chi_\gamma f \boldsymbol{v} \rangle - \left\langle f_\gamma^\mathrm{i} (\boldsymbol{v}_\gamma^\mathrm{i} - \boldsymbol{v}_\mathrm{i}) \cdot \nabla \chi_\gamma \right\rangle \ ,
\end{aligned} \tag{3.24}$$

where the last equality is due to topological equation (3.23).

Now the general averaged balance law for the γ phase in the bulk is obtained by taking the product of eq. (3.12a) with χ_γ and then performing the averaging process:

$$\begin{aligned}
& \frac{\partial}{\partial t} \langle \chi_\gamma \psi_\mathrm{v} \rangle + \nabla \cdot \langle \chi_\gamma \psi_\mathrm{v} \boldsymbol{v} \rangle + \nabla \cdot \left\langle \chi_\gamma \Phi_\mathrm{v}^\Psi \right\rangle - \left\langle \chi_\gamma \pi_\mathrm{v}^\Psi \right\rangle - \left\langle \chi_\gamma \varsigma_\mathrm{v}^\Psi \right\rangle \\
= \ & \left\langle (\psi_{\mathrm{v}\gamma}^\mathrm{i} (\boldsymbol{v}_\gamma^\mathrm{i} - \boldsymbol{v}_\mathrm{i}) + \Phi_{\mathrm{v}\gamma}^{\Psi\mathrm{i}}) \cdot \nabla \chi_\gamma \right\rangle \ .
\end{aligned} \tag{3.25}$$

Similarly, the general averaged balance law at the interface between two phases, say γ and β (with $\nabla\chi_\gamma = -\nabla\chi_\beta$), is obtained by taking the product of eq. (3.12b) with $|\nabla\chi_\gamma|$ and then performing the averaging process[3]:

$$\begin{aligned} & \frac{\partial}{\partial t}\langle|\nabla\chi_\gamma|\psi_\mathrm{s}\rangle + \nabla\cdot\langle|\nabla\chi_\gamma|\psi_\mathrm{s}\boldsymbol{v}_\mathrm{s}\rangle + \nabla\cdot\left\langle|\nabla\chi_\gamma|\Phi_\mathrm{s}^\Psi\right\rangle - \left\langle|\nabla\chi_\gamma|\pi_\mathrm{s}^\Psi\right\rangle - \left\langle|\nabla\chi_\gamma|\varsigma_\mathrm{s}^\Psi\right\rangle \\ = \; & -\left\langle[\![\psi_\mathrm{v}(\boldsymbol{v}-\boldsymbol{v}_\mathrm{i}) + \Phi_\mathrm{v}^\Psi]\!]_-^+\cdot\nabla\chi_\gamma\right\rangle \ . \end{aligned} \tag{3.26}$$

Before we proceed with writing down the particular averaged balance laws, we define the volume fraction of phase γ (*Drew*, 1983):

$$\phi_\gamma = \langle\chi_\gamma\rangle \ . \tag{3.27}$$

Besides, we define the volume variables in terms of weighted averages (as is common in the multi-phase mixture literature) - the phasic (component-weighted) or the mass-weighted average. Which is appropriate is suggested by the appearance of the quantity in the balance equation. The phasic average of a variable φ_v is defined by

$$\tilde{\varphi}_\gamma = \frac{\langle\chi_\gamma\varphi_\mathrm{v}\rangle}{\phi_\gamma} \tag{3.28}$$

and the mass-weighted average of a variable φ_v is defined by

$$\hat{\varphi}_\gamma = \frac{\langle\chi_\gamma\rho\varphi_\mathrm{v}\rangle}{\phi_\gamma\tilde{\rho}_\gamma} \ , \tag{3.29}$$

where

$$\tilde{\rho}_\gamma = \frac{\langle\chi_\gamma\rho\rangle}{\phi_\gamma} \tag{3.30}$$

is the average density of the phase γ. The surface variables, on the other hand, are weighted by the interfacial surface density and so we write

$$\breve{\varphi} = \frac{\langle|\nabla\chi_\gamma|\varphi_\mathrm{s}\rangle}{\alpha} \ . \tag{3.31}$$

The interface variables (defined in the following text) are weighted with the full gradient $\nabla\chi_\gamma$. Taking into account the above definitions and considering the same volume and surface quantities for particular balances as in Section 3.1, we can write:

Balance of mass

The averaged balance of mass in the bulk of the phase γ reads

$$\frac{\partial}{\partial t}(\phi_\gamma\tilde{\rho}_\gamma) + \nabla\cdot(\phi_\gamma\tilde{\rho}_\gamma\hat{\boldsymbol{v}}_\gamma) = \bar{r}_\gamma^\mathrm{i} \ , \tag{3.32}$$

with the average velocity

$$\hat{\boldsymbol{v}}_\gamma = \frac{\langle\chi_\gamma\rho\boldsymbol{v}\rangle}{\phi_\gamma\tilde{\rho}_\gamma} \tag{3.33}$$

[3]The term $-\langle\Phi_\mathrm{s}^\Psi\cdot\nabla|\nabla\chi_\gamma|\rangle$ that originates from the third term on the left-hand side of eq. (3.12b) after applying per partes derivation, is identically zero since Φ_s^Ψ is tangent to the discontinuity Γ and $\nabla|\nabla\chi_\gamma|$ is normal to the same discontinuity.

and the interfacial mass production rate due to phase change

$$\bar{r}^{\mathrm{i}}_{\gamma} = \langle \rho^{\mathrm{i}}_{\gamma} (\boldsymbol{v}^{\mathrm{i}}_{\gamma} - \boldsymbol{v}_{\mathrm{i}}) \cdot \nabla \chi_{\gamma} \rangle \ . \tag{3.34}$$

Similarly, the averaged balance of mass on the interface between the phases γ and β reads

$$\left\langle [\![\rho (\boldsymbol{v} - \boldsymbol{v}_{\mathrm{i}})]\!]^{+}_{-} \cdot \nabla \chi_{\gamma} \right\rangle = 0 \ . \tag{3.35}$$

Balance of linear momentum

The averaged balance of linear momentum in the bulk of the phase γ reads

$$\begin{aligned} & \frac{\partial}{\partial t} (\phi_{\gamma} \tilde{\rho}_{\gamma} \hat{\boldsymbol{v}}_{\gamma}) + \nabla \cdot (\phi_{\gamma} \tilde{\rho}_{\gamma} \hat{\boldsymbol{v}}_{\gamma} \otimes \hat{\boldsymbol{v}}_{\gamma}) \\ = \ & - \nabla (\phi_{\gamma} \tilde{P}_{\gamma}) + \nabla \cdot (\phi_{\gamma} \tilde{\boldsymbol{\sigma}}_{\gamma}) + \phi_{\gamma} \rho_{\gamma} \hat{\boldsymbol{b}}_{\gamma} + \bar{r}^{\mathrm{i}}_{\gamma} \bar{\boldsymbol{v}}^{\mathrm{i}}_{\gamma} + \bar{P}^{\mathrm{i}}_{\gamma} \nabla \phi_{\gamma} + \bar{\boldsymbol{M}}^{\mathrm{i}}_{\gamma} \ , \end{aligned} \tag{3.36}$$

with the average pressure

$$\tilde{P}_{\gamma} = \frac{\langle \chi_{\gamma} P \rangle}{\phi_{\gamma}} \ , \tag{3.37}$$

the average deviatoric stress

$$\tilde{\boldsymbol{\sigma}}_{\gamma} = \frac{\langle \chi_{\gamma} \boldsymbol{\sigma} \rangle}{\phi_{\gamma}} \ , \tag{3.38}$$

the average body force

$$\hat{\boldsymbol{b}}_{\gamma} = \frac{\langle \chi_{\gamma} \rho \boldsymbol{b} \rangle}{\phi_{\gamma} \tilde{\rho}_{\gamma}} \ , \tag{3.39}$$

and the average interfacial momentum sources due to: (i) phase change

$$\bar{r}^{\mathrm{i}}_{\gamma} \bar{\boldsymbol{v}}^{\mathrm{i}}_{\gamma} = \langle \rho^{\mathrm{i}}_{\gamma} \boldsymbol{v}^{\mathrm{i}}_{\gamma} \otimes (\boldsymbol{v}^{\mathrm{i}}_{\gamma} - \boldsymbol{v}_{\mathrm{i}}) \cdot \nabla \chi_{\gamma} \rangle \ , \tag{3.40}$$

with $\bar{\boldsymbol{v}}^{\mathrm{i}}_{\gamma}$ the average interfacial velocity of the phase γ, (ii) interfacial pressure ('buoyant force', cf. *Drew*, 1983)

$$\bar{P}^{\mathrm{i}}_{\gamma} \nabla \phi_{\gamma} = \langle P^{\mathrm{i}}_{\gamma} \boldsymbol{I} \cdot \nabla \chi_{\gamma} \rangle \ , \tag{3.41}$$

with $\bar{P}^{\mathrm{i}}_{\gamma}$ the average interfacial pressure of the phase γ, and (iii) molecular fluxes ('interfacial force density', cf. *Drew*, 1983)

$$\bar{\boldsymbol{M}}^{\mathrm{i}}_{\gamma} = - \langle \boldsymbol{\sigma}^{\mathrm{i}}_{\gamma} \cdot \nabla \chi_{\gamma} \rangle \ . \tag{3.42}$$

Similarly, the averaged balance of linear momentum on the interface between the phases γ and β reads

$$\left\langle [\![\rho \boldsymbol{v} \otimes (\boldsymbol{v} - \boldsymbol{v}_{\mathrm{i}}) - \boldsymbol{\tau}]\!]^{+}_{-} \cdot \nabla \chi_{\gamma} \right\rangle = \nabla (\alpha \breve{\sigma}) \ , \tag{3.43}$$

with the average surface tension

$$\breve{\sigma} = \frac{\langle |\nabla \chi_{\gamma}| \sigma \rangle}{\alpha} \ . \tag{3.44}$$

Balance of energy

The averaged balance of energy in the bulk of the phase γ reads

$$\begin{aligned} & \frac{\partial}{\partial t}(\phi_\gamma\tilde{\rho}_\gamma(\hat{\varepsilon}_\gamma+\frac{1}{2}|\hat{\boldsymbol{v}}_\gamma|^2)) + \nabla\cdot(\phi_\gamma\tilde{\rho}_\gamma(\hat{\varepsilon}_\gamma+\frac{1}{2}|\hat{\boldsymbol{v}}_\gamma|^2)\hat{\boldsymbol{v}}_\gamma) \\ = \;& -\nabla(\phi_\gamma\tilde{P}_\gamma\hat{\boldsymbol{v}}_\gamma) + \nabla\cdot(\phi_\gamma\tilde{\boldsymbol{\sigma}}_\gamma\cdot\hat{\boldsymbol{v}}_\gamma) - \nabla\cdot(\phi_\gamma\tilde{\boldsymbol{q}}_\gamma) + \phi_\gamma\tilde{\rho}_\gamma\hat{\boldsymbol{b}}_\gamma\cdot\hat{\boldsymbol{v}}_\gamma \\ + \;& \phi_\gamma\tilde{Q}_\gamma + \bar{E}^{\mathrm{i}}_\gamma\bar{r}^{\mathrm{i}}_\gamma + \bar{W}^{\mathrm{i}}_\gamma + \bar{Q}^{\mathrm{i}}_\gamma \;, \end{aligned} \tag{3.45}$$

with the average specific internal energy

$$\hat{\varepsilon}_\gamma = \frac{\langle\chi_\gamma\rho\varepsilon\rangle}{\phi_\gamma\tilde{\rho}_\gamma} \;, \tag{3.46}$$

the average heat flux

$$\tilde{\boldsymbol{q}}_\gamma = \frac{\langle\chi_\gamma\boldsymbol{q}\rangle}{\phi_\gamma} \;, \tag{3.47}$$

the average heat source

$$\tilde{Q}_\gamma = \frac{\langle\chi_\gamma Q\rangle}{\phi_\gamma} \;, \tag{3.48}$$

the average interfacial energy source

$$\bar{E}^{\mathrm{i}}_\gamma\bar{r}^{\mathrm{i}}_\gamma = \langle\rho^{\mathrm{i}}_\gamma(\varepsilon^{\mathrm{i}}_\gamma+\frac{1}{2}|\boldsymbol{v}^{\mathrm{i}}_\gamma|^2)(\boldsymbol{v}^{\mathrm{i}}_\gamma-\boldsymbol{v}_{\mathrm{i}})\cdot\nabla\chi_\gamma\rangle \;, \tag{3.49}$$

with $\bar{E}^{\mathrm{i}}_\gamma$ the average interfacial energy per unit mass, the average interfacial power

$$\bar{W}^{\mathrm{i}}_\gamma = -\langle\boldsymbol{\tau}^{\mathrm{i}}_\gamma\cdot\boldsymbol{v}^{\mathrm{i}}_\gamma\cdot\nabla\chi_\gamma\rangle \;, \tag{3.50}$$

and the average interfacial heat source

$$\bar{Q}^{\mathrm{i}}_\gamma = \langle\boldsymbol{q}^{\mathrm{i}}_\gamma\cdot\nabla\chi_\gamma\rangle \;. \tag{3.51}$$

Similarly, the averaged balance of energy on the interface between the phases γ and β reads

$$\left\langle[\![\rho(\varepsilon+\frac{1}{2}|\boldsymbol{v}|^2)(\boldsymbol{v}-\boldsymbol{v}_{\mathrm{i}})-\boldsymbol{\tau}\cdot\boldsymbol{v}+\boldsymbol{q}]\!]^+_-\cdot\nabla\chi_\gamma\right\rangle = -\frac{\partial}{\partial t}(\alpha\check{\xi}) - \nabla\cdot(\alpha\check{\xi}\check{\boldsymbol{v}}_{\mathrm{s}}) + \nabla\cdot(\alpha\check{\sigma}\check{\boldsymbol{v}}_{\mathrm{s}}) \;, \tag{3.52}$$

with the average surface energy

$$\check{\xi} = \frac{\langle|\nabla\chi_\gamma|\xi\rangle}{\alpha} \tag{3.53}$$

and the average interfacial velocity

$$\check{\boldsymbol{v}}_{\mathrm{s}} = \frac{\langle|\nabla\chi_\gamma|\xi\boldsymbol{v}_{\mathrm{s}}\rangle}{\alpha\check{\xi}} \;. \tag{3.54}$$

Balance of entropy

The averaged balance of entropy in the bulk of the phase γ reads

$$\frac{\partial}{\partial t}(\phi_\gamma \tilde{\rho}_\gamma \hat{s}_\gamma) + \nabla \cdot (\phi_\gamma \tilde{\rho}_\gamma \hat{s}_\gamma \hat{\boldsymbol{v}}_\gamma) = -\nabla \cdot (\phi_\gamma \tilde{\boldsymbol{J}}_\gamma) + \phi_\gamma \tilde{\mathcal{S}}_\gamma + \bar{\mathcal{S}}^{\mathrm{i}}_\gamma \ , \tag{3.55}$$

with the average specific entropy

$$\hat{s}_\gamma = \frac{\langle \chi_\gamma \rho s \rangle}{\phi_\gamma \tilde{\rho}_\gamma} \ , \tag{3.56}$$

the average non-convective entropy flux

$$\tilde{\boldsymbol{J}}_\gamma = \frac{\langle \chi_\gamma \boldsymbol{J} \rangle}{\phi_\gamma} \ , \tag{3.57}$$

the average internal entropy source

$$\tilde{\mathcal{S}}_\gamma = \frac{\langle \chi_\gamma \mathcal{S} \rangle}{\phi_\gamma} \ , \tag{3.58}$$

and the average interfacial entropy source (due to convective and molecular fluxes)

$$\bar{\mathcal{S}}^{\mathrm{i}}_\gamma = \langle (\rho^{\mathrm{i}}_\gamma s^{\mathrm{i}}_\gamma (\boldsymbol{v}^{\mathrm{i}}_\gamma - \boldsymbol{v}_{\mathrm{i}}) + \boldsymbol{J}^{\mathrm{i}}_\gamma) \cdot \nabla \chi_\gamma \rangle \ . \tag{3.59}$$

Similarly, the averaged balance of entropy on the interface between the phases γ and β reads

$$\left\langle [\![\rho s (\boldsymbol{v} - \boldsymbol{v}_{\mathrm{i}}) + \boldsymbol{J}]\!]^+_- \cdot \nabla \chi_\gamma \right\rangle = -\frac{\partial}{\partial t}(\alpha \check{\eta}) - \nabla \cdot (\alpha \check{\eta} \check{\boldsymbol{v}}_{\mathrm{s}}) \ , \tag{3.60}$$

with the average surface entropy

$$\check{\eta} = \frac{\langle |\nabla \chi_\gamma | \eta \rangle}{\alpha} \ . \tag{3.61}$$

Note on fluctuation velocities

The velocities that arise due to motion of the interfaces or due to turbulence are, in general, not equal to their average values (cf. *Drew & Passman*, 1999). To account for these effects, the fluctuation velocity, i.e. the microscopic variation of the velocity field, is usually defined as the difference between the complete field and the appropriate averaged field:

$$\boldsymbol{v}'_\gamma = \boldsymbol{v} - \hat{\boldsymbol{v}}_\gamma \ . \tag{3.62}$$

With this definition, several new terms appear after the averaging procedure, such as Reynolds' stresses, fluctuation (Reynolds) energy flux or fluctuation (Reynolds) entropy flux, which all need a real constitutive model. For example, *Drew* (1983) suggests a constitutive equation for the Reynolds' stresses (assuming bubbly air-water flow) that is specified by three material parameters. Nevertheless, since we expect the role of turbulent dynamical effects to be negligible and also for lack of knowledge of the appropriate material parameters, we neglect these fluctuation effects in the above averaged balance laws.

In the following text, we do not further use the tildes, hats, checks and overbars to distinguish between true and averaged values, since from now on we only consider the averaged variables.

3.3 Two-phase equations for water-ice mixture

In the previous section, we have rederived the multi-phase flow equations. Now, we will use this general model in our particular application, that is the mixture of water ice and liquid water. To identify, how many and which balances will be needed, let us define the following structure of multi-phase models (cf. *Hutter*, 1993):

- **Class I** models can be used to describe the diffusive motion of minority phases (contaminants or impurities) in some majority phase. The assumption of equal temperatures is in this case quite reasonable. Similarly, the linear momenta of minority phases can be joint with that of the majority phase. Therefore, the mass balances of all phases are considered, but momentum, energy and entropy balances are only formulated for the multi-phase material as a whole. Model example from this class is the salinity evolution in water.

- **Class II** models are used to describe the dynamics of such system, where the particular phases are present in comparable volumes and their velocities are sufficiently distinct from each other. The interaction forces between the phases are important and enable the phase separation. Accordingly, the balance laws of mass and momentum are formulated for all the phases. On the other hand, a single temperature suffices for all phases and only one energy balance and one entropy balance is formulated for the whole system. Model example from this class can be found in soil mechanics (interaction of soil with water).

- **Class III** models are constructed to describe the system where all balance laws (of mass, momentum, energy, and entropy) have to be used for every phase. The creep deformation of cold firn under the influence of percolating surface meltwater can be considered a model example for this class.

For our application - the production and transport of liquid water within the ice shell - we consider the Class II model, since the molten water mass and velocity cannot be neglected w.r.t. the ice flow, but the temperature of the partially molten material (i.e. the melting temperature) can be considered the same for the whole mixture. Thus, we need to write down the balances of mass and linear momentum for each phase, but only one balance of energy and one entropy balance for the whole system.

We are interested in the behavior of partially molten ice without any additional impurities. Our multi-phase material is thus composed of only two phases - the matrix (ice) and the fluid (water). All the partial quantities will be subscripted by 'm' and 'f', denoting the **m**atrix and **f**luid phase, respectively. The associated volume fractions ϕ_m and ϕ_f are related by the condition

$$\phi_\mathrm{m} + \phi_\mathrm{f} = 1 \ , \tag{3.63}$$

that expresses the non-existence of any voids in the material (well justified for the typically high-pressure conditions within planetary interiors) and allows to keep just one volume fraction, say ϕ_f, as independent. We thus write

$$\phi = \phi_\mathrm{f} \ , \qquad 1-\phi = \phi_\mathrm{m} \ . \tag{3.64}$$

In the following, ϕ is referred to as porosity. We will implicitly assume that

$$0 < \phi < 1 \ , \tag{3.65}$$

i.e. both phases are always present (although one of them possibly in negligible concentration). The presented model cannot be straightforwardly applied in the limit cases of pure substances (for ϕ=0,1), because several assumptions of the model then become violated (especially the equilibrium temperature condition). The model is thus assumed to hold only until one of the limit cases (ϕ=0, 1) is reached. We will write all the mixture balances first and then list all the appropriate constitutive equations.

Balances of mass

We consider separate balances of mass (eq. 3.32) for both components, which, under the assumption of constant material densities ρ_m, ρ_f (both phases are assumed to be incompressible) read as follows:

$$\frac{\partial \phi}{\partial t} + \nabla \cdot (\phi \boldsymbol{v}_\mathrm{f}) = \frac{r_\mathrm{f}^\mathrm{i}}{\rho_\mathrm{f}} \ , \tag{3.66a}$$

$$-\frac{\partial \phi}{\partial t} + \nabla \cdot ((1-\phi) \boldsymbol{v}_\mathrm{m}) = \frac{r_\mathrm{m}^\mathrm{i}}{\rho_\mathrm{m}} \ . \tag{3.66b}$$

However, the interfacial mass production rates r_f^i and r_m^i are not independent, but they are related through the interface jump condition (eq. 3.35), which (considering $\nabla \chi_\mathrm{f} = -\nabla \chi_\mathrm{m}$) leads to

$$\sum_{\gamma=\mathrm{f,m}} r_\gamma^\mathrm{i} = \sum_{\gamma=\mathrm{f,m}} \langle \rho_\gamma^\mathrm{i} (\boldsymbol{v}_\gamma^\mathrm{i} - \boldsymbol{v}_\mathrm{i}) \cdot \nabla \chi_\gamma \rangle = \left\langle [\![\rho (\boldsymbol{v} - \boldsymbol{v}_\mathrm{i})]\!]_-^+ \cdot \nabla \chi_\gamma \right\rangle = 0 \ . \tag{3.67}$$

This allows us to keep only one mass production term - we choose the melt production rate and write

$$r_\mathrm{f}^\mathrm{i} = -r_\mathrm{m}^\mathrm{i} = r_\mathrm{f} \ . \tag{3.68}$$

Moreover, in what follows, it will prove helpful to use the relative velocity between the phases

$$\boldsymbol{v}_\mathrm{r} = \boldsymbol{v}_\mathrm{f} - \boldsymbol{v}_\mathrm{m} \tag{3.69}$$

in the first equation. Finally, the mass balances read:

$$\frac{\partial \phi}{\partial t} + \nabla \cdot (\phi (\boldsymbol{v}_\mathrm{r} + \boldsymbol{v}_\mathrm{m})) = \frac{r_\mathrm{f}}{\rho_\mathrm{f}} \ , \tag{3.70a}$$

$$-\frac{\partial \phi}{\partial t} + \nabla \cdot ((1-\phi) \boldsymbol{v}_\mathrm{m}) = -\frac{r_\mathrm{f}}{\rho_\mathrm{m}} \ . \tag{3.70b}$$

Balances of linear momentum (equations of motion)

Here, again, we consider separate balance laws (eq. 3.36) for both phases:

$$\rho_\mathrm{f}\left(\frac{\partial(\phi\boldsymbol{v}_\mathrm{f})}{\partial t}+\nabla\cdot(\phi\boldsymbol{v}_\mathrm{f}\otimes\boldsymbol{v}_\mathrm{f})\right)=-\phi\nabla P_\mathrm{f}+\nabla\cdot(\phi\boldsymbol{\sigma}_\mathrm{f})+r_\mathrm{f}\boldsymbol{v}_\mathrm{f}^\mathrm{i}+(P_\mathrm{f}^\mathrm{i}-P_\mathrm{f})\nabla\phi+\phi\rho_\mathrm{f}\mathbf{b}_\mathrm{f}+\mathbf{M}_\mathrm{f}^\mathrm{i}\ , \tag{3.71a}$$

$$\rho_\mathrm{m}\left(\frac{\partial((1-\phi)\boldsymbol{v}_\mathrm{m})}{\partial t}+\nabla\cdot((1-\phi)\boldsymbol{v}_\mathrm{m}\otimes\boldsymbol{v}_\mathrm{m})\right)=-(1-\phi)\nabla P_\mathrm{m}+\nabla\cdot((1-\phi)\boldsymbol{\sigma}_\mathrm{m})-r_\mathrm{f}\boldsymbol{v}_\mathrm{m}^\mathrm{i}-(P_\mathrm{m}^\mathrm{i}-P_\mathrm{m})\nabla\phi+(1-\phi)\rho_\mathrm{m}\mathbf{b}_\mathrm{m}+\mathbf{M}_\mathrm{m}^\mathrm{i}\ , \tag{3.71b}$$

Following *Bercovici & Ricard* (2003) we assume that the interfacial velocities as well as the interfacial pressures of both phases are equal[4] and write

$$\boldsymbol{v}_\omega=\boldsymbol{v}_\mathrm{f}^\mathrm{i}=\boldsymbol{v}_\mathrm{m}^\mathrm{i}=\omega\boldsymbol{v}_\mathrm{f}+(1-\omega)\boldsymbol{v}_\mathrm{m}\ , \tag{3.72}$$

$$P_\omega=P_\mathrm{f}^\mathrm{i}=P_\mathrm{m}^\mathrm{i}=(1-\omega)P_\mathrm{f}+\omega P_\mathrm{m}\ , \tag{3.73}$$

where the partitioning parameter ω is specified later in eq. (3.116). In our application, the only body force considered is gravity $\mathbf{g}$ and so

$$\mathbf{b}_\mathrm{f}=\mathbf{b}_\mathrm{m}=\mathbf{g}\ . \tag{3.74}$$

Finally, the interaction forces between the phases, $\mathbf{M}_{\mathrm{f,m}}^\mathrm{i}$, are not independent, but are again related through the interface jump condition (eq. 3.43). The sum over both phases of the interfacial terms on the right-hand side of eq. (3.36) can be written as:

$$\sum_{\gamma=\mathrm{f,m}}\langle(\rho_\gamma^\mathrm{i}\boldsymbol{v}_\gamma^\mathrm{i}\otimes(\boldsymbol{v}_\gamma^\mathrm{i}-\boldsymbol{v}_\mathrm{i})-\boldsymbol{\tau}_\gamma^\mathrm{i})\cdot\nabla\chi_\gamma\rangle=\sum_{\gamma=\mathrm{f,m}}r_\gamma^\mathrm{i}\boldsymbol{v}_\gamma^\mathrm{i}+P_\gamma^\mathrm{i}\nabla\phi_\gamma+\boldsymbol{M}_\gamma^\mathrm{i}=\boldsymbol{M}_\mathrm{f}^\mathrm{i}+\boldsymbol{M}_\mathrm{m}^\mathrm{i}\ , \tag{3.75}$$

where the last equality is due to eqs (3.64), (3.68), (3.72), and (3.73). The same expression can be rewritten using the jump condition (3.43) as:

$$\sum_{\gamma=\mathrm{f,m}}\langle(\rho_\gamma^\mathrm{i}\boldsymbol{v}_\gamma^\mathrm{i}\otimes(\boldsymbol{v}_\gamma^\mathrm{i}-\boldsymbol{v}_\mathrm{i})-\boldsymbol{\tau}_\gamma^\mathrm{i})\cdot\nabla\chi_\gamma\rangle=\left\langle[\![\rho\boldsymbol{v}\otimes(\boldsymbol{v}-\boldsymbol{v}_\mathrm{i})-\boldsymbol{\tau}]\!]_-^+\cdot\nabla\chi_\gamma\right\rangle=\nabla(\alpha\sigma)\ . \tag{3.76}$$

Combining eqs (3.75) and (3.76), we can finally write

$$\boldsymbol{M}_\mathrm{f}^\mathrm{i}+\boldsymbol{M}_\mathrm{m}^\mathrm{i}=\nabla(\sigma\alpha)\ . \tag{3.77}$$

To satisfy this condition, we follow the approach of *Bercovici & Ricard* (2003) and write the interaction forces as

$$\boldsymbol{M}_\mathrm{f}^\mathrm{i}=-c\boldsymbol{v}_\mathrm{r}+\omega\nabla(\sigma\alpha)\ , \tag{3.78a}$$

$$\boldsymbol{M}_\mathrm{m}^\mathrm{i}=c\boldsymbol{v}_\mathrm{r}+(1-\omega)\nabla(\sigma\alpha)\ , \tag{3.78b}$$

[4] In *Drew* (1971), the difference between the interfacial pressures is assumed to be in principle non-zero, and in the presence of surface tension it is assumed to be $P_\mathrm{f}^\mathrm{i}-P_\mathrm{m}^\mathrm{i}\sim\sigma\kappa$, with κ the mean curvature of the interface. In the approach of *Bercovici et al.* (2001) and *Bercovici & Ricard* (2003), which we adopt here, the surface tension does not appear in the difference between the interfacial pressures, but it is contained in the interaction terms $\mathbf{M}_\mathrm{f}^\mathrm{i}$, $\mathbf{M}_\mathrm{m}^\mathrm{i}$.

with c the drag coefficient (specified later in eq. 3.117). Note that we do not include the terms $\pm P_\omega \nabla\phi$ that are present in the expressions for the interaction forces in *Bercovici & Ricard* (2003), since these are already present (in the form perfectly consistent with these authors) in eqs (3.71), merely as a result of the averaging procedure.

In the following, it will show useful to define the pressure difference between the phases

$$\Delta P = P_\mathrm{m} - P_\mathrm{f} \tag{3.79}$$

and the excess water pressure with respect to the hydrostatic equilibrium of pure ice

$$\Pi = P_\mathrm{f} - P_\mathrm{m}^\mathrm{ref} \ , \tag{3.80}$$

where the hydrostatic equilibrium condition reads

$$\mathbf{0} = -\nabla P_\mathrm{m}^\mathrm{ref} + \rho_\mathrm{m}\mathbf{g} \ . \tag{3.81}$$

With the above definitions and taking into account the balances of mass (3.70), the equations of motion for the two phases can finally be written as

$$\begin{aligned}
\phi\rho_\mathrm{f}\frac{\mathrm{D_f}\boldsymbol{v}_\mathrm{f}}{\mathrm{D}t} &= -\phi\nabla\Pi - \phi\Delta\rho\mathbf{g} + \nabla\cdot(\phi\boldsymbol{\sigma}_\mathrm{f}) \\
&\quad - (1{-}\omega)\boldsymbol{v}_\mathrm{r} r_\mathrm{f} + \omega\left(\Delta P\nabla\phi{+}\nabla(\sigma\alpha)\right) - c\boldsymbol{v}_\mathrm{r} \ , \qquad (3.82a) \\
(1{-}\phi)\rho_\mathrm{m}\frac{\mathrm{D_m}\boldsymbol{v}_\mathrm{m}}{\mathrm{D}t} &= -(1{-}\phi)(\nabla\Pi{+}\nabla\Delta P) + \nabla\cdot((1{-}\phi)\boldsymbol{\sigma}_\mathrm{m}) \\
&\quad - \omega\boldsymbol{v}_\mathrm{r} r_\mathrm{f} + (1{-}\omega)\left(\Delta P\nabla\phi{+}\nabla(\sigma\alpha)\right) + c\boldsymbol{v}_\mathrm{r} \ , \qquad (3.82b)
\end{aligned}$$

with the two new convective time derivatives

$$\frac{\mathrm{D_f}\bullet}{\mathrm{D}t} = \frac{\partial\bullet}{\partial t} + \boldsymbol{v}_\mathrm{f}\cdot\nabla\bullet \ , \qquad \frac{\mathrm{D_m}\bullet}{\mathrm{D}t} = \frac{\partial\bullet}{\partial t} + \boldsymbol{v}_\mathrm{m}\cdot\nabla\bullet \ , \tag{3.83}$$

and the density difference

$$\Delta\rho = \rho_\mathrm{m} - \rho_\mathrm{f} \ . \tag{3.84}$$

Balance of energy

Only a single energy balance for the mixture as a whole is considered, corresponding to the assumption that during the investigated process both phases have the same temperature, equal to the equilibrium phase change temperature. Using eq. (3.45) and summing it for both phases we can write

$$\begin{aligned}
&\frac{\partial}{\partial t}\left(\phi\rho_\mathrm{f}\left(\varepsilon_\mathrm{f}{+}\frac{1}{2}|\boldsymbol{v}_\mathrm{f}|^2\right) + (1{-}\phi)\rho_\mathrm{m}\left(\varepsilon_\mathrm{m}{+}\frac{1}{2}|\boldsymbol{v}_\mathrm{m}|^2\right)\right) \\
+ \ &\nabla\cdot\left(\phi\rho_\mathrm{f}\left(\varepsilon_\mathrm{f}{+}\frac{1}{2}|\boldsymbol{v}_\mathrm{f}|^2\right)\boldsymbol{v}_\mathrm{f} + (1{-}\phi)\rho_\mathrm{m}\left(\varepsilon_\mathrm{m}{+}\frac{1}{2}|\boldsymbol{v}_\mathrm{m}|^2\right)\boldsymbol{v}_\mathrm{m}\right) \\
= \ &-\nabla\left(\phi P_\mathrm{f}\boldsymbol{v}_\mathrm{f} + (1{-}\phi)P_\mathrm{m}\boldsymbol{v}_\mathrm{m}\right) + \nabla\cdot\left(\phi\boldsymbol{\sigma}_\mathrm{f}\cdot\boldsymbol{v}_\mathrm{f} + (1{-}\phi)\boldsymbol{\sigma}_\mathrm{m}\cdot\boldsymbol{v}_\mathrm{m}\right) \\
- \ &\nabla\cdot\left(\phi\mathbf{q}_\mathrm{f} + (1{-}\phi)\mathbf{q}_\mathrm{m}\right) + \phi\rho_\mathrm{f}\boldsymbol{v}_\mathrm{f}\cdot\mathbf{g} + (1{-}\phi)\rho_\mathrm{m}\boldsymbol{v}_\mathrm{m}\cdot\mathbf{g} + \phi Q_\mathrm{f} + (1{-}\phi)Q_\mathrm{m} \\
+ \ &(E_\mathrm{f}^\mathrm{i}{-}E_\mathrm{m}^\mathrm{i})r_\mathrm{f} + W_\mathrm{f}^\mathrm{i} + W_\mathrm{m}^\mathrm{i} + Q_\mathrm{f}^\mathrm{i} + Q_\mathrm{m}^\mathrm{i} \ . \qquad (3.85)
\end{aligned}$$

The interfacial source terms on the last line can be rewritten using the interfacial jump condition (eq. 3.52) as:

$$\begin{aligned}
&(E_{\mathrm{f}}^{\mathrm{i}}-E_{\mathrm{m}}^{\mathrm{i}})r_{\mathrm{f}} + W_{\mathrm{f}}^{\mathrm{i}} + W_{\mathrm{m}}^{\mathrm{i}} + Q_{\mathrm{f}}^{\mathrm{i}} + Q_{\mathrm{m}}^{\mathrm{i}} \\
= &\sum_{\gamma=\mathrm{f,m}} \langle(\rho_\gamma^{\mathrm{i}}(\varepsilon_{\mathrm{f}\gamma}^{\mathrm{i}}+\frac{1}{2}|\boldsymbol{v}_\gamma^{\mathrm{i}}|^2)(\boldsymbol{v}_\gamma^{\mathrm{i}}-\boldsymbol{v}_{\mathrm{i}}) - \boldsymbol{\tau}_\gamma^{\mathrm{i}}\cdot\boldsymbol{v}_\gamma^{\mathrm{i}} + \boldsymbol{q}_\gamma^{\mathrm{i}})\cdot\nabla\chi_\gamma\rangle \\
= &\left\langle [\![\rho(\varepsilon+\frac{1}{2}|\boldsymbol{v}|^2))(\boldsymbol{v}-\boldsymbol{v}_{\mathrm{i}}) - \boldsymbol{\tau}\cdot\boldsymbol{v} + \boldsymbol{q}]\!]_-^+ \cdot\nabla\chi_\gamma \right\rangle \\
= &-\frac{\partial}{\partial t}(\alpha\xi) - \nabla\cdot(\alpha\xi\boldsymbol{v}_\omega) + \nabla\cdot(\alpha\sigma\boldsymbol{v}_\omega)\ , \qquad (3.86)
\end{aligned}$$

where we renamed the interfacial velocity $\boldsymbol{v}_{\mathrm{s}}$ to $\boldsymbol{v}_\omega$ (since these are the same quantities). Considering also that the heat fluxes and heat sources are the same in both phases, i.e. $\boldsymbol{q}_{\mathrm{f}}{=}\boldsymbol{q}_{\mathrm{m}}{=}\boldsymbol{q}$ and $Q_{\mathrm{f}}{=}Q_{\mathrm{m}}{=}Q$, respectively, we can write the energy balance as follows:

$$\begin{aligned}
&\frac{\partial}{\partial t}\left(\phi\rho_{\mathrm{f}}\left(\varepsilon_{\mathrm{f}}+\frac{1}{2}|\boldsymbol{v}_{\mathrm{f}}|^2\right) + (1{-}\phi)\rho_{\mathrm{m}}\left(\varepsilon_{\mathrm{m}}+\frac{1}{2}|\boldsymbol{v}_{\mathrm{m}}|^2\right) + \alpha\xi\right) \\
+ &\nabla\cdot\left(\phi\rho_{\mathrm{f}}\left(\varepsilon_{\mathrm{f}}+\frac{1}{2}|\boldsymbol{v}_{\mathrm{f}}|^2\right)\boldsymbol{v}_{\mathrm{f}} + (1{-}\phi)\rho_{\mathrm{m}}\left(\varepsilon_{\mathrm{m}}+\frac{1}{2}|\boldsymbol{v}_{\mathrm{m}}|^2\right)\boldsymbol{v}_{\mathrm{m}} + \alpha\xi\boldsymbol{v}_\omega\right) \\
= &-\nabla\left(\phi P_{\mathrm{f}}\boldsymbol{v}_{\mathrm{f}} + (1{-}\phi)P_{\mathrm{m}}\boldsymbol{v}_{\mathrm{m}}\right) + \nabla\cdot\left(\phi\boldsymbol{\sigma}_{\mathrm{f}}\cdot\boldsymbol{v}_{\mathrm{f}} + (1{-}\phi)\boldsymbol{\sigma}_{\mathrm{m}}\cdot\boldsymbol{v}_{\mathrm{m}} + \alpha\sigma\boldsymbol{v}_\omega\right) \\
- &\nabla\cdot\mathbf{q} + \phi\rho_{\mathrm{f}}\boldsymbol{v}_{\mathrm{f}}\cdot\mathbf{g} + (1{-}\phi)\rho_{\mathrm{m}}\boldsymbol{v}_{\mathrm{m}}\cdot\mathbf{g} + Q\ . \qquad (3.87)
\end{aligned}$$

This equation represents a minor generalization of the energy balance from *Šrámek et al.* (2007), the generalization being in the inclusion of kinetic energies $\frac{1}{2}\rho_{\mathrm{f}}|\boldsymbol{v}_{\mathrm{f}}|^2$, $\frac{1}{2}\rho_{\mathrm{m}}|\boldsymbol{v}_{\mathrm{m}}|^2$ on the left-hand side of eq. (3.87). This is motivated by our attempt for maximum possible generality of the initial model and our intention to perform all simplifications of the model on the grounds of scale analysis. Apart from the classical internal and kinetic energy terms $\varepsilon_{\mathrm{f}}+\frac{1}{2}|\boldsymbol{v}_{\mathrm{f}}|^2$, $\varepsilon_{\mathrm{m}}+\frac{1}{2}|\boldsymbol{v}_{\mathrm{m}}|^2$, the balance (3.87) contains also a contribution from the surface energy density ξ, which is assumed to be advected by an interfacial velocity $\boldsymbol{v}_\omega$ given by eq. (3.72). A corresponding mechanical power exerted by the surface forces also appears in the balance represented by the term $\nabla\cdot(\sigma\alpha\boldsymbol{v}_\omega)$.

The energy equation (3.87), when combined with the balances of mass (3.70) and linear momentum (3.82), allows to express only the internal energy balance:

$$\begin{aligned}
&\phi\rho_{\mathrm{f}}\frac{\mathrm{D}_{\mathrm{f}}\varepsilon_{\mathrm{f}}}{\mathrm{D}t} + (1{-}\phi)\rho_{\mathrm{m}}\frac{\mathrm{D}_{\mathrm{m}}\varepsilon_{\mathrm{m}}}{\mathrm{D}t} - T\frac{\mathrm{D}_\omega}{\mathrm{D}t}\left(\alpha\frac{\mathrm{d}\sigma}{\mathrm{d}T}\right) - \alpha T\frac{\mathrm{d}\sigma}{\mathrm{d}T}\nabla\cdot\boldsymbol{v}_\omega \\
= &\ Q - \nabla\cdot\mathbf{q} + c|\boldsymbol{v}_{\mathrm{r}}|^2 + \phi\boldsymbol{\sigma}_{\mathrm{f}} : \nabla\boldsymbol{v}_{\mathrm{f}} + (1{-}\phi)\boldsymbol{\sigma}_{\mathrm{m}} : \nabla\boldsymbol{v}_{\mathrm{m}} \\
- &\left(\Delta P+\sigma\frac{\mathrm{d}\alpha}{\mathrm{d}\phi}\right)\frac{\mathrm{D}_\omega\phi}{\mathrm{D}t} + r_{\mathrm{f}}\left(\Delta p+\Delta\varepsilon+\frac{1{-}2\omega}{2}|\boldsymbol{v}_{\mathrm{r}}|^2\right)\ . \qquad (3.88)
\end{aligned}$$

Here we introduced new convective time derivative

$$\frac{\mathrm{D}_\omega\bullet}{\mathrm{D}t} = \frac{\partial\bullet}{\partial t} + \boldsymbol{v}_\omega\cdot\nabla\bullet\ , \qquad (3.89)$$

the internal energy difference

$$\Delta\varepsilon = \varepsilon_{\mathrm{m}} - \varepsilon_{\mathrm{f}}\ , \qquad (3.90)$$

the pressure over density difference

$$\Delta p = \frac{P_\mathrm{m}}{\rho_\mathrm{m}} - \frac{P_\mathrm{f}}{\rho_\mathrm{f}} \ , \tag{3.91}$$

and we also employed a thermodynamic relation derived in *Bercovici et al.* (2001)

$$\xi = \sigma - T\frac{\mathrm{d}\sigma}{\mathrm{d}T} \ , \tag{3.92}$$

with T the temperature.

Balance of entropy

Summing again the balance of entropy (eq. 3.55) for both phases, we write:

$$\begin{aligned} & \frac{\partial}{\partial t}\left(\phi\rho_\mathrm{f}s_\mathrm{f} + (1{-}\phi)\rho_\mathrm{m}s_\mathrm{m}\right) + \nabla\cdot\left(\phi\rho_\mathrm{f}s_\mathrm{f}\boldsymbol{v}_\mathrm{f} + (1{-}\phi)\rho_\mathrm{m}s_\mathrm{m}\boldsymbol{v}_\mathrm{m}\right) \\ = \ & -\nabla\cdot\left(\phi\boldsymbol{J}_\mathrm{f} + (1{-}\phi)\boldsymbol{J}_\mathrm{m}\right) + \phi\mathcal{S}_\mathrm{f} + (1{-}\phi)\mathcal{S}_\mathrm{m} + \mathcal{S}^\mathrm{i}_\mathrm{f} + \mathcal{S}^\mathrm{i}_\mathrm{m} \ . \end{aligned} \tag{3.93}$$

As with the other balances, the interfacial entropy sources $\mathcal{S}^\mathrm{i}_{\mathrm{f,m}}$ are not independent, but are related through the jump condition across the interface (eq. 3.60). The sum of the interfacial entropy sources gives:

$$\begin{aligned} \mathcal{S}^\mathrm{i}_\mathrm{f} + \mathcal{S}^\mathrm{i}_\mathrm{m} &= \sum_{\gamma=\mathrm{f,m}} \langle(\rho^\mathrm{i}_\gamma s^\mathrm{i}_\gamma(\boldsymbol{v}^\mathrm{i}_\gamma{-}\boldsymbol{v}_\mathrm{i}) + \boldsymbol{J}^\mathrm{i}_\gamma)\cdot\nabla\chi_\gamma\rangle = \left\langle[\![\rho s(\boldsymbol{v}{-}\boldsymbol{v}_\mathrm{i}) + \boldsymbol{J}]\!]^+_-\cdot\nabla\chi_\gamma\right\rangle \\ &= \frac{\partial}{\partial t}(\alpha\frac{\mathrm{d}\sigma}{\mathrm{d}T}) + \nabla\cdot(\alpha\frac{\mathrm{d}\sigma}{\mathrm{d}T}\boldsymbol{v}_\omega) \ , \end{aligned} \tag{3.94}$$

where we used the expression for the interfacial entropy density from *Bercovici et al.* (2001)

$$\eta = -\frac{\mathrm{d}\sigma}{\mathrm{d}T} \ . \tag{3.95}$$

Assuming further that the entropy fluxes and entropy sources are the same in both phases, i.e. $\boldsymbol{J}_\mathrm{f}{=}\boldsymbol{J}_\mathrm{m}{=}\boldsymbol{J}$ and $\mathcal{S}_\mathrm{f}{=}\mathcal{S}_\mathrm{m}{=}\mathcal{S}$, respectively, and using the balances of mass (3.70), the entropy balance reads

$$\phi\rho_\mathrm{f}\frac{\mathrm{D}_\mathrm{f}s_\mathrm{f}}{\mathrm{D}t} + (1{-}\phi)\rho_\mathrm{m}\frac{\mathrm{D}_\mathrm{m}s_\mathrm{m}}{\mathrm{D}t} - \frac{\mathrm{D}_\omega}{\mathrm{D}t}\left(\alpha\frac{\mathrm{d}\sigma}{\mathrm{d}T}\right) - \alpha\frac{\mathrm{d}\sigma}{\mathrm{d}T}\nabla\cdot\boldsymbol{v}_\omega = -\nabla\cdot\boldsymbol{J} + \mathcal{S} + r_\mathrm{f}\Delta s \ , \tag{3.96}$$

with

$$\Delta s = s_\mathrm{m} - s_\mathrm{f} \tag{3.97}$$

the entropy difference.

Constitutive model

Material properties in terms of closure (constitutive) equations must be supplemented to allow the solution of the system of balance equations. By the incompressibility constraint, both material densities ρ_f, ρ_m are constants (specified in Table 3.1). The specific internal energies $\varepsilon_\mathrm{f}, \varepsilon_\mathrm{m}$ are assumed to be solely functions

of temperature, with the corresponding specific heats[5] c_f, c_m (in general functions of T, e.g. *Lide*, 2004):

$$\varepsilon_\mathrm{f} = \varepsilon_\mathrm{f}(T) \ , \qquad \frac{\mathrm{d}\varepsilon_\mathrm{f}}{\mathrm{d}T} = c_\mathrm{f}(T) \ , \tag{3.98a}$$

$$\varepsilon_\mathrm{m} = \varepsilon_\mathrm{m}(T) \ , \qquad \frac{\mathrm{d}\varepsilon_\mathrm{m}}{\mathrm{d}T} = c_\mathrm{m}(T) \ . \tag{3.98b}$$

The energy balance (eq. 3.88) can now be written as

$$\begin{aligned} & \phi\rho_\mathrm{f}c_\mathrm{f}\frac{\mathrm{D}_\mathrm{f}T}{\mathrm{D}t} + (1{-}\phi)\rho_\mathrm{m}c_\mathrm{m}\frac{\mathrm{D}_\mathrm{m}T}{\mathrm{D}t} - T\frac{\mathrm{D}_\omega}{\mathrm{D}t}\left(\alpha\frac{\mathrm{d}\sigma}{\mathrm{d}T}\right) - \alpha T\frac{\mathrm{d}\sigma}{\mathrm{d}T}\nabla\cdot\boldsymbol{v}_\omega \\ = \ & Q - \nabla\cdot\mathbf{q} + c|\boldsymbol{v}_\mathrm{r}|^2 + \phi\boldsymbol{\sigma}_\mathrm{f} : \nabla\boldsymbol{v}_\mathrm{f} + (1{-}\phi)\boldsymbol{\sigma}_\mathrm{m} : \nabla\boldsymbol{v}_\mathrm{m} \\ - \ & \left(\Delta P{+}\sigma\frac{\mathrm{d}\alpha}{\mathrm{d}\phi}\right)\frac{\mathrm{D}_\omega\phi}{\mathrm{D}t} + r_\mathrm{f}\left(\Delta p{+}\Delta\varepsilon{+}\frac{1{-}2\omega}{2}|\boldsymbol{v}_\mathrm{r}|^2\right) \ . \end{aligned} \tag{3.99}$$

Similarly, the entropy balance (eq. 3.96) can be multiplied by T and, bearing in mind that (for incompressible material) $T\frac{\mathrm{D}s}{\mathrm{D}t}{=}c\frac{\mathrm{D}T}{\mathrm{D}t}$ (Gibbs relation, cf. *Martinec*, 2011), rewritten as:

$$\begin{aligned} & \phi\rho_\mathrm{f}c_\mathrm{f}\frac{\mathrm{D}_\mathrm{f}T}{\mathrm{D}t} + (1{-}\phi)\rho_\mathrm{m}c_\mathrm{m}\frac{\mathrm{D}_\mathrm{m}T}{\mathrm{D}t} - T\frac{\mathrm{D}_\omega}{\mathrm{D}t}\left(\alpha\frac{\mathrm{d}\sigma}{\mathrm{d}T}\right) - \alpha T\frac{\mathrm{d}\sigma}{\mathrm{d}T}\nabla\cdot\boldsymbol{v}_\omega \\ = \ & -\nabla\cdot(T\boldsymbol{J}) + \boldsymbol{J}\cdot\nabla T + T\mathcal{S} + r_\mathrm{f}T\Delta s \ . \end{aligned} \tag{3.100}$$

Comparing these two balances, we obtain

$$\boldsymbol{J} = \frac{1}{T}\boldsymbol{q} \tag{3.101}$$

and

$$\begin{aligned} T\mathcal{S} \ = \ & Q - \frac{1}{T}\boldsymbol{q}\cdot\nabla T + c|\boldsymbol{v}_\mathrm{r}|^2 + \phi\boldsymbol{\sigma}_\mathrm{f} : \nabla\boldsymbol{v}_\mathrm{f} + (1{-}\phi)\boldsymbol{\sigma}_\mathrm{m} : \nabla\boldsymbol{v}_\mathrm{m} \\ - \ & \left(\Delta P{+}\sigma\frac{\mathrm{d}\alpha}{\mathrm{d}\phi}\right)\frac{\mathrm{D}_\omega\phi}{\mathrm{D}t} + r_\mathrm{f}\left(\Delta p{+}\Delta\varepsilon{-}T\Delta s{+}\frac{1{-}2\omega}{2}|\boldsymbol{v}_\mathrm{r}|^2\right) \ . \end{aligned} \tag{3.102}$$

The last equation shows that apart from the classical entropy sources (related to heat production, heat diffusion and dissipation, cf. the terms on the first line), there are two additional entropy sources related to the dynamic pressure difference and to the melting rate. Following the approach of *Šrámek et al.* (2007), we reorganize eq. (3.102) as follows

$$\begin{aligned} T\mathcal{S} \ = \ & Q - \frac{1}{T}\boldsymbol{q}\cdot\nabla T + c|\boldsymbol{v}_\mathrm{r}|^2 + \phi\boldsymbol{\sigma}_\mathrm{f} : \nabla\boldsymbol{v}_\mathrm{f} + (1{-}\phi)\boldsymbol{\sigma}_\mathrm{m} : \nabla\boldsymbol{v}_\mathrm{m} \\ - \ & \left(\Delta P{+}\sigma\frac{\mathrm{d}\alpha}{\mathrm{d}\phi}\right)\left(\frac{\mathrm{D}_\omega\phi}{\mathrm{D}t} - \frac{\rho_\omega}{\rho_\mathrm{f}\rho_\mathrm{m}}r_\mathrm{f}\right) \\ + \ & r_\mathrm{f}\left(\Delta p{+}\Delta\varepsilon{-}T\Delta s{+}\frac{1{-}2\omega}{2}|\boldsymbol{v}_\mathrm{r}|^2 - \frac{\rho_\omega}{\rho_\mathrm{f}\rho_\mathrm{m}}\left(\Delta P{+}\sigma\frac{\mathrm{d}\alpha}{\mathrm{d}\phi}\right)\right) \ , \end{aligned} \tag{3.103}$$

[5] We do not need to distinguish between specific heats at constant volume and constant pressure due to the incompressibility assumption on both phases.

with

$$\rho_\omega = (1-\omega)\rho_\mathrm{f} + \omega\rho_\mathrm{m} \tag{3.104}$$

the effective interface density. The rate of entropy production is now written as a (generalized) product of thermodynamic affinities and fluxes. Concerning the two new terms, the dynamic pressure difference $\Delta P+\sigma\frac{\mathrm{d}\alpha}{\mathrm{d}\phi}$ and the melting rate r_f are chosen as thermodynamic fluxes and the corresponding expressions in parenthesis as thermodynamic affinities. Following the standard procedure of Classical (Linear) Irreversible Thermodynamics (*de Groot & Mazur*, 1984), a coupled linear relationship between these two fluxes and affinities is assumed:

$$\begin{pmatrix} -\Delta P-\sigma\frac{\mathrm{d}\alpha}{\mathrm{d}\phi} \\ r_\mathrm{f} \end{pmatrix} = \begin{pmatrix} L_{11} & L_{12} \\ L_{21} & L_{22} \end{pmatrix} \begin{pmatrix} \frac{\mathrm{D}_\omega\phi}{\mathrm{D}t} - \frac{\rho_\omega}{\rho_\mathrm{f}\rho_\mathrm{m}} r_\mathrm{f} \\ \Delta p+\Delta\varepsilon-T\Delta s+\frac{1-2\omega}{2}|\boldsymbol{v}_\mathrm{r}|^2-\frac{\rho_\omega}{\rho_\mathrm{f}\rho_\mathrm{m}}\left(\Delta P+\sigma\frac{\mathrm{d}\alpha}{\mathrm{d}\phi}\right) \end{pmatrix} . \tag{3.105}$$

Considering that the two fluxes decouple (L_{12}=L_{21}=0, cf. *Šrámek et al.*, 2007, for more discussion) and using the expression for L_{11} from *Bercovici et al.* (2001)

$$L_{11} = \mu_0\frac{\mu_\mathrm{f}+\mu_\mathrm{m}}{\phi(1-\phi)} = \frac{\mu_\mathrm{f}+\mu_\mathrm{m}}{\phi(1-\phi)} , \tag{3.106}$$

with $\mu_0\sim O(1)$ a dimensionless constant (which we will omit in the following), we write for the dynamic pressure difference

$$\begin{aligned} \left(\Delta P+\sigma\frac{\mathrm{d}\alpha}{\mathrm{d}\phi}\right) &= -\frac{\mu_\mathrm{f}+\mu_\mathrm{m}}{\phi(1-\phi)}\left(\frac{\mathrm{D}_\omega\phi}{\mathrm{D}t} - \frac{\rho_\omega}{\rho_\mathrm{f}\rho_\mathrm{m}} r_\mathrm{f}\right) \\ &= -\frac{\mu_\mathrm{f}+\mu_\mathrm{m}}{\phi(1-\phi)}\left((1-\omega)(1-\phi)\nabla\cdot\boldsymbol{v}_\mathrm{m} - \omega\phi\nabla\cdot\boldsymbol{v}_\mathrm{f}\right) \end{aligned} \tag{3.107}$$

and for the melting rate

$$r_\mathrm{f} = L_{22}\left(\Delta p+\Delta\varepsilon-T\Delta s+\frac{1-2\omega}{2}|\boldsymbol{v}_\mathrm{r}|^2-\frac{\rho_\omega}{\rho_\mathrm{f}\rho_\mathrm{m}}\left(\Delta P+\sigma\frac{\mathrm{d}\alpha}{\mathrm{d}\phi}\right)\right) . \tag{3.108}$$

The parameter L_{22} may be rather difficult to evaluate (or measure), which can be overcome by assuming near-thermodynamic-equilibrium conditions. This corresponds to an assumption of very fast kinetics of the melting process with respect to the thermodynamic forces that cause it, that is to assuming $|L_{22}|\to\infty$. In that case, in order to maintain a finite melt production rate, the following equilibrium condition must hold

$$\Delta p + \Delta\varepsilon + L + \frac{1-2\omega}{2}|\boldsymbol{v}_\mathrm{r}|^2 - \frac{\rho_\omega}{\rho_\mathrm{f}\rho_\mathrm{m}}\left(\Delta P+\sigma\frac{\mathrm{d}\alpha}{\mathrm{d}\phi}\right) = 0 , \tag{3.109}$$

with L=$-T\Delta s$ the latent heat of the phase change, assumed to be, in general, a function of temperature T. Equation (3.109) is nothing but a generalized Clapeyron relation that implicitly defines the equilibrium melting temperature T. As we will see, in that case the energy balance (3.99) ceases to be an evolution equation for temperature T, which is no longer independent, but defines the melt production rate r_f.

The temperature dependence of surface tension σ is postulated as in *Straub* (1994) in the form of the Guggenheim-Katayama relation

$$\sigma = \sigma_0\left(1-\frac{T}{T_\mathrm{c}}\right)^\beta , \tag{3.110}$$

with σ_0, β, and T_c constants. For the heat flux, we prescribe the simple Fourier law

$$\mathbf{q} = -k^{\mathrm{T}}(\phi)\nabla T \ , \tag{3.111}$$

where $k^{\mathrm{T}}(\phi)$ is the porosity-dependent heat conductivity (e.g. *McKenzie*, 1984):

$$k^{\mathrm{T}}(\phi) = k^{\mathrm{T}}_{\mathrm{m}} \left(1 - \phi \frac{k^{\mathrm{T}}_{\mathrm{m}} - k^{\mathrm{T}}_{\mathrm{f}}}{\frac{2k^{\mathrm{T}}_{\mathrm{m}} + k^{\mathrm{T}}_{\mathrm{f}}}{3}} \right) \ , \tag{3.112}$$

with $k^{\mathrm{T}}_{\mathrm{m}}$ and $k^{\mathrm{T}}_{\mathrm{f}}$ the heat conductivities of (pure) matrix and (pure) fluid, respectively. Employing (3.107), (3.109) and (3.111), the energy balance (3.99) can be rewritten as:

$$\begin{aligned} & \phi\rho_{\mathrm{f}}c_{\mathrm{f}}\frac{\mathrm{D}_{\mathrm{f}}T}{\mathrm{D}t} + (1-\phi)\rho_{\mathrm{m}}c_{\mathrm{m}}\frac{\mathrm{D}_{\mathrm{m}}T}{\mathrm{D}t} - T\frac{\mathrm{D}_{\omega}}{\mathrm{D}t}\left(\alpha\frac{\mathrm{d}\sigma}{\mathrm{d}T}\right) - \alpha T\frac{\mathrm{d}\sigma}{\mathrm{d}T}\nabla\cdot\boldsymbol{v}_{\omega} + Lr_{\mathrm{f}} \\ = \ & Q + \nabla\cdot(k^{\mathrm{T}}(\phi)\nabla T) + c|\boldsymbol{v}_{\mathrm{r}}|^2 + \phi\boldsymbol{\sigma}_{\mathrm{f}} : \nabla\boldsymbol{v}_{\mathrm{f}} + (1-\phi)\boldsymbol{\sigma}_{\mathrm{m}} : \nabla\boldsymbol{v}_{\mathrm{m}} \\ + \ & \frac{\mu_{\mathrm{f}}+\mu_{\mathrm{m}}}{\phi(1-\phi)}\left((1-\omega)(1-\phi)\nabla\cdot\boldsymbol{v}_{\mathrm{m}} - \omega\phi\nabla\cdot\boldsymbol{v}_{\mathrm{f}}\right)^2 \ . \end{aligned} \tag{3.113}$$

Concerning the constitutive relations for stresses, i.e. the rheology of the material, we assume that both phases behave on the relevant time scales as viscous fluids and that their deviatoric parts of the Cauchy stress tensors can be related to the deviatoric parts of the strain-rate tensors via a stress–strain-rate relation of the form

$$\boldsymbol{\sigma}_{\mathrm{f}} = \mu_{\mathrm{f}}\left(\nabla\boldsymbol{v}_{\mathrm{f}} + (\nabla\boldsymbol{v}_{\mathrm{f}})^{\mathrm{T}} - \frac{2}{3}(\nabla\cdot\boldsymbol{v}_{\mathrm{f}})\mathbf{I}\right) \ , \tag{3.114a}$$

$$\boldsymbol{\sigma}_{\mathrm{m}} = \mu_{\mathrm{m}}\left(\nabla\boldsymbol{v}_{\mathrm{m}} + (\nabla\boldsymbol{v}_{\mathrm{m}})^{\mathrm{T}} - \frac{2}{3}(\nabla\cdot\boldsymbol{v}_{\mathrm{m}})\mathbf{I}\right) \ . \tag{3.114b}$$

The viscosities μ_{f}, μ_{m} are here, in principle, functions of temperature, porosity, deformation, etc. It is, however, reasonable to assume that water viscosity remains constant in the process - its variations are almost entirely governed by temperature (*Lide*, 2004) which in our application changes only due to relatively weak pressure dependence of the melting point. Ice, on the other hand, is known to have a highly nonlinear rheology, which is discussed in more detail in Section 1.6.

The dependence of the average surface density α on porosity ϕ is taken from *Bercovici et al.* (2001) as

$$\alpha = \alpha_0\phi^a(1-\phi)^b \ , \tag{3.115}$$

where $\alpha_0 \sim \frac{1}{d}$ and a, b are constants (both ≤ 1). For the surface partitioning parameter ω, *Bercovici & Ricard* (2003) provide a sophisticated guess

$$\omega = \frac{\phi\mu_{\mathrm{f}}}{\phi\mu_{\mathrm{f}} + (1-\phi)\mu_{\mathrm{m}}} \ , \tag{3.116}$$

which we apply here as well. For the drag coefficient c, the probably most general form, consistent also with most others, is given in *Bercovici et al.* (2001) in the form

$$c = \frac{\mu_{\mathrm{m}}\mu_{\mathrm{f}}\phi^2(1-\phi)^2}{\mu_{\mathrm{f}}k(1-\phi)\phi^2 + \mu_{\mathrm{m}}k(\phi)(1-\phi)^2}, \tag{3.117}$$

where $k(\cdot)$ is the porosity-dependent permeability, discussed in more detail in Section 2.2.

3.4 Scale analysis

The objective of this section is to introduce the physical scales and parameters appropriate for the problem of water transport through the outer shells of icy satellites, such as Europa, Enceladus, etc. Evaluation of these scales will allow certain reduction of the model - the terms insignificant from the perspective of scaling will be dropped and only the relevant physical processes will be kept in the description.

3.4.1 Scales

Each field quantity φ is assumed to possess certain characteristic scale denoted $[\varphi]$ and a dimensionless counterpart $\tilde{\varphi}$, defined by $\varphi = [\varphi]\tilde{\varphi}$. We start by defining the following 'primitive' scales:

$$\begin{aligned}
&\phi = [\phi]\tilde{\phi} && \mathbf{r} = [\mathbf{r}]\tilde{\mathbf{r}} && \mu_{\mathrm{m}} = [\mu_{\mathrm{m}}]\tilde{\mu}_{\mathrm{m}} = \mu_{\mathrm{m}}^{\mathrm{ref}}\tilde{\mu}_{\mathrm{m}} \\
&\sigma = [\sigma]\tilde{\sigma} = \sigma_0\tilde{\sigma} && L = [L]\tilde{L} && T = [T]\tilde{T} = T_0\tilde{T} \\
&c_{\mathrm{m}} = [c_{\mathrm{m}}]\tilde{c}_{\mathrm{m}} && c_{\mathrm{f}} = [c_{\mathrm{f}}]\tilde{c}_{\mathrm{f}} && k^{\mathrm{T}} = [k^{\mathrm{T}}]\tilde{k}^{\mathrm{T}} = k_{\mathrm{m}}^{\mathrm{T}}\tilde{k}^{\mathrm{T}} \ .
\end{aligned} \tag{3.118}$$

Using these scales and representative material parameters (listed in Table 3.1), the following secondary, or derived scales can be defined:

$$\begin{aligned}
&\nabla = \tfrac{1}{[\mathbf{r}]}\tilde{\nabla} && \boldsymbol{v}_{\mathrm{m}} = [\boldsymbol{v}_{\mathrm{m}}]\tilde{\boldsymbol{v}}_{\mathrm{m}} = \tfrac{k_{\mathrm{m}}^{\mathrm{T}}}{[\mathbf{r}]\rho_{\mathrm{m}}[\mathbf{c}_{\mathrm{m}}]}\tilde{\boldsymbol{v}}_{\mathrm{m}} \\
&\Delta P = [\Delta P]\tilde{\Delta P} = \tfrac{[\mu_{\mathrm{m}}][\boldsymbol{v}_{\mathrm{m}}]}{[\phi][\mathbf{r}]}\tilde{\Delta P} && \boldsymbol{v}_{\mathrm{r}} = [\boldsymbol{v}_{\mathrm{r}}]\tilde{\boldsymbol{v}}_{\mathrm{r}} = \tfrac{k_0|\Delta\rho||\mathbf{g}|}{\mu_{\mathrm{f}}}[\phi]^{n-1}\tilde{\boldsymbol{v}}_{\mathrm{r}} \\
&\Pi = [\Pi]\tilde{\Pi} = |\Delta\rho||\mathbf{g}|[\mathbf{r}][\phi]\tilde{\Pi} && \boldsymbol{v}_{\mathrm{f}} = [\boldsymbol{v}_{\mathrm{f}}]\tilde{\boldsymbol{v}}_{\mathrm{f}} = [\boldsymbol{v}_{\mathrm{r}}]\tilde{\boldsymbol{v}}_{\mathrm{f}} \\
&t = [t]\tilde{t} = \tfrac{[\mathbf{r}]\mu_{\mathrm{f}}}{k_0|\Delta\rho||\mathbf{g}|[\phi]^{n-1}}\tilde{t} && \boldsymbol{q} = [\boldsymbol{q}]\tilde{\boldsymbol{q}} = k_{\mathrm{m}}^{\mathrm{T}}\tfrac{T_0}{[\mathbf{r}]}\tilde{\boldsymbol{q}} \\
&r_{\mathrm{f}} = [r_{\mathrm{f}}]\tilde{r}_{\mathrm{f}} = \tfrac{\rho_{\mathrm{m}}k_0|\Delta\rho||\mathbf{g}|}{[\mathbf{r}]\mu_{\mathrm{f}}}[\phi]^n\tilde{r}_{\mathrm{f}} && Q = [Q]\tilde{Q} = \tfrac{\rho_{\mathrm{m}}k_0|\Delta\rho||\mathbf{g}|L}{[\mathbf{r}]\mu_{\mathrm{f}}}[\phi]^n\tilde{Q} \\
&c = [c]\tilde{c} = \tfrac{\mu_{\mathrm{f}}[\phi]^{2-n}}{k_0}\tilde{c} && \omega = [\omega]\tilde{\omega} = [\phi]\tfrac{\mu_{\mathrm{f}}}{[\mu_{\mathrm{m}}]}\tilde{\omega} \\
&\alpha = [\alpha]\tilde{\alpha} = \alpha_0[\phi]^a\tilde{\alpha} && \xi = [\xi]\tilde{\xi} = \sigma_0\tilde{\xi} \\
&\Delta\varepsilon = [\Delta\varepsilon]\tilde{\Delta\varepsilon} = L\tilde{\Delta\varepsilon} \ .
\end{aligned} \tag{3.119}$$

Let us comment briefly on the above choices of scales. It is difficult to justify them a priori, without having any knowledge about the process itself (i.e. about the solution). The choice of scales already reflects certain particular regime of the studied physical system which, in principle, can only be justified either by inferring the scales directly by measurement on the real system, or by investigating the solution (e.g. numerical) of the full non-approximated problem. When neither of these is available as in our case, we may at least attempt to comment on the implicit physical assumptions to which our choice of scales corresponds.

- The gradient operator is scaled by $\frac{1}{[\mathbf{r}]}$, corresponding to an assumption of the spatial-variation scale being of the order of the domain dimension (due to our choice of $[\mathbf{r}]$ in Table 3.1). This assumption may not be satisfied e.g. for porosity ϕ and the porosity-dependent quantities in the case of formation of localized porosity waves. As no universally valid scale for the gradient is in fact available, our choice is just the simplest one. We can thus not rely on having dimensionless gradients of dimensionless quantities of the order of unity and a special attention must be paid whenever gradient terms are considered (and possibly omitted as a result of the formal scale analysis).

- Concerning the scale $[\boldsymbol{v}_\mathrm{m}]$ for ice velocity, our choice is typical for a system in a convective regime. We assume that the matrix velocities correspond to a (background) thermal convection process - the scale $[\boldsymbol{v}_\mathrm{m}]$ then comes from equilibration of the convective and diffusive term in the energy balance, i.e. by setting $\rho_\mathrm{m}[c_\mathrm{m}][\boldsymbol{v}_\mathrm{m}][\nabla T] = [\nabla]k_\mathrm{m}^\mathrm{T}[\nabla T]$.

- Since we will be interested preferably in the situation when the effects of surface tension are negligible, the scale for the pressure difference $[\Delta P]$ is obtained by setting it equal to the scale of the right-hand side in eq. (3.107), assuming in addition $\mu_\mathrm{f} \ll [\mu_\mathrm{m}]$ (relevant for water-ice mixture, cf. Table 3.1), in which case $\omega \sim 0$, cf. eq. (3.116).

- Scales for the 'percolation' velocity $[\boldsymbol{v}_\mathrm{r}]$ and the excess water pressure $[\Pi]$ can be inferred from the equations of motion (3.82) in the stationary limit (neglecting the effect of inertial forces on the left-hand sides), near a thermodynamic equilibrium (i.e. for melt production $r_\mathrm{f}=0$), when also the contribution of stresses $\boldsymbol{\sigma}_\mathrm{f}$, $\boldsymbol{\sigma}_\mathrm{m}$ is neglected, and again in the limit regime $\mu_\mathrm{f} \ll [\mu_\mathrm{m}]$, that is for $\omega \sim 0$ and $[c]=\frac{\mu_\mathrm{f}[\phi]^{2-n}}{k_0}$ (cf. eq. 3.117). Equation (3.82a) then yields $c\boldsymbol{v}_\mathrm{r} = -\phi\nabla\Pi - \phi\Delta\rho\mathbf{g}$ and by summing eqs (3.82a) and (3.82b) under the same assumptions (and neglecting surface tension, $\sigma \sim 0$), one obtains $\nabla\Pi = -\nabla((1-\phi)\Delta P) - \phi\Delta\rho\mathbf{g}$. From here, we can see that the gradient of the excess water pressure Π is given by the combination of a hydrostatic part due to the density contrast and a dynamic part originating in the viscous deformation of the matrix (through the term ΔP). These two mechanisms also control the drag $c\boldsymbol{v}_\mathrm{r}$. We shall assume, just for the purpose of scaling, that both scales for Π and $\boldsymbol{v}_\mathrm{r}$ are determined mainly by the density difference (hydrostatic) contribution, from where we obtain the scales as chosen above. Nevertheless, we keep in mind, that the dynamic contribution through ΔP may possibly dominate in some situations. Let us note that our choice of scale for $[\boldsymbol{v}_\mathrm{r}]$ matches the scaling by *Spiegelman* (1993a).

- The scale for $[\boldsymbol{v}_\mathrm{f}]$ need not be introduced, but we define it for convenience, assuming that the percolation velocity $\boldsymbol{v}_\mathrm{r}$ is much larger than the ice-flow velocity $\boldsymbol{v}_\mathrm{m}$, and the scale for $\boldsymbol{v}_\mathrm{f}$ thus coincides with the scale for $\boldsymbol{v}_\mathrm{r}$.

- The time scale $[t]$ is determined by the water transport process, and naturally defined by $[t] = \frac{[\mathbf{r}]}{[\boldsymbol{v}_\mathrm{r}]}$.

- The heat flux scale follows from the Fourier law (eq. 3.111) and the scales for both $[r_\mathrm{f}]$ and $[Q]$ are obtained from the requirement to have the dimensionless $\tilde{r}_\mathrm{f}$ and $\tilde{Q}$ of the order of unity in the dimensionless form of the energy balance (eq. 3.113).

- The scale for the drag coefficient $[c]$ follows from eqs (3.117) and (2.1) under the assumption $\mu_\mathrm{f} \ll [\mu_\mathrm{m}]$ and the scale for ω follows from eq. (3.116).

- The scale for the interfacial surface density $[\alpha]$ follows from eq. (3.115) in the regime $[\phi] \ll 1$, in which we will be mostly interested (corresponding to only partially molten matrix).

- The interfacial energy density scale $[\xi]$ is taken equal to the surface tension scale σ_0, according to eq. (3.92).

- The scale for the internal energy difference $\Delta\varepsilon$ is inferred from eq. (3.109) assuming that the mechanical work associated with the phase change is of secondary importance compared to the entropy-change contribution (latent heat).

3.4.2 Dimensionless balance laws

We have introduced in total 14 independent dimensional scales and parameters ($[\mathbf{r}]$, T_0, $|\Delta\rho|$, ρ_m, k_m^T, k_f^T, $[c_\mathrm{m}]$, $[c_\mathrm{f}]$, $|\mathbf{g}|$, k_0, $[L]$, $\alpha_0\sigma_0$, μ_f, $\mu_\mathrm{m}^\mathrm{ref}$)[6] and we use 4 physical units (m, kg, s, K) - it follows from the Buckingham's Π theorem (e.g. *Hutter & Jöhnk*, 2004) that there exist 14−4=10 independent dimensionless numbers which, accompanied by the already dimensionless $[\phi]$ and the appropriate constitutive law parameters, fully characterize the system. These are:

$$\begin{array}{llllll} \mathcal{C} = \frac{[c_\mathrm{m}]}{[c_\mathrm{f}]} & \mathcal{K} = \frac{k_\mathrm{m}^\mathrm{T} - k_\mathrm{f}^\mathrm{T}}{\frac{2k_\mathrm{m}^\mathrm{T} + k_\mathrm{f}^\mathrm{T}}{3}} & \mathcal{L} = \frac{g[\mathbf{r}]}{[L]} & \mathcal{M} = \frac{[\mu_\mathrm{m}]}{\mu_\mathrm{f}} & \mathcal{P} = \frac{[c_\mathrm{m}][\mu_\mathrm{m}]}{k_\mathrm{m}^\mathrm{T}} & \\ \mathcal{R} = \frac{|\Delta\rho|}{\rho_\mathrm{m}} & \mathcal{S} = \frac{\alpha_0\sigma_0}{[\Delta P]} & \mathcal{T} = \frac{[c_\mathrm{m}]T_0}{[L]} & \mathcal{V} = \frac{[\boldsymbol{v}_\mathrm{m}]}{[\boldsymbol{v}_\mathrm{r}]} & \mathcal{X} = \frac{k_0}{[\mathbf{r}]^2} & \end{array} \tag{3.120}$$

With our choice of scales, we can write down the corresponding dimensionless form of the governing equations. Writing all the dimensionless field variables without tildes for better clarity, the dimensionless form reads as follows:

Balances of mass

$$\frac{\partial\phi}{\partial t} + \nabla\cdot(\phi\boldsymbol{v}_\mathrm{r}) + \mathcal{V}\nabla\cdot(\phi\boldsymbol{v}_\mathrm{m}) = \frac{r_\mathrm{f}}{1+\mathcal{R}}\ , \tag{3.121a}$$

$$-\frac{\partial\phi}{\partial t} + \frac{\mathcal{V}}{[\phi]}\nabla\cdot((1-[\phi]\phi)\boldsymbol{v}_\mathrm{m}) = -r_\mathrm{f}\ . \tag{3.121b}$$

[6] We consider α_0 and σ_0 as one parameter, since they only appear in all equations as a product. Also, we do not count the material parameters that appear within exponential constitutive laws, such as ice viscosity activation parameters, etc.

Equations of motion

$$\begin{aligned}
\mathscr{A}\phi\frac{\mathrm{D_f}\boldsymbol{v}_\mathrm{f}}{\mathrm{D}t} &= -[\phi]\phi\nabla\Pi - \phi\mathbf{e}_\mathrm{z} && \text{(3.122a)}\\
&\quad + \mathscr{X}[\phi]^{n-1}\nabla\cdot\left(\phi\left(\nabla\boldsymbol{v}_\mathrm{f}+(\nabla\boldsymbol{v}_\mathrm{f})^\mathrm{T}-\frac{2}{3}(\nabla\cdot\boldsymbol{v}_\mathrm{f})\mathbf{I}\right)\right)\\
&\quad - \mathscr{B}(1-[\omega]\omega)\boldsymbol{v}_\mathrm{r}r_\mathrm{f} + \mathscr{C}[\omega]\omega\Delta P\nabla\phi + \mathscr{D}[\omega]\omega\nabla(\sigma\alpha) - c\boldsymbol{v}_\mathrm{r}\ ,\\
\mathscr{E}(1-[\phi]\phi)\frac{\mathrm{D_m}\boldsymbol{v}_\mathrm{m}}{\mathrm{D}t} &= -\frac{1-[\phi]\phi}{[\phi]}\left(\mathscr{C}\nabla\Delta P + [\phi]\nabla\Pi\right) && \text{(3.122b)}\\
&\quad + \mathscr{C}\nabla\cdot\left((1-[\phi]\phi)\mu_\mathrm{m}\left(\nabla\boldsymbol{v}_\mathrm{m}+(\nabla\boldsymbol{v}_\mathrm{m})^\mathrm{T}-\frac{2}{3}(\nabla\cdot\boldsymbol{v}_\mathrm{m})\mathbf{I}\right)\right)\\
&\quad - \mathscr{B}[\omega]\omega\boldsymbol{v}_\mathrm{r}r_\mathrm{f} + (1-[\omega]\omega)\left(\mathscr{C}\Delta P\nabla\phi + \mathscr{D}\nabla(\sigma\alpha)\right) + c\boldsymbol{v}_\mathrm{r}\ .
\end{aligned}$$

The dimensionless form of the dynamic pressure difference (eq. 3.107) reads

$$\begin{aligned}
\Delta P + \mathcal{S}[\phi]^{a-1}\sigma\frac{\mathrm{d}\alpha}{\mathrm{d}\phi} \quad &= -\frac{1}{\phi(1-[\phi]\phi)}\left(\frac{1}{\mathcal{M}}+\mu_\mathrm{m}\right) && \text{(3.123)}\\
&\quad \left((1-[\omega]\omega)(1-[\phi]\phi)\nabla\cdot\boldsymbol{v}_\mathrm{m} - \frac{[\phi][\omega]}{\mathcal{V}}\phi\omega\nabla\cdot\boldsymbol{v}_\mathrm{f}\right)\ .
\end{aligned}$$

Energy balance

$$\begin{aligned}
&\mathscr{F}\phi c_\mathrm{f}\left(\frac{\partial T}{\partial t} + \boldsymbol{v}_\mathrm{r}\cdot\nabla T + \mathcal{V}\boldsymbol{v}_\mathrm{m}\cdot\nabla T\right) + \mathcal{T}\frac{1-[\phi]\phi}{[\phi]}c_\mathrm{m}\left(\frac{\partial T}{\partial t} + \mathcal{V}\boldsymbol{v}_\mathrm{m}\cdot\nabla T\right)\\
-\ &\mathscr{G}T\left(\frac{\partial}{\partial t}\left(\alpha\frac{\mathrm{d}\sigma}{\mathrm{d}T}\right) + ([\omega]\omega\boldsymbol{v}_\mathrm{r}+\mathcal{V}\boldsymbol{v}_\mathrm{m})\cdot\nabla\left(\alpha\frac{\mathrm{d}\sigma}{\mathrm{d}T}\right)\right)\\
-\ &\mathscr{G}\alpha T\frac{\mathrm{d}\sigma}{\mathrm{d}T}\nabla\cdot([\omega]\omega\boldsymbol{v}_\mathrm{r}+\mathcal{V}\boldsymbol{v}_\mathrm{m}) + Lr_\mathrm{f} = Q + \mathscr{H}\nabla\cdot\left((1-\mathcal{K}[\phi]\phi)\nabla T\right)\\
+\ &\mathscr{I}c|\boldsymbol{v}_\mathrm{r}|^2 + \mathscr{J}\phi\nabla\boldsymbol{v}_\mathrm{f}\colon\left(\nabla\boldsymbol{v}_\mathrm{f}+(\nabla\boldsymbol{v}_\mathrm{f})^\mathrm{T}-\frac{2}{3}(\nabla\cdot\boldsymbol{v}_\mathrm{f})\mathbf{I}\right)\\
+\ &\mathscr{K}(1-[\phi]\phi)\mu_\mathrm{m}\nabla\boldsymbol{v}_\mathrm{m}\colon\left(\nabla\boldsymbol{v}_\mathrm{m}+(\nabla\boldsymbol{v}_\mathrm{m})^\mathrm{T}-\frac{2}{3}(\nabla\cdot\boldsymbol{v}_\mathrm{m})\mathbf{I}\right)\\
+\ &\frac{\mathscr{K}(\frac{1}{\mathcal{M}}+\mu_\mathrm{m})}{\phi(1-[\phi]\phi)}\left((1-[\omega]\omega)(1-[\phi]\phi)\nabla\cdot\boldsymbol{v}_\mathrm{m} - \frac{[\omega][\phi]}{\mathcal{V}}\omega\phi\nabla\cdot\boldsymbol{v}_\mathrm{f}\right)^2\ . \qquad \text{(3.124)}
\end{aligned}$$

The dimensionless form of implicit melting temperature relation (eq. 3.109) reads

$$\begin{aligned}
\Delta\varepsilon + L \quad &= -\mathscr{I}\tfrac{1}{1+\mathcal{R}}\left(P_\mathrm{m}^\mathrm{ref} + \mathcal{R}[\phi]\Pi + [\omega]\mathscr{C}\mathcal{R}\omega\Delta P\right)\\
&\quad +\mathscr{G}\left(1-[\omega]\omega\tfrac{\mathcal{R}}{1+\mathcal{R}}\right)\left(\sigma\tfrac{\mathrm{d}\alpha}{\mathrm{d}\phi}\right) - \tfrac{1-2[\omega]\omega}{2}\mathscr{L}|\boldsymbol{v}_\mathrm{r}|^2\ . \qquad \text{(3.125)}
\end{aligned}$$

Symb.	Variable	Value	Unit	Reference
α_{m}	*ice thermal expansivity*	1.6×10^{-4}	1/K	*Lide* (2004)
α_0	*surface area density parameter*	$1/d$	1/m	*Bercovici et al.* (2001)
a	*surface area density parameter*	$\in\langle 0,1\rangle$	-	*Bercovici et al.* (2001)
b	*surface area density parameter*	$\in\langle 0,1\rangle$	-	*Bercovici et al.* (2001)
β	*ice-water surf. tension exponent*	0.8	-	*Lide* (2004)
$[c_{\mathrm{f}}]$	*heat capacity of water**	4180	J/kg/K	*Lide* (2004)
$[c_{\mathrm{m}}]$	*heat capacity of ice**	2100	J/kg/K	*Lide* (2004)
d	*average ice grain size*	10^{-3}	m	*Barr & Showman* (2009)
$\lvert\Delta\rho\rvert$	*density difference*	80	kg/m^3	*Lide* (2004)
$[\phi]$	*porosity scale*	5×10^{-2}	-	-
$\lvert\mathbf{g}\rvert$	*surface gravity*$^{\mathrm{E}}$	1.32	m/s^2	-
k_0	*permeability constant*	10^{-9}	m^2	*Golden et al.* (2007) *Petrich & Eicken* (2009)
k_0^{c}	*permeability decrease below* ϕ_{c}	10^{-5}	-	-
$k_{\mathrm{f}}^{\mathrm{T}}$	*water thermal conductivity**	0.56	W/m/K	*Lide* (2004)
$k_{\mathrm{m}}^{\mathrm{T}}$	*ice thermal conductivity**	2.3	W/m/K	*Lide* (2004)
$[L]$	*latent heat of melting of ice**	333×10^3	J/kg	*Lide* (2004)
μ_{f}	*water shear viscosity**	1.793×10^{-3}	Pa s	*Lide* (2004)
$\mu_{\mathrm{m}}^{\mathrm{ref}}$	*reference ice shear viscosity**	10^{14}	Pa s	-
n	*permeability exponent*	2	-	*Golden et al.* (2007)
$[\mathbf{r}]$	*ice layer thickness*$^{\mathrm{E}}$	30	km	-
ρ_{f}	*water density**	1000	kg/m^3	*Lide* (2004)
ρ_{m}	*ice density**	920	kg/m^3	*Lide* (2004)
σ_0	*surf. tension of system ice-water*	3×10^{-2}	J/m^2	*Van Oss et al.* (1992)
T_0	*ice melt. temp. at pressure* P_0	273.15	K	*Lide* (2004)
T_{c}	*critical temperature of water*	647.14	K	*Lide* (2004)
p	*constant in melt. temp.*	-395.2×10^6	Pa	*Chizhov* (1993)
q	*constant in melt. temp.*	9	-	*Chizhov* (1993)
P_0	*reference pressure*	0	Pa	*Chizhov* (1993)
γ_{m}	*porosity weakening exponent*	45	-	*Tobie et al.* (2003)

Table 3.1: Model parameters. Symbol * denotes the value at temperature T=273.15 K and symbol $^{\mathrm{E}}$ denotes the values corresponding to the ice shell of Europa.

In all the above equations, we introduced several auxiliary dimensionless products which are defined as:

$$\begin{aligned}
&\mathscr{A}=\tfrac{\mathcal{X}\mathcal{M}(1+\mathcal{R})}{\mathcal{V}\mathcal{P}}[\phi]^{n-1} && \mathscr{B}=\tfrac{\mathcal{X}\mathcal{M}}{\mathcal{V}\mathcal{P}}[\phi]^{n-1} && \mathscr{C}=\mathcal{V}\mathcal{X}\mathcal{M}[\phi]^{n-2}\\
&\mathscr{D}=\mathcal{S}\mathcal{V}\mathcal{X}\mathcal{M}[\phi]^{n+a-3} && \mathscr{E}=\tfrac{\mathcal{X}\mathcal{M}}{\mathcal{P}}[\phi]^{n-2} && \mathscr{F}=\tfrac{\mathcal{T}}{\mathcal{C}}(1+\mathcal{R})\\
&\mathscr{G}=\mathcal{S}\mathcal{L}\mathcal{V}\mathcal{X}\mathcal{M}\mathcal{R}[\phi]^{n+a-3} && \mathscr{H}=\tfrac{\mathcal{T}\mathcal{V}}{[\phi]} && \mathscr{I}=\mathcal{R}\mathcal{L}\\
&\mathscr{J}=\mathcal{R}\mathcal{L}\mathcal{X}[\phi]^{n-1} && \mathscr{K}=\mathcal{R}\mathcal{L}\mathcal{X}\mathcal{M}\mathcal{V}^2[\phi]^{n-2} && \mathscr{L}=\tfrac{\mathcal{L}\mathcal{X}\mathcal{R}\mathcal{M}[\phi]^{n-1}}{\mathcal{V}\mathcal{P}}
\end{aligned} \tag{3.126}$$

3.4.3 Reduced balance laws

We now proceed in a standard manner and attempt to assess the importance of each term in the balance equations above by evaluating all dimensionless numbers

and their products in the setting of our particular application. The values of all the physical parameters and of the principal scales are listed in Table 3.1. For such choice, the dimensionless numbers and their products are as follows

$$\begin{array}{llll} \mathcal{C} = 5.0{\times}10^{-1} & \mathcal{K} = 1.0 & \mathcal{L} = 1.2{\times}10^{-1} & \mathcal{M} = 5.6{\times}10^{16} \\ \mathcal{P} = 9.1{\times}10^{16} & \mathcal{R} = 8.7{\times}10^{-2} & \mathcal{S} = 1.1 - 1.1{\times}10^{2} & \mathcal{T} = 1.7 \\ \mathcal{V} = 1.3{\times}10^{-5} & \mathcal{X} = 1.1{\times}10^{-18} & & \end{array} \tag{3.127}$$

$$\begin{array}{lll} \mathscr{A} = 2.8{\times}10^{-15} & \mathscr{B} = 2.6{\times}10^{-15} & \mathscr{C} = 8.0{\times}10^{-7} \\ \mathscr{D} = 8.8{\times}10^{-7} - 1.8{\times}10^{-3} & \mathscr{E} = 6.8{\times}10^{-19} & \mathscr{F} = 3.7 \\ \mathscr{G} = 9.2{\times}10^{-9} - 1.8{\times}10^{-5} & \mathscr{H} = 4.4{\times}10^{-4} & \mathscr{I} = 1.0{\times}10^{-2} \\ \mathscr{J} = 5.7{\times}10^{-22} & \mathscr{K} = 1.1{\times}10^{-13} & \mathscr{L} = 2.7{\times}10^{-17} \end{array} \tag{3.128}$$

Now we attempt to simplify the system of equations (3.121)–(3.125) by omitting the terms of negligible physical importance.

Balances of mass

Despite the parameter $\mathcal{V}$ in eq. (3.121) is of the order $O(10^{-5})$ and compared to the remaining terms apparently of the order $O(1)$, we decide not to omit this term. Since the scale for gradient operator was taken as $[\nabla] = \frac{1}{[\mathbf{r}]}$, the dimensionless spatial derivatives are of the order $O(1)$ only provided the quantity varies on the scale $[\mathbf{r}]$. This (as we will see in numerical simulations) is not satisfied for $\phi\boldsymbol{v}_\mathrm{m}$, which varies on much finer spatial scale, and its dimensionless derivative may thus be orders of magnitude larger. The dimensionless form of mass balances is therefore kept unchanged:

$$\frac{\partial\phi}{\partial t} + \nabla\cdot(\phi\boldsymbol{v}_\mathrm{r}) + \mathcal{V}\nabla\cdot(\phi\boldsymbol{v}_\mathrm{m}) = \frac{r_\mathrm{f}}{1+\mathcal{R}}\ , \tag{3.129a}$$

$$-\frac{\partial\phi}{\partial t} + \frac{\mathcal{V}}{[\phi]}\nabla\cdot((1-[\phi]\phi)\boldsymbol{v}_\mathrm{m}) = -r_\mathrm{f}\ . \tag{3.129b}$$

Equations of motion

Inspecting the values of dimensionless numbers (3.127) and their products (3.128), we can see that in the fluid momentum balance (eq. 3.122a), we can safely neglect the inertial term on the left-hand side (by setting $\mathscr{A}$=0), the viscous stresses in the fluid phase (by setting $\mathcal{X}$=0), the momentum transfer due to melting/freezing (by setting $\mathscr{B}$=0) and the joined effect of the dynamic pressure difference and surface tension (by setting $[\omega]$=0), and arrive at

$$c\boldsymbol{v}_\mathrm{r} = -[\phi]\phi\nabla\Pi - \phi\mathbf{e}_\mathrm{z}\ . \tag{3.130}$$

We now simplify the pressure difference relation (eq. 3.123) by setting $[\omega]$=0, $\frac{1}{\mathcal{M}}$=0 and $\frac{[\omega]}{\mathcal{V}}$=0, which yields

$$\Delta P = -\mathcal{S}[\phi]^{a-1}\sigma\frac{\mathrm{d}\alpha}{\mathrm{d}\phi} - \frac{\mu_\mathrm{m}}{\phi}\nabla\cdot\boldsymbol{v}_\mathrm{m}\ . \tag{3.131}$$

Here, the expression $\frac{\mu_\mathrm{m}}{\phi}$ can be interpreted as a porosity-dependent bulk viscosity ζ (cf. *Ricard et al.*, 2001). Concerning the equation of motion for the ice phase (eq. 3.122b), we observe that we can again safely neglect the effect of inertial forces (by setting $\mathscr{E}$=0), the effect of momentum transfer due to melting/freezing (by setting $\mathscr{B}$=0) and also set $[\omega]$=0. Employing now relation (3.131) in eq. (3.122b) we arrive at

$$\begin{aligned}(1-[\phi]\phi)\nabla\Pi &= c\boldsymbol{v}_\mathrm{r} + \mathscr{C}\nabla\cdot\left((1-[\phi]\phi)\mu_\mathrm{m}\left(\nabla\boldsymbol{v}_\mathrm{m}+(\nabla\boldsymbol{v}_\mathrm{m})^\mathrm{T}-\frac{2}{3}(\nabla\cdot\boldsymbol{v}_\mathrm{m})\boldsymbol{I}\right)\right)\\ &+ \mathscr{C}\nabla\left(\frac{(1-[\phi]\phi)}{[\phi]}\left(\mathcal{S}[\phi]^{a-1}\sigma\frac{\mathrm{d}\alpha}{\mathrm{d}\phi}+\frac{\mu_\mathrm{m}}{\phi}\nabla\cdot\boldsymbol{v}_\mathrm{m}\right)\right)+\mathscr{D}\nabla(\sigma\alpha)\ .\end{aligned} \tag{3.132}$$

Energy balance

In the energy balance (eq. 3.124), we only keep the term $\mathscr{G}T\frac{\partial}{\partial t}\left(\alpha\frac{\mathrm{d}\sigma}{\mathrm{d}T}\right)$ from the contribution of surface energy to the total internal energy balance (by setting $[\omega]$=0 and $\mathscr{G}\mathcal{V}$=0). The deformational work of both phases can also be neglected (by setting $\mathscr{J}$=0, $\mathscr{K}$=0, $\frac{[\omega]}{\mathcal{V}}$=0) and we arrive at

$$\begin{aligned}&\mathscr{F}\phi c_\mathrm{f}\left(\frac{\partial T}{\partial t}+\boldsymbol{v}_\mathrm{r}\cdot\nabla T+\mathcal{V}\boldsymbol{v}_\mathrm{m}\cdot\nabla T\right)+\mathcal{T}\frac{1-[\phi]\phi}{[\phi]}c_\mathrm{m}\left(\frac{\partial T}{\partial t}+\mathcal{V}\boldsymbol{v}_\mathrm{m}\cdot\nabla T\right)\\ -\ &\mathscr{G}T\frac{\partial}{\partial t}\left(\alpha\frac{\mathrm{d}\sigma}{\mathrm{d}T}\right)+Lr_\mathrm{f}=Q+\mathscr{H}\nabla\cdot\left((1-\mathcal{K}[\phi]\phi)\nabla T\right)+\mathscr{I}c|\boldsymbol{v}_\mathrm{r}|^2\end{aligned} \tag{3.133}$$

We have mentioned earlier that in the partially molten region, by employing an assumption of very fast melting kinetics, we can assume an equilibrium condition (of the type of eq. 3.109 or its dimensionless form, eq. 3.125) to hold, which implicitly defines the melting temperature as a function of the given conditions. According to values of dimensionless numbers (3.127) and their products (3.128), we can neglect all the dynamic pressure effects ($\sim\Pi, \sim\Delta P$), surface tension effect and 'kinetic energy' effect ($\sim|\boldsymbol{v}_\mathrm{r}|^2$) and keep just the leading-order effect of the background (static) pressure $P_\mathrm{m}^\mathrm{ref}$ on the equilibrium, i.e. we set $[\omega]\mathscr{C}$=0, $\mathscr{G}$=0, $\mathscr{L}$=0 and also $\mathscr{I}\mathcal{R}[\phi]$=0 in eq. (3.125) and arrive at

$$\Delta\varepsilon + L = -\frac{\mathscr{I}}{1+\mathcal{R}}P_\mathrm{m}^\mathrm{ref}\ . \tag{3.134}$$

Since, due to eqs (3.98), $\Delta\varepsilon=\Delta\varepsilon(T)$, $L=L(T)$, and the equilibrium static pressure $P_\mathrm{m}^\mathrm{ref}$ is assumed to be a known function of position $\mathbf{r}$ (depth typically), eq. (3.134) is an implicit melting-temperature–depth relation. An explicit (dimensional) counterpart to this relation is considered in the form (*Simon & Glatzel*, 1929):

$$T_\mathrm{M}(P_\mathrm{m}) = T_0\left(\frac{P_\mathrm{m}^\mathrm{ref}-P_0}{p}+1\right)^{\frac{1}{q}}\ , \tag{3.135}$$

where T_0 denotes the melting temperature at reference pressure P_0, and p, q are the empirical constants (with values taken from *Chizhov*, 1993).

Role of surface tension

So far, we have kept some of the terms involving surface tension in our reduced formulation. In fact, we cannot safely neglect the remaining terms involving σ in the matrix linear momentum balance (eq. 3.132) and the energy balance (eq. 3.133) just based on the scale analysis. Despite the magnitude of the terms is apparently at most $O(10^{-4})$, whether this is true again depends on the validity of the implicit assumptions on scaling of temporal and spatial derivatives. For processes with short-scale temporal or spatial variations, the magnitude of these terms would increase and their contribution may possibly become important. A proper treatment of surface energy contribution in the momentum and energy balances would, however, require a more detailed information about the microstructure of the material, such as grain size distribution, interfacial geometry, etc., in order to reliably estimate the parameters a, b, α_0 in eq. (3.115). Discussion of these microstructural details would require a substantial further effort going beyond the scope of this work, and such information may even not be available in our (planetary) application. Morover, in Section 5.5 we numerically investigate the role of surface tension for several combinations of parameters a, b, and α_0, and find that it is negligible in the context of this work. We will thus systematically omit the surface tension effects from our considerations by setting $\mathscr{G}$=0, $\mathscr{D}$=0.

3.4.4 Final reduced model

Here, the governing equations (3.129)–(3.133) are slightly reformulated and given in a compact form for better clarity. Instead of the two mass balances (3.129a), (3.129b), we use the second one and the sum of the two. Also, we substitute for $c\boldsymbol{v}_\mathrm{r}$ from eq. (3.130) into eq. (3.132) so we can explicitly express the gradient of the excess water pressure $\nabla\Pi$. The model now reads as follows:

$$\frac{\partial\phi}{\partial t} - \frac{\mathcal{V}}{[\phi]}\nabla\cdot((1-[\phi]\phi)\boldsymbol{v}_\mathrm{m}) = r_\mathrm{f}\ , \tag{3.136a}$$

$$\frac{\mathcal{V}}{[\phi]}\nabla\cdot\boldsymbol{v}_\mathrm{m} + \nabla\cdot(\phi\boldsymbol{v}_\mathrm{r}) = -\frac{\mathcal{R}}{1+\mathcal{R}}r_\mathrm{f}\ , \tag{3.136b}$$

$$c\boldsymbol{v}_\mathrm{r} = -\phi\mathbf{e}_\mathrm{z} - [\phi]\phi\nabla\Pi\ , \tag{3.136c}$$

$$\begin{aligned}\nabla\Pi = {}& -\phi\mathbf{e}_\mathrm{z} \\ & + \mathscr{C}\nabla\cdot\left((1-[\phi]\phi)\mu_\mathrm{m}\left(\frac{1}{[\phi]\phi}(\nabla\cdot\boldsymbol{v}_\mathrm{m})\mathbf{I} + \nabla\boldsymbol{v}_\mathrm{m} + (\nabla\boldsymbol{v}_\mathrm{m})^\mathrm{T} - \frac{2}{3}(\nabla\cdot\boldsymbol{v}_\mathrm{m})\mathbf{I}\right)\right)\ ,\end{aligned} \tag{3.136d}$$

$$\begin{aligned}&\mathscr{F}\phi c_\mathrm{f}\left(\frac{\partial T}{\partial t} + \boldsymbol{v}_\mathrm{r}\cdot\nabla T + \mathcal{V}\boldsymbol{v}_\mathrm{m}\cdot\nabla T\right) + \mathcal{T}\frac{1-[\phi]\phi}{[\phi]}c_\mathrm{m}\left(\frac{\partial T}{\partial t} + \mathcal{V}\boldsymbol{v}_\mathrm{m}\cdot\nabla T\right) + Lr_\mathrm{f} \\ &= Q + \mathscr{H}\nabla\cdot\left((1-\mathcal{K}[\phi]\phi)\nabla T\right) + \mathscr{I}c|\boldsymbol{v}_\mathrm{r}|^2\ .\end{aligned} \tag{3.136e}$$

Zero compaction length approximation

In certain applications, the presented physical model may be reduced even more by imposing the so-called 'zero compaction length approximation', which is based on the following observation. The formula for the gradient of the excess water pressure Π (eq. 3.136d) reveals that the parameter $\mathscr{C}$ and the spatial scale at which $\nabla \boldsymbol{v}_\mathrm{m}$ (or, in fact $(1-[\phi]\phi)\nabla \boldsymbol{v}_\mathrm{m}$) changes, determine the extent to which the deformation of the matrix affects the excess water pressure Π and via eq. (3.136c) also the fluid flow. The classical length scale parameter - compaction length δ, introduced e.g. by *Spiegelman* (1993a), can be inferred from eq. (3.136d) provided we assume μ_m to be a constant, take $\zeta = \frac{\mu_\mathrm{m}}{\phi}$ as a constant bulk viscosity, and neglect the term $[\phi]\phi$ compared to 1 in the parenthesis. If the true scale of spatial variations of $\boldsymbol{v}_\mathrm{m}$ is δ (instead of unity as would correspond to the introduced scale of ∇), we can see that the second term on the right-hand side would be of the same order ($O(1)$) as the first term provided $\delta = \sqrt{\mathscr{C}}$, in which case the dynamic coupling between the fluid flow and matrix deformation becomes important. Depending on whether the model of the particular process requires to include these coupling effects or not, we speak about the 'non-zero $\mathscr{C}$ approximation' and 'zero $\mathscr{C}$ approximation', respectively.[7]

In the zero $\mathscr{C}$ approximation (i.e. by setting $\mathscr{C}$=0), the flow law for the fluid is rather simple as can be seen from eqs (3.136d) and (3.136c). It reads

$$c\boldsymbol{v}_\mathrm{r} = -(1-[\phi]\phi)\phi\mathbf{e}_\mathrm{z} \ , \tag{3.137}$$

and indicates that the fluid flow is driven solely by the buoyancy force. Since by setting $\mathscr{C}$=0 the coupling term of the highest differential order is omitted, the mathematical character of the problem changes and the solution can be expected to differ even qualitatively from the non-zero $\mathscr{C}$ case. It is indeed the case as we will observe in numerical simulations in Section 5.6 - while in the zero $\mathscr{C}$ approximation, the problem is essentially a nonlinear hyperbolic transport law for porosity, with a tendency to produce discontinuous (shock) solutions, in the latter case, when the coupling phenomena are present, the solutions exhibit formation of wave trains. We will inspect the character and differences between the (numerical) solutions of our system in both the zero $\mathscr{C}$ and non-zero $\mathscr{C}$ approximations in simplified 1d geometry in Section 5.6. The zero $\mathscr{C}$ version of the final model (3.136) is obtained simply by setting $\mathscr{C}$=0 in eq. (3.136d).

[7] Expressing $\sqrt{\mathscr{C}}$ in terms of the physical parameters according to (3.126) and (3.120), does not produce Spiegelman's formula for δ. The reason is a different scaling of velocities - while we are using separate scales for $[\boldsymbol{v}_\mathrm{m}]$ and $[\boldsymbol{v}_\mathrm{r}]$, respectively, *Spiegelman* (1993a) uses a single velocity scale for both. Our formula for δ thus differs from Spiegelman's by a multiplicative factor $\mathcal{V} = \frac{[\boldsymbol{v}_\mathrm{m}]}{[\boldsymbol{v}_\mathrm{r}]}$.

4. Numerical methods

In this chapter, we describe the numerical methods employed throughout this thesis. Since we have used two very different approaches, the following text is divided accordingly - we begin with our own code based on finite volume method and written in FORTRAN90 (Section 4.1) and then continue with codes that use a free finite element software package FEniCS (http://fenicsproject.org/, Sections 4.2 and 4.3).

4.1 FORTRAN90 code for temperate or polythermal ice simulations (1d)

The first code that was developped during this work is written in FORTRAN90 and enables to solve two kinds of problems: (i) the gravity-driven extraction of a prescribed partially molten reservoir in a purely temperate ice layer or (ii) the formation and subsequent evolution of a partially molten reservoir in a polythermal ice layer. Since the code enables to solve the problems only in one-dimensional setting, we start with summarizing the one-dimensional governing equations and the appropriate boundary conditions (Section 4.1.1), then we describe the numerical method used to solve this problem (Section 4.1.2) and finally we perform several tests in order to verify the code (Section 4.1.3).

4.1.1 Governing equations and boundary conditions (1d)

Governing equations

The system of governing equations in the one-dimensional Cartesian geometry is obtained from eqs (3.136) by considering only vertical motion and vertical dependence of all quantities (with z the vertical coordinate oriented upwards and ranging from 0 to 1 in the dimensionless equations system):

$$\frac{\partial \phi}{\partial t} + \frac{\partial}{\partial z}\Big(\phi(v_\mathrm{r}+\mathcal{V}v_\mathrm{m})\Big) = \frac{r_\mathrm{f}}{1+\mathcal{R}} \ , \tag{4.1a}$$

$$\begin{aligned}&\frac{\mathcal{V}}{[\phi]}\frac{\partial v_\mathrm{m}}{\partial z} - \frac{\partial}{\partial z}\left\{[\phi]\phi^2\mathscr{C}\frac{\partial}{\partial z}\left((1-[\phi]\phi)\left(\frac{1}{[\phi]\phi}+\frac{4}{3}\right)\frac{\partial v_\mathrm{m}}{\partial z}\right)\right\}\\ &= \frac{\partial}{\partial z}\Big(\phi^2(1-[\phi]\phi)\Big) - \frac{\mathcal{R}}{1+\mathcal{R}}r_\mathrm{f} \ ,\end{aligned} \tag{4.1b}$$

$$v_\mathrm{r} = -(1-[\phi]\phi)\phi - [\phi]\phi\mathscr{C}\frac{\partial}{\partial z}\left((1-[\phi]\phi)\left(\frac{1}{[\phi]\phi}+\frac{4}{3}\right)\frac{\partial v_\mathrm{m}}{\partial z}\right) \ , \tag{4.1c}$$

$$\begin{aligned}&\left(\mathscr{F}\phi + \mathcal{T}\frac{1-[\phi]\phi}{[\phi]}\right)\frac{\partial T}{\partial t} + r_\mathrm{f} = -\left(\mathscr{F}\phi(v_\mathrm{r}+\mathcal{V}v_\mathrm{m}) + \mathcal{T}\mathcal{V}\frac{1-[\phi]\phi}{[\phi]}v_\mathrm{m}\right)\frac{\partial T}{\partial z}\\ &+ Q + \mathscr{H}\frac{\partial}{\partial z}\left((1-\mathscr{K}[\phi]\phi)\frac{\partial T}{\partial z}\right) + \mathscr{I}|v_\mathrm{r}|^2 \ .\end{aligned} \tag{4.1d}$$

Here, for numerical reasons, we took eq. (3.129a) instead of eq. (3.136a) as a transport equation for porosity (since they are equivalent). We also substituted

for $\frac{\partial \Pi}{\partial z}$ from eq. (3.136d) to eq. (3.136c) and then for v_r from eq. (3.136c) to eq. (3.136b), thus completely eliminating the excess water pressure Π from the system in this one-dimensional setting and reducing the number of equations accordingly. We considered (dimensionless) c=1 (corresponding to permeability law given by eq. 2.1 with n=2), and μ_m=1, L=1, c_f=1, c_m=1 (corresponding to constant material parameters). Equation (4.1c) expresses the balance of the drag force (left-hand side), the gravitational force (first term on the right-hand side) and the force induced by mechanical coupling between the deformation of the ice matrix and the movement of liquid water through the ice matrix (second term on the right-hand side). The zero $\mathscr{C}$ approximation is obtained by setting $\mathscr{C}$=0 in eqs (4.1b) and (4.1c).

Note, that in a purely temperate setting, the temperature is not independent but is equal to (constant-in-time) melting temperature T_M (eq. 3.135) and its role is taken over by porosity ϕ. Equation (4.1d) then enables to compute the melting rate r_f which is controlled by heat advection (first term on the right-hand side), volumetric heating (second term on the right-hand side), conductive heat transfer (third term on the right-hand side) and frictional heating due to water movement through the ice matrix (last term on the right-hand side).

If the ice is cold, i.e. $T<T_\mathrm{M}$, there is no interstitial water present (ϕ=0) and equations (4.1a) and (4.1c) need not be solved. Due to the numerical scheme used (cf. below), equation (4.1b) can be solved even for ϕ=0 and finally, eq. (4.1d) reduces for ϕ=0 to standard heat equation for unknown temperature T.

Few remarks on the character of the system

Specification of the boundary conditions for multi-phase systems is a delicate problem per se. In the cold ice case, the boundary conditions can be chosen from the standard ones, but for the temperate ice, the choice is less obvious. Before specifying the particular boundary conditions, we attempt to give a very simple characterization of the studied system, which might provide us with an useful insight. Let us first inspect the simpler of the two cases, the zero $\mathscr{C}$ system - eq. (4.1c) then gives v_r as an explicit function of ϕ. As for v_m, we can neglect melting for the moment (by setting r_f=0) and integrate (4.1b) from 0 to z:

$$v_\mathrm{m}(z,t) - v_\mathrm{m}(0,t) = \frac{[\phi]}{\mathcal{V}}\Big(\phi^2(z,t)(1-[\phi]\phi(z,t)) - \phi^2(0,t)(1-[\phi]\phi(0,t))\Big) \ . \quad (4.2)$$

If we now prescribe homogeneous Dirichlet boundary condition for ice velocity at the base of the domain, $v_\mathrm{m}(0,t)$=0 (which will, indeed, be the case, cf. eq. 4.5) and take $\phi(0,t)$=0, the porosity transport would be governed by the following nonlinear hyperbolic equation

$$\frac{\partial \phi}{\partial t} - 2\phi(1-[\phi]\phi)(1-2[\phi]\phi)\frac{\partial \phi}{\partial z} = 0 \ . \quad (4.3)$$

The solution of this equation can be easily found by advection of the initial condition $\phi^0(z)$=$\phi(z,0)$ along the characteristic curves. Character of the porosity advection velocity indicates already quite a complex behavior - one can expect shock development and propagation as a result of characteristics intersection, which can be achieved for suitably chosen initial data. We will demonstrate this

well known (e.g. *Evans*, 1998) phenomenon later in numerical simulations. Note, that in our example, the slope of the characteristics changes sign for $[\phi]\phi^0 = 0.5$, in which case the direction of wave propagation gets reversed. Since for a hyperbolic equation the boundary condition needs to be specified only at the boundary from which the characteristics emanate, we observe a rather complex picture - depending on the initial condition, the emanating boundary may be either only one (top or bottom boundary) or both or none.

In the case of non-zero $\mathscr{C}$ approximation, we can no longer simply integrate v_m (and thus arrive at a single transport equation for porosity ϕ), and we are forced to deal with the coupled nonlinear system (4.1). It was shown that the two-phase gravity driven transport described by these equations exhibits formation of nonlinear wave trains (e.g. *Scott & Stevenson*, 1984; *Scott et al.*, 1986; *Olson & Christensen*, 1986; *Spiegelman*, 1993a). However, some decoupling will be, at least for the numerical solution, necessary and will be achieved by an appropriate choice of the numerical scheme described in Section 4.1.2.

Boundary conditions

For a polythermal ice shell (investigated in Chapter 7), we assume the following boundary conditions for temperature:

$$T|_{z=1,t} = T_\mathrm{s} \ , \tag{4.4a}$$

$$T|_{z=0,t} = T_\mathrm{M}|_{z=0} \ , \tag{4.4b}$$

where T_s denotes the surface temperature and $T_\mathrm{M}|_{z=0}$ is the melting temperature at the base of the ice shell which is considered to be the interface with the internal ocean. If we deal with an ice shell in a purely temperate state (Chapter 5), no boundary condition for temperature T is needed.

Concerning the mechanical boundary conditions, situation is relatively straightforward for the ice phase, for which we shall assume the same conditions as if there had been no melt - for ice velocity, we assume a homogeneous Dirichlet boundary condition at the bottom boundary:

$$v_\mathrm{m}|_{z=0,t} = 0 \ , \tag{4.5}$$

which serves to fix the bottom boundary of the ice layer. This is a legitimate choice if we assume that no significant surface melting occurs at this boundary. A physically more appropriate boundary condition would be a Neumann-type condition of equality of traction forces, which would, however, require determination of the water pressure below the ice layer. At the top boundary, we consider free surface condition, which in the one-dimensional setting and with surface pressure set to zero reduces to:

$$\frac{\partial v_\mathrm{m}}{\partial z}|_{z=1,t} = 0 \ . \tag{4.6}$$

Regarding the boundary conditions for porosity ϕ (when considering purely temperate ice shell in Chapter 5), for the zero $\mathscr{C}$ approximation we inferred (under some simplifying assumptions) a nonlinear hyperbolic character of the transport equation and consequent requirement to specify ϕ at the part of the boundary

from which the characteristics emanate. For sufficiently small initial porosities (such that $\max_{z\in\langle 0,1\rangle}[\phi]\phi^0(z)\leq 0.5$), the emanating boundary is the upper boundary. Expecting the downward porosity propagation also for the general non-zero $\mathscr{C}$ case and since we do not consider any source of liquid water above the ice shell, we set

$$\phi|_{z=1,t} = 0 \ . \tag{4.7}$$

In the case of polythermal ice shell (Chapter 7), the top boundary is always cold (i.e. below melting point) due to the prescribed temperature boundary condition (eq. 4.4a) and thus we do not consider any condition for porosity.

Two typical outflux conditions are of interest at the base of the domain. The first one is an impermeable boundary condition, for which the outflux is zero, i.e. $-\phi \boldsymbol{v}_\mathrm{r} \cdot \boldsymbol{e}_\mathrm{z}=0$, which according to eq. (4.1c) can be achieved by setting

$$(1-[\phi]\phi) = -[\phi]\mathscr{C}\frac{\partial}{\partial z}\left((1-[\phi]\phi)\left(\frac{1}{[\phi]\phi}+\frac{4}{3}\right)\frac{\partial v_\mathrm{m}}{\partial z}\right)|_{z=0,t} \ , \tag{4.8}$$

and for zero $\mathscr{C}$ approximation coincides with the zero porosity condition

$$\phi|_{z=0,t} = 0 \ . \tag{4.9}$$

Alternatively, some kind of free flux condition would be favorable in situations when the melt outflow is not constrained (e.g. when there is a melt reservoir below the ice shell). We formulate such condition in terms of vanishing of the dynamic (non-hydrostatic) part of the excess water pressure Π, that is assuming

$$(\nabla\Pi + \phi\boldsymbol{e}_\mathrm{z}) \cdot \boldsymbol{e}_\mathrm{z}|_{z=0,t} = 0 \ , \tag{4.10}$$

which in the one-dimensional setting reads more explicitly as

$$\frac{\partial}{\partial z}\left((1-[\phi]\phi)\left(\frac{1}{[\phi]\phi}+\frac{4}{3}\right)\frac{\partial v_\mathrm{m}}{\partial z}\right)|_{z=0,t} = 0 \ . \tag{4.11}$$

This condition corresponds to the water outflow from the domain that is mechanically uncoupled from the ice matrix deformation which can be seen (using eq. 4.1c) as a condition on the outflux ϕv_r to be given just by the zero $\mathscr{C}$ approximation. We shall use this boundary condition in our numerical simulations, owing to an expected underlying water reservoir (cf. Chapter 1).

4.1.2 Description of the FORTRAN90 code

For numerical treatment, we will assume a uniform time discretization $\{t^k\}_{k=0}^N$. The system of governing equations (4.1) is then solved using Algorithm 1. In a purely temperate ice shell and assuming further uniform melting temperature, eq. (4.1d) serves only to compute the melting rate r_f from heating Q and dissipation due to relative motion between the two phases $\mathscr{I}|v_\mathrm{r}|^2$. The subproblems (ii) and (iii) comprise the main challenges of Algorithm 1, so we now briefly describe their numerical implementation.

Algorithm 1 Description of the FORTRAN90 code.

Initialize temperature $T^0(z)=T(z,t^0)$ and porosity $\phi^0(z)=\phi(z,t^0)$.
Compute the initial velocities $v_{\rm m}^0(z) = v_{\rm m}(z,t^0)$ and $v_{\rm r}^0(z) = v_{\rm r}(z,t^0)$ by solving eqs (4.1b) and (4.1c), respectively.
for k=1, ..., N **do**
(i) Evaluate the right-hand side (denoted $\mathrm{rhs}^{k-1}(z)$) of eq. (4.1d) using velocities $v_{\rm r}^{k-1}(z)$, $v_{\rm m}^{k-1}(z)$ and temperature $T^{k-1}(z)$ from the previous time step.

if $T^{k-1}(z)<T_{\rm M}(z)$ (and so $\phi^{k-1}(z)=0$) **then**
Compute the new temperature as $T^k(z)=T^{k-1}(z)+\Delta t\frac{[\phi]}{\mathcal{T}}\mathrm{rhs}^{k-1}(z)$.
if $T^k(z)\geq T_{\rm M}(z)$ **then**
Compute the new melting rate as $r_{\rm f}^k(z)=\frac{T^k(z)-T_{\rm M}(z)}{\Delta t}\frac{\mathcal{T}}{[\phi]}$.
Fix the temperature at the melting point: $T^k(z)=T_{\rm M}(z)$.
end if
else
Compute the new melting rate as $r_{\rm f}^k(z)=\mathrm{rhs}^{k-1}(z)$.
Fix the temperature at the melting point: $T^k(z)=T_{\rm M}(z)$.
end if
(ii) Solve the porosity advection equation (4.1a) using velocities from the previous time step, $v_{\rm r}^{k-1}(z)$, $v_{\rm m}^{k-1}(z)$ and the actual melting rate, $r_{\rm f}^k(z)$, to obtain porosity at the new time level, $\phi^k(z)$.
(iii) Compute the ice velocity at the new time level, $v_{\rm m}^k(z)$ from the actual values of porosity $\phi^k(z)$ and melting rate $r_{\rm f}^k(z)$ by solving the boundary-value problem (4.1b).
(iv) Evaluate the new relative velocity $v_{\rm r}^k(z)$ using eq. (4.1c).
end for

The porosity transport equation (eq. 4.1a)

Concerning the porosity transport, we prefer a numerical approach universal enough to treat both the zero $\mathscr{C}$ and non-zero $\mathscr{C}$ case. Our strategy is based on the requirement to capture shocks in the first step, and then attempt to generalize the approach accordingly in the non-zero $\mathscr{C}$ setting. As observed in eq. (4.3), in the zero $\mathscr{C}$ approximation, the porosity solution may exhibit discontinuities (shocks), which implies that a use of a more advanced numerical method is necessary. We shall view eq. (4.1a) as a hyperbolic law of the type

$$\frac{\partial}{\partial t}\phi(z,t) + \frac{\partial}{\partial z}\tilde{f}(\phi(z,t),z,t) = g(z,t)\ , \tag{4.12}$$

where

$$\tilde{f}(\phi(z,t),z,t) = \phi(z,t)(v_{\rm r}(z,t)+\mathcal{V}v_{\rm m}(z,t)) \tag{4.13}$$

and

$$g(z,t) = \frac{r_{\rm f}(z,t)}{1+\mathcal{R}}\ . \tag{4.14}$$

The explicit dependence of $\tilde{f}$ on (z,t), resulting from the non-local dependence of $v_{\rm r}$ and $v_{\rm m}$ on ϕ according to eqs (4.1b) and (4.1c), is very unfortunate since most numerical schemes and corresponding theoretical convergence results typically concern a simpler setting with $\tilde{f}$ of the type $\tilde{f}(\phi(z,t))$.

For the reconstruction of numerical fluxes, we employ the finite-volume Essentially Non-Oscillatory (ENO) schemes (*Shu*, 1998), designed to treat the following (homogeneous) conservation hyperbolic law:

$$\frac{\partial}{\partial t}\phi(z,t) + \frac{\partial}{\partial z} f(\phi(z,t)) = 0 \ . \tag{4.15}$$

For a uniform spatial discretization, the integration of eq. (4.15) over the whole computational domain $\langle 0,1\rangle$ yields the volume-averaged evolution equation

$$\frac{d\bar{\phi}_i(t)}{dt} = -\frac{1}{\Delta z}\left(f(\phi(z_{i+\frac{1}{2}})) - f(\phi(z_{i-\frac{1}{2}}))\right) \ , \tag{4.16}$$

where $\bar{\phi}_i(t)$ denotes the i-th cell average, i.e.

$$\bar{\phi}_i(t) = \int_{z_{i-\frac{1}{2}}}^{z_{i+\frac{1}{2}}} \phi(z',t)\ dz' \ . \tag{4.17}$$

The volume-averaged equation (4.16) is approximated by

$$\frac{d\bar{\phi}_i(t)}{dt} = -\frac{1}{\Delta z}\left(f_{i+\frac{1}{2}} - f_{i-\frac{1}{2}}\right) \ , \tag{4.18}$$

where $f_{i\pm\frac{1}{2}}$ are the numerical fluxes, in the ENO procedure given by

$$f_{i\pm\frac{1}{2}} = h(\phi^-_{i\pm\frac{1}{2}}, \phi^+_{i\pm\frac{1}{2}}) \ . \tag{4.19}$$

Here $\phi^-_{i\pm\frac{1}{2}}$ and $\phi^+_{i\pm\frac{1}{2}}$ are the ENO reconstructions from both sides of the computational point $z_{i\pm\frac{1}{2}}$ (which are not identical in the case of a shock - discontinuity) and $h(.,.)$ is a suitably chosen flux function - we employed the Lax-Friedrichs flux:

$$h(u,v) = \frac{1}{2}\left(f(u) + f(v) - \psi(v-u)\right) \ , \tag{4.20}$$

where ψ=max$_w|f'(w)|$.

Now we require a generalization of this approach for our non-homogenous equation (4.1a) with the additional explicit (z,t)-dependence of $\tilde{f}(\phi(z,t),z,t)$ of the form given by eq. (4.13). We choose to discretize it as

$$\frac{d\bar{\phi}_i(t)}{dt} = -\frac{1}{\Delta z}\left(\tilde{f}_{i+\frac{1}{2}} - \tilde{f}_{i-\frac{1}{2}}\right) \ + \bar{g}_i(t) \ , \tag{4.21}$$

with the volume-averaged right-hand side

$$\bar{g}_i(t) = \int_{z_{i-\frac{1}{2}}}^{z_{i+\frac{1}{2}}} g(z',t)\ dz' \ , \tag{4.22}$$

and the numerical fluxes defined by

$$\tilde{f}_{i\pm\frac{1}{2}} = \tilde{h}((\phi_{i\pm\frac{1}{2}}(v_{\rm r} + \mathcal{V}v_{\rm m})_{i\pm\frac{1}{2}})^-, (\phi_{i\pm\frac{1}{2}}(v_{\rm r} + \mathcal{V}v_{\rm m})_{i\pm\frac{1}{2}})^+) \ , \tag{4.23}$$

where $\tilde{h}$ is an analogue of h (eq. 4.20) only with $\tilde{f}$ given by eq. (4.13) in place of f and with ψ replaced by $\tilde{\psi}$=max$_w|\frac{\partial\tilde{f}(w,z,t)}{\partial w}|$. Despite the fact that for this extension

we can no longer use any theoretical convergence results valid for the original ENO schemes and thus cannot justify its performance theoretically, the extension is consistent in the sense that it reduces to the classical ENO Lax-Friedrichs scheme for constant velocity ($v_\mathrm{r}+\mathcal{V}v_\mathrm{m}$) and also in the case when ($v_\mathrm{r}+\mathcal{V}v_\mathrm{m}$) is an explicit function of ϕ. Nevertheless, the main argument for applicability of this flux reconstruction will be its numerical performance and the results of numerical tests shown in the next section. In the case of the zero $\mathscr{C}$ approximation, an analogous procedure is followed, except we now explicitly express $v_\mathrm{r}+\mathcal{V}v_\mathrm{m}$.

For the time discretization, two explicit (required by the ENO procedure) schemes are used - the first-order (forward) Euler scheme and the fourth-order Runge-Kutta scheme (e.g. *Press et al.*, 1992). The time stepping is thus constrained by the Courant-Friedrichs-Lewy (CFL) stability condition which, combined with relatively high spatial resolution required by the solver for matrix velocity (described below) in order to reach sufficient accuracy, leads to rather short time stepping. Comparison of the results between these two schemes reveals negligible difference, however the use of the Runge-Kutta scheme allows for slightly larger time steps.

Equation for ice matrix velocity (eq. 4.1b)

Assuming $\phi^k(z)$ at some time level t^k is known, $v_\mathrm{m}^k(z)$ is obtained by solving the boundary-value problem (eq. 4.1b), accompanied by the appropriate boundary conditions. In the zero $\mathscr{C}$ case, v_m^k can be simply integrated as in eq. (4.2). In the non-zero $\mathscr{C}$ case, we reformulate the third-order nonlinear partial differential equation for matrix velocity v_m in terms of an auxiliary variable

$$\xi^k(z) = (1-[\phi]\phi^k(z))\frac{\mathrm{d}v_\mathrm{m}^k(z)}{\mathrm{d}z} \ , \tag{4.24}$$

for which it reduces to a second-order equation

$$\begin{aligned} &\frac{\mathcal{V}}{(1-[\phi]\phi^k)[\phi]}\xi^k - \mathscr{C}\frac{\mathrm{d}}{\mathrm{d}z}\left(\left(\phi^k + \frac{4}{3}[\phi](\phi^k)^2\right)\frac{\mathrm{d}\xi^k}{\mathrm{d}z}\right) + \mathscr{C}\frac{\mathrm{d}}{\mathrm{d}z}\left(\frac{\mathrm{d}\phi^k}{\mathrm{d}z}\xi^k\right) \\ = \ &\frac{\mathrm{d}}{\mathrm{d}z}\left((1-[\phi]\phi^k)(\phi^k)^2\right) - r_\mathrm{f}^k\frac{\mathcal{R}}{1+\mathcal{R}} \ . \end{aligned} \tag{4.25}$$

The source term r_f on the right-hand side has already been computed (in step (i) of Algorithm 1) - eq. (4.25) thus turns into a linear elliptic equation for ξ^k with non-constant coefficients. In view of the definition of ξ, assuming the free upper surface condition (4.6) and the free outflow bottom condition (4.11), the boundary conditions for ξ^k read

$$\xi^k|_{z=1,t} = 0 \ , \tag{4.26}$$

$$\frac{d\xi^k}{dz}\left(\phi^k + \frac{4}{3}[\phi](\phi^k)^2\right)|_{z=0,t} = \xi^k\frac{d\phi^k}{dz}|_{z=0,t} \ . \tag{4.27}$$

Equation (4.25) together with boundary conditions (4.26) and (4.27) is solved in the weak sense, i.e. assuming $\phi^k \in W^{1,\infty}(I)$, $I=\langle 0,1\rangle$, and bounded $0<[\phi]\phi<1$, we

look for $\xi^k \in X$ where $X=\{\psi \in W^{1,2}(I); \psi(1)=0\}$ such that

$$\int_0^1 \frac{\mathcal{V}}{(1-[\phi]\phi^k)[\phi]}\xi^k\varphi \,\mathrm{d}z + \mathscr{C}\int_0^1 \left((\phi^k+\frac{4}{3}[\phi](\phi^k)^2)\frac{\mathrm{d}\xi^k}{\mathrm{d}z} - \frac{\mathrm{d}\phi^k}{\mathrm{d}z}\xi^k\right)\frac{\mathrm{d}\varphi}{\mathrm{d}z}\,\mathrm{d}z$$
$$= \int_0^1 \frac{\mathrm{d}}{\mathrm{d}z}\left((1-[\phi]\phi^k)(\phi^k)^2\right)\varphi\,\mathrm{d}z - \int_0^1 \frac{\mathcal{R}}{1+\mathcal{R}}r_\mathrm{f}^k\varphi\,\mathrm{d}z \qquad \forall\varphi\in X\ , \tag{4.28}$$

where we are using the standard notation $W^{k,p}$ for the Sobolev spaces (e.g. *Evans*, 1998). Equation (4.28) is discretized by the classical Galerkin finite element method using an approximation of the space X by a finite-dimensional space of piece-wise linear functions for simplicity. Finally, v_m^k is obtained from eq. (4.24) by numerical integration with the use of eq. (4.5). Note, that equation (4.28) do not diverge even for ϕ=0 and can thus be solved throughout the whole ice shell not depending on whether the ice is cold or temperate.

4.1.3 Numerical tests

We perform several tests in order to verify the performance of our implementation. As has already been noted, the main challenge is the solution of the mechanical part of the problem (eqs 4.1a–4.1c), and thus we neglect melting in this section (i.e. r_f=0 and equation 4.1d is not solved).

Zero $\mathscr{C}$ approximation - shocks

We first examine the ability of our numerical implementation to capture porosity shocks produced by nonlinear hyperbolic equations of the type (4.3). Instead of eq. (4.3), we look for a solution of a slightly simpler equation obtained by neglecting one of the terms $(1-[\phi]\phi)$ in order to reduce the polynomial order, i.e. we solve the following equation:

$$\frac{\partial\phi}{\partial t} - \frac{\partial}{\partial z}\left(\phi^2(1-[\phi]\phi)\right) = \frac{\partial\phi}{\partial t} - 2\phi\left(1-\frac{3}{2}[\phi]\phi\right)\frac{\partial\phi}{\partial z} = 0\ . \tag{4.29}$$

If we prescribe the initial condition $\phi(z,0)$ such that $[\phi]\phi(z,0)\leq\frac{2}{3}$ $\forall z\in\langle 0,1\rangle$, all the characteristics, given by

$$z = z_0 - 2\phi(z_0,0)\left(1-\frac{3}{2}[\phi]\phi(z_0,0)\right)t\ , \tag{4.30}$$

are oriented downwards and hence we only need to specify the boundary condition at the upper boundary. For this problem and for suitable initial condition, we can find the corresponding (weak, cf. *Evans*, 1998) solution analytically. We prescribe the initial porosity profile as

$$\phi(z,0) = \begin{cases} a & z_2 \leq z \leq 1 \\ \frac{1-\sqrt{1+3[\phi](\alpha z-\beta)}}{3[\phi]} & z_1 \leq z \leq z_2 \\ b & 0 \leq z \leq z_1 \end{cases} \tag{4.31}$$

(Figure 4.1, panel a, red line), with

$$\alpha=\frac{k_\mathrm{a}-k_\mathrm{b}}{z_1-z_2} \qquad \beta=\frac{z_1k_\mathrm{a}-z_2k_\mathrm{b}}{z_1-z_2}\ ,$$
$$k_\mathrm{a}=\frac{\mathrm{d}z}{\mathrm{d}t}(a)=-(2a-3[\phi]a^2) \quad k_\mathrm{b}=\frac{\mathrm{d}z}{\mathrm{d}t}(b)=-(2b-3[\phi]b^2)\ . \tag{4.32}$$

Naturally, the upper boundary condition is taken as $\phi|_{z=1,t}=a$. The solution can be found by advecting the initial profile along the characteristics - it remains classical (i.e. valid point-wise) until time

$$t_\mathrm{s} = \frac{z_2 - z_1}{k_\mathrm{a} - k_\mathrm{b}} \ , \tag{4.33}$$

when the characteristics start to intersect and a discontinuity (shock) develops at the position

$$z_\mathrm{s}(t_\mathrm{s}) = \frac{z_1 k_\mathrm{a} - z_2 k_\mathrm{b}}{k_\mathrm{a} - k_\mathrm{b}} \ . \tag{4.34}$$

The initial profile is chosen such that all the characteristics emanating from the interval $\langle z_1, z_2 \rangle$ intersect at the same point $(z_\mathrm{s}, t_\mathrm{s})$. The generalized (weak) solution for $t{>}t_\mathrm{s}$ is then unique and given by a discontinuous function (shock):

$$\phi = \begin{cases} a & \text{if } z{>}z_\mathrm{s}(t) \\ b & \text{if } z{<}z_\mathrm{s}(t) \ . \end{cases} \tag{4.35}$$

The discontinuity propagates with velocity $\dot{z}_s(t)$ determined by the Rankine-Hugoniot condition (e.g. *Evans*, 1998) for the flux $F{=}{-}\phi^2(1{-}[\phi]\phi)$:

$$\dot{z}_\mathrm{s} = \frac{[F(\phi)]}{[\phi]} = \frac{-(a^2{-}[\phi]a^3) + (b^2{-}[\phi]b^3)}{a{-}b} = [\phi](a^2{+}ab{+}b^2) - (a{+}b) \ . \tag{4.36}$$

In Figure 4.1, we plot the results (in dimensional variables) of our numerical simulation for the parameters $a{=}2\%$, $b{=}0.5\%$. The spatial resolution was 10^3 grid

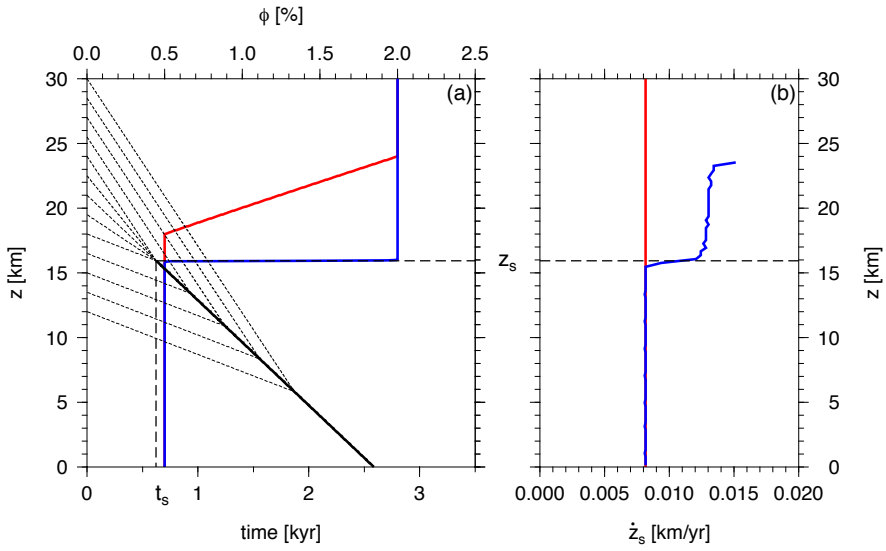

Figure 4.1: (a) The initial porosity condition (eq. 4.31, red line) and the fully developed shock (blue line). Thin dashed lines show the characteristics computed using eq. (4.30). The analytically computed location and time of shock full development $(z_\mathrm{s}, t_\mathrm{s})$ are marked. Thick black line corresponds to the evolution of a fully developed shock. (b) Dependence of the shock velocity $\dot{z}_\mathrm{s}$ on depth z - by Rankine-Hugoniot condition (eq. 4.36, red line) and the numerical (cell-averaged) velocity of the point of maximal steepness (blue line). The horizontal line indicates the analytically computed location of the shock development z_s.

points and we used the time discretization of 5×10^3 time levels, corresponding roughly to a (quite strict) constraint CFL=0.1. We used the ENO flux reconstruction of the third order (cf. *Shu*, 1998). Panel a of Figure 4.1 shows the initial porosity profile (red), the corresponding characteristics (thin dashed lines), and the numerical solution at time t_s (blue line) when, according to the analytical solution, the shock appears at depth z_s (also indicated in Figure 4.1). A satisfactory match is observed between the analytical and the numerical solution. Panel b of Figure 4.1 depicts the corresponding (depth-parametrized) evolution of the shock velocity. In blue color we track the position and the cell-averaged numerical velocity of the point of maximal steepness of $\phi(t,z)$ - such point coincides with the shock position for $z<z_\mathrm{s}$ ($t>t_\mathrm{s}$). In red we plot the analytical value of the shock velocity according to the Rankine-Hugoniot condition (eq. 4.36). We can see that shortly after the theoretical shock development at $(t_\mathrm{s}, z_\mathrm{s})$, the numerical shock velocity matches with the theoretical value. The minor delay in the time (depth) of matching is an artifact of the applied numerical characterization of the shock position.

Non-zero $\mathscr{C}$ approximation - wave trains

Here we investigate the ability of our implementation to produce wave trains in the non-zero $\mathscr{C}$ setting. At first, we performed benchmarks of the accuracy of the finite element routine for computation of v_m (eq. 4.28) against the finite element solver Comsol Multiphysics (version 4.2a, www.comsol.com). These tests provided us with estimates of the necessary spatial resolution required to reach a sufficient computational accuracy. Now, in order to test the performance of the whole numerical scheme, we recompute the study by *Spiegelman* (1993b). Some minor modifications has to be applied, since in the cited paper the formulation differs by neglecting systematically the terms $(1-[\phi]\phi)$, taking a different permeability exponent $n=3$ in eq. (2.1) and assuming constant bulk viscosity ζ (cf. text below eq. 3.131). We reformulated our system to match that of *Spiegelman* (1993a), altered the numerical code accordingly and computed the evolution of the initial profile given in *Spiegelman* (1993b):

$$\phi(z,0) = \begin{cases} 1 & z\leq z_0 \\ \phi_1 + (1-\phi_1)\mathrm{sech}\left(\frac{z-z_0}{\lambda}\right) & z>z_0 \end{cases}, \tag{4.37}$$

with $z_0=300\delta$ and $\lambda=2.5\delta$ where δ is the compaction length (e.g. *Spiegelman*, 1993a), defined as

$$\delta = \sqrt{\frac{k(\phi)\left(\zeta+\frac{4}{3}\mu_\mathrm{m}\right)}{\mu_\mathrm{f}}} \tag{4.38}$$

and the material parameters are taken as $\mu_\mathrm{f}=1$ Pa s, $\mu_\mathrm{m}=\zeta=10^{19}$ Pa s, $k_0=10^{-9}$ m^2, $\rho_\mathrm{f}=3300$ kg m^{-3}, $\rho_\mathrm{m}=2800$ kg m^{-3}, and ϕ_1 is varied. Our solution (to be compared with Figure 3 in *Spiegelman*, 1993b) is depicted in Figure 4.2 - we observe a satisfactory qualitative and quantitative match in terms of the shape and the advance speed of the produced wave trains. Our simulations result in slightly smaller amplitudes of the waves, especially for larger initial steps (smaller ϕ_1) which can be seen in Figure 4.3, where the leading-wave amplitudes are depicted for various values of ϕ_1 (compare with Figure 4b in *Spiegelman*, 1993b). We

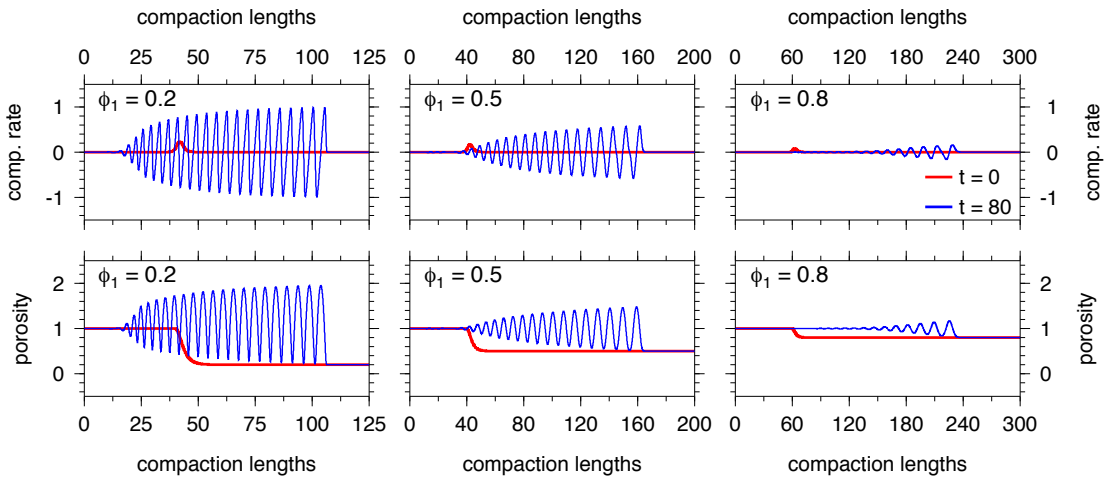

Figure 4.2: Superposition of the initial profiles (t=0, red lines) and the final profiles at time t=80 (blue lines) (as in *Spiegelman*, 1993b). Compaction rate (top) and porosity (bottom) for three different values of ϕ_1: 0.2 (left), 0.5 (middle) and 0.8 (right). All variables are dimensionless. Figures were rotated around the y-axis a translated by 340δ and 360δ, respectively, in order to match the original figure of *Spiegelman* (1993b).

believe this difference results from a rather high sensitivity of the solutions with respect to the chosen spatial discretization. Such sensitivity is not surprising since the accuracy and resolution of ϕ^k at the k-th time level influences strongly the velocity solution v_{m}^k due to the presence of ϕ^k as a coefficient in the leading term in eq. (4.25). Simultaneously, any error in v_{m}^k affects ϕ^{k+1} in the next time level, and so on. Since we are not able to provide any theoretical error estimates for our particular numerical scheme, we confine ourselves in all the simulations to simple numerical error estimation by refining the spatial and temporal discretization until the results converge numerically within a prescribed tolerance.

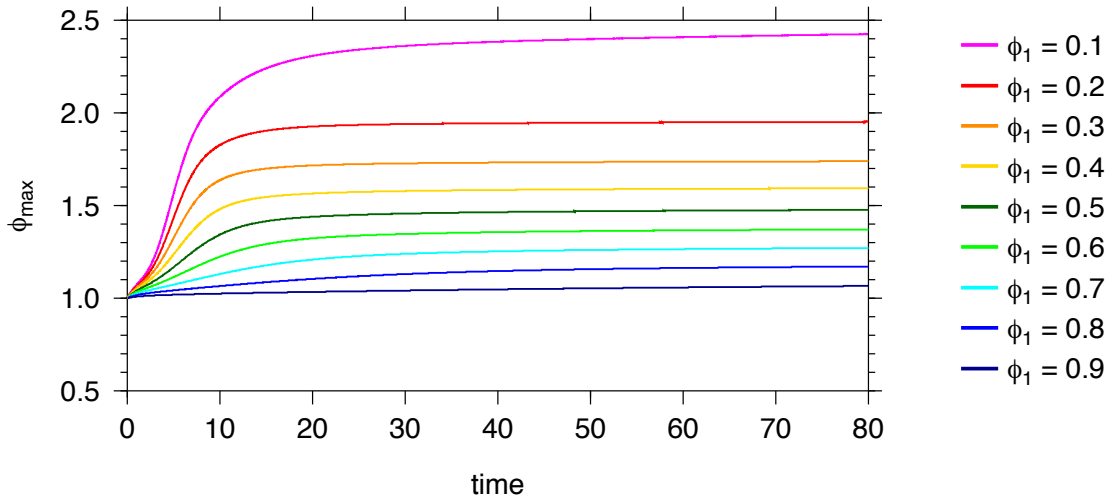

Figure 4.3: Amplitude of the leading wave for differenet initial conditions as a function of time. All variables are dimensionless.

In order to further test our numerical method, we compare the propagation velocity of porosity waves from the numerical solution with the analytically computed value in a purely mechanical setting (i.e. neglecting melting as already noted). We follow the approach of *Rabinowicz et al.* (2002) to derive the analytical formula for porosity waves phase velocity. We start with the balance equations (3.136) in the one-dimensional setting:

$$\frac{\partial \phi}{\partial t} - \frac{\mathcal{V}}{[\phi]} \frac{\partial v_\mathrm{m}}{\partial z} = 0 \ , \tag{4.39a}$$

$$\frac{\mathcal{V}}{[\phi]} \frac{\partial v_\mathrm{m}}{\partial z} + \frac{\partial S_\mathrm{r}}{\partial z} = 0 \ , \tag{4.39b}$$

$$S_\mathrm{r} = -\phi^2 - [\phi]\phi^2 \mathscr{C} \frac{\partial}{\partial z} \left(\left(\frac{1}{[\phi]\phi} + \frac{4}{3} \right) \frac{\partial v_\mathrm{m}}{\partial z} \right) \ , \tag{4.39c}$$

where, again, we substituted for $\frac{\partial \Pi}{\partial z}$ from eq. (3.136d) to eq. (3.136c), neglected the factor $(1-[\phi]\phi)$ in eqs (4.39a) and (4.39c), multiplied eq. (3.136c) by ϕ and finally introduced the separation velocity

$$S_\mathrm{r} = \phi v_\mathrm{r} \ . \tag{4.40}$$

Substituting now from eq. (4.39b) into eq. (4.39a) and eq. (4.39c) we arrive at

$$\frac{\partial \phi}{\partial t} + \frac{\partial S_\mathrm{r}}{\partial z} = 0 \ , \tag{4.41a}$$

$$S_\mathrm{r} = -\phi^2 + \alpha \phi^2 \frac{\partial}{\partial z} \left(\left(\frac{1}{[\phi]\phi} + \frac{4}{3} \right) \frac{\partial S_\mathrm{r}}{\partial z} \right) \ , \tag{4.41b}$$

where we introduced

$$\alpha = \frac{[\phi]^2 \mathscr{C}}{\mathcal{V}} \tag{4.42}$$

for better clarity. Since we seek for solitary waves, we write the solution as

$$\phi = F(z - ct) \ , \tag{4.43}$$

with F the solitary wave shape function and c its phase velocity. Integration of eq. (4.41a) gives

$$S_\mathrm{r} = c(F + K) \ , \tag{4.44}$$

with K yet unknown integration constant. Substitution of eq. (4.44) into eq. (4.41b) leads to

$$\alpha \frac{\partial}{\partial z} \left(F' \left(\frac{1}{[\phi]F} + \frac{4}{3} \right) \right) - \frac{F + K}{F^2} = \frac{1}{c} \ , \tag{4.45}$$

where $F' = \frac{\partial F}{\partial z}$. Taking $F(0) = \phi_\mathrm{min}$ and $F'(0) = F''(0) = 0$ (corresponding to 'witch hat' waves in *Rabinowicz et al.*, 2002), we can write the integration constant K as:

$$K = -\phi_\mathrm{min} - \frac{\phi_\mathrm{min}^2}{c} \ . \tag{4.46}$$

Multiplying eq. (4.45) by $F'(\frac{1}{[\phi]F} + \frac{4}{3})$ and integrating this product, we obtain

$$\frac{1}{2}\alpha \left(F' \left(\frac{1}{[\phi]F} + \frac{4}{3} \right) \right)^2 - \left(\frac{4}{3} + \frac{1}{c[\phi]} \right) \ln(F) + \left(\frac{1}{[\phi]} + \frac{4}{3}K \right) \frac{1}{F} + \frac{K}{2[\phi]} \frac{1}{F^2} - \frac{4}{3c} F + A = 0 \ , \tag{4.47}$$

with A a new integration constant:

$$A = \left(\frac{4}{3}+\frac{1}{c[\phi]}\right)\ln(\phi_{\min}) - \left(\frac{1}{[\phi]}+\frac{4}{3}K\right)\frac{1}{\phi_{\min}} - \frac{K}{2[\phi]\phi_{\min}^2} + \frac{4}{3c}\phi_{\min} \ . \tag{4.48}$$

Rewriting eq. (4.47) at the top of the wave, where $F{=}\phi_{\max}$ and $F'{=}F''{=}0$, we get

$$\begin{aligned} &\left(\frac{4}{3} - \frac{1}{c[\phi]}\right)\ln\left(\frac{\phi_{\max}}{\phi_{\min}}\right) + \left(\frac{1}{[\phi]} + \frac{4}{3}K\right)\left(\frac{1}{\phi_{\max}} - \frac{1}{\phi_{\min}}\right) \\ + \ &\frac{K}{2[\phi]}\left(\frac{1}{\phi_{\max}^2} - \frac{1}{\phi_{\min}^2}\right) - \frac{4}{3c}(\phi_{\max} - \phi_{\min}) = 0 \ . \end{aligned} \tag{4.49}$$

Finally, substituting for K from eq. (4.46) we arrive at

$$c_{\rm A} = \phi_{\min}\frac{-\ln(r) - \frac{4}{3}[\phi](\phi_{\max}{-}\phi_{\min})(r{-}1) + \frac{1}{2}(r^2{-}1)}{\frac{4}{3}[\phi]\phi_{\min}\ln(r) - (\frac{4}{3}[\phi]\phi_{\min}{-}1)(r{-}1) - \frac{1}{2}(r^2{-}1)} \ , \tag{4.50}$$

where we introduced

$$r = \frac{\phi_{\min}}{\phi_{\max}} \ . \tag{4.51}$$

Figure 4.4 shows the wave trains at two different times t_1, t_2 for the initial condition (4.37) with $z_0{=}950\delta$, $\lambda{=}14\delta$, and $\phi_1{=}0.5$. The maximum and minimum values of porosity at time t_2 are $\phi_{\max}{\doteq}1.68$ and $\phi_{\min}{=}0.5$, respectively, which leads to the analytically computed wave velocity $c_{\rm A}{\doteq}{-}1.54$. The wave velocity obtained numerically from our simulation from these two time instants is $c_{\rm N}{\doteq}-1.36$. The few percents difference between these two values might be due to several reasons (the wave train is not yet fully evolved, the analytical formula neglects the factors $(1{-}[\phi]\phi)$, etc.), however, such agreement is similar to that reported in *Rabinowicz et al.* (2002).

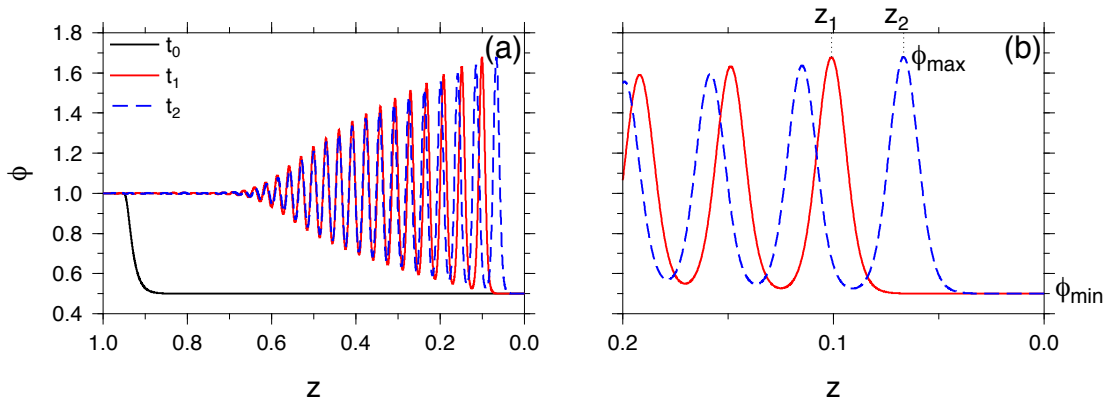

Figure 4.4: (a) Porosity at the beginning of the simulation (t_0, black line) and in two time instants (t_1 and t_2, red and blue lines, respectively). (b) Detail of panel (a). All variables are dimensionless.

4.2 FEniCS code (1d or 2d) for temperate ice simulations

The second code developped during this thesis employs an open source finite element software package FEniCS (http://fenicsproject.org, *Logg et al.*, 2012) which is a powerful library allowing the use of many up-to-date numerical approaches and algebraic solvers together with an efficient MPI-based parallelization. Besides, it allows quite convenient change of dimensionality. In this section, we describe and test the implementation of a purely temperate ice shell problem in FEniCS - we start with the weak formulation of the problem (Section 4.2.1) and then continue with testing of the new numerical tool (Section 4.2.2).

4.2.1 Weak formulation of the problem

The system of governing equations (3.136) is supplemented with the following boundary conditions. Free slip condition for the ice velocity is prescribed on bottom and side boundaries ($\Gamma_\mathrm{B} \cup \Gamma_\mathrm{S}$) in the form:

$$\begin{aligned} \boldsymbol{v}_\mathrm{m} \cdot \boldsymbol{n} &= 0 \\ \left((1-[\phi]\phi)\mu_\mathrm{m} \left(\frac{1}{[\phi]\phi}(\nabla \cdot \boldsymbol{v}_\mathrm{m})\boldsymbol{I} + \nabla \boldsymbol{v}_\mathrm{m} + (\nabla \boldsymbol{v}_\mathrm{m})^\mathrm{T} - \frac{2}{3}(\nabla \cdot \boldsymbol{v}_\mathrm{m})\boldsymbol{I} \right) \cdot \boldsymbol{n} \right)_\mathrm{t} &= \boldsymbol{0} \ , \end{aligned} \tag{4.52}$$

while at the top boundary (Γ_T), free surface is considered as:

$$(1-[\phi]\phi)\mu_\mathrm{m} \left(\frac{1}{[\phi]\phi}(\nabla \cdot \boldsymbol{v}_\mathrm{m})\boldsymbol{I} + \nabla \boldsymbol{v}_\mathrm{m} + (\nabla \boldsymbol{v}_\mathrm{m})^\mathrm{T} - \frac{2}{3}(\nabla \cdot \boldsymbol{v}_\mathrm{m})\boldsymbol{I} \right) \cdot \boldsymbol{n} = \boldsymbol{0} \ . \tag{4.53}$$

These two conditions are modifications of standard free slip and free surface conditions with a new term that can be interpreted as a volume deformation with a porosity dependent bulk viscosity (cf. text below eq. 3.131). Condition (4.53) represents a natural boundary condition of eq. (3.136d) in the sense that it eliminates the boundary integrals in the weak form. The modified free slip is then formulated as in eq. (4.52) in order to keep consistency.

Concerning the water transport, free flux condition (water outflow mechanically uncoupled from the matrix deformation, cf. discussion above eq. 4.10) of the form:

$$\nabla \Pi \cdot \boldsymbol{n} = \phi \tag{4.54}$$

is prescribed at the bottom boundary (Γ_B). At the top boundary (Γ_T), we assume a zero excess water pressure

$$\Pi = 0 \tag{4.55}$$

and a fixed (non-zero) porosity

$$\phi = \phi^\mathrm{off} = \mathrm{const} \ . \tag{4.56}$$

Finally, the side boudaries (Γ_S) are considered to be impermeable for water

$$\boldsymbol{v}_\mathrm{r} \cdot \boldsymbol{n} = 0 \ , \tag{4.57}$$

which can be alternatively written as

$$\nabla\Pi \cdot \boldsymbol{n} = 0 \ . \tag{4.58}$$

Temperature is not an independent quantity, but is everywhere equal to the melting temperature (here considered only as a function of the vertical coordinate z), and thus we do not need to prescribe any temperature boundary conditions.

The system of eqs (3.136) together with the boundary conditions (4.52)–(4.58) is solved in the weak sense, i.e. we look for $\boldsymbol{\zeta}=\{\phi, \Pi, \boldsymbol{v}_\mathrm{r}, \boldsymbol{v}_\mathrm{m}, r_\mathrm{f}\}\in\boldsymbol{X}$ where $\boldsymbol{X}=[P, W, \boldsymbol{R}, \boldsymbol{M}, K]$ is a mixed finite element space composed of

$$\begin{aligned} P &= \{\psi \in W^{1,2}(\Omega); \psi|_{\Gamma_\mathrm{T}} = 0\} \\ W &= \{\psi \in W^{1,2}(\Omega); \psi|_{\Gamma_\mathrm{T}} = 0\} \\ \boldsymbol{R} &= \{\boldsymbol{\chi} \in W^{1,2}(\Omega); \boldsymbol{\chi}\cdot\boldsymbol{n}|_{\Gamma_\mathrm{S}} = 0\} \\ \boldsymbol{M} &= \{\boldsymbol{\chi} \in W^{1,2}(\Omega); \boldsymbol{\chi}\cdot\boldsymbol{n}|_{\Gamma_\mathrm{B}\cup\Gamma_\mathrm{S}} = 0\} \\ K &= \{\psi \in W^{1,2}(\Omega)\} \ . \end{aligned} \tag{4.59}$$

We use classical Galerkin finite element method (e.g. *Quarteroni & Valli*, 1994) approximating the spaces P, W, K by a finite-dimensional space of piece-wise linear functions and the spaces $\boldsymbol{R}, \boldsymbol{M}$ by a finite-dimensional space of piece-wise quadratic functions (cf. *Taylor & Hood*, 1973; *Rhebergen et al.*, 2013). For time discretization we use the θ-scheme (e.g. *Quarteroni & Valli*, 1994) defined as:

$$\frac{\partial P}{\partial t} = Q(t) \quad : \quad \frac{P^k - P^{k-1}}{\Delta t} = \theta Q^k + (1-\theta)Q^{k-1} \ , \tag{4.60}$$

which together with a value θ=0.5 results in the second order semi-implicit Crank-Nicolson scheme. The time-stepping is adaptive with the time step controlled by the CFL criterion:

$$\Delta t^{\mathrm{k+1}} = \frac{C_\mathrm{CFL} h_\mathrm{min}}{\max(|\mathcal{V}\boldsymbol{v}_\mathrm{m}^\mathrm{k}|, |\boldsymbol{v}_\mathrm{r}^\mathrm{k}|)} \ , \tag{4.61}$$

where $C_\mathrm{CFL}\leq 1$ and h^min is the size of the smallest mesh element. The weak formulation of eqs (3.136) reads:

Porosity transport equation (mass balance of ice)

$$\begin{aligned} & \int_\Omega \phi^k\varphi \,\mathrm{d}x - \int_\Omega \phi^{k-1}\varphi \,\mathrm{d}x - \int_\Omega \Delta t\,\theta\,\frac{\mathcal{V}}{[\phi]}(1-[\phi]\phi^k)(\nabla\cdot\boldsymbol{v}_\mathrm{m}^k)\varphi \,\mathrm{d}x \\ - & \int_\Omega \Delta t(1-\theta)\frac{\mathcal{V}}{[\phi]}(1-[\phi]\phi^{k-1})(\nabla\cdot\boldsymbol{v}_\mathrm{m}^{k-1})\varphi \,\mathrm{d}x + \int_\Omega \Delta t\,\theta\,\mathcal{V}(\boldsymbol{v}_\mathrm{m}^k\cdot\nabla\phi^k)\varphi \,\mathrm{d}x \\ + & \int_\Omega \Delta t(1-\theta)\mathcal{V}(\boldsymbol{v}_\mathrm{m}^{k-1}\cdot\nabla\phi^{k-1})\varphi \,\mathrm{d}x - \int_\Omega \Delta t\theta r_\mathrm{f}^k\varphi \,\mathrm{d}x \\ - & \int_\Omega \Delta t(1-\theta) r_\mathrm{f}^{k-1}\varphi \,\mathrm{d}x = 0 \qquad\qquad \forall\varphi\in P \end{aligned} \tag{4.62}$$

Equation for the water excess pressure (sum of mass balances)

(here we substituted for $\boldsymbol{v}_\mathrm{r}$ from eq. 3.136c)

$$\begin{aligned}
&\int_\Omega \frac{\mathcal{V}}{[\phi]}(\nabla\cdot\boldsymbol{v}_\mathrm{m})\,\omega\,\mathrm{d}x - \int_{\Gamma_\mathrm{B}}[\phi]\phi^3\omega\,\mathrm{d}s + \int_\Omega[\phi]\phi^2\nabla\Pi\cdot\nabla\omega\,\mathrm{d}x \\
-\ &\int_\Omega 2\phi\nabla\phi\cdot\boldsymbol{e}_\mathrm{z}\omega\,\mathrm{d}x + \int_\Omega\frac{\mathcal{R}}{1+\mathcal{R}}r_\mathrm{f}\,\omega\,\mathrm{d}x = 0 \qquad\qquad \forall\omega\in W \qquad (4.63)
\end{aligned}$$

Darcy velocity (momentum balance of water)

$$\int_\Omega \boldsymbol{v}_\mathrm{r}\cdot\boldsymbol{\rho}\,\mathrm{d}x + \int_\Omega\phi\boldsymbol{e}_\mathrm{z}\cdot\boldsymbol{\rho}\,\mathrm{d}x + \int_\Omega[\phi]\phi\nabla\Pi\cdot\boldsymbol{\rho}\,\mathrm{d}x = 0 \qquad \forall\boldsymbol{\rho}\in\boldsymbol{R} \qquad (4.64)$$

Ice velocity (momentum balance of ice)

$$\begin{aligned}
&\int_\Omega\nabla\Pi\cdot\boldsymbol{\mu}\,\mathrm{d}x + \int_\Omega\phi\boldsymbol{e}_\mathrm{z}\cdot\boldsymbol{\mu}\,\mathrm{d}x + \int_\Omega\mathscr{C}\mu_\mathrm{m}\frac{1-[\phi]\phi}{[\phi]\phi}(\nabla\cdot\boldsymbol{v}_\mathrm{m})(\nabla\cdot\boldsymbol{\mu})\,\mathrm{d}x \\
+\ &\int_\Omega\mathscr{C}\mu_\mathrm{m}(1-[\phi]\phi)(\nabla\boldsymbol{v}_\mathrm{m}+(\nabla\boldsymbol{v}_\mathrm{m})^\mathrm{T}-\frac{2}{3}(\nabla\cdot\boldsymbol{v}_\mathrm{m})\boldsymbol{I}):(\nabla\boldsymbol{\mu})^\mathrm{T}\,\mathrm{d}x = 0 \\
&\qquad\qquad\qquad\qquad\qquad\qquad\qquad\qquad\qquad\qquad \forall\boldsymbol{\mu}\in\boldsymbol{M} \qquad (4.65)
\end{aligned}$$

Energy balance

$$\begin{aligned}
&\int_\Omega\mathscr{F}\phi\Big(\boldsymbol{v}_\mathrm{r}\cdot\nabla T+\mathcal{V}\boldsymbol{v}_\mathrm{m}\cdot\nabla T\Big)\xi\,\mathrm{d}x + \int_\Omega\mathcal{T}\frac{1-[\phi]\phi}{[\phi]}\mathcal{V}\boldsymbol{v}_\mathrm{m}\cdot\nabla T\xi\,\mathrm{d}x \\
+\ &\int_\Omega r_\mathrm{f}\xi\,\mathrm{d}x - \int_\Omega Q\xi\,\mathrm{d}x - \int_{\partial\Omega}\mathscr{H}\xi(1-\mathcal{K}[\phi]\phi)\nabla T\cdot\boldsymbol{n}\mathrm{d}s \\
+\ &\int_\Omega\mathscr{H}(1-\mathcal{K}[\phi]\phi)\nabla T\cdot\nabla\xi\mathrm{d}x - \int_\Omega\mathscr{I}|\boldsymbol{v}_\mathrm{r}|^2\xi\,\mathrm{d}x = 0 \qquad \forall\xi\in K \qquad (4.66)
\end{aligned}$$

Regularization of the parabolic equation for the porosity advection

The classical Galerkin methods (i.e. where test functions are equal to the basis functions) show oscillations in the solutions for advection-dominated problems (cf. *Quarteroni & Valli*, 1994). A similar situation can be found in the finite difference method context when central differences are used for the discretization of the advective operator - the standard way to proceed is then to discretize it using the upwinding scheme that helps to stabilize the solution and eliminate the oscilations (e.g. *Ferziger & Perić*, 2002). In the context of finite element method, the Streamline-Upwind/Petrov-Galerkin (SUPG) method introduced by *Brooks & Hughes* (1982) is considered as the first successful stabilization technique to prevent oscillations in advection-dominated problems. Its main steps can be described as: (i) introduce the artificial diffusion in a streamline direction only, (ii) interpret this as a modification of the test function of the advection terms, and (iii) enforce consistency, such that this modified test function is applied to all terms of the weak form. Then, the term artificial diffusion is no longer fully applicable, but the exact solution of the problem still satisfies the SUPG stabilized

weak form. The porosity advection equation (4.62) is thus reformulated using the SUPG method, i.e. instead of test function φ, we use

$$\varphi + \tau^{\mathrm{A}} \mathcal{V} \boldsymbol{v}_{\mathrm{m}} \cdot \nabla \varphi \ , \tag{4.67}$$

where

$$\tau^{\mathrm{A}} = \frac{\tau h^{\min}}{2\mathcal{V}|v_{\mathrm{m}}^{\max}|} \ , \tag{4.68}$$

with τ a constant to be chosen:

$$\begin{aligned}
& \int_\Omega \phi^k \varphi \,\mathrm{d}x + \int_\Omega \phi^k \tau^{\mathrm{A}} \mathcal{V} (\boldsymbol{v}_{\mathrm{m}}^k \cdot \nabla \varphi) \,\mathrm{d}x - \int_\Omega \phi^{k-1} \varphi \,\mathrm{d}x \\
- & \int_\Omega \phi^{k-1} \tau^{\mathrm{A}} \mathcal{V} (\boldsymbol{v}_{\mathrm{m}}^{k-1} \cdot \nabla \varphi) \,\mathrm{d}x - \int_\Omega \Delta t \theta \frac{\mathcal{V}}{[\phi]} (1 - [\phi]\phi^k)(\nabla \cdot \boldsymbol{v}_{\mathrm{m}}^k) \varphi \,\mathrm{d}x \\
- & \int_\Omega \Delta t \theta \frac{\mathcal{V}}{[\phi]} (1 - [\phi]\phi^k)(\nabla \cdot \boldsymbol{v}_{\mathrm{m}}^k) \tau^{\mathrm{A}} \mathcal{V} (\boldsymbol{v}_{\mathrm{m}}^k \cdot \nabla \varphi) \,\mathrm{d}x \\
- & \int_\Omega \Delta t (1-\theta) \frac{\mathcal{V}}{[\phi]} (1 - [\phi]\phi^{k-1})(\nabla \cdot \boldsymbol{v}_{\mathrm{m}}^{k-1}) \varphi \,\mathrm{d}x \\
- & \int_\Omega \Delta t (1-\theta) \frac{\mathcal{V}}{[\phi]} (1 - [\phi]\phi^{k-1})(\nabla \cdot \boldsymbol{v}_{\mathrm{m}}^{k-1}) \tau^{\mathrm{A}} \mathcal{V} (\boldsymbol{v}_{\mathrm{m}}^{k-1} \cdot \nabla \varphi) \,\mathrm{d}x \\
+ & \int_\Omega \Delta t \theta \mathcal{V} (\boldsymbol{v}_{\mathrm{m}}^k \cdot \nabla \phi^k) \varphi \,\mathrm{d}x + \int_\Omega \Delta t \theta \mathcal{V} (\boldsymbol{v}_{\mathrm{m}}^k \cdot \nabla \phi^k) \tau^{\mathrm{A}} \mathcal{V} (\boldsymbol{v}_{\mathrm{m}}^k \cdot \nabla \varphi) \,\mathrm{d}x \\
+ & \int_\Omega \Delta t (1-\theta) \mathcal{V} (\boldsymbol{v}_{\mathrm{m}}^{k-1} \cdot \nabla \phi^{k-1}) \varphi \,\mathrm{d}x + \int_\Omega \Delta t (1-\theta) \mathcal{V} (\boldsymbol{v}_{\mathrm{m}}^{k-1} \cdot \nabla \phi^{k-1}) \\
& \tau^{\mathrm{A}} \mathcal{V} (\boldsymbol{v}_{\mathrm{m}}^{k-1} \cdot \nabla \varphi) \,\mathrm{d}x - \int_\Omega \Delta t \theta r_{\mathrm{f}}^k \varphi \,\mathrm{d}x - \int_\Omega \Delta t \theta r_{\mathrm{f}}^k \tau^{\mathrm{A}} \mathcal{V} (\boldsymbol{v}_{\mathrm{m}}^k \cdot \nabla \varphi) \,\mathrm{d}x \\
- & \int_\Omega \Delta t (1-\theta) r_{\mathrm{f}}^{k-1} \varphi \,\mathrm{d}x - \int_\Omega \Delta t (1-\theta) r_{\mathrm{f}}^{k-1} \tau^{\mathrm{A}} \mathcal{V} (\boldsymbol{v}_{\mathrm{m}}^{k-1} \cdot \nabla \varphi) \,\mathrm{d}x = 0 \quad \forall \varphi \in P \ .
\end{aligned} \tag{4.69}$$

As with all stabilization methods that use some kind of supplementary diffusion, the drawback of the SUPG stabilization method lies in the risk of smoothing the details of the solution too much (and thus for example lose the volume), therefore, a special care must be taken when choosing the parameter τ.

The nonlinear system of eqs (4.63)–(4.66) and (4.69) is solved by the Newton iteration method, with the linear systems within each iteration solved using the LU decomposition (e.g. *Quarteroni & Valli*, 1994).

4.2.2 Comparison of 1d FORTRAN90 with 1d and 2d FEniCS

As shown earlier, the solution of the system of governing equations (3.136) results in the propagation of a wave train (for suitably chosen initial condition, cf. *Spiegelman*, 1993a). To verify the performance of the above described FEniCS code we compare its results (in 1d and 2d geometry and considering constant ice viscosity, i.e. setting the dimensionless μ_{m}=1) with these obtained by the 1d FORTRAN90 code described and carefully tested in the previous Section 4.1. Since the FEniCS code is not capable to tackle with the zero porosity, we prescribe

the following initial condition

$$\phi(x,z,0) = \frac{-10(z-1)}{1+(10(z-1))^4} + \phi^{\text{off}} \ , \tag{4.70}$$

with ϕ^{off} a slight offset from zero. Note, that this initial condition only depends on the z coordinate and represents a subsurface partially molten reservoir - by solving the governing equations, we investigate its gravity-driven propagation through the temperate ice layer. We are interested in the local properties of the solution, such as the magnitude of each wave in the wave train or an actual propagation velocity of the waves, as well as in the global properties, such as the overall amount of liquid water within the ice shell or the time needed to transport water from the initial subsurface reservoir down to the bottom boundary (and thus to the underlying ocean). For the sake of simplicity, we consider constant melting temperature and zero volumetric heating Q, however, melting is still possible due to heat dissipated as a result of the relative motion between the phases (the last term in eq. 4.66). The solution computed by the FORTRAN90 code on 10^4 cells is taken as a reference since this solver was already tested in Section 4.1.3. For the FEniCS simulations, several mesh resolutions are used: in 1d geometry, we compute the solution on meshes consisting of 25, 50, 75, 100, 150, 200, 300, 400, 500, and 1000 elements with a constant time step $\Delta t{=}10^{-2}$ (for the purpose of comparison), while in 2d geometry, we use meshes with 25×25, 50×50, 75×75, 100×100, 150×150, and 200×200 elements with the same time-stepping. For numerical reasons, in 2d geometry, we use triangular elements with both, left and right diagonals, that ensure higher symmetry of the solution. Also, based on several numerical tests, we choose to use $\tau{=}0$ corresponding to no stabilization for the purpose of comparison in this section, since the simulations with $\tau{=}0$ give the best solutions. This is probably due to one-dimensionl nature of the problem (conserved also in two dimensions for the special choice of the initial condition, cf. eq. 4.70). However, for simulations where the flow pattern is more complicated, or the choice of material parameters less favorable (cf. Chapter 6), the SUPG stabilization method will prove useful.

Figure 4.5 shows time evolution of the water column height, defined as the global content of water in the domain (i.e. porosity integrated throughout the shell) computed for $\phi^{\text{off}}{=}0.5\%$ by the 1d FEniCS code and compared with the FORTRAN90 code solution. We observe that the solution computed on the coarsest mesh (25 elements) strongly differs from the reference solution, especially if the absolute amount of water is considered. For slightly finer meshes (50, 75, and 100 elements), the solutions still show some differences from the reference solution when investigating the amount of water (cf. details d_1 and d_3), however, the time when the first porosity wave reaches the bottom boundary and the outflow of water from the domain begins (marked by the sharp decrease in water content at approximately 0.65 kyr) and the shape of the outflow curve are almost undistiguishable from that of the reference solution (cf. detail d_2). When further increasing the resolution (150–1000 elements), the FEniCS solutions seem to converge even though they do not match the FORTRAN90 solution exactly.

Figure 4.6 shows time evolution of the water column height computed by the 2d FEniCS code (the actual water content computed by the 2d code was divided by the domain width in order to obtain its 1d equivalent that can be compared

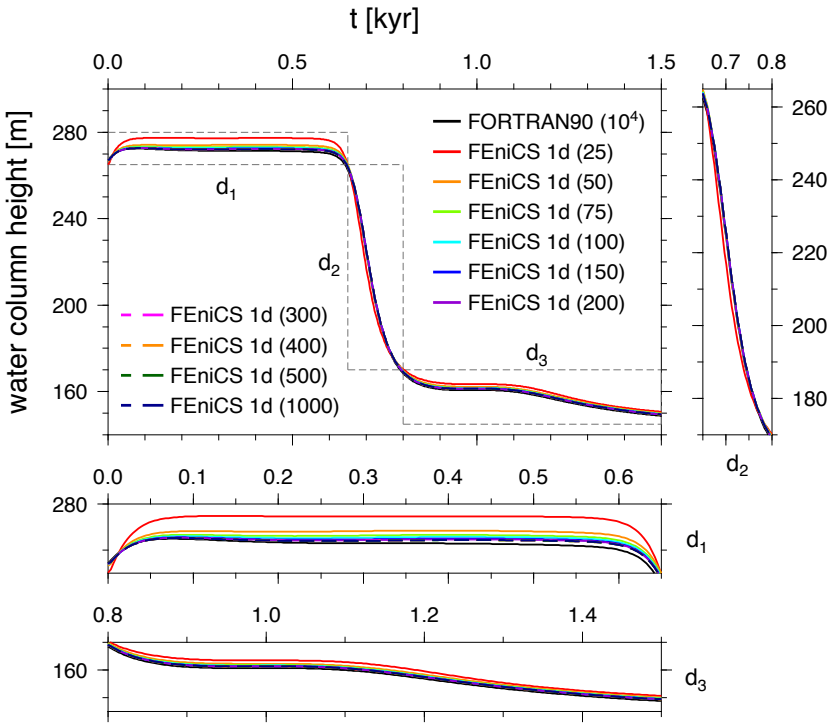

Figure 4.5: Time evolution of the water column height (cf. text) computed by the FORTRAN90 code (black line) and the 1d FEniCS code (colored lines). Numbers in parentheses give the number of cells/elements. Three details are shown for better clarity.

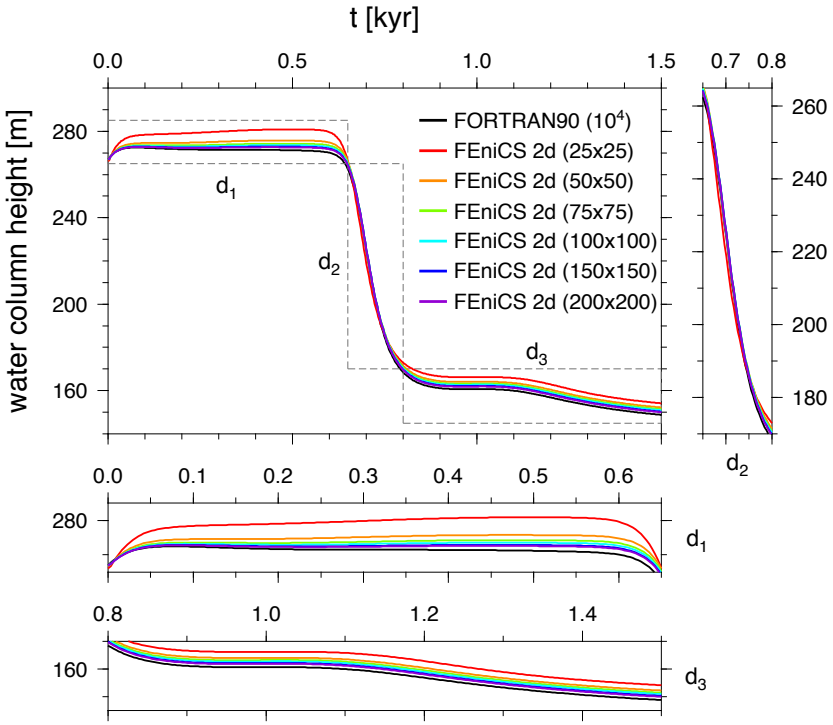

Figure 4.6: The same as in Figure 4.5 but for the 2d FEniCS code.

the with results of the 1d code). Again, the solution computed on the coarsest mesh (25×25 elements) differs strongly from the reference solution, moreover, also the solutions computed on slightly finer meshes (50×50, 75×75, and 100×100 elements) still differ substantially from the reference solution, especially when the absolute amount of water is investigated (details d_1 and d_3). Increasing further the resolution (150×150 and 200×200 elemets) slightly improves the solution, even though again, we do not reach an exact match with the reference FOR-

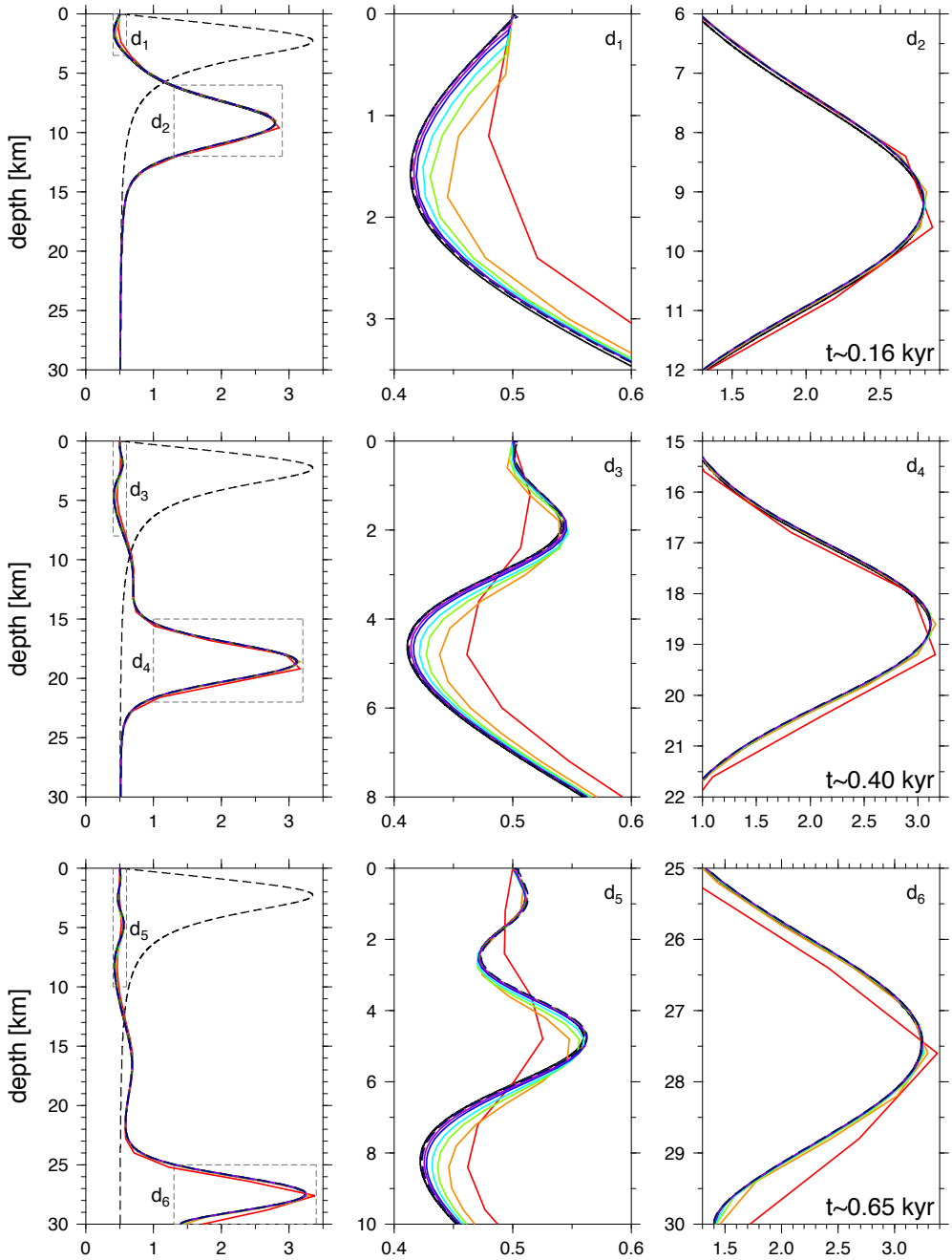

Figure 4.7: Porosity as a function of depth in three time instants (t∼0.16, 0.40, 0.65 kyr) computed by the FORTRAN90 code (black line) and the 1d FEniCS code (colored lines). Two details are shown for each time for better clarity. Colors are the same as in Figure 4.5.

TRAN90 solution. Concerning the time of the beginning of the outflow from the domain and the shape of the outflow curve (detail d_2), the solutions computed on the meshes 50×50 elements and finer agree well with the reference solution. Thus, when concerned with the overall evolution, meshes with the resolution 150 and 150×150 elements, respectively, and finer, are found to be acceptable.

We investigate also the spatial agreement between the solutions. Figure 4.7 shows three snapshots from time evolution of the initial profile (eq. 4.70 and black dashed lines in left panels) computed by the FORTRAN90 code and by the 1d FEniCS code for the same mesh resolutions as above. The entire solutions in

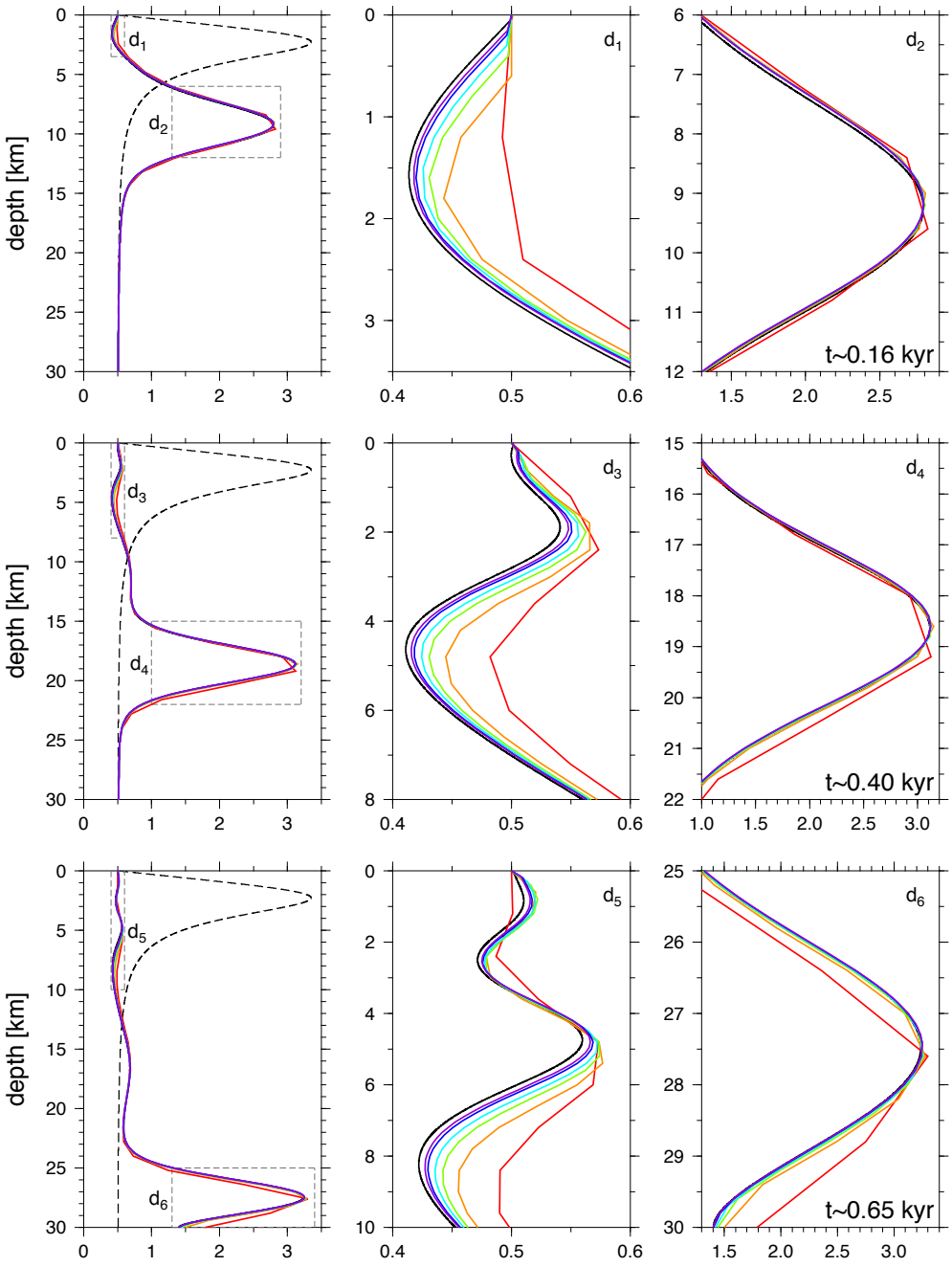

Figure 4.8: The same as in Figure 4.7 but for the 2d FEniCS code. Colors are the same as in Figure 4.6.

left panels show that the solution computed on the coarsest mesh (25 elements) strongly differs from the reference solution. The details added in the middle and right column indicate that also some of the finer meshes give solutions that still substantially differ from the reference one. However, this difference quickly decreases with increasing mesh resolution. Figure 4.8 shows three snapshots from time evolution of the initial profile computed by the FORTRAN90 code and by the 2d FEniCS code[1]. The results are quite similar with those shown in Figure 4.7 - we observe expected improvement of the solution with the mesh refinement.

It is clear that the coarsest meshes are not adequate for our simulations, however, it is difficult to decide which resolution is sufficient from the above figures. That is why we computed the relative errors of all the solutions w.r.t. the reference solution computed by the FORTRAN90 code. The time evolution of their maxima in each time step is plotted in Figure 4.9 (panel a for the 1d FEniCS, panel b for the 2d FEniCS). We observe that the errors of solutions computed on meshes composed of 150 and 150×150 elements, respectively, and finer, stay well below 5% during the whole simulation for both 1d and 2d simulations and therefore we consider these as sufficiently fine for our simulations.

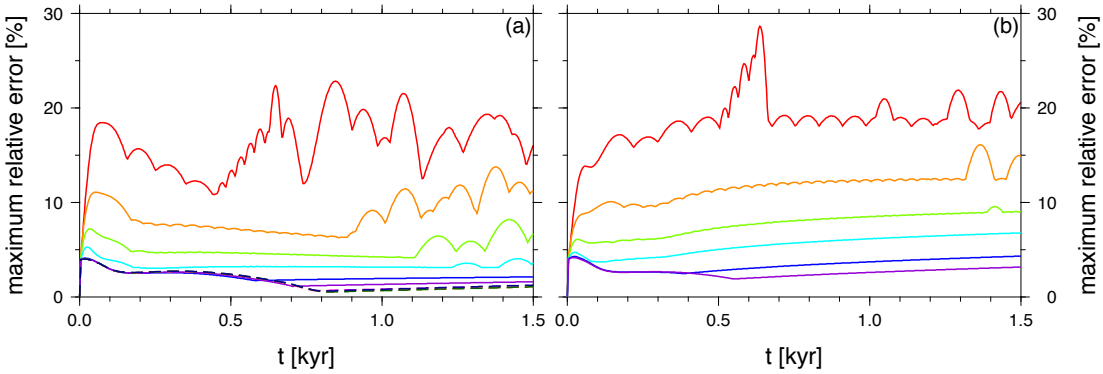

Figure 4.9: (a) The relative errors of the 1d FEniCS solutions w.r.t. the FORTRAN90 solutions. Colors are the same as in Figure 4.5. (b) The same as in panel a, only for the 2d FEniCS code. Colors are the same as in Figure 4.6.

4.3 FEniCS code (2d) for polythermal ice simulations

Finally, we implement the problem of water generation and transport in a polythermal ice shell in the impermeable limit (cf. below) by using FEniCS. Since the problem is rather complicated, we divide the numerical method description as follows: (i) we start with a summary of the governing equations and boundary conditions (Section 4.3.1), (ii) we continue with the weak formulation and description of the chosen time-discretization scheme (Section 4.3.2), (iii) considering a problem without melting/freezing process, i.e. assuming that only the

[1]Here again, for the purpose of comparison, we represent the 1d solution by the 2d solution while considering $x \sim 0.5$, i.e. we take the solution from the center of the domain.

initially present melt can be advected with the (convecting) ice matrix, we perform tests of this convection code (Section 4.3.3), and (iv) we conclude with the description of the melting/freezing process and its implementation (Section 4.3.4).

4.3.1 Governing equations and boundary conditions

Governing equations

First of all, we modify the linear momentum balance of the ice matrix in order to enable convective heat transfer in a polythermal ice shell. We start with a dimensional eq. (3.71b):

$$\begin{aligned}\rho_{\mathrm{m}}\left(\frac{\partial((1-\phi)\boldsymbol{v}_{\mathrm{m}})}{\partial t}+\nabla\cdot((1-\phi)\boldsymbol{v}_{\mathrm{m}}\otimes\boldsymbol{v}_{\mathrm{m}})\right) &= -(1-\phi)\nabla P_{\mathrm{m}}+\nabla\cdot((1-\phi)\boldsymbol{\sigma}_{\mathrm{m}}) \\ &- r_{\mathrm{f}}\boldsymbol{v}_{\mathrm{m}}^{\mathrm{i}}-(P_{\mathrm{m}}^{\mathrm{i}}-P_{\mathrm{m}})\nabla\phi \qquad (4.71)\\ &+ (1-\phi)\rho_{\mathrm{m}}(1-\alpha_{\mathrm{m}}\Delta T)\mathbf{b}_{\mathrm{m}}+\mathbf{M}_{\mathrm{m}}^{\mathrm{i}}\ ,\end{aligned}$$

in which we have already included the ice density variations due to thermal expansion with coefficient α_{m} (i.e. we linearized the state equation with respect to temperature deviations $\Delta T{=}T{-}T_0$ from the reference state T_0, e.g. *Ricard*, 2007). Using the equations (3.72)–(3.74), (3.78b), (3.79)–(3.81), and the mass balance for matrix (eq. 3.70b) we can write

$$\begin{aligned}(1-\phi)\rho_{\mathrm{m}}\frac{\mathrm{D}_{\mathrm{m}}\boldsymbol{v}_{\mathrm{m}}}{\mathrm{D}t} &= -(1-\phi)(\nabla\Pi{+}\nabla\Delta P)+\nabla\cdot((1-\phi)\boldsymbol{\sigma}_{\mathrm{m}})-\omega\boldsymbol{v}_{\mathrm{r}}r_{\mathrm{f}}\\ &+ (1-\omega)\left(\Delta P\nabla\phi{+}\nabla(\sigma\alpha)\right)+c\boldsymbol{v}_{\mathrm{r}}-(1-\phi)\rho_{\mathrm{m}}\alpha_{\mathrm{m}}\Delta T\boldsymbol{g}\ ,\end{aligned} \qquad (4.72)$$

which differs from eq. (3.82b) by a last (buoyancy) term on the right-hand side. Using the primary (3.118) and secondary scales (3.119), the definitions of dimensionless numbers (3.120) and their products (3.126), employing the relation for pressure difference (eq. 3.131), neglecting the same terms as in equation (3.132) plus the effect of surface tension, and substituting for $c\boldsymbol{v}_{\mathrm{r}}$ from eq. (3.130) we finally arrive at the following form of a dimensionless balance of linear momentum:

$$\begin{aligned}\nabla\Pi &= -\phi\boldsymbol{e}_{\mathrm{z}}+(1-[\phi]\phi)\frac{\mathcal{A}}{\mathcal{R}[\phi]}\Delta T\boldsymbol{e}_{\mathrm{z}} \qquad (4.73)\\ &+ \mathscr{C}\nabla\cdot\left((1-[\phi]\phi)\mu_{\mathrm{m}}\left(\frac{1}{[\phi]\phi}(\nabla\cdot\boldsymbol{v}_{\mathrm{m}})\mathbf{I}+\nabla\boldsymbol{v}_{\mathrm{m}}{+}(\nabla\boldsymbol{v}_{\mathrm{m}})^{\mathrm{T}}{-}\frac{2}{3}(\nabla\cdot\boldsymbol{v}_{\mathrm{m}})\mathbf{I}\right)\right)\ ,\end{aligned}$$

with $\mathcal{A}{=}\alpha_{\mathrm{m}}T_0$ and $\Delta T{=}T{-}1$.

As a first step towards a more complicated model, we consider the impermeable limit of two-phase equations by setting the ice permeability $k(\phi)$ to zero. This approach (corresponding to that of *Tobie et al.*, 2003) results in zero relative velocity between the phases ($\boldsymbol{v}_{\mathrm{r}}{=}\mathbf{0}$) - liquid water is locked within and advected with the ice matrix. Also, we do not compute the melting/freezing of water using the porosity advection equation (the right-hand side is set to zero) since we treat this process independently together with the temperature modification (cf. Algorithm 3). More details on the melting/freezing process are given in Sections 4.3.2 and 4.3.4. For temperature, only single-phase balance is considered that can be

obtained from eq. (3.136e) by setting ϕ=0 and r_f=0 (as mentioned above, computation of the melting rate will be performed by a different approach described later in Section 4.3.4). This is motivated by the fact that temperature can only change within a cold ice region, while in the temperate parts of the shell, it equals the (pressure) melting point. The governing equations can finally be written as

$$\frac{\partial\phi}{\partial t} - \frac{\mathcal{V}}{[\phi]}\nabla\cdot((1-[\phi]\phi)\boldsymbol{v}_\mathrm{m}) = 0 \ , \tag{4.74a}$$

$$\frac{\mathcal{V}}{[\phi]}\nabla\cdot\boldsymbol{v}_\mathrm{m} = -\frac{\mathcal{R}}{1+\mathcal{R}}r_\mathrm{f} \ , \tag{4.74b}$$

$$\begin{aligned}\nabla\Pi = &-\phi\boldsymbol{e}_\mathrm{z} + (1-[\phi]\phi)\frac{\mathcal{A}}{\mathcal{R}[\phi]}\Delta T\boldsymbol{e}_\mathrm{z} \\ &+ \mathscr{C}\nabla\cdot\left((1-[\phi]\phi)\mu_\mathrm{m}\left(\frac{1}{[\phi]\phi}(\nabla\cdot\boldsymbol{v}_\mathrm{m})\mathbf{I} + \nabla\boldsymbol{v}_\mathrm{m} + (\nabla\boldsymbol{v}_\mathrm{m})^\mathrm{T} - \frac{2}{3}(\nabla\cdot\boldsymbol{v}_\mathrm{m})\mathbf{I}\right)\right) \ ,\end{aligned} \tag{4.74c}$$

$$\frac{\partial T}{\partial t} + \mathcal{V}\boldsymbol{v}_\mathrm{m}\cdot\nabla T = \mathcal{V}\nabla^2 T + \frac{[\phi]}{\mathcal{T}}Q \ , \tag{4.74d}$$

where we considered constant specific heat (c_m=1). We note, that even though the two phases (ice and water) are both considered incompressible, the mixture as a whole compacts/extends when the melting/freezing occurs, i.e. when $r_\mathrm{f}\neq 0$ (cf. eq. 4.74b).

Boundary conditions

We prescribe (as in the one-dimensional case, cf. eq. 4.4) fixed temperatures at the top (Γ_T) and bottom (Γ_B) boundaries, respectively:

$$T = T_\mathrm{s} \ , \tag{4.75a}$$

$$T = T_\mathrm{M}|_{z=0} \ , \tag{4.75b}$$

with T_s the surface temperature and $T_\mathrm{M}|_{z=0}$ the melting temperature at the base of the ice shell (underlaid by the internal ocean), and reflecting symmetry at the side (Γ_S) boundaries, i.e.

$$\nabla T\cdot\boldsymbol{n} = 0 \ . \tag{4.76}$$

Alternatively, when benchmarking the code (Section 4.3.3, case 3), we prescribe zero heat flux also at the bottom boundary (Γ_B).

Concerning the mechanical part of the problem, several combinations of boundary conditions are used. In the benchmark Section 4.3.3, either free slip is prescribed at the whole boundary ($\partial\Omega$, cases 1a–c, 2a)

$$\begin{aligned}\boldsymbol{v}_\mathrm{m}\cdot\boldsymbol{n} &= 0 \\ \left((1-[\phi]\phi)\mu_\mathrm{m}\left(\frac{1}{[\phi]\phi}(\nabla\cdot\boldsymbol{v}_\mathrm{m})\boldsymbol{I} + \nabla\boldsymbol{v}_\mathrm{m} + (\nabla\boldsymbol{v}_\mathrm{m})^\mathrm{T} - \frac{2}{3}(\nabla\cdot\boldsymbol{v}_\mathrm{m})\boldsymbol{I}\right)\cdot\boldsymbol{n}\right)_\mathrm{t} &= \mathbf{0} \ ,\end{aligned} \tag{4.77}$$

(cf. discussion below eq. 4.53 for the unusual form of this condition) or alternatively free slip is kept at the side walls (Γ_S) and no slip is prescribed at the top (Γ_T) and bottom (Γ_B) boundaries (case 3):

$$\boldsymbol{v}_\mathrm{m} = 0 \ . \tag{4.78}$$

In both cases, the dynamical pressure is fixed in the left bottom corner

$$\Pi|_{x=0,z=0,t} = 0 \ . \tag{4.79}$$

In simulations with melting/freezing (Chapter 8), free slip (eq. 4.77) is prescribed at the bottom (Γ_B) and side (Γ_S) boundaries, while free surface of the form

$$(1-[\phi]\phi)\mu_\mathrm{m}\left(\frac{1}{[\phi]\phi}(\nabla\cdot\boldsymbol{v}_\mathrm{m})\boldsymbol{I}+\nabla\boldsymbol{v}_\mathrm{m}+(\nabla\boldsymbol{v}_\mathrm{m})^\mathrm{T}-\frac{2}{3}(\nabla\cdot\boldsymbol{v}_\mathrm{m})\boldsymbol{I}\right)\cdot\boldsymbol{n}=\boldsymbol{0}\ . \tag{4.80}$$

(cf. again discussion below eq. 4.53 for the unusual form of this condition) is prescribed at the top boundary (Γ_T) together with the fixed dynamical pressure:

$$\Pi = 0 \ . \tag{4.81}$$

Contrary to the FORTRAN90 code described earlier in Section 4.1, we cannot solve the system of eqs (4.74) for a zero porosity. Therefore we shall assume a small background value is permanently present, even if the ice is below the melting temperature. This (constant) background porosity ϕ^off is then prescribed at the beginning of the simulation (cf. Algorithm 2) as well as fixed at the (open) top boundary (Γ_T) during the simulation:

$$\phi = \phi^\mathrm{off} \ . \tag{4.82}$$

Since water is locked within the ice matrix and the relative velocity $\boldsymbol{v}_\mathrm{r}$ is zero, we do not have to prescribe any boundary conditions for water in/outflow.

4.3.2 Weak formulation of the problem

The system of governing equations (4.74) together with the appropriate boundary conditions chosen among eqs (4.75)–(4.82 is solved in the weak sense, i.e. we look for $\boldsymbol{\zeta}=\{\phi,\Pi,\boldsymbol{v}_\mathrm{m},T\}\in\boldsymbol{X}$ where $\boldsymbol{X}=[P,W,\boldsymbol{M},K]$ is a mixed finite element space composed of[2]

$$\begin{aligned} P &= \{\psi\in W^{1,2}(\Omega);\psi|_{\Gamma_\mathrm{T}}=0\} \\ W &= \{\psi\in W^{1,2}(\Omega);\psi|_{\Gamma_\mathrm{T}}=0\} \\ \boldsymbol{M} &= \{\boldsymbol{\chi}\in W^{1,2}(\Omega);\boldsymbol{\chi}\cdot\boldsymbol{n}|_{\Gamma_\mathrm{B}\cup\Gamma_\mathrm{S}}=0\} \\ K &= \{\psi\in W^{1,2}(\Omega);\psi|_{\Gamma_\mathrm{T}\cup\Gamma_\mathrm{B}}=0\}\ . \end{aligned} \tag{4.83}$$

We use classical Galerkin finite element method (*Quarteroni & Valli*, 1994) and approximate the spaces P,W by a finite-dimensional space of piece-wise linear functions and the spaces $\boldsymbol{M},K$ by a finite-dimensional space of piece-wise quadratic functions (cf. *Taylor & Hood*, 1973; *Rhebergen et al.*, 2013).

In contrast to the temperate ice setting (Section 4.2), where the equations were solved together, we use the decoupling predictor-corrector scheme (e.g. *Hansen & Ebel*, 1988; *van den Berg et al.*, 1993) with the predictor step discretized in

[2]We list the elements spaces for the simulations from Chapter 8. For the benchmark cases from Section 4.3.3, the element spaces were modified accordingly to the applied boundary conditions.

time using a backward (implicit) Euler method and the corrector step computed with the semi-implicit Crank-Nicolson scheme (eq. 4.60 with θ=0.5). The time-stepping is adaptive with the time step controlled by the CFL criterion

$$\Delta t^{\mathrm{k+1}} = \frac{C_{\mathrm{CFL}} h_{\min}}{\mathcal{V}|\boldsymbol{v}_{\mathrm{m}}^{\mathrm{k}}|} \ . \tag{4.84}$$

We use the SUPG stabilization method for porosity advection (cf. Section 4.2.1). The weak formulation of eqs 4.74 reads:

Porosity transport equation (mass balance of ice)

$$\begin{aligned}
& \int_\Omega \phi^k \varphi \,\mathrm{d}x + \int_\Omega \phi^k \tau^{\mathrm{A}} \mathcal{V}(\boldsymbol{v}_{\mathrm{m}}^k \cdot \nabla\varphi)\,\mathrm{d}x - \int_\Omega \phi^{k-1}\varphi \,\mathrm{d}x \\
- & \int_\Omega \phi^{k-1} \tau^{\mathrm{A}} \mathcal{V}(\boldsymbol{v}_{\mathrm{m}}^{k-1} \cdot \nabla\varphi)\,\mathrm{d}x - \int_\Omega \Delta t\theta \frac{\mathcal{V}}{[\phi]}(1-[\phi]\phi^k)(\nabla\cdot\boldsymbol{v}_{\mathrm{m}}^k)\varphi\,\mathrm{d}x \\
- & \int_\Omega \Delta t\theta \frac{\mathcal{V}}{[\phi]}(1-[\phi]\phi^k)(\nabla\cdot\boldsymbol{v}_{\mathrm{m}}^k)\tau^{\mathrm{A}}\mathcal{V}(\boldsymbol{v}_{\mathrm{m}}^k\cdot\nabla\varphi)\,\mathrm{d}x \\
- & \int_\Omega \Delta t(1-\theta) \frac{\mathcal{V}}{[\phi]}(1-[\phi]\phi^{k-1})(\nabla\cdot\boldsymbol{v}_{\mathrm{m}}^{k-1})\varphi\,\mathrm{d}x \\
- & \int_\Omega \Delta t(1-\theta) \frac{\mathcal{V}}{[\phi]}(1-[\phi]\phi^{k-1})(\nabla\cdot\boldsymbol{v}_{\mathrm{m}}^{k-1})\tau^{\mathrm{A}}\mathcal{V}(\boldsymbol{v}_{\mathrm{m}}^{k-1}\cdot\nabla\varphi)\,\mathrm{d}x \\
+ & \int_\Omega \Delta t\theta \mathcal{V}(\boldsymbol{v}_{\mathrm{m}}^k\cdot\nabla\phi^k)\varphi\,\mathrm{d}x + \int_\Omega \Delta t\theta\mathcal{V}(\boldsymbol{v}_{\mathrm{m}}^k\cdot\nabla\phi^k)\tau^{\mathrm{A}}\mathcal{V}(\boldsymbol{v}_{\mathrm{m}}^k\cdot\nabla\varphi)\,\mathrm{d}x \\
+ & \int_\Omega \Delta t(1-\theta)\mathcal{V}(\boldsymbol{v}_{\mathrm{m}}^{k-1}\cdot\nabla\phi^{k-1})\varphi\,\mathrm{d}x + \int_\Omega \Delta t(1-\theta)\mathcal{V}(\boldsymbol{v}_{\mathrm{m}}^{k-1}\cdot\nabla\phi^{k-1}) \\
& \tau^{\mathrm{A}}\mathcal{V}(\boldsymbol{v}_{\mathrm{m}}^{k-1}\cdot\nabla\varphi)\,\mathrm{d}x = 0 \qquad\qquad \forall\varphi\in P \ .
\end{aligned} \tag{4.85}$$

Equation for the water excess pressure (sum of mass balances)

$$\int_\Omega \frac{\mathcal{V}}{[\phi]}(\nabla\cdot\boldsymbol{v}_{\mathrm{m}})\,\omega\,\mathrm{d}x + \int_\Omega \frac{\mathcal{R}}{1+\mathcal{R}} r_{\mathrm{f}}\,\omega\,\mathrm{d}x = 0 \qquad \forall\omega\in W \ . \tag{4.86}$$

Ice velocity (momentum balance of ice)

$$\begin{aligned}
& \int_\Omega \nabla\Pi\cdot\boldsymbol{\mu}\,\mathrm{d}x + \int_\Omega \phi\boldsymbol{e}_{\mathrm{z}}\cdot\boldsymbol{\mu}\,\mathrm{d}x + \int_\Omega \mathscr{C}\mu_{\mathrm{m}}\frac{1-[\phi]\phi}{[\phi]\phi}(\nabla\cdot\boldsymbol{v}_{\mathrm{m}})(\nabla\cdot\boldsymbol{\mu})\,\mathrm{d}x \\
+ & \int_\Omega \mathscr{C}\mu_{\mathrm{m}}(1-[\phi]\phi)(\nabla\boldsymbol{v}_{\mathrm{m}} + (\nabla\boldsymbol{v}_{\mathrm{m}})^{\mathrm{T}} - \frac{2}{3}(\nabla\cdot\boldsymbol{v}_{\mathrm{m}})\boldsymbol{I}) : (\nabla\boldsymbol{\mu})^{\mathrm{T}}\,\mathrm{d}x \\
- & \int_\Omega (1-[\phi]\phi)\frac{\mathcal{A}}{\mathcal{R}[\phi]}\Delta T\boldsymbol{e}_{\mathrm{z}}\cdot\boldsymbol{\mu} = 0 \qquad\qquad \forall\boldsymbol{\mu}\in\boldsymbol{M} \ .
\end{aligned} \tag{4.87}$$

Energy balance

- **Predictor step**: backward Euler scheme, implicit w.r.t. temperature T, the ice velocity and the (temperature-dependent) volumetric heating are taken from the previous time step, $\boldsymbol{v}_{\mathrm{m}}^{k-1}$ and Q^{k-1}=$Q(T^{k-1})$, respectively.

$$\int_\Omega T^k\xi\,\mathrm{d}x - \int_\Omega T^{k-1}\xi\,\mathrm{d}x + \int_\Omega \Delta t\mathcal{V}\boldsymbol{v}_\mathrm{m}^{k-1}\cdot\nabla T^k\xi\,\mathrm{d}x$$
$$+ \int_\Omega \Delta t\mathcal{V}\nabla T^k\cdot\nabla\xi\,\mathrm{d}x - \int_\Omega \Delta t\frac{[\phi]}{\mathcal{T}}Q^{k-1}\xi\,\mathrm{d}x = 0 \qquad \forall\xi{\in}K\ . \quad (4.88)$$

- **Corrector step**: semi-implicit Crank-Nicolson scheme, the 'implicit' ice velocity is taken from the mechanical problem predictor, $\boldsymbol{v}_\mathrm{m}^\mathrm{pr}$, and the (temperature-dependent) volumetric heating is computed from the predicted temperature $Q^\mathrm{pr}{=}Q(T^\mathrm{pr})$.

$$\int_\Omega T^k\xi\,\mathrm{d}x - \int_\Omega T^{k-1}\xi\,\mathrm{d}x + \int_\Omega \Delta t\theta\mathcal{V}\boldsymbol{v}_\mathrm{m}^\mathrm{pr}\cdot\nabla T^k\xi\,\mathrm{d}x$$
$$+ \int_\Omega \Delta t(1{-}\theta)\mathcal{V}\boldsymbol{v}_\mathrm{m}^{k-1}\cdot\nabla T^{k-1}\xi\,\mathrm{d}x + \int_\Omega \Delta t\theta\mathcal{V}\nabla T^k\cdot\nabla\xi\,\mathrm{d}x$$
$$+ \int_\Omega \Delta t(1{-}\theta)\mathcal{V}\nabla T^{k-1}\cdot\nabla\xi\,\mathrm{d}x - \int_\Omega \Delta t\frac{[\phi]}{\mathcal{T}}Q^\mathrm{pr}\xi\,\mathrm{d}x = 0 \qquad \forall\xi{\in}K\ .$$

The whole system is solved using Algorithm 2.

Algorithm 2 A predictor-corrector scheme for ice convection with melting/freezing.

Initialize temperature $T^0{=}T(t^0)$ and porosity $\phi^0{=}\phi(t^0){=}\phi^\mathrm{off}$.
Set the initial ice velocity $v_\mathrm{m}^0{=}v_\mathrm{m}(t^0)$ and melting rate $r_\mathrm{f}^0{=}r_\mathrm{f}(t^0)$ to zero.
Choose the first time-step Δt^1.
for $k = 1,\ldots,N$ **do**
(i) Solve the predictor (implicit) step of thermal equation (4.88) using $\boldsymbol{v}_\mathrm{m}^{k-1}$ and $Q(T^{k-1})$ to obtain the predicted temperature, T^pr.
(ii) For $\mu_\mathrm{m}(T^\mathrm{pr},\boldsymbol{v}_\mathrm{m}^\mathrm{pr},\phi^{k-1})$ and r_f^{k-1} solve the mechanical part of the problem (eqs 4.85–4.87) to obtain the predicted values of porosity, dynamic pressure, and ice velocity, ϕ^pr, Π^pr, and $\boldsymbol{v}_\mathrm{m}^\mathrm{pr}$, respectively.
(iii) Solve the corrector (semi-implicit) step of thermal equation (4.89) using $\boldsymbol{v}_\mathrm{m}^\mathrm{pr}$ and $Q(T^\mathrm{pr})$ to obtain the corrected temperature, T^cor.
(iv) For $\mu_\mathrm{m}(T^\mathrm{cor},\boldsymbol{v}_\mathrm{m}^\mathrm{cor},\phi^\mathrm{pr})$ and r_f^{k-1} solve the mechanical part of the problem (eqs 4.85–4.87) to obtain the corrected values of porosity, dynamic pressure, and ice velocity, ϕ^cor, $\Pi^\mathrm{cor}{=}\Pi^k$, and $\boldsymbol{v}_\mathrm{m}^\mathrm{cor}{=}\boldsymbol{v}_\mathrm{m}^k$, respectively.
(v) Using ϕ^cor and T^cor, evaluate the melting/freezing rate r_f^k and modify the porosity and temperature fields accordingly using Algorithm 3 (cf. Section 4.3.4) to obtain $\phi^{\mathrm{cor}*}{=}\phi^k$ and $T^{\mathrm{cor}*}{=}T^k$, respectively.
(vi) Compute the value of a new time-step Δt^{k+1} using eq. (4.84).
end for

4.3.3 Thermal convection benchmark

In order to test our numerical code, we perform a comparison with the convection benchmark of *Blankenbach et al.* (1989). Even though the benchmark is well documented in the original paper, we give a short overview of each of the studied cases for better clarity. In the original benchmark, several expressions were compared - we decided to compare the (dimensionless) Nusselt number

$$\mathrm{Nu} = -h\frac{\int_{\Gamma_\mathrm{T}} \nabla T \cdot \boldsymbol{n}\mathrm{d}s}{\int_{\Gamma_\mathrm{B}} T\mathrm{d}s} \tag{4.89}$$

(i.e. the mean surface temperature gradient over the mean bottom temperature) with h the domain height and the (dimensionless) rms velocity

$$v_\mathrm{rms} = \frac{1}{hl}\left(\int_\Omega \boldsymbol{v}_\mathrm{m}\cdot\boldsymbol{v}_\mathrm{m}\mathrm{d}x\right)^{1/2}, \tag{4.90}$$

with l the domain width. The values of all physical parameters used in this study are summarized in Table 4.1.

Symbol	Variable	Value	Unit
α	thermal expansion coefficient	2.5×10^{-5}	1/K
c_p	heat capacity	1.25×10^{3}	J/kg/K
ΔT	temperature contrast (cases 1 and 2)	1000	K
g	gravity acceleration	10	m/s^2
h	height of cell	10^6	m
κ	thermal diffusivity	10^{-6}	m^2/s
ν	kinematic viscosity	2.5×10^{19} (1a)	m^2/s
		2.5×10^{18} (1b)	m^2/s
		2.5×10^{17} (1c)	m^2/s
		1.1574×10^{18} (3)	m^2/s
ν_0	kinematic viscosity at surface	2.5×10^{19} (2a)	m^2/s
Q	volumetric heating rate (case 3)	5×10^{-9}	W/m^3
ρ	density	4×10^{3}	kg/m^3

Table 4.1: Parameters for the benchmark based on *Blankenbach et al.* (1989).

Case 1

In this case, the steady convection with constant viscosity in a square box (i.e. l/h=1) is studied. Temperature is fixed at the top and bottom boundaries, zero heat flux (reflecting symmetry) is considered on the sidewalls and zero shear stress (free slip condition) is prescribed at the whole boundary. Results for three different Rayleigh numbers (Ra=$10^4, 10^5, 10^6$) are investigated where the Rayleigh number is defined as:

$$\mathrm{Ra} = \frac{\alpha g \Delta T h^3}{\kappa\nu}, \tag{4.91}$$

with α the thermal expansion coefficient, g the gravity acceleration, ΔT the temperature difference across the box, κ the thermal diffusivity, and ν the (constant) kinematic viscosity (cf. Table 4.1). All calculations were performed on the uniform grid consisting of 100×100 elements. The use of grid refinement in boundary layers would probably improve our results, however, since we can not estimate the solution structure for the simulations where melting/freezing is enabled (Chapter 8), we prefer to obtain reasonably accurate solutions on a uniform grid. For cases 1a–c and 2a, our results (values of Nusselt number and rms velocity) are summarized in Table 4.2 together with the values from *Blankenbach et al.* (1989) and the relative errors.

case	Nu	reference	relat. error	v_{rms}	reference	relat. error
1a	4.888230	4.884409	0.08%	42.864781	42.864947	0.0004%
1b	10.574566	10.534095	0.38%	193.214532	193.21454	4×10^{-6} %
1c	22.364936	21.972465	1.79%	833.977344	833.98977	0.001%
2a	10.0791	10.0660	0.13%	479.7522	480.4334	0.14%

Table 4.2: Steady-state thermal convection results: Nusselt number and rms velocity for four different sets of parameter values (cases 1a–2a) obtained in this study and compared with the reference values from *Blankenbach et al.* (1989) for each case. The relative errors in percents are given in the fourth and seventh column, respectively.

Figure 4.10 shows time evolution of the Nusselt number and the rms velocity for the lowest value of Rayleigh number, Ra=10^4 (case 1a). Steady-state is reached at t∼0.34 with Nu=4.888230 and v_{rms}=42.864781. The corresponding temperature and velocity fields are depicted in Figure 4.11 in panels a and b, respectively. For case 1a (Ra=10^4), the relative error of our value of Nusselt

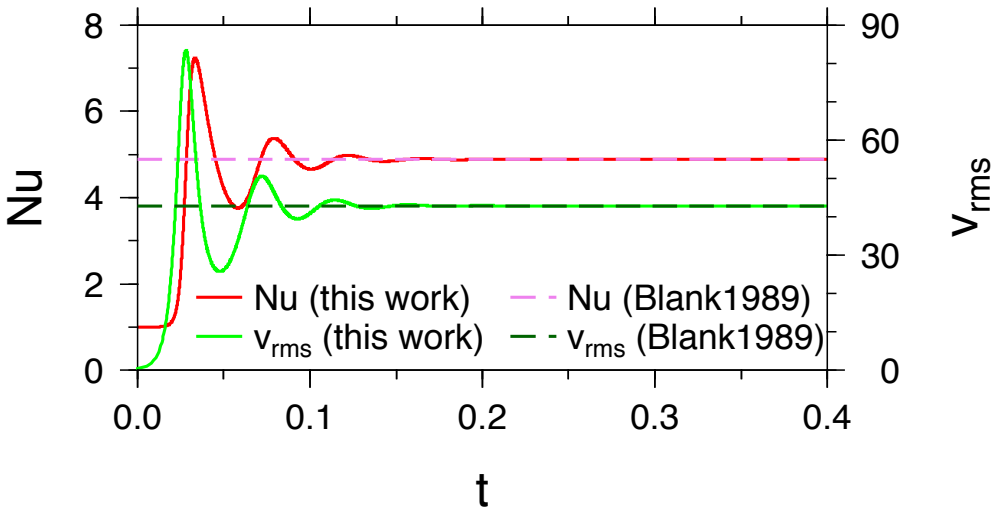

Figure 4.10: Nusselt number (red line) and rms velocity (green line) for the steady-state case 1a (Ra=10^4). The dashed lines show the benchmark values. All variables are dimensionless.

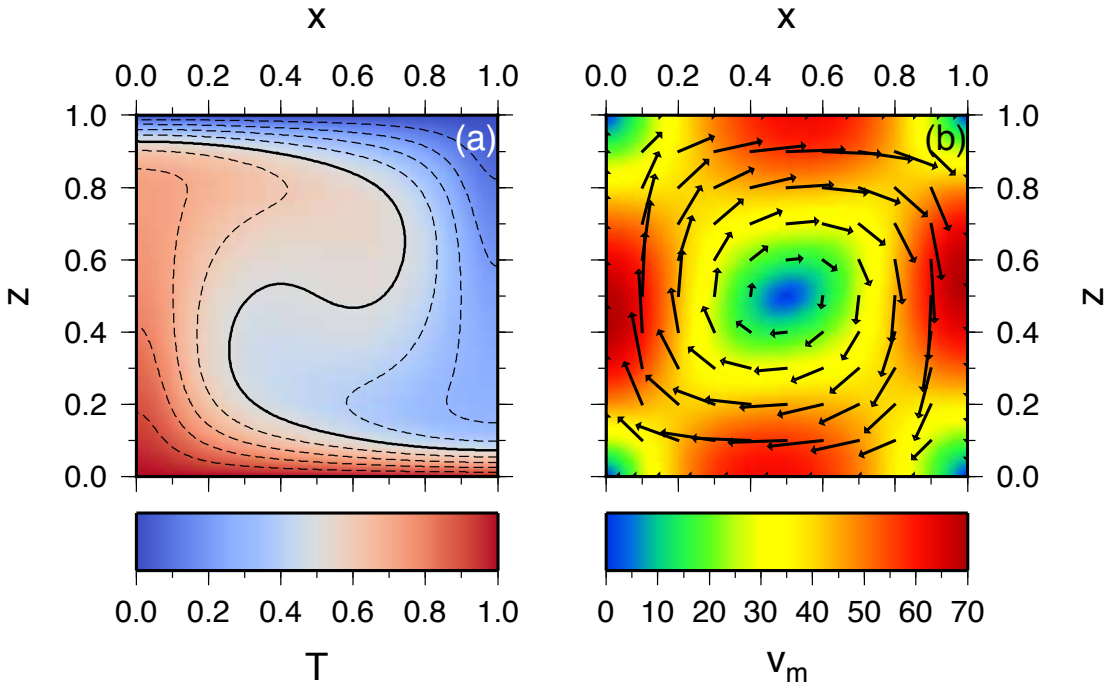

Figure 4.11: Steady-state for case 1a (Ra=10^4) (a) Temperature. Dashed contours are spaced by 0.1, the full contour corresponds to T=0.5. (b) Velocity. All variables are dimensionless.

number is 0.08% and the relative error of rms velocity is 0.0004% (cf. Table 4.2).

Results for higher value of Rayleigh number, Ra=10^5 (case 1b) are shown in Figures 4.12 and 4.13. We reach steady-state at t∼0.18 and obtain values of Nu=10.574566 and $v_{\rm rms}$=193.214532 with the corresponding relative errors of 0.38% and 4×10^{-6}%, respectively (cf. Table 4.2).

Finally, Figures 4.14 and 4.15 depict the solution for the highest Rayleigh number, Ra=10^6 (case 1c). Steady-state is reached at t∼0.14 and the cor-

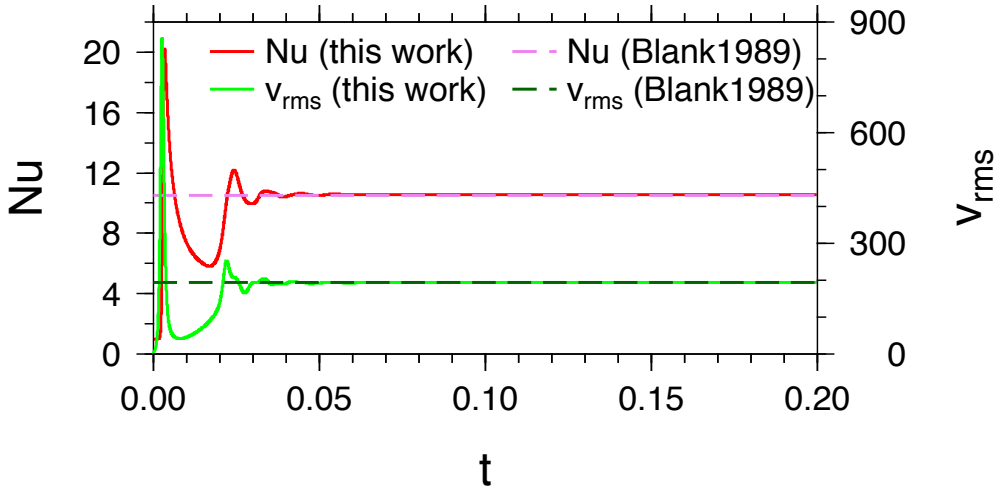

Figure 4.12: The same as in Figure 4.10 but for Ra=10^5 (case 1b).

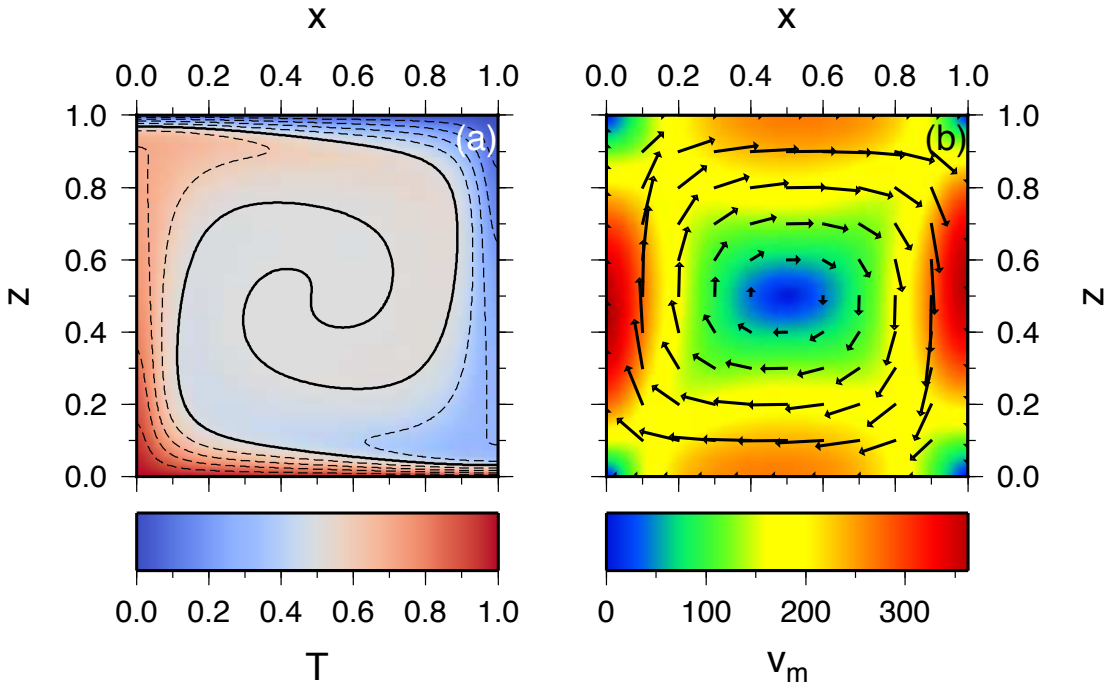

Figure 4.13: The same as in Figure 4.11 but for Ra=10^5 (case 1b).

responding values of Nusselt number and rms velocity are Nu=22.364936 and $v_{\rm rms}$=833.977344, respectively, leading to relative errors of 1.79% and 0.001% (cf. Table 4.2).

As can be seen from Table 4.2, we reach at least two orders of magnitude (in terms of relative errors) better results for the rms velocity than for the Nusselt number. This might be due to inacurate evaluation of temperature gradient on the top boundary. With increasing Rayleigh number the agreement of our results with the benchmark values worsens, however, for given resolution (100×100 elements), our errors correspond to those reported by *Vynnytska et al.* (2013) who also use

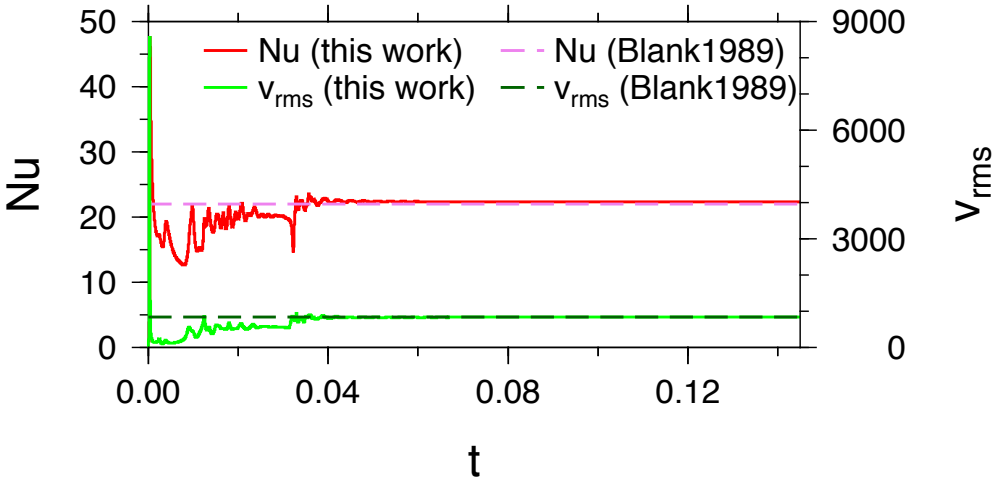

Figure 4.14: The same as in Figure 4.10 but for Ra=10^6 (case 1c).

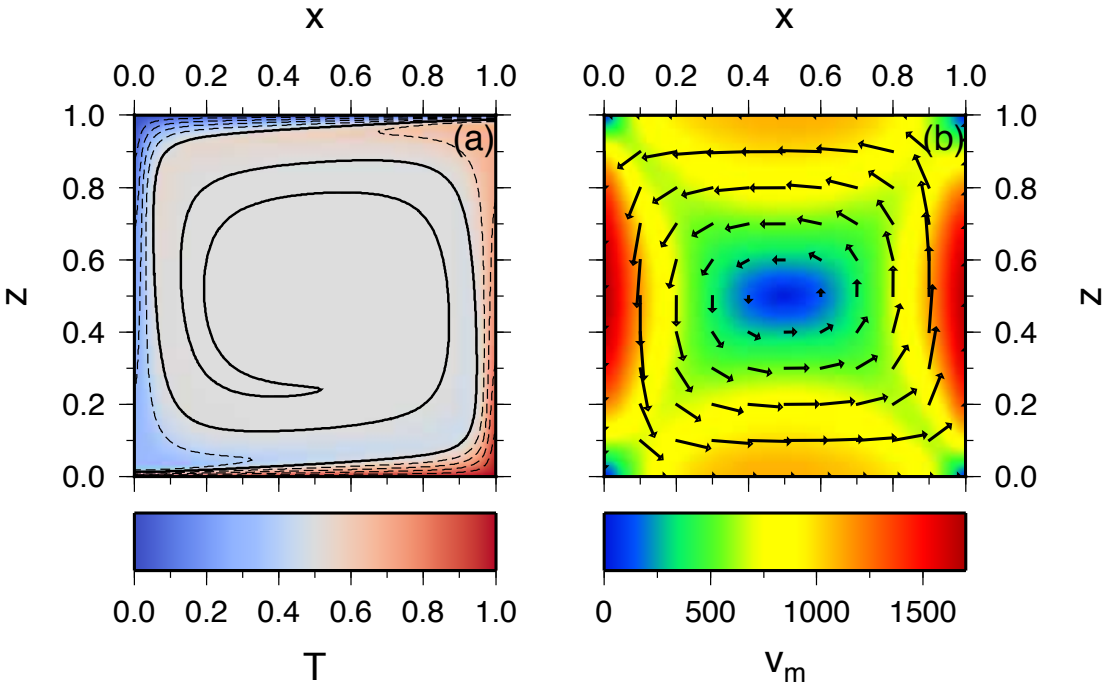

Figure 4.15: The same as in Figure 4.11 but for Ra=10^6 (case 1c).

FEniCS.

Case 2a

Steady convection with temperature-dependent viscosity in a square box (l/h=1) is investigated in this case. The kinematic viscosity is considered as

$$\nu = \nu_0 \exp\left(-\frac{bT}{\Delta T}\right) , \tag{4.92}$$

with ν_0 the viscosity at surface and b=ln(1000). The Rayleigh number is modified accordingly:

$$\mathrm{Ra}_0 = \frac{\alpha g \Delta T h^3}{\kappa \nu_0} \tag{4.93}$$

and the value Ra_0=10^4 is assumed. All boundary conditions are the same as in case 1.

The temperature and velocity fields for this setting are depicted in Figure 4.16. We obtain value of Nusselt number Nu=10.0791 and the rms velocity v_{rms}=479.7522 with the corresponding relative errors 0.13% and 0.14%, respectively (cf. Table 4.2). Again, we report similar results as *Vynnytska et al.* (2013).

Case 3

Finally, time-dependent convection with constant viscosity and internal heating in the rectangular box (l/h=1.5) is studied. No slip is prescribed at the top and bottom boundaries, while free slip is kept at the side walls. Temperature is fixed

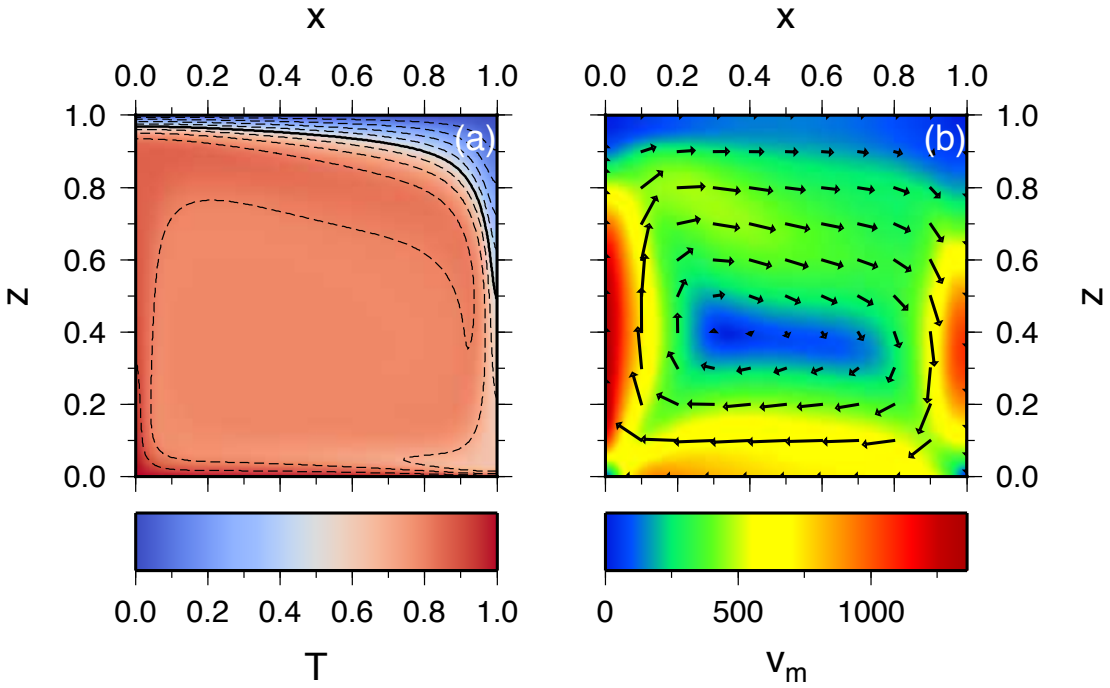

Figure 4.16: The same as in Figure 4.11 but for temperature-dependent viscosity and Ra_0=10^4 (case 2a).

at the top boundary and zero heat flux is considered at the remaining boundaries. The Rayleigh number is redefined as

$$\mathrm{Ra}_\mathrm{Q} = \frac{\alpha g Q h^5}{\kappa^2 \rho c_\mathrm{p} \nu} \ , \tag{4.94}$$

with Q the volumetric heating rate, ρ the density and c_p the heat capacity, and the initial condition is taken from *Lennie et al.* (1988):

$$T^0(x,z) = \frac{1}{2}(1-z^2) + \frac{1}{100}\cos\left(\frac{\pi x}{l}\right)\sin\left(\frac{\pi z}{h}\right) \ . \tag{4.95}$$

Periodic behavior is studied for Ra_Q=216 000.

Time evolution of the Nusselt number and the rms velocity computed on a mesh consisting of 150×100 elements in a periodic ($P2$, cf. *Blankenbach et al.*, 1989) regime is shown in Figure 4.17 (panels a and b, respectively). The period is 0.04805 and corresponds to that reported in the benchmark. Panel c of Figure 4.17 depicts the phase diagram with the Nusselt number over the rms velocity, illustrating again the $P2$ nature of the flow after the decay of the initial transient stage. Values of subsequent minima and maxima of the Nusselt number and the rms velocity are summarized in Table 4.3 together with the reference values and relative errors. We report slightly better agreement with the benchmark values than in the previous cases. Finally, temperature and velocity fields at four time instants within the periodic stage corresponding to v_rms minima and maxima (marked in panel c of Figure 4.17) are shown in Figure 4.18.

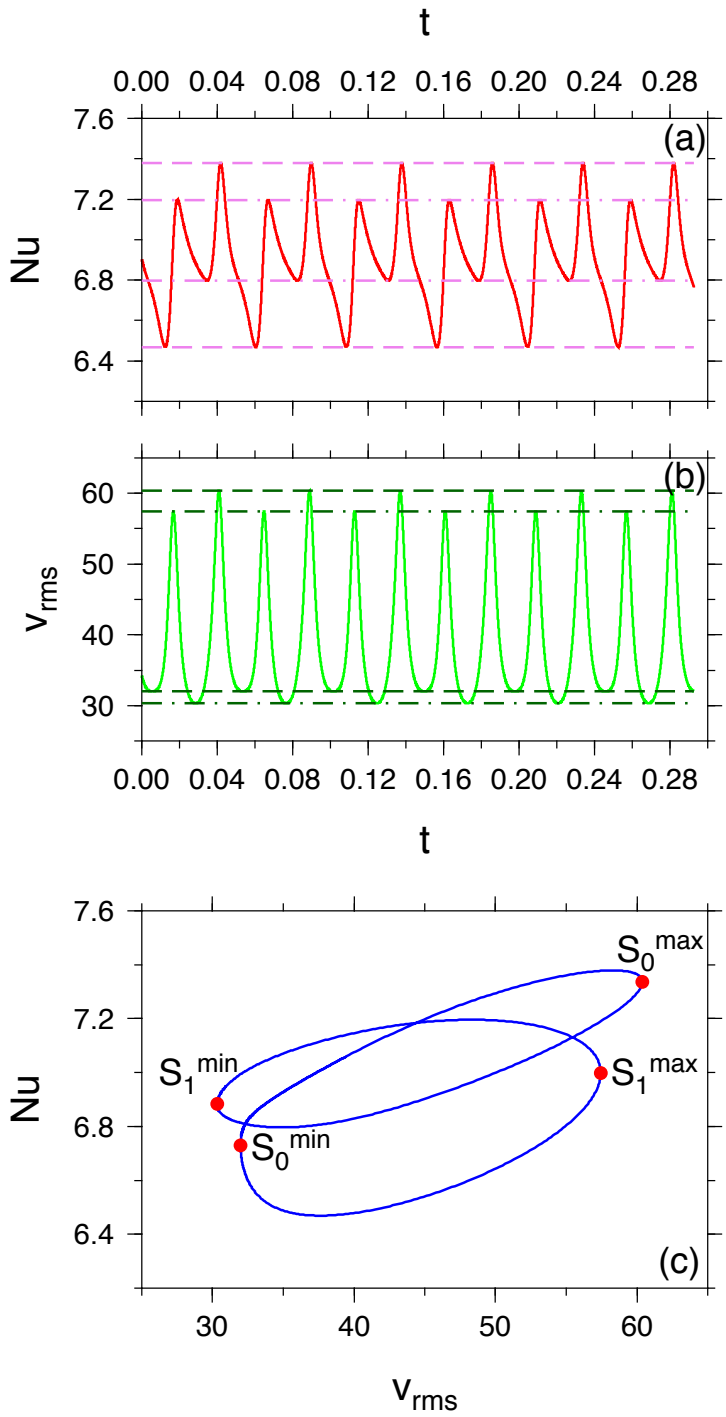

Figure 4.17: Time evolution of results for case 3. (a) Nusselt number. (b) Rms velocity. Dashed and dot-dashed lines correspond to values from *Blankenbach et al.* (1989) for the first (S_0) and second (S_1) stage of the $P2$ cycle, respectively (cf. Table 4.3). The figure was shifted in time (time t=0 was set at the beginning of the periodic stage) in order to better match Figure 7 from *Blankenbach et al.* (1989). (c) Phase diagram of the Nusselt number over the rms velocity with a distinct P2 structure. Minima and maxima of the rms velocity of both (S_0 and S_1, respectively) stages are marked.

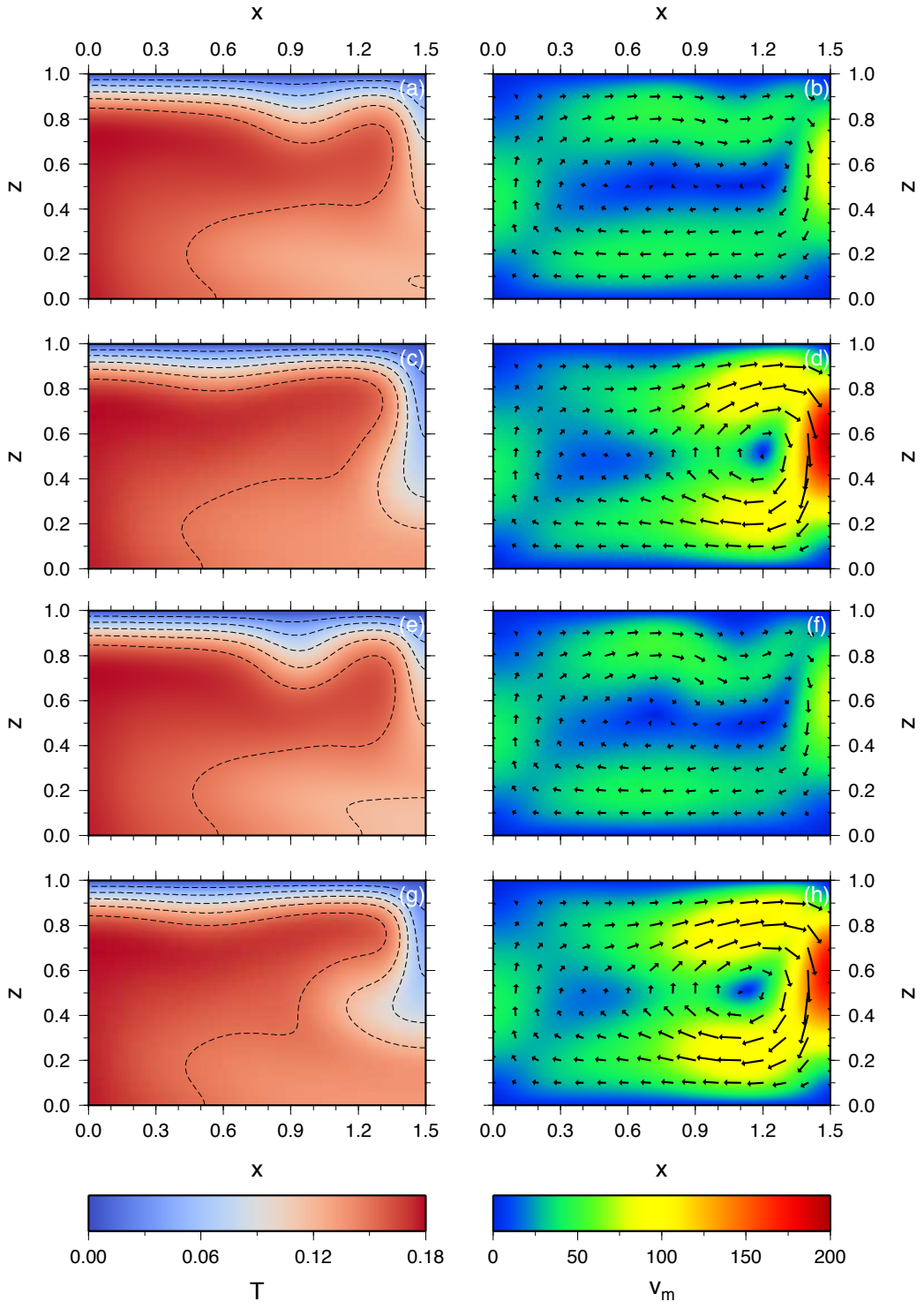

Figure 4.18: Snapshots of field variables for time-dependent convection with internal heating (case 3) after the periodic state is achieved. Temperature (left column) and velocity (right column). The first line corresponds to S_0 v_{rms} minimum, the second to S_1 v_{rms} maximum, the third to S_1 v_{rms} minimum, and the last to S_0 v_{rms} maximum (cf. also panel c in Figure 4.17. All variables are dimensionless.

stage	solution	period	$\mathrm{Nu}_{\max}$	$\mathrm{Nu}_{\min}$	$v_{\mathrm{rms,max}}$	$v_{\mathrm{rms,min}}$
S_0	this work	0.04805	7.3791	6.4690	60.3690	31.9813
	reference	0.04803	7.379	6.468	60.367	31.981
	relative error	0.04%	0.001%	0.015%	0.003%	0.001%
S_1	this work		7.1959	6.7964	57.4300	30.3220
	reference		7.196	6.796	57.43	30.32
	relative error		0.001%	0.006%	0.000%	0.007%

Table 4.3: Time-dependent thermal convection results: period, Nusselt number and rms velocity. Following *Vynnytska et al.* (2013), we label the minimum-maximum pairs within each $P2$ cycle by S_0 and S_1 (S_0 corresponds to the largest local maximum and following minimum, and S_1 to the next pair). The period was computed by comparing the time at which the S_0 maxima for the Nusselt number occurred for the last two computed complete cycles. The reference values are taken from *Blankenbach et al.* (1989).

4.3.4 Description of the melting/freezing process

We conclude the chapter about numerical methods used throughout this thesis with a description of the melting/freezing process in the (convecting) ice shell and its numerical implementation in FEniCS.

In a (tidally) heated ice shell, the melting temperature (determined only by pressure since we do not take into account any impurities) can be reached, leading to ice melting, liquid water production and local cooling due to latent heat absorption. If transport of water by percolation through the microscopic channels is neglected (as in our case, cf. above), all the water is locked and advected

Algorithm 3 Computation of the amount of melting/freezing.

For given T compute the difference from the melting point: $\Delta T{=}T_{\mathrm{M}}{-}T$.
For given ϕ compute the difference from the background value: $\Delta\phi{=}\phi^{\mathrm{off}}{-}\phi$.
if $T{\geq}T_{\mathrm{M}}$ (and thus $\Delta T{\leq}0 \Rightarrow$ melting) **then**
  $\delta T{=}\Delta T{\leq}0$ (temperature drop due to latent heat absorption)
  $\delta\phi{=}-\frac{\mathcal{T}}{[\phi]}\Delta T{\geq}0$ (porosity increase due to melting)
end if
if ($T{<}T_{\mathrm{M}}$ **and** $\phi{>}\phi^{\mathrm{off}}$) (and thus ($\Delta T{>}0$ **and** $\Delta\phi{<}0$) $\Rightarrow$ freezing) **then**
  if $|\frac{\mathcal{T}}{[\phi]}\Delta T|{\leq}|\Delta\phi|$ **then**
    $\delta T{=}\Delta T{>}0$ (temperature increase due to latent heat release)
    $\delta\phi{=}-\frac{\mathcal{T}}{[\phi]}\Delta T{<}0$ (porosity decrease due to freezing)
  else
    $\delta T{=}-\frac{[\phi]}{\mathcal{T}}\Delta\phi{>}0$ (temperature increase due to latent heat release)
    $\delta\phi{=}\Delta\phi{<}0$ (porosity decrease due to freezing)
  end if
end if
Compute the new temperature $T^*{=}T{+}\delta T$.
Compute the new porosity $\phi^*{=}\phi{+}\delta\phi$.
Compute the melting rate $r_{\mathrm{f}}{=}\frac{\delta\phi}{\Delta t}$.

within the ice. During this process it can refreeze if advected to regions with lower than melting temperature, leading to local warming due to released latent heat. Whether melting/freezing occurs depends on the local values of temperature and porosity. The numerical implementation of this process is decribed in Algorithm 3 which for known values of porosity ϕ and temperature T returns the corrected values ϕ^* and T^* and the corresponding melting rate r_{f} (cf. also Algorithm 2).

Part III

Parametric studies in temperate ice shells

5. Water transport in temperate planetary ice shells by two-phase flow - a 1d parametric study

In this section we perform a series of numerical experiments in order to assess the importance of the physical parameters in the system of governing equations (3.136)[1]. We focus on the effects of ice permeability, ice rheology, heating, surface tension and the dimensionless parameter $\mathscr{C}$ (related to the so-called compaction length, cf. discussion in Section 3.4.4).

The main reason to investigate these effects is that some of the assumptions commonly used in the majority of multi-phase models, like the assumption of constant viscosity of the constituents, is probably invalid when dealing with complex materials such as ice. Expecting that the two-phase gravity driven transport exhibits formation of nonlinear wave trains (e.g. *Scott & Stevenson*, 1984; *Scott et al.*, 1986; *Olson & Christensen*, 1986; *Spiegelman*, 1993a), large local space-temporal variations of porosity would occur in the ice matrix. Since ice viscosity is highly sensitive to the amount of interstitial fluids present (*Duval*, 1977; *De La Chapelle et al.*, 1999), such porosity variations would inevitably induce significant viscosity variations, the role of which we would like to estimate. Additional interaction mechanism, often neglected in applications, is the effect of surface tension, which cannot be ruled out a priori in our setting (cf. discussion in Section 3.4.3). We will study the sensitivity of the water transport to its various parameterizations.

In all experiments, we consider the same initial condition for porosity ϕ as in the numerical tests in Section 4.2.2 (eq. 4.70). This form of the initial condition does not have any particular physical significance, the analytical profile (cf. the black line in panel a of Figure 5.1) merely mimics a possible initial meltwater distribution with a maximum at shallow depth (cca 2.5 km). We investigate the gravity-driven propagation of this initial subsurface meltwater reservoir through the temperate ice layer. In the sections below, we use the reference values of material parameters from Tables 1.1 and 3.1 if not specified otherwise.

5.1 Reference simulation

We start with a brief description of a reference solution computed for $\phi^{\text{off}}=0$ on which we illustrate the basic characteristics in which we will be interested throughout this chapter. The time evolution of porosity profiles is depicted in Figure 5.1. Apparently, porosity is transported downwards in the form of successive waves (wave train) formed due to the coupling between the fluid motion and the matrix deformation. Their wavelength is governed by the values of ice viscosity μ_{m} and permeability $k(\phi)$ - the higher the value of μ_{m} and/or $k(\phi)$, the larger the compaction length (eq. 4.38), and thus the larger the wavelength of the waves (*Rabinowicz et al.*, 2002). This effect will be well illustrated in Sections 5.2

[1]The results summarized in this chapter were published in *Souček et al.* (2014).

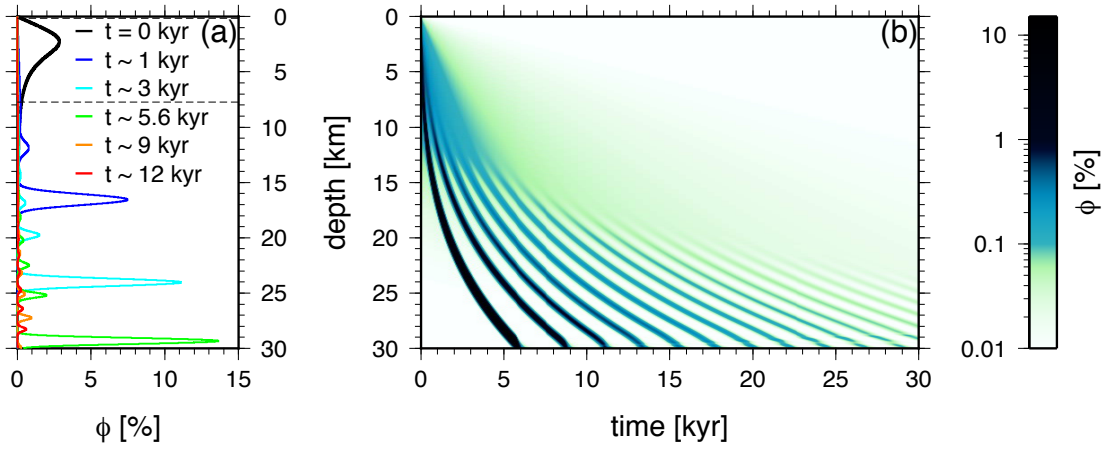

Figure 5.1: (a) Evolution of porosity in selected time instants (colored lines) obtained for parameters from Table 3.1. The initial porosity profile is plotted in black. Dashed line marks the border of the subsurface region. (b) Space-time evolution of porosity in a partially molten ice layer for the same set of parameters.

and 5.3 that investigate the role of ice permeability and ice viscosity, respectively.

The total amount of water in the ice shell (water column height, i.e. porosity integrated throughout the domain) drops each time a wave reaches the bottom boundary (cf. Figure 5.2, panel a). The first porosity wave that contains about 75% of the total water volume arrives at the bottom approximately 6 kyr after the beginning of the simulation. After only 15 kyr, less than 10% of the initial water content remains in the ice shell. As indicated in the panel b of Figure 5.2, the maximum porosity in the subsurface region (uppermost 8 km) rapidly decays due to the efficient downward propagation of the porosity waves. The maximum porosity in this region drops below 1% after only ∼250 years, indicating that for this choice of material parameters, a large volume of water is not sustainable inside a fully temperate region.

The time needed to extract $1/e$ of the initial amount of water from the layer of

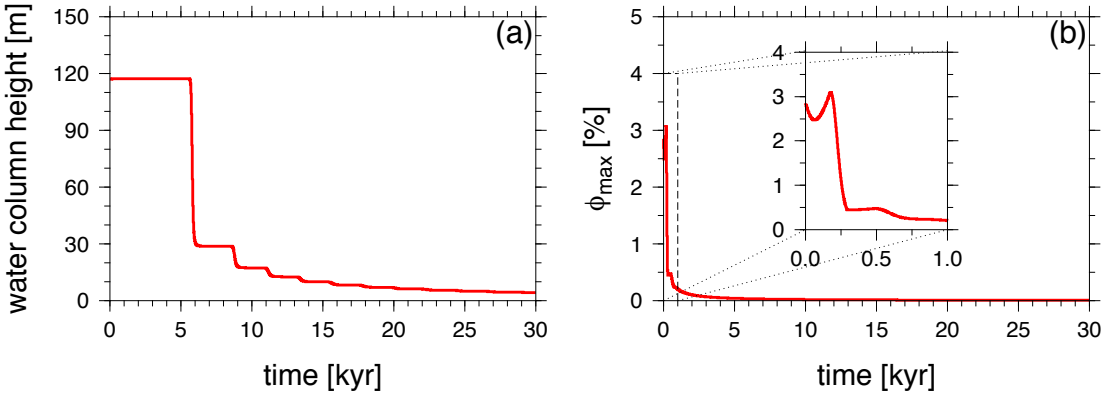

Figure 5.2: (a) Time evolution of water column height (porosity integrated throughout the domain). (b) Time evolution of maximum porosity in the subsurface region (top 8 km). Computed for the same set of parameters as Figure 5.1.

thickness D can be estimated using the compaction time scale (*McKenzie*, 1989) [2]:

$$t_{\mathrm{D}} = \frac{D\mu_{\mathrm{f}}\phi}{k(\phi)\Delta\rho g} \ . \tag{5.1}$$

For D=30 km and porosity of the order of few tenths of percent (the average porosity at the beginning of the simulation is ∼0.39%) this formula yields extraction times of a few kiloyears, which is in good agreement with the time of 6 kyr obtained from Figure 5.2.

5.1.1 The role of background porosity

The propagation of water can be sensitive to the value of background porosity, which is parameterized here by the value of porosity offset ϕ^{off} (eq. 4.70). This value affects both permeability (eq. 2.1) and effective bulk viscosity ($\frac{\mu_{\mathrm{m}}}{\phi}$, cf. text below eq. 3.131). Figure 5.3 shows the porosity as a function of depth at four different times (with time increasing from left to right) for several values of ϕ^{off}. With decreasing value of ϕ^{off} the propagation velocity and the wavelength decrease while the wave amplitudes increase, which leads to an enhanced localization of porosity. Figure 5.4, that shows time evolution of water column height above the background value (i.e. $\int_V(\phi-\phi^{\mathrm{off}})\mathrm{d}V$), illustrates a dependence of the time evolution of water column height on the background porosity. Only a slight change of ϕ^{off} from 0 to 0.005% changes the travel time of the leading wave by more than 1 kyr (this effect is larger than that induced by a change of viscosity from 10^{12} to 10^{14} Pa s, as will be shown in Section 5.3). However, the difference in travel times decreases with the increasing value of ϕ^{off} indicating that once some non-zero value is considered (which is necessary for numerical reasons), its

[2] Let us note that this definition fits the time scale used in our scaling analysis, cf. Section 3.4.1

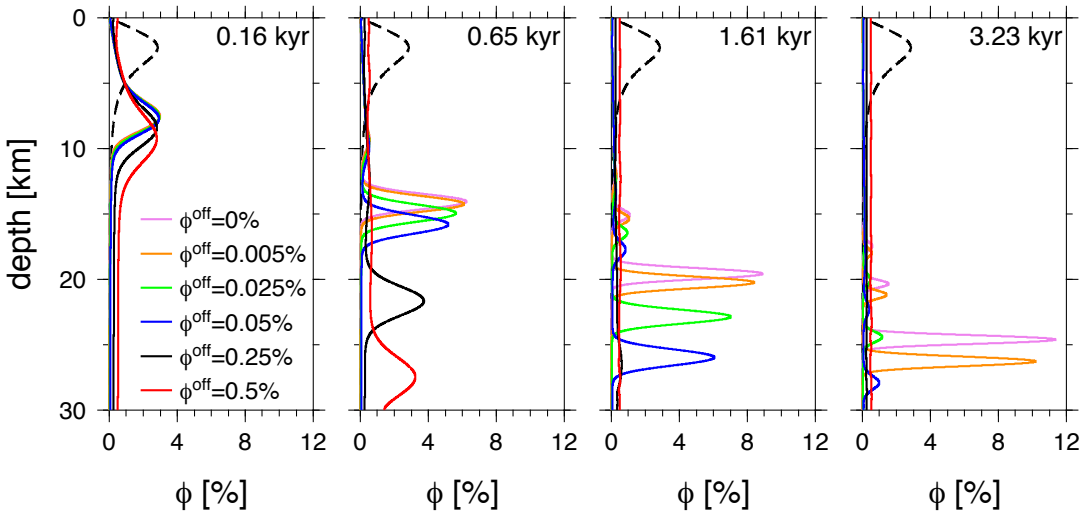

Figure 5.3: Snapshots of time evolution of porosity profiles for various values of ϕ^{off}. Time increases from left to right. In all panels, black dashed line shows the initial distribution of porosity (eq. 4.70 with ϕ^{off}=0%).

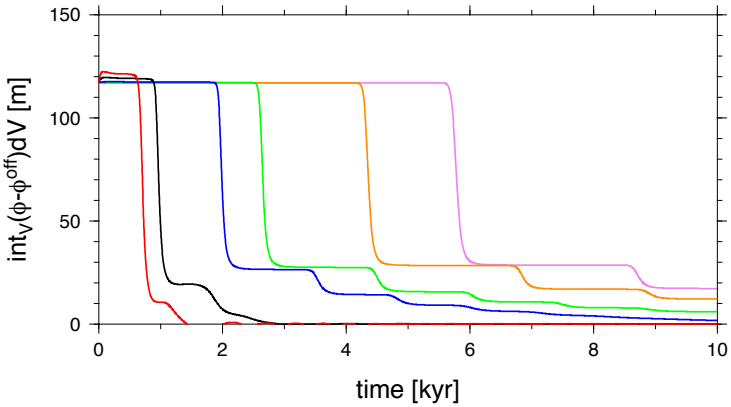

Figure 5.4: Time evolution of water column height above the background value (cf. text) for various values of ϕ^{off} (for legend, see Figure 5.3).

magnitude does not have a large impact on the results (especially when compared with the effect of permeability described in the next section). These observations are in agreement with the notion of the compaction time scale (eq. 5.1) which due to permeability definition (eq. 2.1) depends on the absolute value of porosity as ϕ^{1-n} with $n \geq 2$, and thus decreases for larger values of ϕ and vice versa.

5.2 The role of permeability

In this section, we investigate the role of permeability $k(\phi)$, i.e. the ability of a material to transmit fluids. The formula for the drag coefficient (eq. 3.117) reveals the crucial role of permeability on the speed of propagation of the liquid phase through the ice matrix. As mentioned earlier in Section 3.3, ice permeability depends on several parameters. In order to illustrate the role of permeability, we test various combinations of the permeability constant k_0 and exponent n (cf. eq. 2.1) in the following Section 5.2.1 and the effect of percolation threshold ϕ_c is discussed later in Section 5.2.2.

5.2.1 The role of permeability constant and exponent

We vary the permeability constant k_0 over two orders of magnitude (10^{-10}–10^{-8} m^2) and test also both end-member values of the permeability exponent (n=2 and 3). The results are depicted (for ϕ^{off}=0.25%) in Figures 5.5 and 5.6 and indicate that the wave train propagation speed is largely controlled by the value of permeability and, for given n, depends approximately linearly on k_0 (in agreement with eq. 5.1). Note, that also the wavelength of the waves increases with increasing value of k_0 in accord with eq. (4.38).

Using a larger value of the permeability exponent (n=3, green lines in Figures 5.5 and 5.6) causes reduction of the permeability. Since the porosity in our experiment is of the order of a few percent, the wavelength of the porosity waves decreases approximately ten times in comparison with the case where n=2 (to be compared with the red line in Figure 5.5). The effect on the speed of propagation is significant (decreasing it approximately by two orders of magnitude)

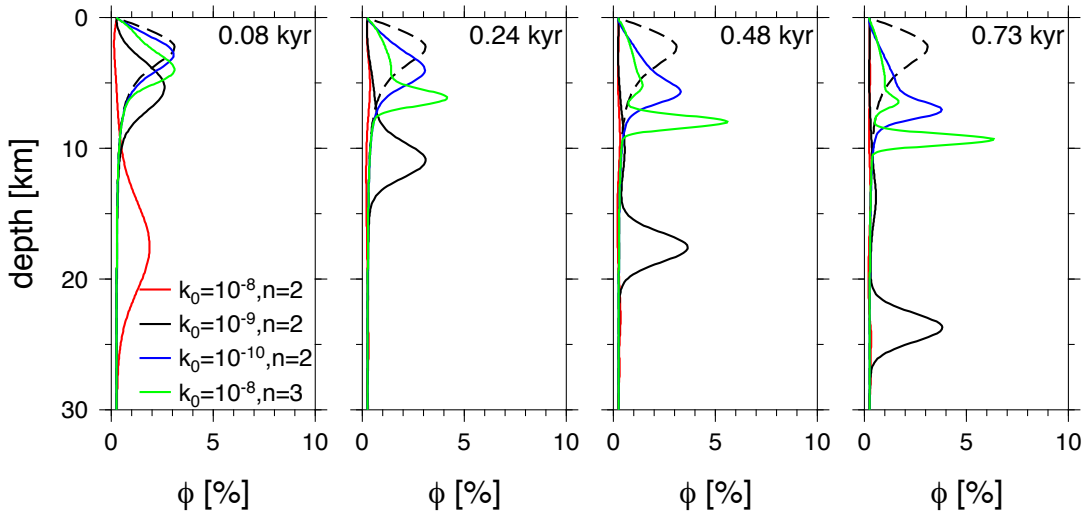

Figure 5.5: The same as in Figure 5.3 but for various combinations of permeability constant k_0 and exponent n (ϕ^{off}=0.25%).

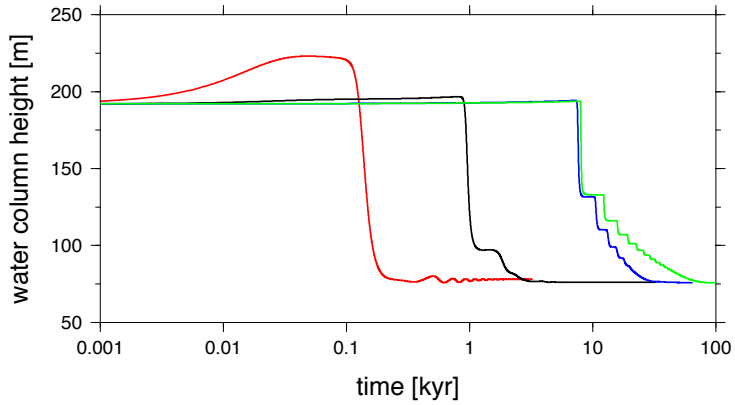

Figure 5.6: Time evolution of water column height for various combinations of permeability constant k_0 and exponent n (for legend, see Figure 5.5). The time scale is logarithmic.

and becomes even more pronounced for small porosities after the outflow starts (Figure 5.6).

5.2.2 The role of percolation threshold

In Figures 5.7 and 5.8, we show the results of simulations where the values of the percolation threshold ϕ_c (eq. 2.2) are varied. Again, the former figure displays porosity as a function of depth at four time instants, while the latter shows the time evolution of the water column height. Depending on the difference between ϕ_c and offset ϕ^{off} we can obtain three basic evolution scenarios.

If the percolation threshold is chosen larger than the maximum value of the initial porosity profile (ϕ_c=5%), the permeability is significantly reduced (cf. eq. 2.2) and water propagation is effectively stopped. The porosity wave (orange lines in Figure 5.7) still evolves but its downward propagation is by several orders of

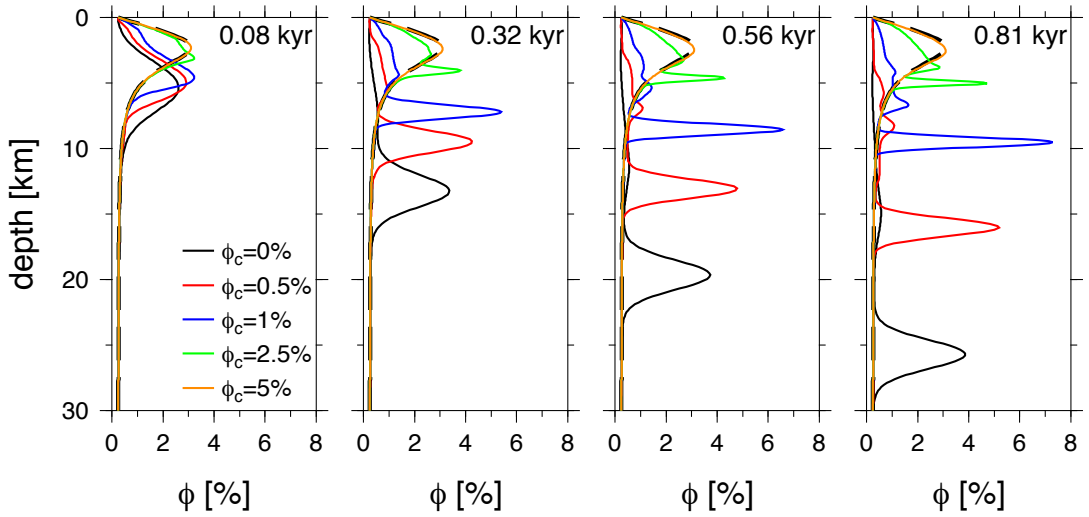

Figure 5.7: The same as in Figure 5.3 but for various values of percolation threshold ϕ_c.

magnitude slower than in the simulation without percolation threshold. Consequently, the overall water volume in the domain remains approximately constant during the whole simulation (Figure 5.8).

If the percolation threshold is chosen so that its value is smaller than the initial porosity, but only locally (ϕ_c=2.5%), the porosity waves evolve with a considerably reduced velocity (green lines in Figure 5.7). The overall water volume in the domain remains again approximately constant during the whole 30-kyr simulation (Figure 5.8), as no water is extracted during this time.

Finally, if the percolation threshold is chosen so that a significant part of the initial porosity profile exceeds its value (ϕ_c=0.5% and 1%), the downward propagation of porosity waves is enhanced when compared with the above cases (red and blue lines in Figure 5.7). However, the waves still propagate more slowly than in the case with ϕ_c=0% (black full lines in Figure 5.7) due to the decrease of permeability corresponding to the term $(\phi-\phi_c)^2$ in eq. (2.2). The outflow of

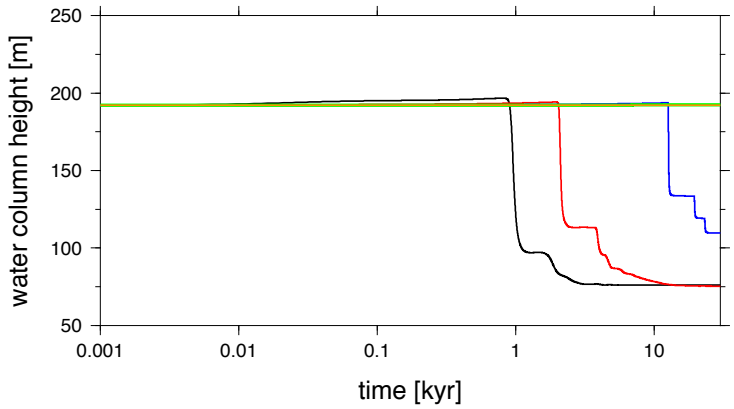

Figure 5.8: The same as in Figure 5.6 but for various values of percolation threshold ϕ_c (for legend, see Figure 5.7). The time scale is logarithmic.

water from the domain (Figure 5.8) starts already during the time period of 30 kyr considered for the simulation. Obviously, if our simulations spanned a longer period of time, the first waves would arrive at the bottom boundary even in the cases with larger percolation thresholds. However, their arrival times would be much larger than 100 kyr. Further inspection of Figure 5.7 reveals again a decrease in the wavelength with the increasing value of ϕ_c corresponding to the decrease of permeability.

5.3 The role of ice rheology

As already discussed in Section 1.6.1, ice viscosity is a highly nonlinear function of temperature, grain size and stress, with at least four known deformation mechanisms (*Goldsby & Kohlstedt*, 2001; *Durham et al.*, 2001). Moreover, the presence of meltwater within the ice matrix drastically reduces its viscosity (*De La Chapelle et al.*, 1999). The role of composite ice rheology has been widely investigated in the models of solid-state convection (e.g. *Barr et al.*, 2004; *Barr & Pappalardo*, 2005; *Moore*, 2006; *Freeman et al.*, 2006; *Barr & McKinnon*, 2007; *Běhounková et al.*, 2013), however, none of these studies considered the transport of liquid water through the convecting ice shell. We first address the role of composite ice rheology involving four deformation mechanisms (Section 5.3.1). We discuss its possible simplification for a particular grain-size and stress regime, leading to a temperature-dependent parameterization of ice viscosity, an approximation which might be convenient in the numerical simulations (Section 5.3.2). In Section 5.3.3, we investigate the effect of porosity weakening of viscosity due to lubrication. Finally, in Section 5.3.4, we study the complex rheology which combines all these effects.

5.3.1 The role of composite ice rheology

We simulate water transport for ice viscosity given by eqs (1.1) and (1.2) and compare the results with several constant-viscosity cases. We consider ϕ^{off}=0.25% and three values of the grain size d. Figure 5.9 shows porosity (top) and viscosity (bottom) as a function of depth at four different time instants. For the smallest value of grain size (d=0.1 mm), the viscosity (orange lines in Figure 5.9, bottom) ranges between 2×10^{12} and 4×10^{12} Pa s. The velocity of porosity waves can in this case be estimated from below and above by constant-viscosity cases with 10^{12} Pa s and 10^{13} Pa s, respectively (cf. orange, pink and red lines in Figure 5.9, top). The time evolution of water column height (Figure 5.10) shows similar behavior, with the transport velocity confined between the appropriate constant-viscosity cases. For the middle value of grain size (d=1 mm), the viscosity ranges between 10^{14} and 4×10^{15} Pa s (Figure 5.9, bottom) and the time evolution of porosity and water column height can be both estimated by the constant-viscosity cases with 10^{14} and 10^{15} Pa s. For d=10 mm, the viscosity ranges between 10^{15} and 2×10^{16} Pa s, and water transport can be approximated by the constant-viscosity cases with 10^{15} and 5×10^{15} Pa s. Note that the value of viscosity influences the wavelength of the porosity waves in a similar manner as permeability - the smaller the viscosity, the shorter the wavelength (cf. compaction length in Section 5.2.1). According to equation (5.1), the time needed to extract a substantial amount of

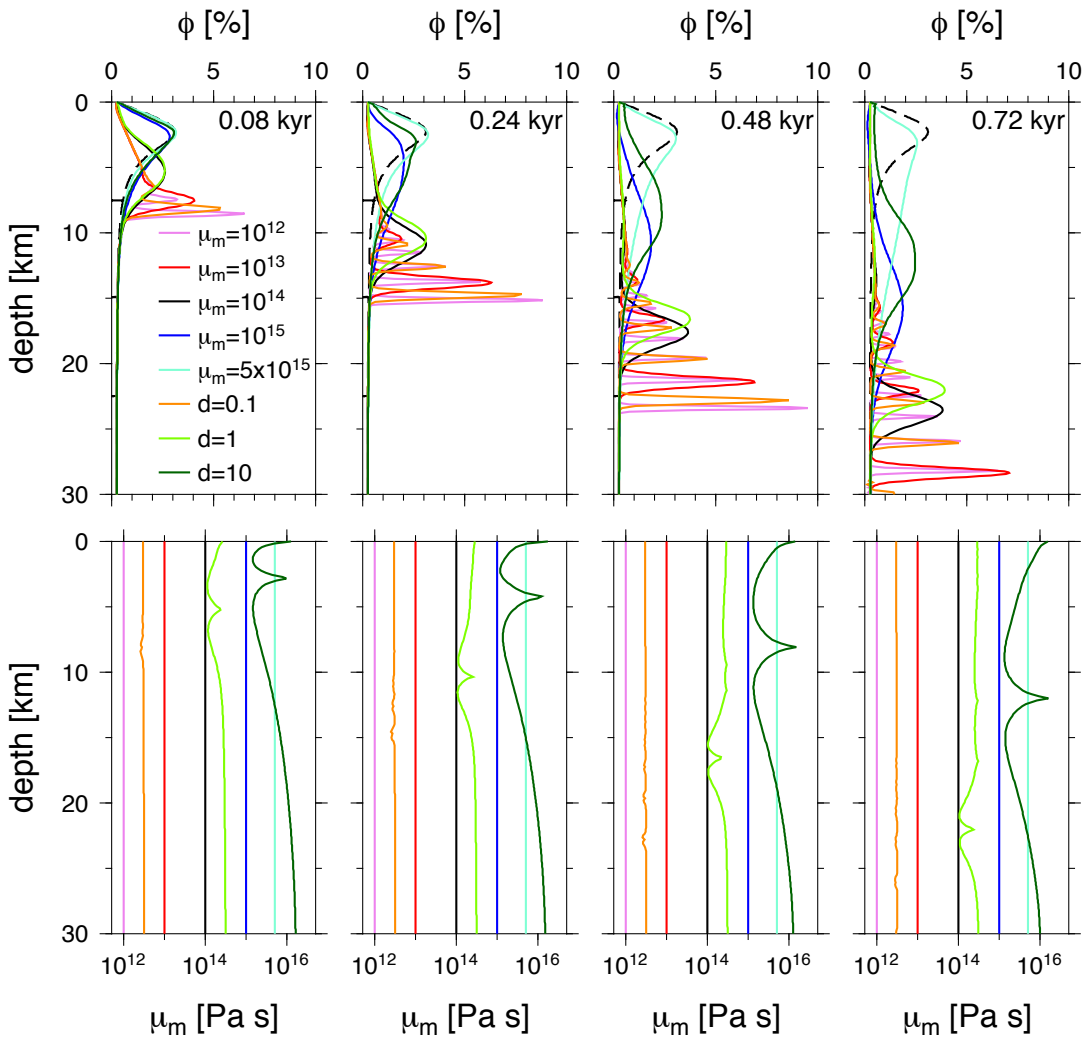

Figure 5.9: *Top*: The same as in Figure 5.3 but for different viscosity laws (constant vs. composite). *Bottom*: Viscosity corresponding to porosity profiles in the top line.

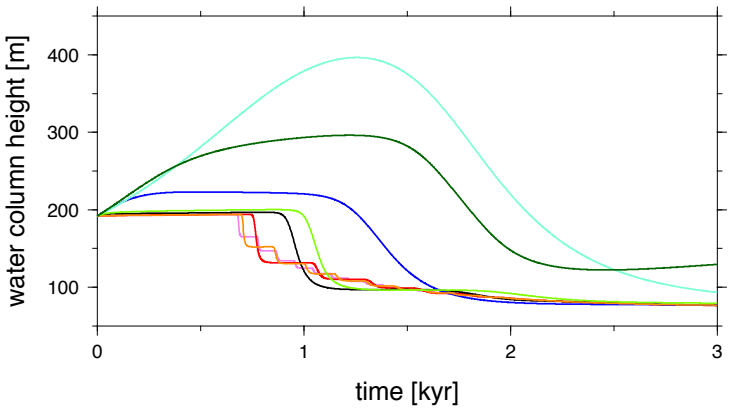

Figure 5.10: The same as in Figure 5.6 but for different viscosity laws (constant vs. composite, for legend, see Figure 5.9).

water from the temperate ice layer does not depend on the ice viscosity which is in agreement with these results.

Comparing the viscosities of particular deformation mechanisms, we find that for small grain sizes (d=0.1 mm), the dominant mechanism is the stress-independent diffusion creep. For d=1 and 10 mm, the ice matrix deforms also by grain-boundary sliding, which, due to its stress dependence, dominates in the vicinity of the porosity peak.

5.3.2 The role of temperature

In certain applications, it might be suitable to neglect the stress and grain-size dependence of composite ice viscosity and to keep only the temperature dependence. To estimate the role of temperature dependence of viscosity on the water transport, we compare the results obtained using a simplified viscosity law (eq. 1.3) with the constant-viscosity simulations. The results obtained for two different values of activation energy are illustrated in Figures 5.11 and 5.12. We observe that for both variable-viscosity cases the qualitative behavior closely resembles the constant-viscosity solutions, due to the relatively mild depth-dependence of temperature. In the case with and without premelting, the speed of porosity waves propagation can be estimated by the constant-viscosity solutions with viscosity ranging from 10^{12} to 10^{13} Pa s and from 10^{14} to 10^{15} Pa s, respectively. The same holds approximately for the time evolution of water column height (Figure 5.12).

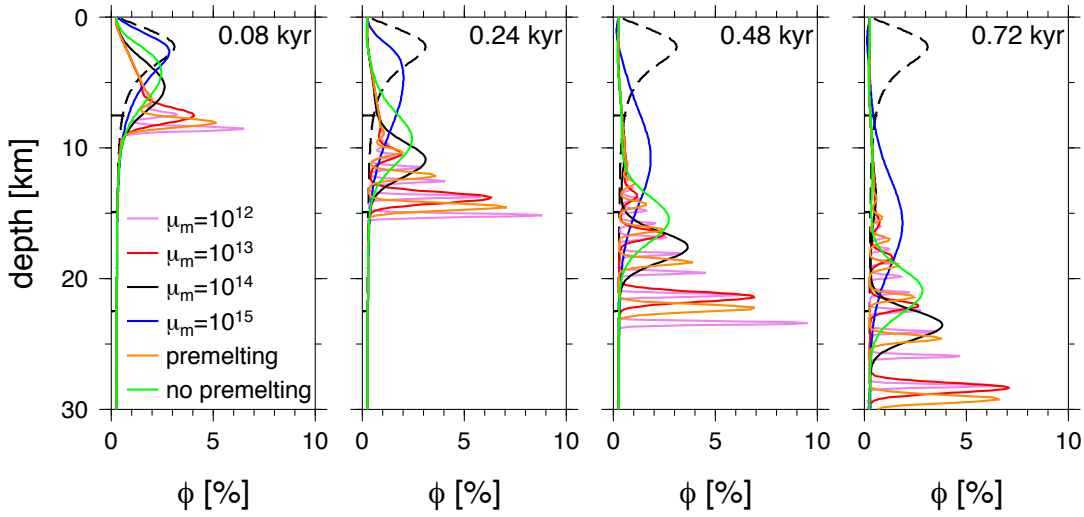

Figure 5.11: The same as in Figure 5.3 but for different viscosity laws (constant vs. temperature-dependent).

5.3.3 The role of porosity weakening

The presence of meltwater is expected to significantly affect the ice viscosity even at small volumes. To assess the significance of this effect, we compare the results obtained using eq. (1.5) with $\mu_{\mathrm{m}}^{\mathrm{pure}}$=$10^{14}$ Pa s and three different values of the weakening parameter (γ_{m}=15, 30 and 45), with the results obtained for

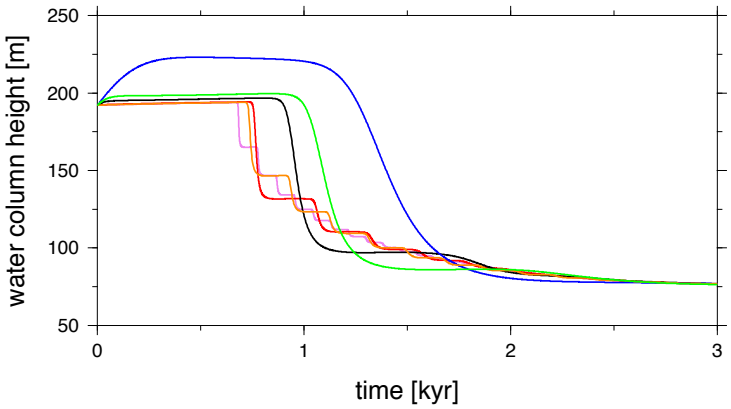

Figure 5.12: The same as in Figure 5.6 but for different viscosity laws (constant vs. temperature-dependent, for legend, see Figure 5.11).

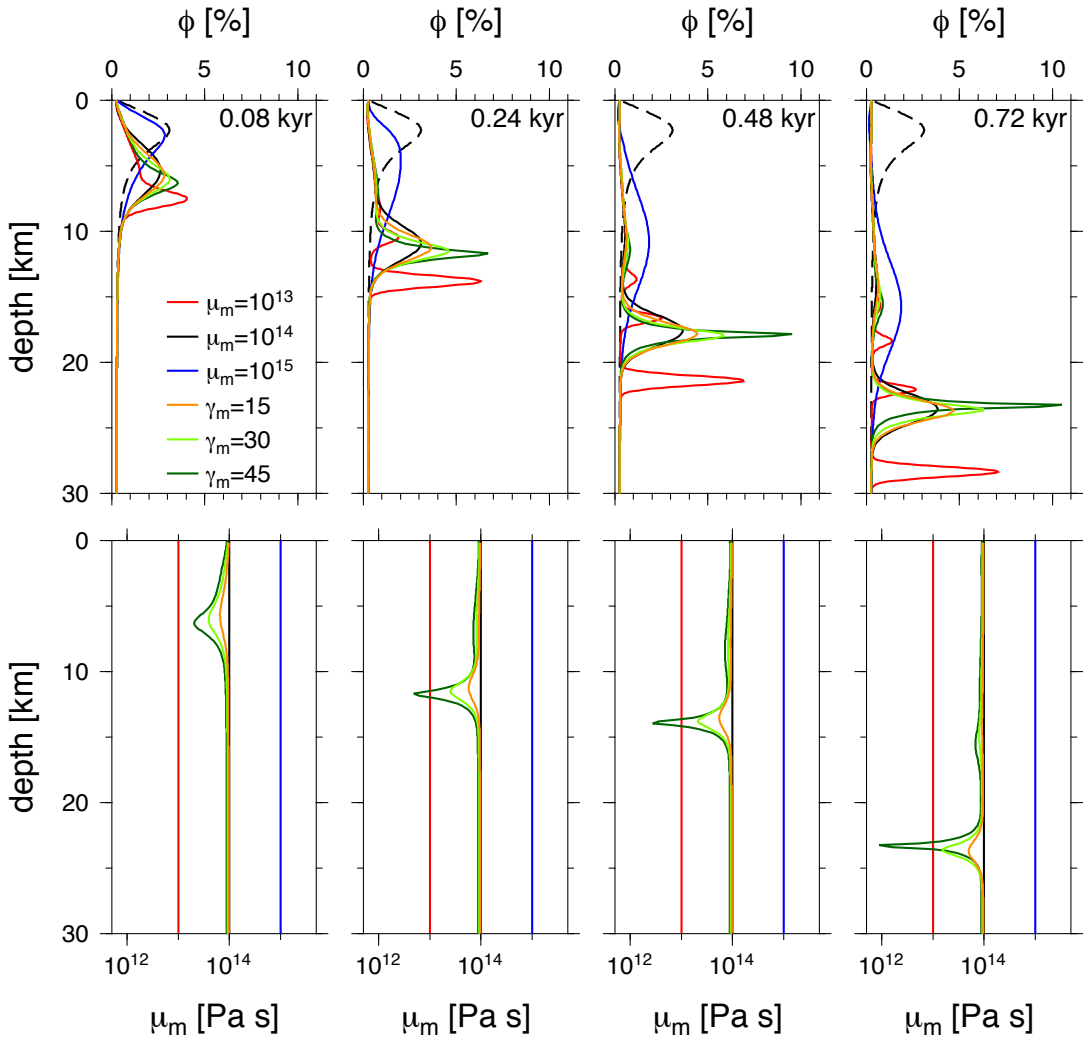

Figure 5.13: *Top*: The same as in Figure 5.3 but for different viscosity laws (constant vs. porosity-dependent). *Bottom*: Viscosity corresponding to porosity profiles in the top line.

different constant viscosities (Figures 5.13–5.14). We can see that the leading wave propagates in all the three cases approximately with the same velocity as for the constant-viscosity case with 10^{14} Pa s (Figure 5.13, top). The amplitude of the leading wave increases with γ_{m} due to the localizing effect of viscosity reduction. Even though locally the viscosity decreases by as much as two orders of magnitude for $\gamma_{\mathrm{m}} = 45$ (Figure 5.13, bottom), the overall water transport appears to be determined by the average viscosity in the layer below the wave and is thus (for all values of γ_{m} used) comparable with the constant-viscosity case with 10^{14} Pa s (Figure 5.14).

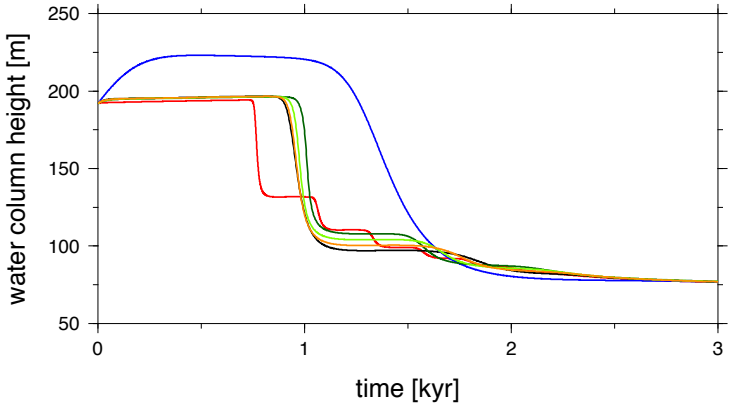

Figure 5.14: The same as in Figure 5.6 but for different viscosity laws (constant vs. porosity-dependent, for legend, see Figure 5.13).

5.3.4 Parameterization of the complex ice rheology

The results of the previous sections indicate that parameterization of ice rheology by a constant viscosity of some appropriate value may be sufficient, especially when we are concerned with the global characteristics of the water transport. So far, we have studied the influence of individual rheological parameters separately. In this section, we compare the results for constant-viscosity simulations with a fully general case, where the ice viscosity is described by eqs (1.1), (1.2) and (1.5). This rheology combines the composite flow law (Section 5.3.1) with the porosity weakening effect (Section 5.3.3) and can be considered as a realistic approximation of the mechanical properties of ice in the studied context.

In Figures 5.15–5.16, we show the results for two grain sizes (d=1 and 10 mm) and three values of the porosity weakening exponent (γ_m=15, 30 and 45). For both grain sizes, the porosity profiles for the complex-rheology simulations are significantly more localized compared to the constant-viscosity cases, mainly due to porosity weakening (cf. Section 5.3.3). For d=1 mm, the corresponding viscosity decreases down to $\sim 10^{12}$ Pa s, but only in the close vicinity of the porosity peak. In the rest of the ice shell, viscosity is almost constant with a value of 2–4×10^{14} Pa s. For grain size d=10 mm, the values of viscosity are approximately by two orders of magnitude larger and the propagation is accordingly slower. The results suggest that the water transport velocity and the evolution of the water column height in our simulation with the complex ice rheology can be reasonably well parameterized by constant viscosities from the range of 10^{14}–5×10^{15} Pa s.

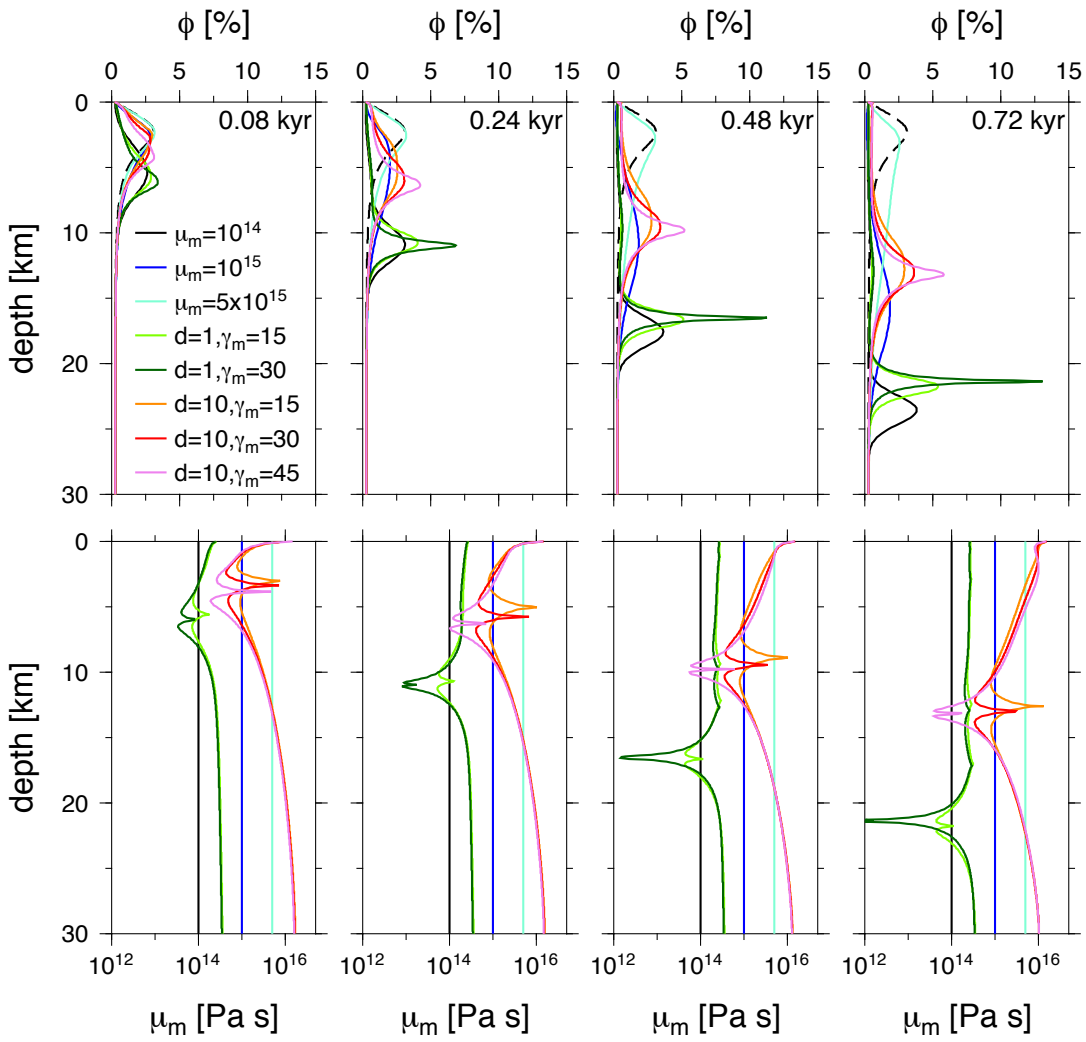

Figure 5.15: *Top*: The same as in Figure 5.3 but for different viscosity laws (constant vs. complex). *Bottom*: Viscosity corresponding to porosity profiles in the top line.

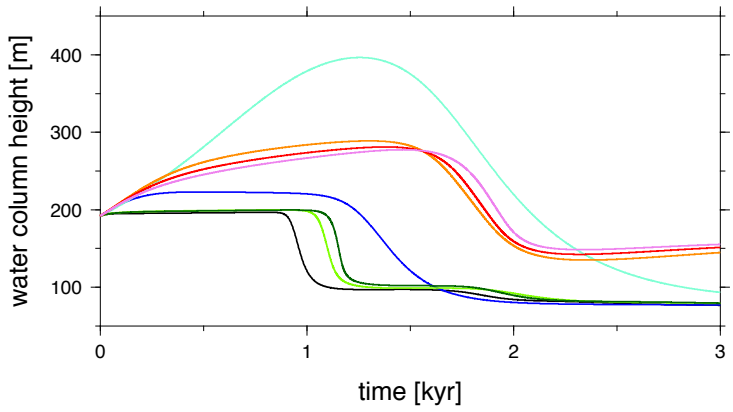

Figure 5.16: The same as in Figure 5.6 but for different viscosity laws (constant vs. complex, for legend, see Figure 5.15).

5.4 The role of heating

As mentioned earlier in Chapter 1, tidal forces due to Europa's eccentric orbit around Jupiter play a significant role in its thermal-orbital evolution. The associated tidal deflection results in elevated heating, mostly located in the warm convective part of the ice shell and locally also along tectonic faults in the upper part of the ice shell. To investigate the effect of heating on the transport processes within a temperate ice shell, we prescribe a constant volumetric heating H_t=2×10^{-6} W m^{-3} (cf. left panel of Figure 1.11) in the whole shell and/or a constant shear heating H_s=10^{-4} W m^{-3} in the uppermost layer of thickness h_s=3 km (cf. right panel of Figure 1.11). Figures 5.17–5.18 display the results of these simulations (for ϕ^{off}=0%). The volumetric heating of 2×10^{-6} W m^{-3} (red color) reduces the time needed for the first wave to arrive at the bottom more than twice (2.5 kyr instead of 6 kyr for the case with no melting, cf. black line). This is again in agreement with the compaction time scale (eq. 5.1) as the melting in the

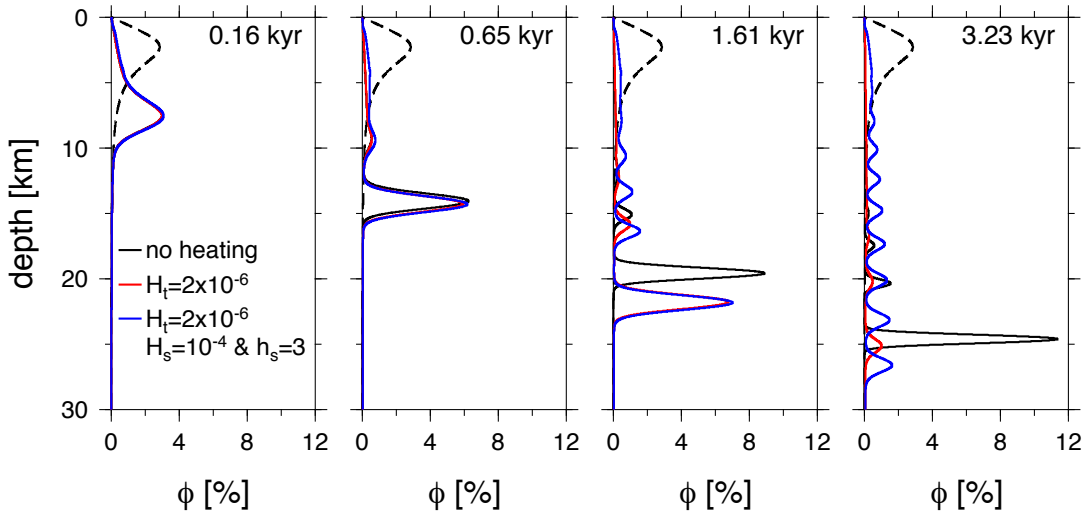

Figure 5.17: The same as in Figure 5.3 but for various heating scenarios (see text).

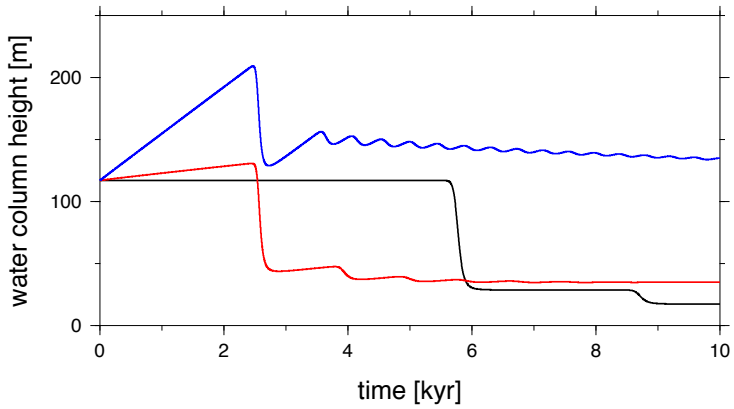

Figure 5.18: The same as in Figure 5.6 but for various heating scenarios (for legend, see Figure 5.17).

whole volume increases porosity and thus reduces the porosity wave travel time. Adding a localized source of heat imposed in the uppermost 3 km influences the overall amount of molten water in the ice shell (cf. Figure 5.18) but has negligible effect on the porosity wave travel time since it increases porosity only above the propagating waves and thus cannot influence the underlying permeability value that is crucial for the propagation velocity.

5.5 The role of surface tension

A possibly non-negligible role of surface tension in water transport dynamics cannot be ruled out a priori based on the scaling analysis (cf. eq. 3.131 and parameter $\mathcal{S}$ in 3.127). To assess its importance, we performed a series of simulations, where surface tension was included and parameterized by eq. (3.110). We varied the parameters describing the interfacial area density (pore geometry), namely the constant α_0 and the exponents a, b (eq. 3.115). Since the former is inversely proportional to the characteristic grain size (*Bercovici et al.*, 2001), we take $\alpha_0{=}1/d$ for two values of the grain size (d=1 and 10 mm). The exponents a and b must satisfy $0{<}a, b{<}1$; moreover in a medium where the melt is interconnected even at low porosities, $a{\ll}b$ holds (*Bercovici et al.*, 2001). We have tested several combinations of parameters a and b and in all simulations the effect of inclusion of the surface tension was found to be completely negligible.

5.6 The role of compaction length

Here, we discuss the role of compaction length expressed in our formulation by a dimensionless parameter $\mathscr{C}$. This parameter describes the strength of the dynamic coupling between the fluid flow and the matrix deformation. In particular, we investigate the case when this coupling is completely neglected ($\mathscr{C}{=}0$ in eq. 3.136d), leading to the so-called *zero compaction length approximation* (cf. *Scott & Stevenson*, 1989; *Spiegelman*, 1993a,b).

In Figure 5.19, the evolution of porosity for a non-zero $\mathscr{C}$ case is compared with the zero compaction length solution ($\mathscr{C}{=}0$). In contrast to the non-zero $\mathscr{C}$ solution, where a wave train evolves, for $\mathscr{C}{=}0$ a single porosity shock develops. Due to the reduction of the mechanical coupling between the phases, the propagation of the shock is significantly faster than that of the wave train. The peak porosities differ also significantly - while for $\mathscr{C}{=}0$ the porosity never exceeds the maximum initial value ($\sim$3%), in the non-zero $\mathscr{C}$ case the amplitude of the wave train gradually grows up to 10% before the outflow initiates. The time evolution of the water column height in the domain is shown in Figure 5.20 - the two solutions differ mainly in the time of the onset of outflow, which is delayed (by almost 5 kyr) in the non-zero $\mathscr{C}$ case due to a lower propagation speed. With decreasing amount of water in the domain, the two solutions gradually converge.

Let us investigate the behavior of the non-zero $\mathscr{C}$ solution in limit $\mathscr{C}{\to}0$ in order to establish a connection between the two regimes. We repeat the above simulation with decreasing values of $\mathscr{C}$, keeping all the other parameters fixed. Figure 5.21 (top) shows the evolution of the initial porosity profile (eq. 4.70) for five values of the parameter $\mathscr{C}^i{=}10^{-i}\mathscr{C}$, $i{=}0, 1, 2, 3, 4$, and for $\mathscr{C}{=}0$. We observe

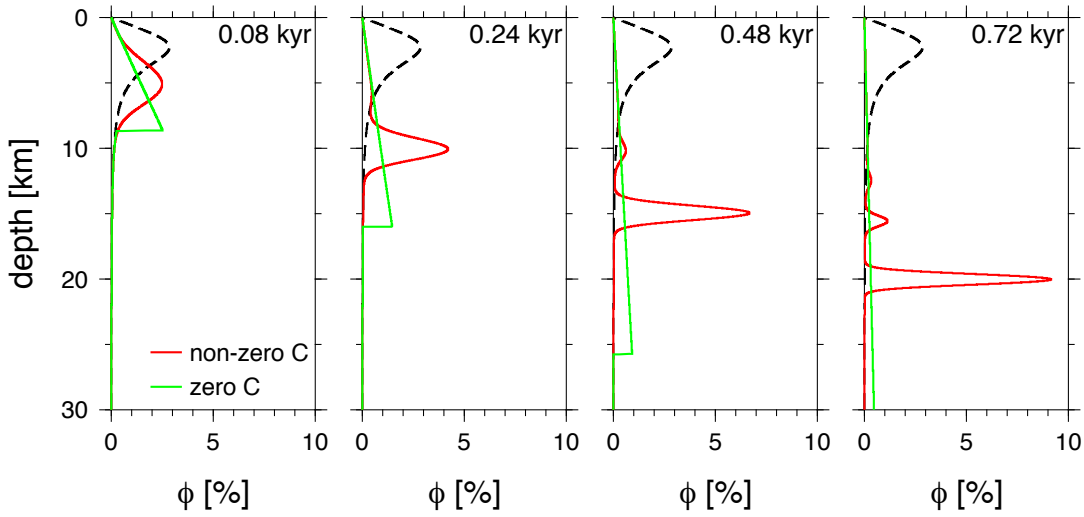

Figure 5.19: The same as in Figure 5.3 but for the non-zero and zero $\mathscr{C}$ setting. The dashed line corresponds to ϕ^{off}=0%.

that with the gradually decreasing value of $\mathscr{C}^i$, the corresponding porosity profiles ϕ^i exhibit enhanced oscillations with shorter wavelength, while the time lag between the front wave and the position of the shock in the zero $\mathscr{C}$ solution decreases. This allows us to speculate that the zero $\mathscr{C}$ solution possibly corresponds to the weak limit (in the sense of distributions) of the non-zero $\mathscr{C}$ model. This idea seems to be supported by the numerical evaluation of the running-window averages by convolution

$$(\phi^i * \varphi_\varepsilon)(z,t) = \int_{-\infty}^{\infty} \phi_e^i(y,t)\varphi_\varepsilon(z-y)\,dy\ , \tag{5.2}$$

where ϕ_e^i is an extension of ϕ^i by zero outside the interval $\langle 0,1\rangle$, and φ_ε is the mollifier

$$\varphi_\varepsilon(x) = \begin{cases} \frac{K}{\varepsilon}\exp\left(-\frac{1}{1-\left|\frac{x}{\varepsilon}\right|^2}\right) & |x|<\varepsilon \\ 0 & |x|\geq\varepsilon \end{cases}\ , \tag{5.3}$$

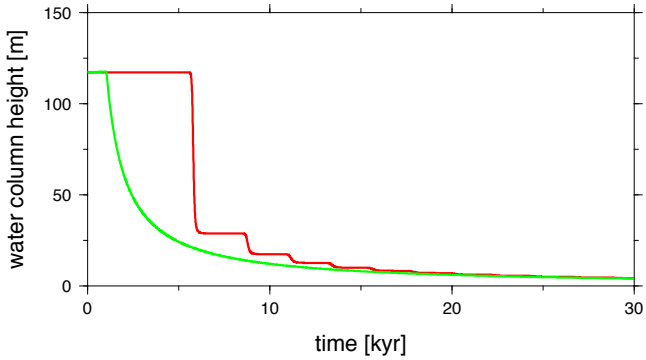

Figure 5.20: The same as in Figure 5.6 but for the non-zero and zero $\mathscr{C}$ setting (for legend, see Figure 5.19).

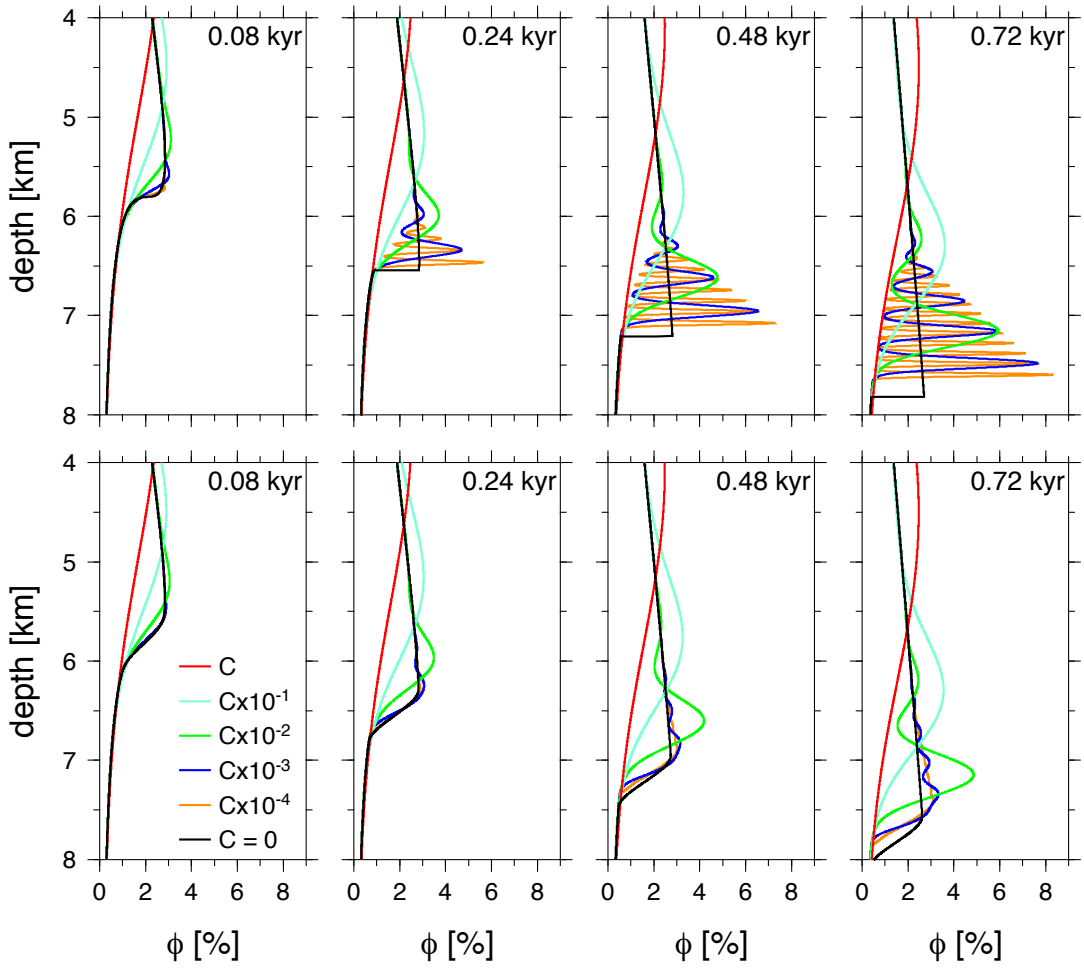

Figure 5.21: *Top*: The same as in Figure 5.3 but for the non-zero $\mathscr{C}^i$ and zero $\mathscr{C}$ setting. Only vicinity of the shock is depicted. *Bottom*: All quantities mollified by convolution with the kernel given by eq. (5.3).

with $\varepsilon=\frac{1}{100}$ and the normalization factor $K=(\int_{-1}^{1}\exp(-\frac{1}{1-|x|^2})\,dx)^{-1}$. The weak convergence of $\mathscr{C}^i$ solutions to the shock solution ($\mathscr{C}=0$) for $i\to\infty$ would imply point-wise convergence of their convolutions with φ_ε, which seems to be supported by the numerical simulation (Figure 5.21, bottom). We are however unable to present a rigorous proof of this statement and leave it as a mere hypothesis.

5.7 Summary

Our numerical experiments confirm the major impact of the ice permeability on the time scale of water propagation and the wavelength of porosity waves. While the propagation velocity depends on permeability approximately linearly, the wavelength scales with its square root. The value and functional form of permeability thus strongly influence the flow pattern on both local and global scale.

In order to assess the role of ice rheology in water transport, we compare the results obtained for constant viscosity with those computed for viscosity parameterizations based on experimental and theoretical data. We find that the ice

rheology mainly influences the water flow on a local scale. The most important effect is the strong viscosity reduction due to porosity weakening, which enhances localization of waves and leads to a significant increase of peak porosity values. The inclusion of deformation mechanisms and temperature dependence has only moderate and minor effect, respectively. Although the ice rheology affects the flow pattern on a local scale, the global scale transport properties, such as the characteristic time of propagation and the total meltwater volume, can be reasonably well reproduced by a constant viscosity model.

The addition of volumetric heating as well as the increasing value of background porosity ϕ^{off} decrease the wave train propagation time. Heating source locallized above the initial porosity maximum increases the total amount of water in the ice shell but plays negligible role in the transport process. Concerning the effect of surface tension, we have numerically confirmed that it is negligible in the context of our physical setting.

We have also investigated the role of the dimensionless parameter $\mathscr{C}$, which defines the strength of mechanical coupling between the phases and is related to the so-called compaction length. In particular, we numerically explore the relation between a zero compaction length model and the models where the coupling coefficient approaches zero. Our simulations suggest that there is only a weak correspondence (in the sense of distributions) between the two cases. The use of the zero compaction length model is thus misleading as far as the local character of the water flow is concerned while it may be appropriate for recovering the global (integral) transport properties.

6. Water transport in temperate planetary ice shells by two-phase flow - a 2d parametric study

In this section, we perform a series of numerical simulations of water transport through a temperate ice layer in two-dimensional geometry with the aim to assess the importance of some of the material parameters. At first, we test several numerical parameters, namely the SUPG regularization (cf. Section 4.2.1) coefficient τ, the mesh discretization, the element spaces used and the value of background porosity ϕ^{off} (Section 6.2). Then, taking into account the results of Chapter 5 we focus on the effects of ice permeability (Section 6.3) and ice rheology (Section 6.4), while neglecting surface tension. We consider only the non-zero $\mathscr{C}$ (non-zero compaction length) approximation since the effects of the mechanical coupling between water motion and ice deformation were found to be significant, especially at the local scale. Since the source of heating is inseparably connected with the considered geodynamical context (hot plume or strike-slip fault), we leave its investigation for Chapter 8.

6.1 Reference simulation

As in Chapter 5, we start with a brief description of the reference simulation. We consider the following initial condition:

$$\phi(x,z,0) = \frac{-10(z-1)}{1+(10(z-1))^4}\sin(\pi x) + \phi^{\text{off}} \tag{6.1}$$

(Figure 6.1, panel a) which mimics a lense of partially molten material at shallow depth and represents a possible initial meltwater distribution. After investigating the results of numerical tests in Section 4.2.2 we chose the mesh resolution of 150×150 elements with both diagonals (leading to 45 301 global vertices). The SUPG regularization parameter for this reference simulation is prescribed to τ=0.5 (this value will be varied later on) and the CFL criterion is set quite strictly as C_{CFL}=0.5. We use the values of material parameters from Table 3.1 with the exception of ice matrix viscosity - since smaller ice viscosity results in smaller wavelength (cf. Chapter 5), the characteristics of the solution are better visible for a constant viscosity value μ_{m}=10^{13} Pa s and we thus compute our reference solution with this value. The value of background porosity is chosen as ϕ^{off}=0.5% and will be again varied later on in Section 6.2.4.

Figure 6.1 shows a few snapshots of the porosity evolution - we observe a rather efficicent transport of meltwater by microscopic percolation through the temperate ice layer. While some characteristics of the flow resemble those present in the one-dimensional setting, certain new characteristics appear in two dimensions. Wave trains are formed, as in the one-dimensional experiments, due to coupling between the fluid motion and the matrix deformation with the leading wave containing the largest amount of water (panels c–h). Their wavelength is governed by ice permeability and viscosity, the role of which will be illustrated

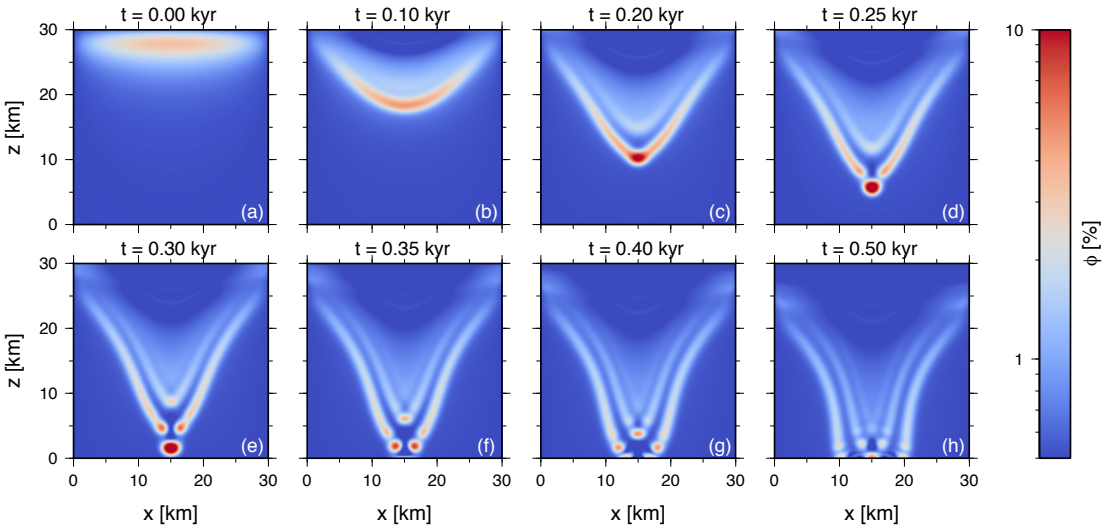

Figure 6.1: Snapshots of porosity evolution (with ϕ^{off}=0.5%) with the time increasing from left to right and from top to bottom. The initial condition (eq. 6.1) is depicted in panel a. The porosity scale is logarithmic.

later in Sections 6.3 and 6.4. Contrary to one-dimensional simulations, where only vertical motions were possible, in two dimensions water flows not only vertically but also in the inward direction leading to very strong melt localization (panel c) and even separation of a local porosity maximum (panels d and f). This is given by the porosity-dependence of both the fluid phase velocity $\boldsymbol{v}_{\text{f}}$, and the relative velocity between the two phases $\boldsymbol{v}_{\text{r}}$ (cf. eq. 3.136c) - the larger the porosity, the larger the water velocity, which eventually leads to the separation.

Snapshots of water and ice velocities, $\boldsymbol{v}_{\text{f}}$ and $\boldsymbol{v}_{\text{m}}$, respectively, corresponding to the porosity fields depicted in Figure 6.1 are shown in Figure 6.2. We observe that water is dominantly transported downwards due to its larger density with weak lateral flows (best visible in panels b1–d1) leading to localization and quickening of the transport process. The flow of ice matrix accompanies water percolation - parts of matrix that contain higher amount of water (larger porosity) descend towards the bottom boundary while the surrounding matrix material flows upwards compensating the downwelling. Let us note that even though both phases, ice and water flow downwards seemingly together in the center of the domain, the water velocities are about one order of magnitude larger than the ice velocities. The ice flow accompanying water percolation might become particularly important when deformation-dependent ice viscosity is considered (Section 6.4.1).

Time evolution of the total water content (i.e. porosity integrated throughout the domain) depicted in Figure 6.3 shows that the first porosity wave arrives at the bottom boundary ∼0.3 kyr after the start of the simulation decreasing the overall water amount by 6%. At the end of our simulation (after only 3 kyr) the total amount of water in the domain is $\sim 4.5\times10^6$ m^2 corresponding to the background porosity ϕ^{off}=0.5% integrated through the computational domain. For $\phi\sim$3% (maximum amplitude at the beginning of the simulation), the compaction time scale (eq. 5.1) is approximately 0.5 kyr which is slightly more than the travel

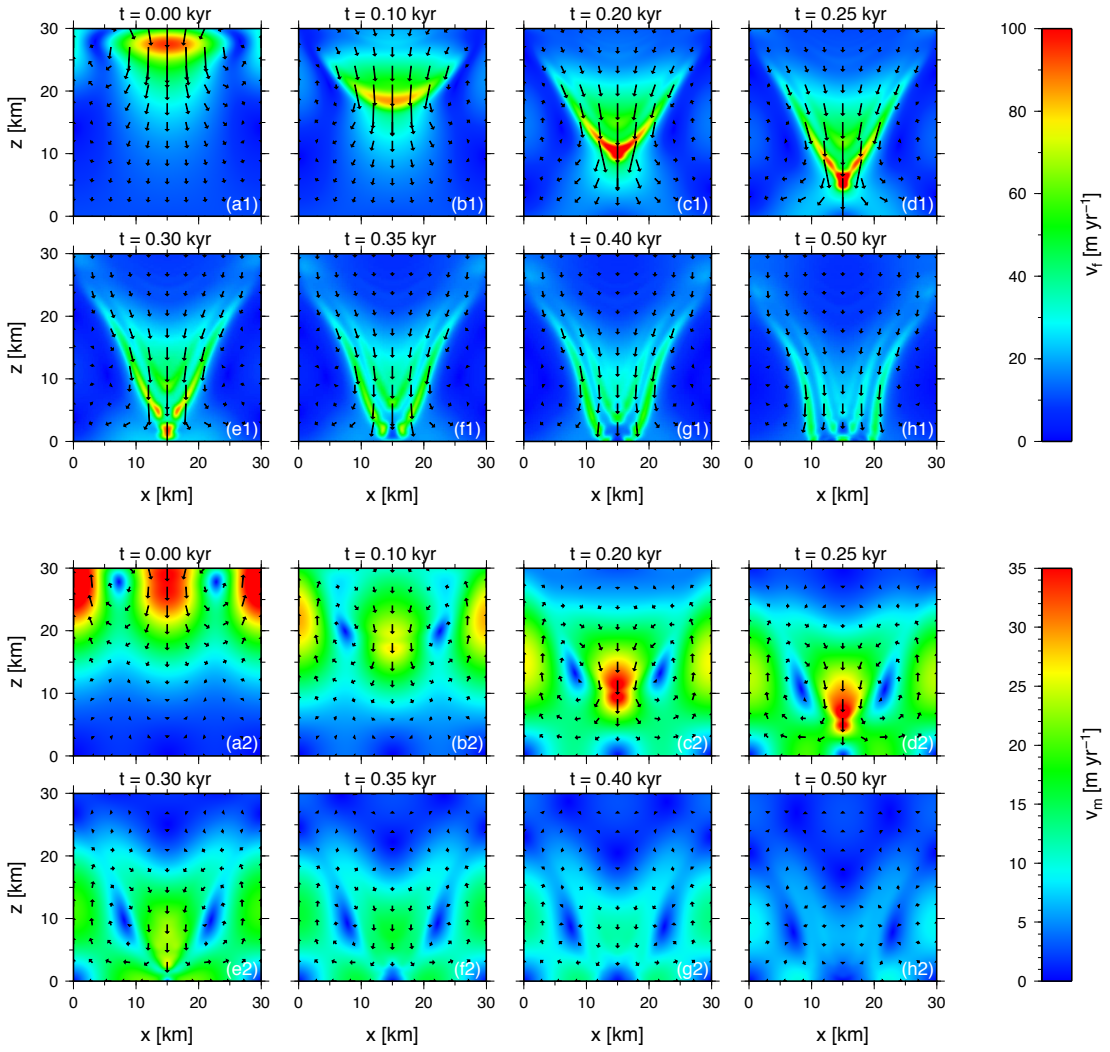

Figure 6.2: Snapshots of water velocity $\boldsymbol{v}_{\mathrm{f}}$ (first two lines) and ice velocity $\boldsymbol{v}_{\mathrm{m}}$ (third and fourth line) evolution corresponding to porosity from Figure 6.1.

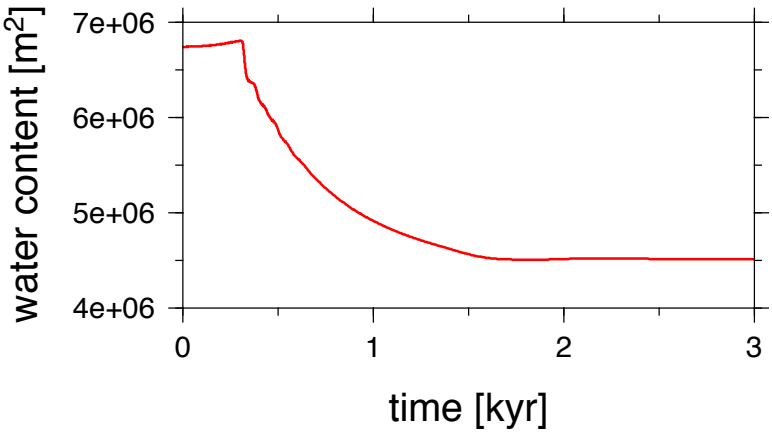

Figure 6.3: Time evolution of water content (porosity integrated throughout the domain). Computed for the same set of parameters as Figure 6.1.

time of the first wave in our simulation (0.3 kyr). However, the amplitude of the leading wave increases substantially during the simulation to reach as much as 20% just before the outflow starts (Figure 6.1, panel e). This significantly enhances the flow velocity and causes earlier beginning of the outflow - the time scale of such a highly nonlinear process is hard to estimate more precisely by a simple scaling law of the type of eq. (5.1). When compared with the results of a similar simulation (i.e. considering the same material parameters and the same background value of porosity, ϕ^{off}=0.5%) in one dimension (cf. Figure 5.10, red line), the porosity transport in two dimensions is slightly faster due to melt localizing effect that further enhances the melt flow velocity (cf. the discussion above).

6.2 Numerical tests

6.2.1 The role of SUPG regularization

As mentioned in Chapter 4, the classical Galerkin methods show oscillations in the solutions for advection-dominated problems (*Quarteroni & Valli*, 1994). A widely-used stabilization technique to prevent these oscillations is the SUPG method introduced by *Brooks & Hughes* (1982). Here, we test its performance. Figure 6.4 shows porosity at two different times, t=0.15 kyr (top line) and t=0.30 kyr (bottom line), and for various values of the method parameter, τ=0, 0.1, 0.3, and 0.5 (from left to right). The figures look quite similar for all the values of τ apart from the top corners - these (the left ones) are shown in more detail in Figure 6.5. Clearly, no stabilization (panels a, e) results in significant oscillations,

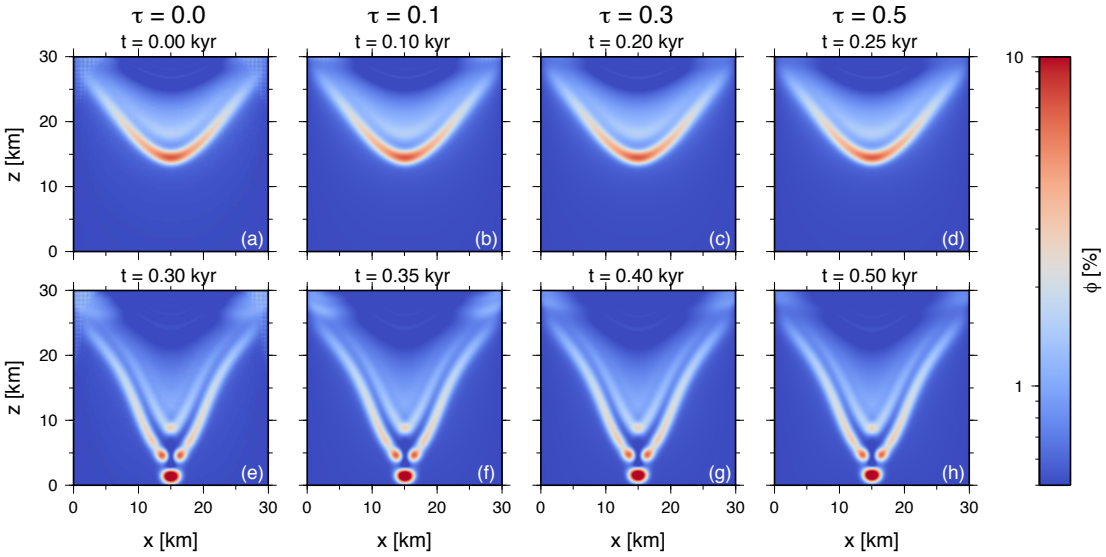

Figure 6.4: Snapshots of porosity evolution for various values of the SUPG stabilization parameter with τ=0 (no stabilization, panels a, e), τ=0.1 (panels b, f), τ=0.3 (panels c, g), and τ=0.5 (panels d, h). The first line corresponds to time t=0.15 kyr, the second to t=0.30 kyr. All other parameters are the same as in Figure 6.1. The porosity scale is logarithmic.

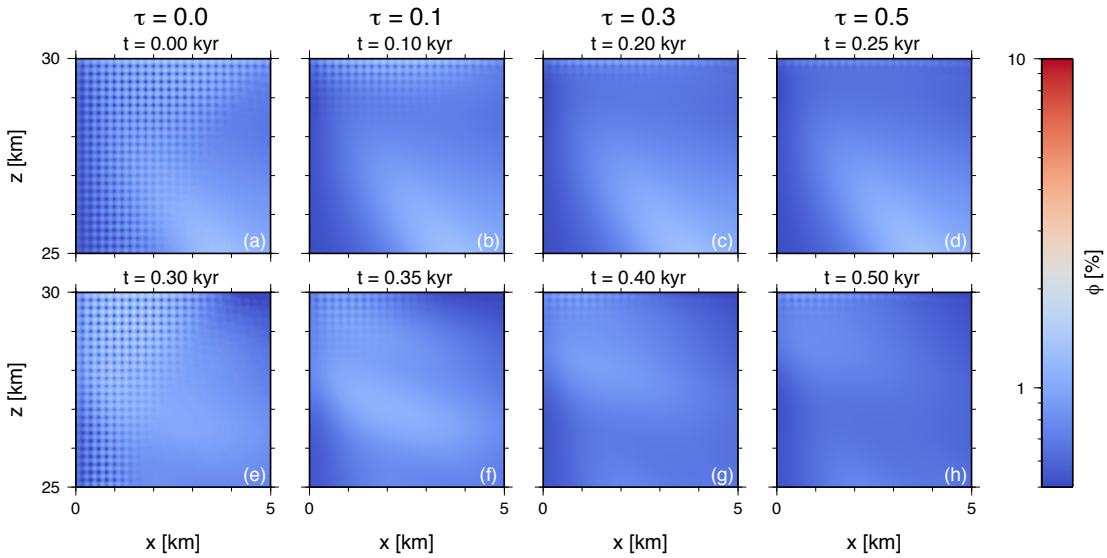

Figure 6.5: The same as in Figure 6.4 with only the top left corners of each panel shown.

which become less important with the increasing value of τ. For the largest value, τ=0.5, the porosity field is almost smooth, even though there are still small oscillations traceable very close to the top boundary.

Figure 6.6 displays the time evolution of the water content for the set of simulations from Figure 6.4. As all artificial diffusion methods, the SUPG method causes non-negligible volume loss (cf. *Quarteroni & Valli*, 1994). However, the overall time evolution and, most importantly, the time of the first wave arrival at the bottom boundary (∼0.3 kyr) in which we are mainly interrested, remains the same for all values of τ. Moreover, the largest difference in the water content appears when the solution with no regularization (τ=0, black line) is compared with the regularized solutions, while the differences between the solutions with different (but non-zero) τ are less pronounced. In order to further test our nu-

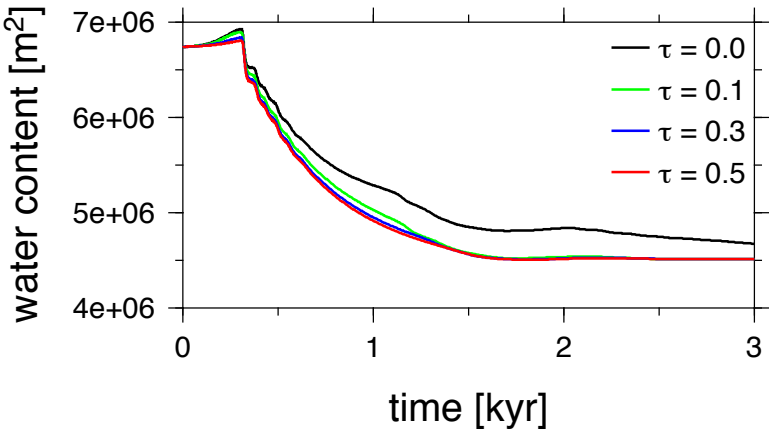

Figure 6.6: The same as in Figure 6.3 but for various values of the SUPG stabilization parameter τ.

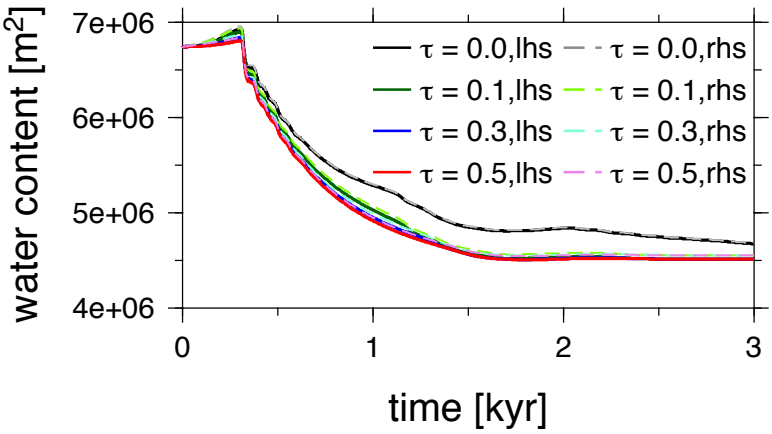

Figure 6.7: Comparison of the left-hand side and right-hand side of equation (6.2).

merical method, let us have a look at the porosity transport equation (3.136a). Integrating this mass balance over the whole domain and over time from t=0 to t=T, we get (taking into account boundary conditions 4.52):

$$\int_\Omega \phi \mathrm{d}x(t{=}T) = \int_\Omega \phi \mathrm{d}x(t{=}0) + \int_0^T \int_{\Gamma_T} \frac{\mathcal{V}}{[\phi]}(1{-}[\phi]\phi)\boldsymbol{v}_\mathrm{m}\cdot\boldsymbol{n}\mathrm{d}s\mathrm{d}t + \int_0^T \int_\Omega r_\mathrm{f}\mathrm{d}x\mathrm{d}t\ . \tag{6.2}$$

Figure 6.7 shows the comparison of the left-hand side of equation (6.2), i.e. the overal water content in the domain at certain time T, and its right-hand side (the initial water content modified by melt advection and ice melting). The balance is well satisfied for the solution with no stabilization (τ=0, black and gray lines), while the regularized solutions show slightly smaller left-hand sides (the instantaneous water content), again lost due to SUPG regularization. Overall, even though this regularization method causes significant volume losses, we decided to keep it in our numerical method since it efficiently reduces the oscillations and does not modify the porosity waves travel times. In the following (if not stated otherwise) we use the value τ=0.5.

6.2.2 The role of mesh discretization

We have already performed some discretization tests in Section 4.2.2 where we have compared the solution obtained by the 2d FEniCS code with the solution obtained by the 1d FORTRAN90 code (described in Section 4.1). Even though the calculations by FEniCS were made in two dimensions, the real geometry of the problem was only one-dimensional (dependent only on the vertical coordinate z). Here we compare solutions of our reference problem on four different meshes consisting of 50×50, 100×100, 150×150, and 200×200 elements, in order to investigate more closely the effect of mesh discretization in a real two-dimensional (x, z-dependent) problem. Figure 6.8 shows time evolution of the water content computed on these four meshes. We observe slight differences, especially for the coarsest grid (50×50 elements), however, the overall evolution does not differ substantially - the arrival time of the leading wave, as well as the arrival times of the subsequent waves are the same, as is the terminal value. In the following,

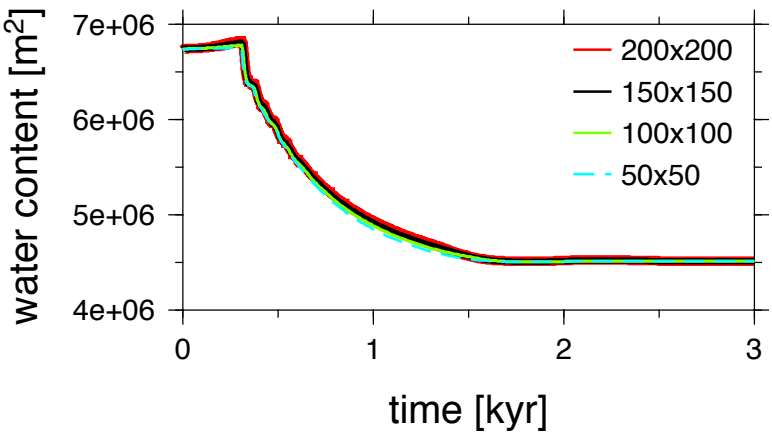

Figure 6.8: The same as in Figure 6.3 but for various mesh discretizations.

if not stated otherwise, we will use meshes consisting of 150×150 elements as a good compromise between solution accuracy and computational time demands.

6.2.3 The role of elements spaces choice

In this section, we investigate the role of our choice of elements spaces. The reference solution is computed with linear Lagrange elements for scalar quantities (ϕ, Π, r_f) and quadratic Lagrange elements for vector quantities ($\boldsymbol{v}_\mathrm{r}$, $\boldsymbol{v}_\mathrm{m}$, Taylor-Hood elements, cf. Section 4.2.1). This setting together with a mesh discretization of 150×150 results in 858 307 Degrees of Freedom (DoFs). For some more complicated problems (e.g. with a stress-dependent rheology, cf. Section 6.4.1), it can prove useful to reduce the number of DoFs while maintaining the same mesh resolution. We recomputed our reference solution with two other elements spaces choices - we used linear elements for all unknowns (resulting in 317 107 DoFs) and the combination of linear Lagrange elements for scalar quantities together with the so-called MINI elements (cf. *Arnold et al.*, 1984) for vector quantities (resulting in 677 107 DoFs). The time evolution of water content for these three simulations is depicted in Figure 6.9 and indicates that the results do not differ

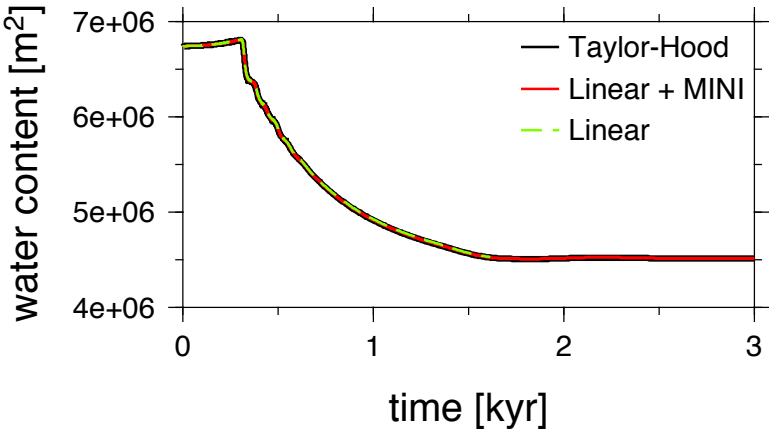

Figure 6.9: The same as in Figure 6.3 but for various elements spaces choice.

considerably.

If we investigated porosity as a function of spatial coordinates (as in Figure 6.1), we would not find a significant difference. However, the simulation with linear elements only (green dashed line in Figure 6.9) diverged at approximately 1.6 kyr, while the two other simulations went on till the end of simulation (∼3 kyr). This is due to instability of the linear elements choice for given problem (cf. *Logg et al.*, 2012). The computational time, however, was greatly decreased (about five times) for the linear elements choice when compared with the two other cases (between which there was not a substantial difference). Therefore, we keep the Taylor-Hood elements choice for most problems in the following study and use linear elements only when we need to dramatically shorten the computational times.

6.2.4 The role of background porosity

In Section 5.1.1 we have found that the background value of porosity (ϕ^{off}) affects the porosity wave propagation through a layer of partially molten (temperate) ice. Here, we investigate its role in two dimensions. Figure 6.10 displays few

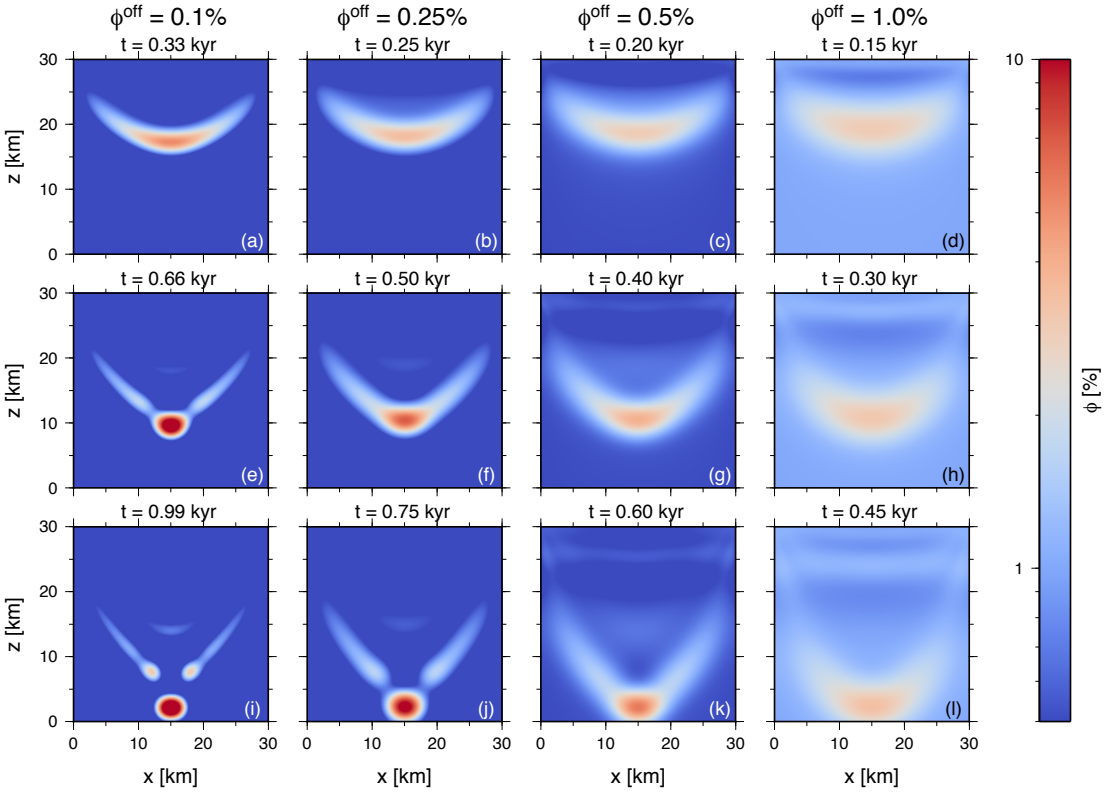

Figure 6.10: Snapshots of porosity evolution for various values of background porosity: ϕ^{off}=0.1% (panels a, e, i), ϕ^{off}=0.25% (panels b, f, j), ϕ^{off}=0.5% (panels c, g, k), and ϕ^{off}=1% (panels d, h, l). For each value of ϕ^{off}, three time instants are selected: the time just before the outflow starts (t=t_{o}, bottom line) and its two fractions: t=$\frac{1}{3}t_{\text{o}}$ (top line) and t=$\frac{2}{3}t_{\text{o}}$ (middle line). These time instants differ for different background values. The porosity scale is logarithmic.

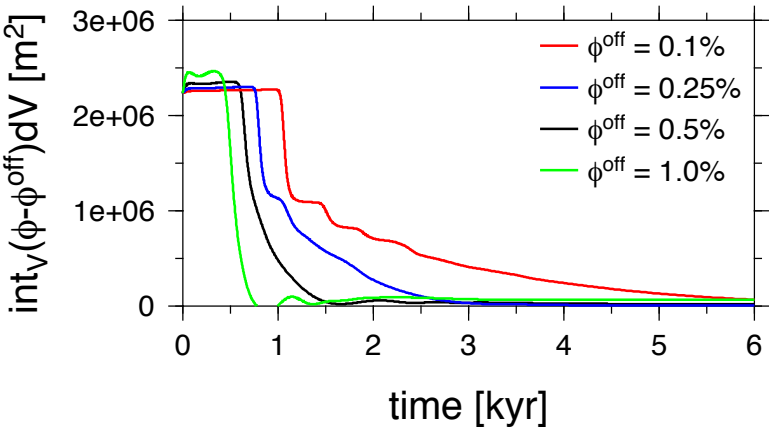

Figure 6.11: Time evolution of water content above the background porosity ϕ^{off} (i.e. $\int_V(\phi-\phi^{\text{off}})\mathrm{d}V$).

snapshots of the time evolution of porosity for four different background values: ϕ^{off}=0.1, 0.25, 0.5, and 1% (the material parameters are the same as in the reference solution, only with ice viscosity $\mu_{\text{m}}=10^{14}$ Pa s). We observe that with the decreasing value of ϕ^{off} the wavelength as well as the propagation speed decrease, while the maximum wave amplitude increases, leading to enhanced porosity localization. While a porosity maximum separates for the smaller values of the offset (ϕ_{off}=0.1% and 0.25%, the first two columns from left in Figure 6.10) with the difference between maximum and minimum values of porosity by far exceeding 10%, this difference is only $\sim$ 2.5% when ϕ^{off}=1% and no separation is detectable.

Figure 6.11 shows time evolution of water content above the background porosity ϕ^{off} (i.e. $\int_V(\phi-\phi^{\text{off}})\mathrm{d}V$). We observe that even though the value of ϕ^{off} affects the time scale of the process, its role is not crucial and is for example negligible when compared with the role of permeability (cf. next section). A comparison with Figure 5.3 (that displays the time evolution of water content for various values of the porosity background ϕ^{off} in one-dimensional geometry) further shows that for the same values of ϕ^{off} and identical porosity maxima of the initial conditions (eqs 4.70 and 6.1), the travel times are slightly shorter in two-dimensions (cf. black line in Figure 5.3 and blue line in Figure 6.11 for ϕ^{off}=0.25%, and red line in Figure 5.3 and black line in Figure 6.11 for ϕ^{off}=0.5%, respectively) due to more effective localizing process that accelerates the water percolation. Since for numerical reasons we have to consider a non-zero background value of porosity, in the following we will use value ϕ^{off}=0.5% that represents a compromise between numerical requirements and the effect on the drainage time scale.

6.3 The role of permeability

In this section, we investigate the role of permeability in the transport of water through the temperate ice layer. In Section 5.2, we have already shown that permeability plays a crucial role in this process, so here we merely want to investigate possible effects related to the change of dimensionality. We again test

various combinations of permeability constant k_0 and permeability exponent n in the next Section 6.3.1 and the effect of percolation threshold ϕ_c is illustrated later in Section 6.3.2.

6.3.1 The role of permeability constant and exponent

We vary the permeability constant k_0 over two orders of magnitude (10^{-10}–10^{-8} m^2) and test also both end-member values of the permeability exponent (n=2 and 3) - together with eq. (2.1) these values approximate well the measured permeability values (cf. Figure 2.3). Some snapshots of the evolution of porosity (for ϕ^{off}=0.5%) are depicted in Figure 6.12. These results confirm that the wavelength strongly decreases with decreasing permeability constant k_0 (first to third column in Figure 6.12) and with increasing permeability exponent n (first and fourth column in Figure 6.12) in agreement with eq. (4.38).

Figure 6.13 shows time evolution of the water content and proves that permeability controls the speed of wave train propagation - for given n, it depends approximately linearly on k_0 (cf. results of Section 5.2.1 and eq. 5.1). Using a larger value of the permeability exponent (n=3, green line in Figure 6.13) causes reduction of the wave train propagation speed from more than one order (at the beginning of the simulation till the beginning of the outflow) to more than two

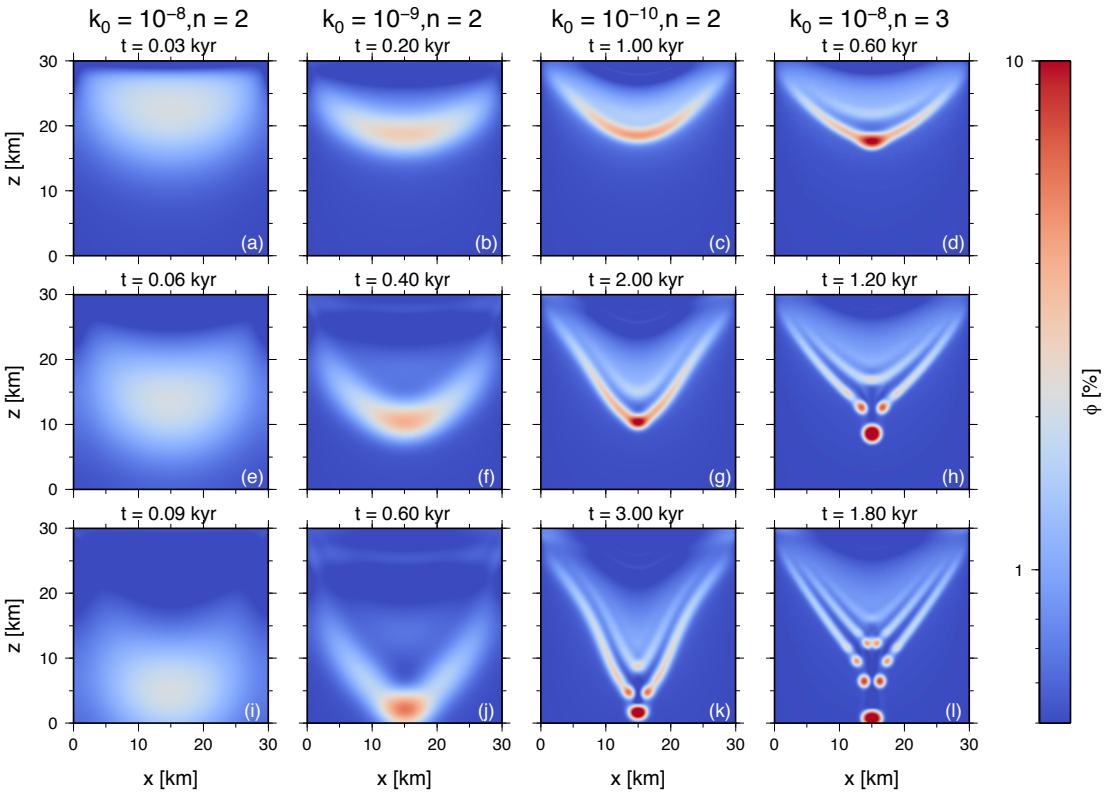

Figure 6.12: The same as in Figure 6.10 but for various combinations of permeability constant k_0 and exponent n: k_0=10^{-8} m^2, n=2 (panels a, e, i), k_0=10^{-9} m^2, n=2 (panels b, f, j), k_0=10^{-10} m^2, n=2 (panels c, g, k), and k_0=10^{-8} m^2, n=3 (panels d, h, l).

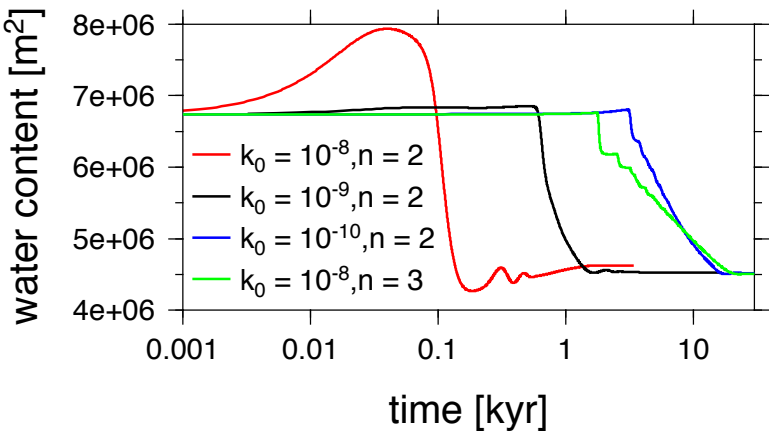

Figure 6.13: The same as in Figure 6.3 but for various combinations of k_0 and n. The time scale is logarithmic.

orders at the end of simulation, when the porosities are smaller (cf. red and green lines in Figure 6.13).

6.3.2 The role of percolation threshold

Here, we study the role of an abrupt decrease of permeability below the so-called percolation threshold, ϕ_c. Permeability in these simulations is considered in the form given by eq. (2.2) and we use several values of the threshold, ϕ_c=0.5%, 1%, 3%, and 5%. We remind, that the use of porosity threshold mimics the observed abrupt decrease in permeability measured for the terrestrial sea ice - the measured value was 5% (cf. *Golden et al.*, 1998).

Results are shown in Figures 6.14 and 6.15. In the case of very small porosity threshold (ϕ_c=0.5%, the first column in Figure 6.14 and red line in Figure 6.15), porosity exceeds (or equals) the threshold in almost whole domain (since $\phi_c=\phi^{\text{off}}$) implying permeability large enough to enable water transport by microscopic percolation. The leading wave has smaller wavelength when compared to the case with ϕ_c=0% (the second column in Figure 6.12 and black line in Figure 6.15) but arrives at the bottom boundary only slightly retarded.

For a little larger value of threshold (ϕ_c=1%>ϕ^{off}, the second column in Figure 6.14 and blue line in Figure 6.15), only parts of the porosity waves exceed the threshold (cf. the black contour in Figure 6.14) implying permeability, at least locally, large enough to enable percolative transport of water through the ice shell. The arrival time of the leading wave is even more delayed and the wavelength decreases considerably leading to very strong localization and local porosity maxima separation. However, for both as yet described cases, the leading waves still arrive at the bottom of the shell within a few kiloyears from the beginning of the simulation.

In the case of very large threshold (ϕ_c=5%$\gg\phi^{\text{off}}$, the fourth column in Figure 6.14 and yellow line in Figure 6.15), the permeability is so small that the layer is effectively impermeable for water transport through a system of intergranular veins. However, as discussed in Section 2.3, a partially molten reservoir is not gravitationally stable within an ice layer and is destabilized due to formation

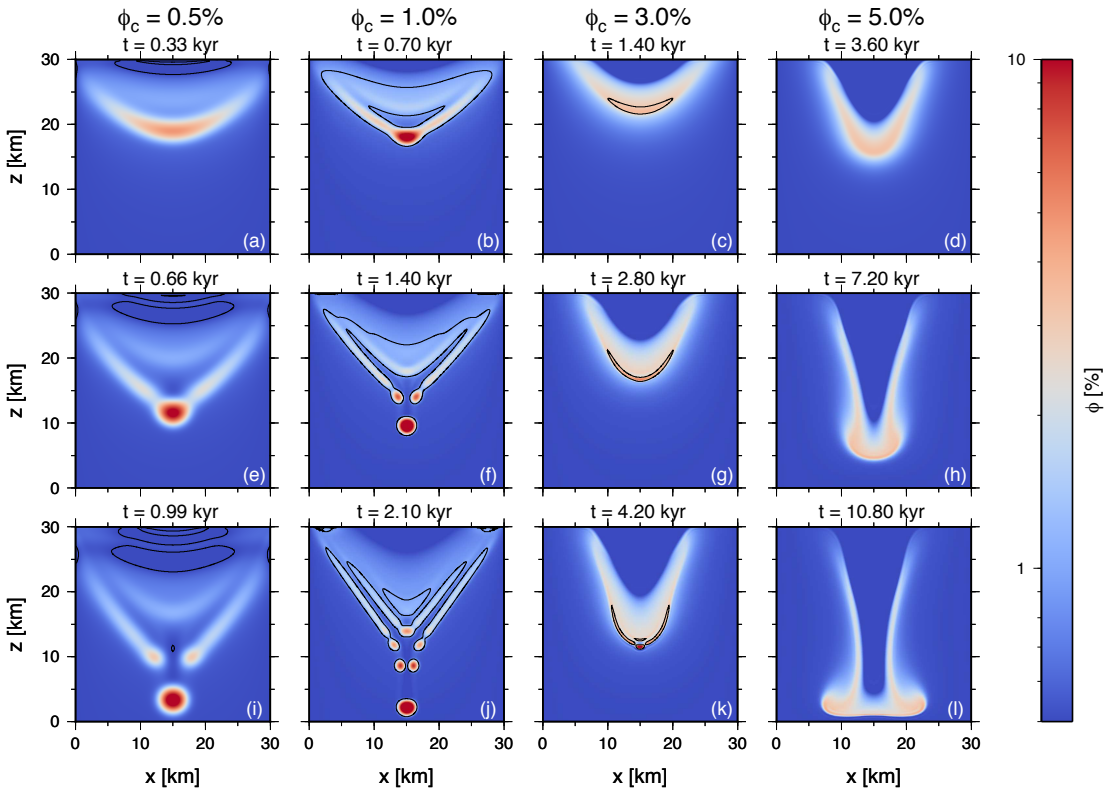

Figure 6.14: The same as in Figure 6.10 but for various values of percolation threshold: ϕ_c=0.5% (panels a, e, i), ϕ_c=1% (panels b, f, j), ϕ_c=3% (panels c, g, k), and ϕ_c=5% (panels d, h, l). Black contours in each panel denote the value of corresponding threshold.

of gravitational (Rayleigh-Taylor-like) instability. Since the (constant) viscosity of ice is here considered to be only 10^{14} Pa s (ice at the melting temperature), the time necessary to destabilize a reservoir of few percents (with a maximum of about 3%) is quite short and within 10 kyr the majority of the partially molten

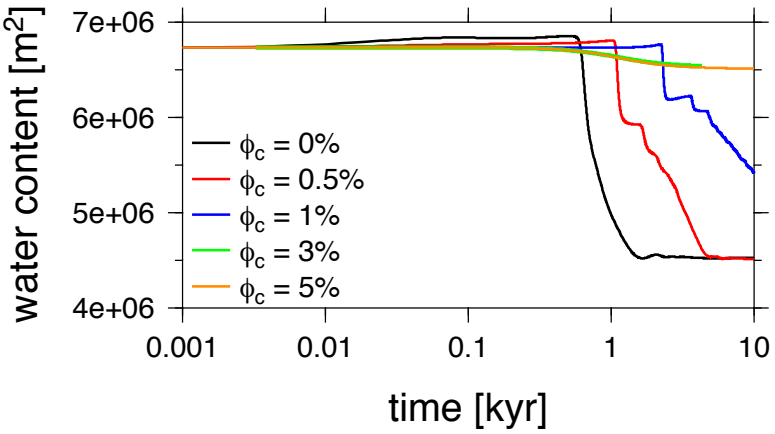

Figure 6.15: The same as in Figure 6.3 but for various values of percolation threshold ϕ_c. The time scale is logarithmic.

material is advected within the collapsing ice matrix to the bottom boundary, where it stays since the bottom boundary is impermeable for matrix material (cf. eq. 4.52).

For an intermediate value of porosity threshold (ϕ_c=3%, the third column in Figure 6.14 and green line in Figure 6.15), the permeability is very low and the partially molten lense starts to collapse down due to formation of gravitational instability. However, since the permeability is not as small as for ϕ_c=5%, a wave train starts to develop with a very small wavelength, which does not arrive at the bottom boundary within a reasonable computational time.

Overall, the results of this section naturally depend not only on the value of porosity threshold but rather on the relation between the threshold ϕ_c and the chosen background value ϕ^{off}. However, for reasonably small offsets ($\phi^{off} \lesssim 1\%$), the measured value of ϕ_c=5% remains well above the chosen offset value and the results of this section do not change substantially.

6.4 The role of ice rheology

The very complex ice viscosity (in general depending on temperature, rate of deformation, water content, grain size, etc.) can have a major impact on the transport of water through the temperate ice layer. In Section 5.3, we have shown that in one-dimensional geometry, the complex ice viscosity can be approximated by a constant viscosity model with viscosities from the range of 10^{12}–5×10^{15} Pa s. However, in one dimension, only the vertical matrix deformation is included while the horizontal effects cannot be treated. Therefore, we repeat the study from Section 5.3 in two dimensions, focusing on the role of composite ice rheology involving four deformational mechanisms (Section 6.4.1), the role of porosity weakening (Section 6.4.2) and finally, in Section 6.4.3, we study the complex rheology combining both these effects.

6.4.1 The role of composite ice rheology

We consider ice viscosity given by eqs (1.1) and (1.2) and compare the results with several constant-viscosity cases. We take ϕ^{off}=0.5% and use four values of grain size, d=0.5, 1, 5, 10 mm. Given the complexity of this problem, we use linear elements for all variables - this decreases the stability of a problem, but keeps the computational times reasonable, while maintaining adequate accuracy (cf. Section 6.2.3). Figure 6.16 (top three lines) shows few snapshots of porosity evolution - we observe that with increasing value of grain size d (from left to right) and while maintaining all other parameters the same, the wavelength significantly increases. For two smaller values of grain size, d=0.5 and 1 mm (first and second column), the leading wave is well distinguishable, with the formation of subsequent waves visible for the smallest value of grain size (d=0.5 mm, panel i1). For the larger values of grain size (d=5 and 10 mm, third and fourth column), water is transported downwards in a one large wave rather than in a wave train. The wavelength is so large, that it approximately equals half the size of a computational domain.

As has been already mentioned, the wavelength is governed by the value of viscosity - the effective viscosities corresponding to porosity fields from top three

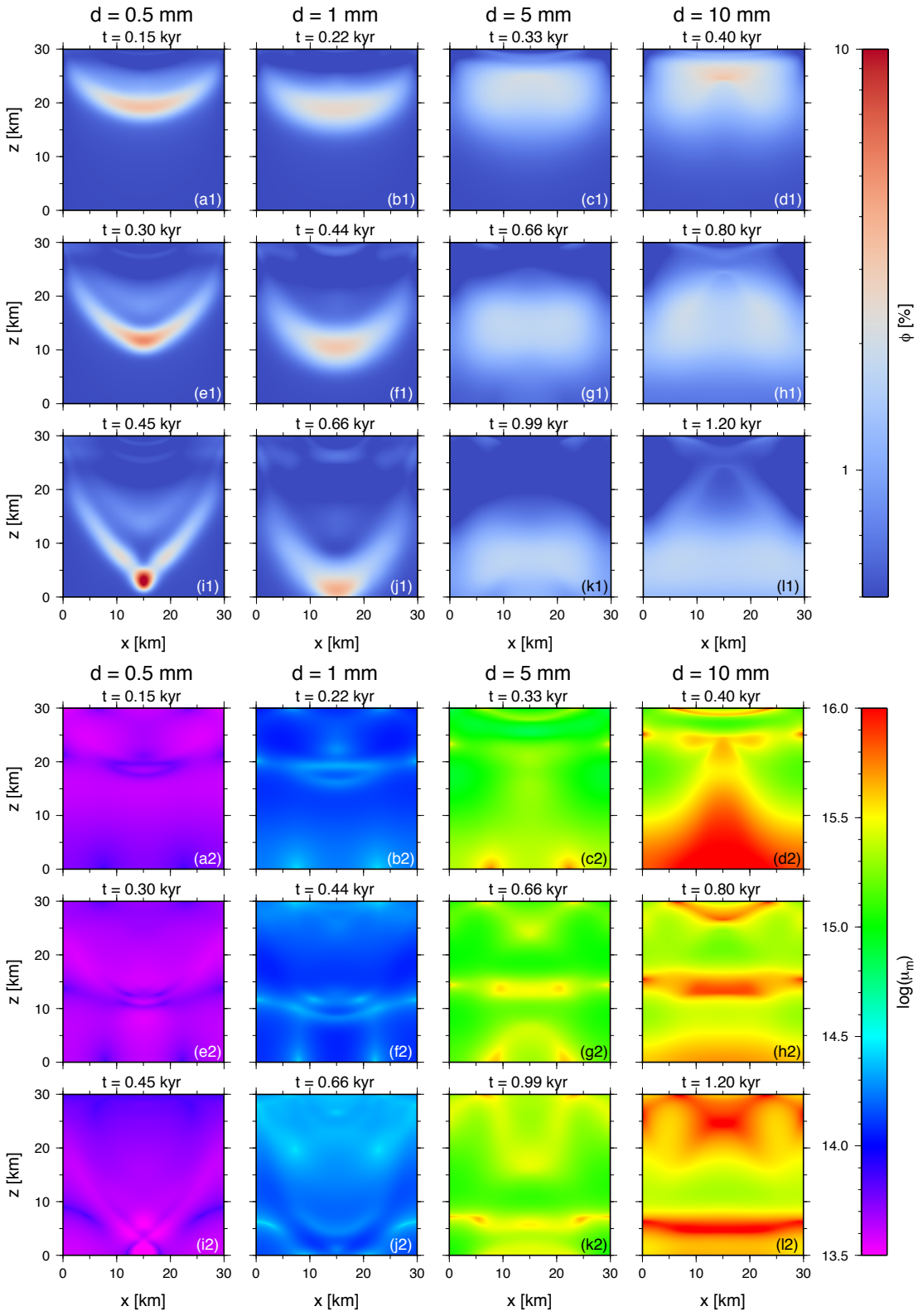

Figure 6.16: Top three lines: the same as in Figure 6.10 but for composite rheology and various values of grain size: d=0.5 mm (panels a1, e1, i1), d=1 mm (panels b1, f1, j1), d=5 mm (panels c1, g1, k1), and d=10 mm (panels d1, h1, l1). Bottom three lines: corresponding viscosity.

lines of Figure 6.16 are depicted in the bottom three lines of the same figure and range approximately from 3×10^{13} to 10^{16} Pa s. While they vary substantially with the different value of grain size (different columns in the bottom three lines of Figure 6.16), for a fixed value of grain size (within a particular column), they all span approximately less than order of magnitude. Comparing the viscosities of particular deformation mechanisms, we find that for the smallest grain size used (d=0.5 mm), the dominant mechanism is the stress-independent diffusion creep, while for d=1 mm, grain-boundary sliding becomes important, especially in the vicinity of porosity maximum. For even larger grain sizes (d=5 and 10 mm), grain-boundary sliding is the dominant mechanism.

Time evolution of water content depicted in Figure 6.17 shows that for the composite ice rheology given by the combination of diffusion creep, dislocation creep, basal slip and grain-boundary sliding and for grain sizes from the range of 0.5 to 10 mm, the transport of liquid water through a temperate ice layer can be (especially in terms of water drainage time scales) approximated by a scenario with constant viscosities from the range of 10^{13} to 5×10^{15} Pa s.

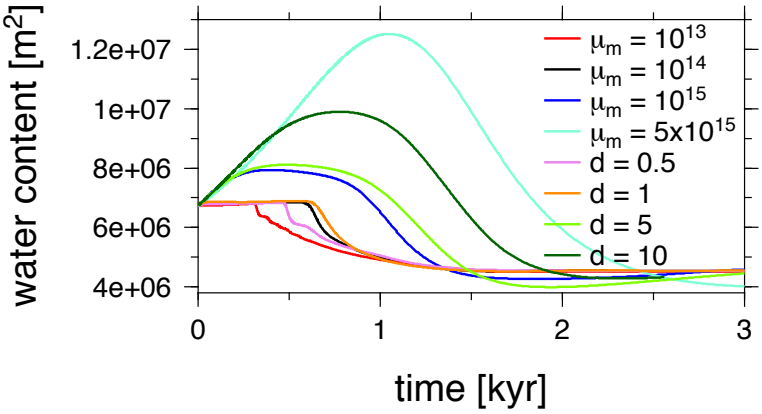

Figure 6.17: The same as in Figure 6.3 but for composite rheology and various values of grain size d.

6.4.2 The role of porosity weakening

In Section 5.3.3 we found that in one dimension, the porosity weakening of the form given by eq. (1.5) with $\mu_{\rm m}^{\rm pure}$=10^{14} Pa s leads to significant porosity localisation increasing its maxima three times (for $\gamma_{\rm m}$=45). Even though the corresponding values of viscosity decreased as much as two orders of magnitude, the overall water transport was comparable with the constant viscosity case (i.e. $\gamma_{\rm m}$=0). Here, we again concentrate on potential effects related with the change of dimensionality. The top three lines of Figure 6.18 show few snapshots of porosity evolution for four values of the weakening parameter: $\gamma_{\rm m}$=0, 15, 30, 45 and the reference value of viscosity $\mu_{\rm m}^{\rm pure}$=10^{15} Pa s (larger value of water-free reference viscosity was chosen for numerical reasons, cf. below). We observe more pronounced localization with the increasing value of weakening parameter $\gamma_{\rm m}$ (from left to right), however, for this large value of reference viscosity, $\mu_{\rm m}^{\rm pure}$=10^{15} Pa s, the effect is not very strong - viscosity (depicted in bottom three lines of Figure 6.18) decreases locally only about one order of magnitude (for $\gamma_{\rm m}$=45, fourth

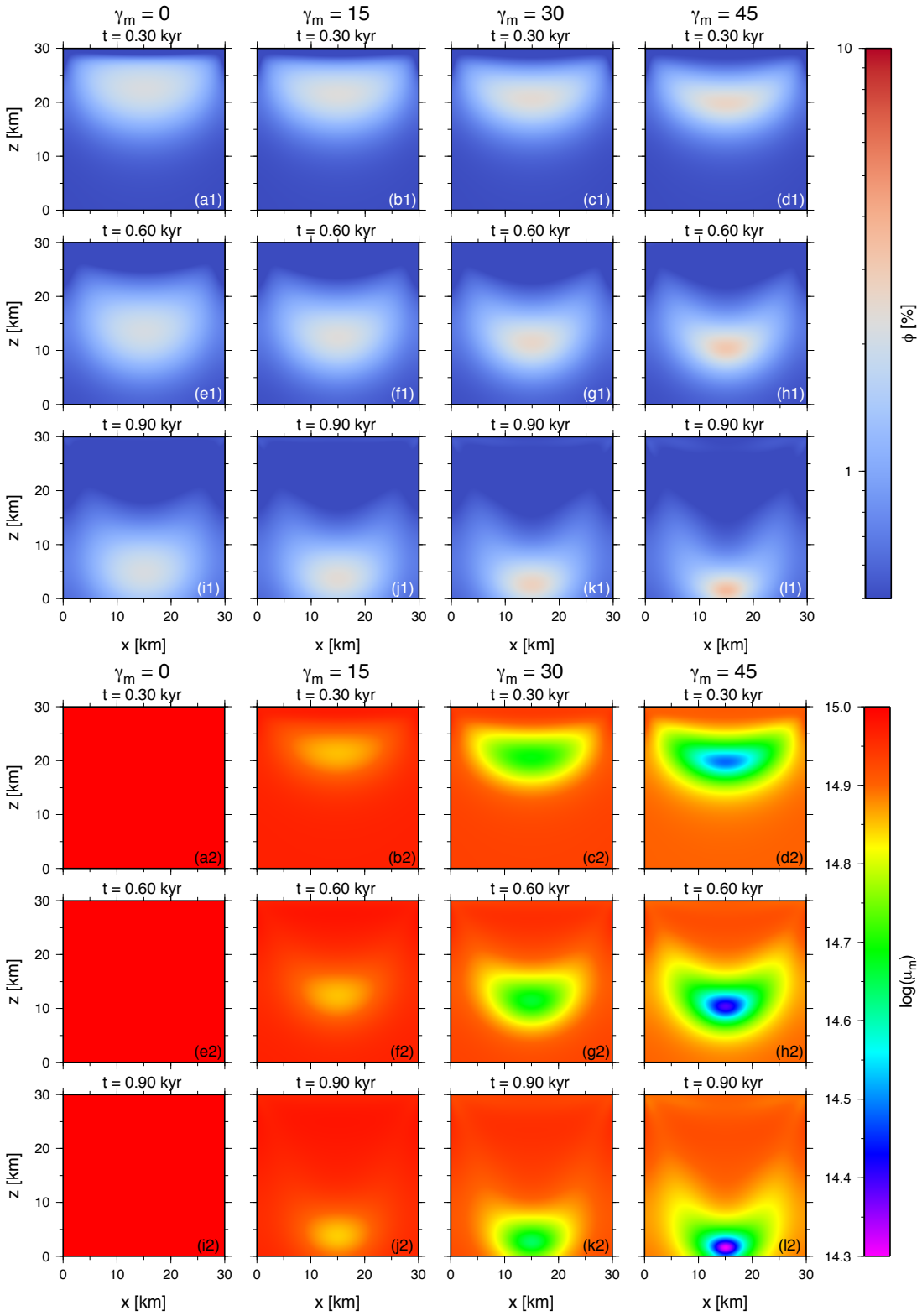

Figure 6.18: Top three lines: the same as in Figure 6.10 but for porosity weakened viscosity and various values of weakening parameter: γ_m=0 (panels a1, e1, i1), γ_m=15 (panels b1, f1, j1), γ_m=30 (panels c1, g1, k1), and γ_m=45 (panels d1, h1, l1). Bottom three lines: corresponding viscosity.

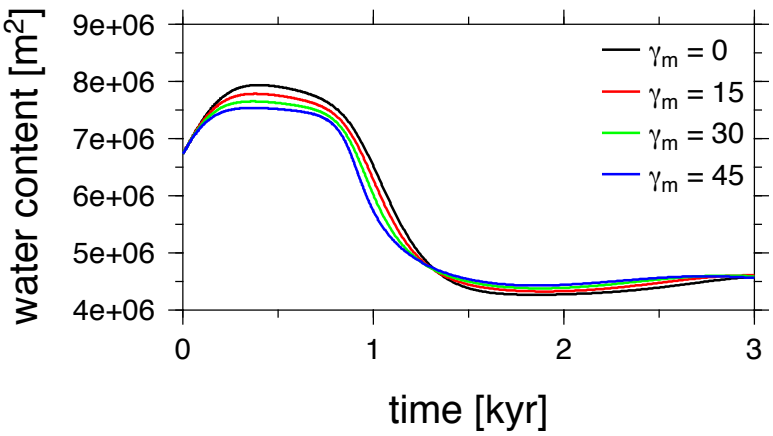

Figure 6.19: The same as in Figure 6.3 but for porosity weakened viscosity and various values of weakening parameter γ_m.

column) due to smaller porosity amplitudes. Unfortunately, for a smaller value of reference water-free viscosity (μ_m^{pure}=10^{14} Pa s), we were able to obtain results using only much smaller values of the weakening parameter $\gamma_m \leq 10$ that caused solely slight changes from the case with no porosity weakening (γ_m=0). Solutions with μ_m^{pure}=10^{14} Pa s and a larger values of γ_m (>10) are unfortunately not attainable with our current numerical tool.

Time evolution of water content for simulations from Figure 6.18 is displayed in Figure 6.19 and shows a result comparable with the results of one-dimensional simulations - the overall water transport appears to be determined by the average viscosity in the layer below the wave and is thus (for all values of γ_m used) comparable with the constant-viscosity case of μ_m=10^{15} Pa s and γ_m=0.

6.4.3 Parametrization of the complex ice rheology

As in the one-dimensional study, we consider also a complex rheology combining composite ice rheology (eqs 1.1 and 1.2, studied separately in Section 6.4.1) with

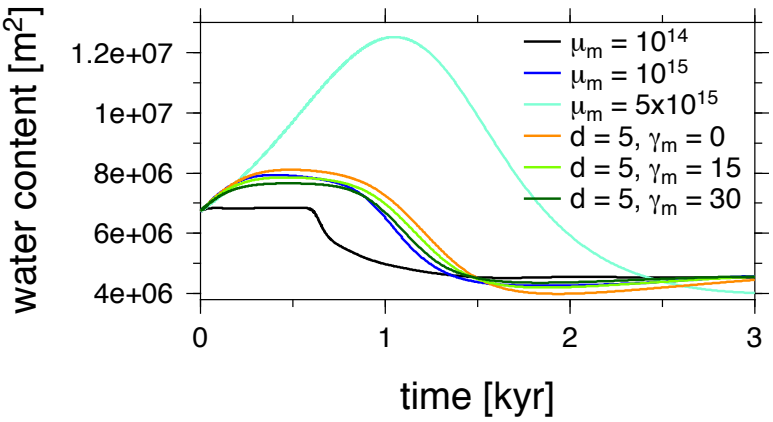

Figure 6.20: The same as in Figure 6.3 but for complex ice rheology and various combinations of grain size d and porosity weakening parameter γ_m.

porosity weakening (eq. 1.5, studied in the previous Section 6.4.2). We use middle value of grain size, d=5 mm, and two values of porosity weakening parameter, γ_m=15 and 30. Time evolution of water content computed for these two cases is shown in Figure 6.20 together with results computed with composite rheology assuming d=5 mm (and no porosity weakening) and results computed with constant viscosities. Compared with the case of composite rheology and grain size d=5 mm (yellow line), the extra porosity weakening has only minor influence leading to slight decrease of the overall water content (green lines). Thus, for these particular values of d and γ_m, the overal evolution can be parametrized by cases with constant viscosities from the range of 10^{14}–5×10^{15} Pa s. Assuming that the role of porosity weakening on time evolution of a problem with complex ice rheology would be similar also for other values of grain sizes (d=0.5–10 mm) and even for a larger value of weakening parameter γ_m=45, we estimate the range of suitable viscosities that could reasonably well parametrize the complex viscosity in our temperate ice shell setting as 10^{13}–5×10^{15} Pa s.

6.5 Summary

In this chapter, we concentrated on the role of material parameters in the transport of liquid water through a temperate ice shell in two dimensions. At first, we investigated several numerical parameters in order to reach a compromise between reasonable accuracy and computational time. We found that mesh discretization of 150×150 and the SUPG method parameter τ=0.5 should be suitable for the most of our calculations. While Taylor-Hood elements assure solution stability, using the linear elements for all unknowns can be unstable, but does not decrease the solution accuracy and can therefore be tried and used in cases where the use of Taylor-Hood elements would lead to extremely long computational times. As for the background value of porosity ϕ^{off}, we confirm its role found in Section 5.1.1 in that it affects the porosity wavelength as well as the water extraction time scale. However, given the necessity of using a non-zero value and since the effect on the time scale is not that pronounced as, for example, the effect of permeability, we decided to keep a constant value of ϕ^{off}=0.5% for all the simulations throughout this section to eliminate its effect on the results of parametric study as much as possible.

Our two-dimensional numerical experiments confirm our findings from Chapter 5 that the ice permeability has the most important impact on the time scale of water propagation and affects also the wavelength of porosity waves. Simulations with percolation threshold (Section 6.3.2) further reveal that even for very low permeability (caused by relatively large value of threshold ϕ_c=5%), water lense at the top of temperate ice layer is not gravitationaly stable and collapses down due to formation of gravitational (Rayleigh-Taylor-like) instability. This result differs from the result of the same experiment in one dimension (Section 5.2.2), in which the layer stayed almost immobile at the initial position. These findings suggest that reservoirs stable at the top of the shell in one dimensional simulations could be destabilized by the formation of gravitational instability in two dimensions.

We also investigated the role of ice rheology in water transport by comparing the results obtained for constant viscosity with those computed for viscosity parameterizations. The results of two-dimensional simulations do not differ sub-

stantially from those obtained in one-dimension - the effect of ice rheology is important on local scale by strongly affecting the wavelength, while the global scale transport properties can be reasonably well reproduced by a constant viscosity model with values from the range of 10^{13}–5×10^{15} Pa s.

In summary, we find that water transport through a temperate ice shell is very efficient with times necessary to deliver the majority of the initial water content to the bottom boundary ranging from less than one kiloyear to few tens of kiloyears.

6.6 Peak collision

To terminate this chapter, we demonstrate a particular behavior of the two-phase water transport through a temperate ice shell. Since the velocity of water propagation strongly depends on the amount of water available (i.e. porosity ϕ), a model situation can occur where initially larger amount of water travels faster than the other, initially smaller amount of water. This is illustrated in Figure 6.21 where an initially larger Gaussian peak catches up with a smaller one.

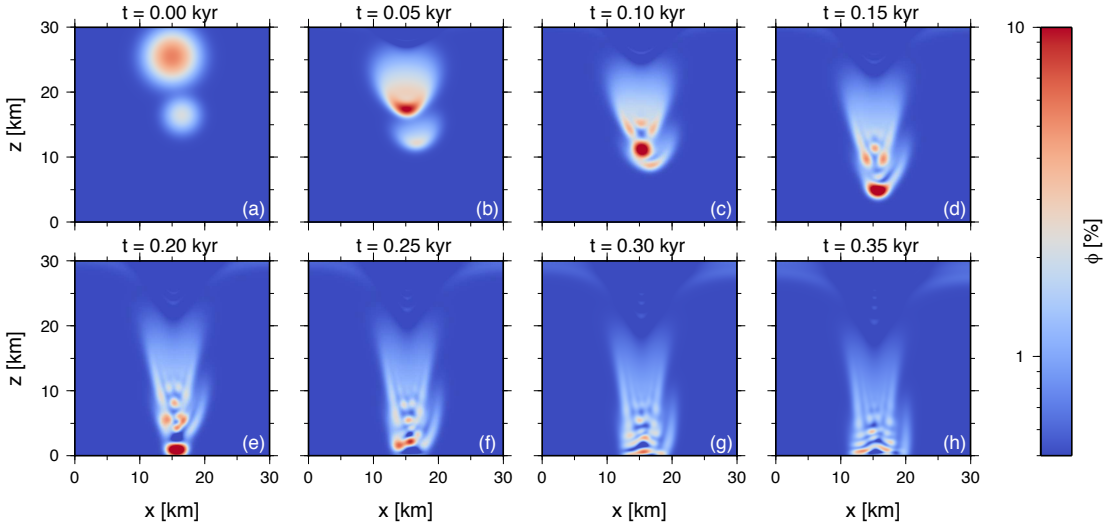

Figure 6.21: The same as in Figure 6.1 but for a different initial condition.

Part IV

Liquid water in Europa's ice shell: Results of numerical modeling

7. Ice melting and downward transport of meltwater by two-phase flow in Europa's ice shell (1d)

In the previous part of this thesis (Chapters 5 and 6) we have investigated the transport of a partially molten material through a temperate ice shell. However, in reality, when tidally-induced melting occurs at shallow depths (cf. Chapter 1), the underlying ice is not necessarily at the melting point. In this case, the downward extraction of the melt produced in the region with enhanced heating might be delayed and efficient extraction by two-phase flow occurs only once the melting point is reached below this domain. In this chapter, we consider two different geophysical contexts which we implement by imposing specific initial temperature profiles and heating scenarios in one dimension.[1] The first one corresponds to melting in the head of a hot plume (hot plume set-up, Sections 7.1.1 and 7.2.1, after *Sotin et al.*, 2002), while in the second one the melt is produced by shear motions on a strike-slip fault (strike-slip fault set-up, Sections 7.1.2 and 7.2.2, after *Nimmo & Gaidos*, 2002).

As already discussed in Section 1.6.1, viscosity of ice depends in general on numerous factors such as temperature, strain rate, water content etc. (*Durham et al.*, 2001; *Goldsby & Kohlstedt*, 2001; *De La Chapelle et al.*, 1999). Although in the cold ice strong viscosity variations can be expected, e.g. in thermal boundary layers or in the vicinity of localized thermal sources, their effect cannot be manifested in our 1d formalism, as we do not consider any shear deformation and viscous compaction in cold ice. In the temperate ice, the effect of temperature on viscosity is negligible (T=T_M), however, the influence of porosity (water content) can be significant. The role of ice viscosity on the transport properties in temperate ice in one dimension was tested in Chapter 5 - we found that the global scale transport properties, such as the characteristic time of propagation and the total meltwater volume, can be reasonably well reproduced by a constant viscosity model. Moreover, the effect of ice viscosity on the water-extraction time scale (cf. compaction time scale, eq. 5.1) is almost negligible. Since our main goal is the estimate of this time scale, for the sake of simplicity, we consider a constant value of viscosity μ_{m}=10^{14} Pa s in our simulations.

Besides viscosity, the other crucial parameter is the ice permeability, which was shown to have a major effect on the speed of the porosity waves propagation (cf. Section 5.2). Since we are interested in the upper estimate for the water-extraction time which determines the stability of the water reservoirs, we choose the minimum admissible value (k_0=10^{-10} m^2, cf. Section 2.2) of the ice permeability constant.

We start this chapter with a description of the numerical implementation of the two geophysical contexts (Section 7.1) and then, in Section 7.2, we describe our results. The model assumptions and their consequences for the obtained

[1] The results summarized in this chapter were published in *Kalousová et al.* (2014).

results are discussed in Section 7.3 and a short summary of this chapter is given in Section 7.4.

7.1 Heating scenarios

7.1.1 Hot plume set-up

Since we cannot properly model thermal evolution of a hot plume in one-dimensional geometry, we must approximate it by choosing a suitable parametrization of the heat source. In the context of subsurface water generation, it is crucial to describe the relatively short period in the plume evolution when melting starts to occur in the plume head (e.g. *Sotin et al.*, 2002; *Tobie et al.*, 2003; *Běhounková et al.*, 2010). The temperature evolution is governed by eq. (4.1d) in which the source term Q includes the combined effect of tidal heating H_t and convective cooling H_c. According to numerical simulations of *Tobie et al.* (2003), the total heating rate $H_\mathrm{t}-H_\mathrm{c}$ is typically equal to 10–20% of the tidal heating rate, which allows the following parametrization in terms of a scaling parameter x:

$$Q = H_\mathrm{t} - H_\mathrm{c} = xH_\mathrm{t} \ . \tag{7.1}$$

Following *Tobie et al.* (2003), the viscosity-dependent tidal heating can be expressed as (cf. also Section 1.6.2):

$$H_\mathrm{t} = \frac{2H_\mathrm{t}^\mathrm{max}}{\mu_\mathrm{m}/\mu_\mathrm{m}^\mathrm{max} + \mu_\mathrm{m}^\mathrm{max}/\mu_\mathrm{m}} \ , \tag{7.2}$$

where $H_\mathrm{t}^\mathrm{max}$ is the maximum heating rate that occurs for viscosity $\mu_\mathrm{m}^\mathrm{max}$. We consider $H_\mathrm{t}^\mathrm{max}$=5×10^{-6} W m^{-3} that corresponds to the average estimate of the heating due to tides (cf. *Tobie et al.*, 2003).

The role of matrix viscosity on the dynamics of polythermal ice has been discussed above - we concluded that using a constant value does not affect the water-extraction time by two-phase flow. However, when the effect of viscosity on tidal heating is concerned, the temperature and porosity dependence cannot be neglected. Here we choose the following parametrization (Frank-Kamenetskii approximation combined with the porosity softening, cf. *Tobie et al.*, 2003):

$$\mu_\mathrm{m} = \mu_\mathrm{m}^\mathrm{bot} \exp\left(-\frac{E_\mathrm{a}(T-T_\mathrm{M})}{RT_\mathrm{M}^2}\right) \exp(-\gamma_\mathrm{m}\phi) \ , \tag{7.3}$$

where E_a is the activation energy, R is the universal gas constant, T_M is the melting temperature at the bottom of the ice shell, and $\mu_\mathrm{m}^\mathrm{bot}$ is the melting point ice viscosity - for the sake of simplicity, we assume $\mu_\mathrm{m}^\mathrm{max}$=$\mu_\mathrm{m}^\mathrm{bot}$=10^{14} Pa s. The exponential terms in eq. (7.3) describe the temperature and porosity effects, respectively. The value of parameter γ_m is chosen so that the increase of porosity by 5% induces viscosity decrease by one order of magnitude (*De La Chapelle et al.*, 1999; *Tobie et al.*, 2003). The initial temperature profile, which is also estimated from *Tobie et al.* (2003), and the initial heating profiles for several values of x are shown in Figure 7.1.

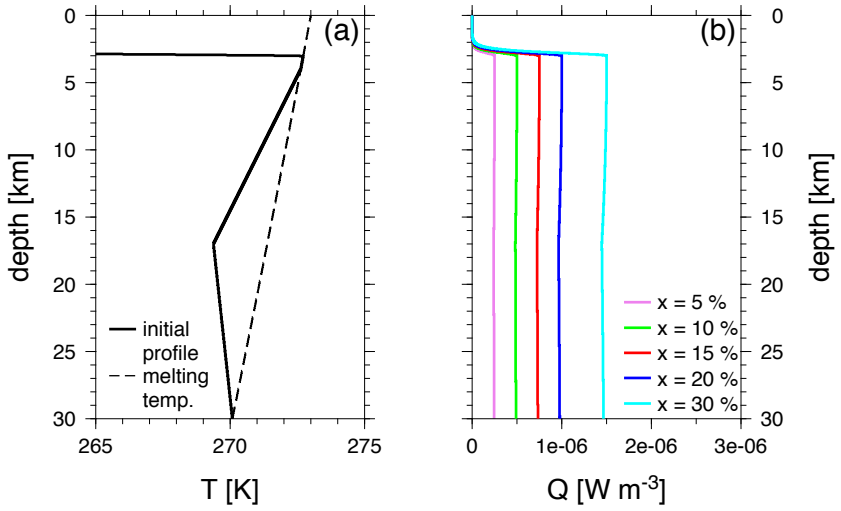

Figure 7.1: Hot plume set-up. (a) Melting temperature and initial temperature profile. (b) Initial heating computed from eqs (7.1)–(7.3) for different values of x and for the initial temperature profile shown in panel a. Spatial variations are due to temperature dependence of viscosity used in evaluating the heating term (eq. 7.2).

7.1.2 Strike-slip fault set-up

This set-up represents the process of melt production due to tidally-induced displacement along a strike-slip fault. In addition to the volumetric tidal heating H_t (eq. 7.2), we also include a localized heat source corresponding to shear heating along and just below a strike-slip fault (cf. *Nimmo & Gaidos*, 2002, and Section 1.6.2). The layer is assumed to be in a conductive state (no convective cooling, x=1). The initial temperature profile corresponds to the conductive steady-state obtained for temperature boundary conditions (eq. 4.4) and the volumetric tidal heating source H_t (eq. 7.2).

At the beginning of the simulation, shear heating rate H_s (the values adapted from *Nimmo & Gaidos*, 2002) is imposed throughout a shear zone of depth d_s. The initial temperature profile and the corresponding heating for various values of shear zone depth d_s and shear heating amplitude H_s are depicted in Figure 7.2. Once melting occurs, shear heating is expected to decrease rapidly due to reduction of the friction coefficient (cf. *Oksanen & Keinonen*, 1982). Assuming that this reduction is similar as in the case of ice viscosity μ_m, we parameterize it in the same way as in eq. (7.3):

$$Q_\mathrm{s}(d) = H_\mathrm{s} \exp(-\gamma_\mathrm{s}\phi) \qquad d \leq d_\mathrm{s} \ , \tag{7.4}$$

where d_s is the shear zone depth and γ_s is a weakening parameter. Due to the lack of knowledge, we assume γ_s=γ_m≐45 in the reference solution and vary its value later.

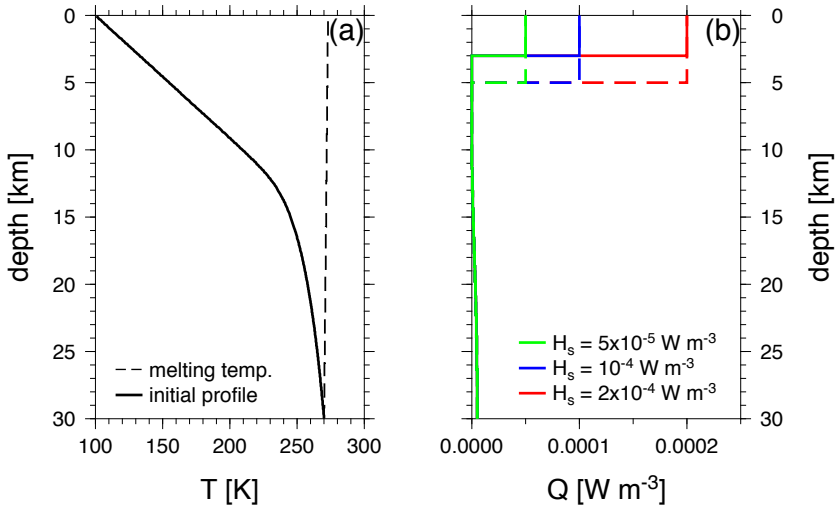

Figure 7.2: Strike-slip fault set-up. (a) Melting temperature and initial temperature profile. (b) Initial heating computed as $Q{=}H_{\rm t}{+}H_{\rm s}$ from eqs (7.1)–(7.4) for $x{=}1$, the initial temperature profile shown in panel a and three different values of $H_{\rm s}$ (distinguished by different colors). Two values of $d_{\rm s}$ are considered: $d_{\rm s}{=}3$ km (full lines) and $d_{\rm s}{=}5$ km (dashed lines).

7.2 Results

7.2.1 Hot plume set-up

The results for the hot plume simulation with $x{=}15\%$ and the model parameters given in Table 3.1 are depicted in Figure 7.3. At the beginning of the simulation, the melting temperature is reached only at the bottom boundary and melting just occurs at the base of the ice shell - the water produced there is transported almost immediately to the underlying ocean. The molten (temperate) region where water can propagate spreads gradually from the bottom boundary to the head of the plume. As long as the porosity profile is monotonic with maximum at the bottom boundary, porosity waves do not form (cf. conditions for shock wave formation in *Spiegelman*, 1993a). At approximately 90 kyr, melting begins also at the depth of about 10 km and porosity waves start to develop. However, their migration is limited within the temperate ice region where temperature is at the melting point. Roughly 40 kyr later (130 kyr after the beginning of the simulation), both temperate regions connect, thus permitting an efficient transport of water in the partially molten zone all the way to the bottom boundary (Figure 7.3, panel a). Melting temperature is reached in approximately two thirds of the ice shell but the value of porosity never exceeds 1% (Figure 7.3, panel b). The outflow of liquid water from the domain is associated with a small subsidence of the top boundary - after 300 kyr of simulation, the thickness of the computational domain is reduced by ∼250 m due to the combined effect of matrix melting and water outflow from the domain.

The total amount of liquid water in the domain as a function of time is shown in Figure 7.4 (panel a, red color). It gradually grows from zero up to a maximum value of about 35 m, which is reached at the time just before the first porosity

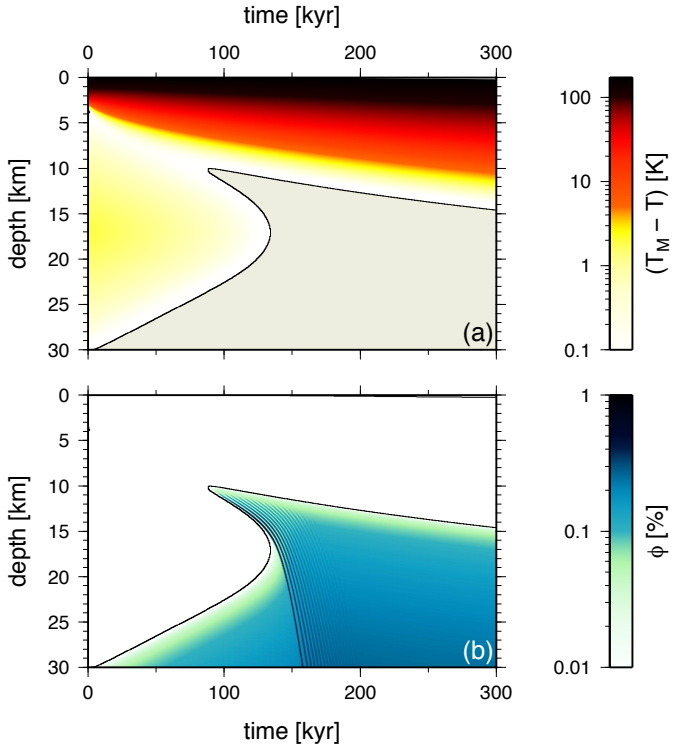

Figure 7.3: Hot plume set-up, x=15 %. (a) Space-time evolution of $T_{\mathrm{M}}-T$. The shaded region (corresponding to the colored region in panel b) marks the partially molten material at the melting temperature (temperate ice). (b) Space-time evolution of porosity. In both panels, the black line represents the boundary between the temperate ice (with non-zero porosity and temperature at the melting point, thus enabling downward water transport) and the cold ice (with zero porosity, temperature below the melting point and no water transport).

wave arrives at the bottom boundary (∼160 kyr). From that moment, the water outflow is more efficient than the water production and the overall amount of water in the ice shell gradually decreases. At the end of the simulation, a 25 m high water column still remains in the ice shell, however, the water is distributed

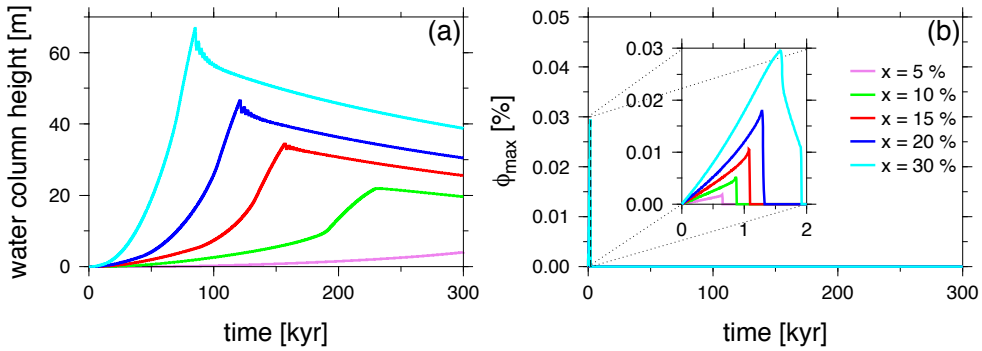

Figure 7.4: Hot plume set-up, results for different values of x. (a) Time evolution of water column height. (b) Time evolution of porosity maximum in the subsurface region (top 4 km).

over the whole temperate domain and porosity never exceeds 1% (Figure 7.3, panel b).

The detail of the time evolution of the maximum value of porosity ϕ in the subsurface region (top 4 kilometers) is illustrated in Figure 7.4 (panel b, red color). The maximum values of porosity remain very small, indicating that water produced at shallow depths never accumulates there and is transported very efficiently downwards to the internal water ocean.

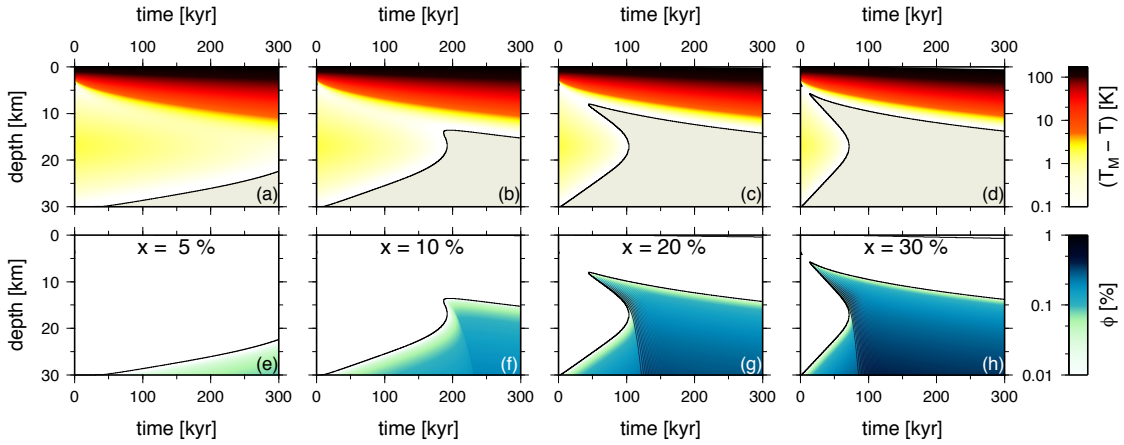

Figure 7.5: The same as in Figure 7.3 but for x=5, 10, 20, 30% (from left to right).

For higher values of x (20% and 30%), which correspond to less efficient convection and thus more efficient warming of the ice shell, the two distinct melting regions form again (Figure 7.5, panels c, g, and d, h). Since the tidal heating rate is higher, melting starts earlier and more water is produced (Figure 7.4, panel a, blue and cyan color). On the other hand, both regions coalesce earlier permitting water outflow already at approximately 120 kyr and 85 kyr, respectively. When the value of x is decreased to 10%, corresponding to enhanced convective cooling and slower warming of the ice shell, melting occurs only in the lower half of the ice shell (Figure 7.5, panels b and f) and less water is produced (Figure 7.4, panel a, green color). For an even smaller value of x (5%) melting occurs only at the base of the ice shell during the whole simulation (Figure 7.5, panels a and e), resulting in a very small amount of water produced (Figure 7.4, panel a, violet color). For all tested values of x, the maximum porosity at shallow depth stays well below 1% and thus no water accumulates there (Figure 7.4, panel b). To summarize, either no melt is produced in the subsurface region at all due to insufficient heating (x=5 and 10%), or both the subsurface and bottom temperate regions become connected within a few tens of thousands of years, allowing rapid water transport towards the bottom boundary.

7.2.2 Strike-slip fault set-up

The results for the strike-slip fault simulation with H_s=2×10^{-4} W m^{-3}, d_s=3 km and γ_s=45 are displayed in Figure 7.6 (for the values of other parameters see Table 3.1). As in the previous (hot plume) case, the first melt appears at the bottom boundary and the water flows freely from the domain to the underlying

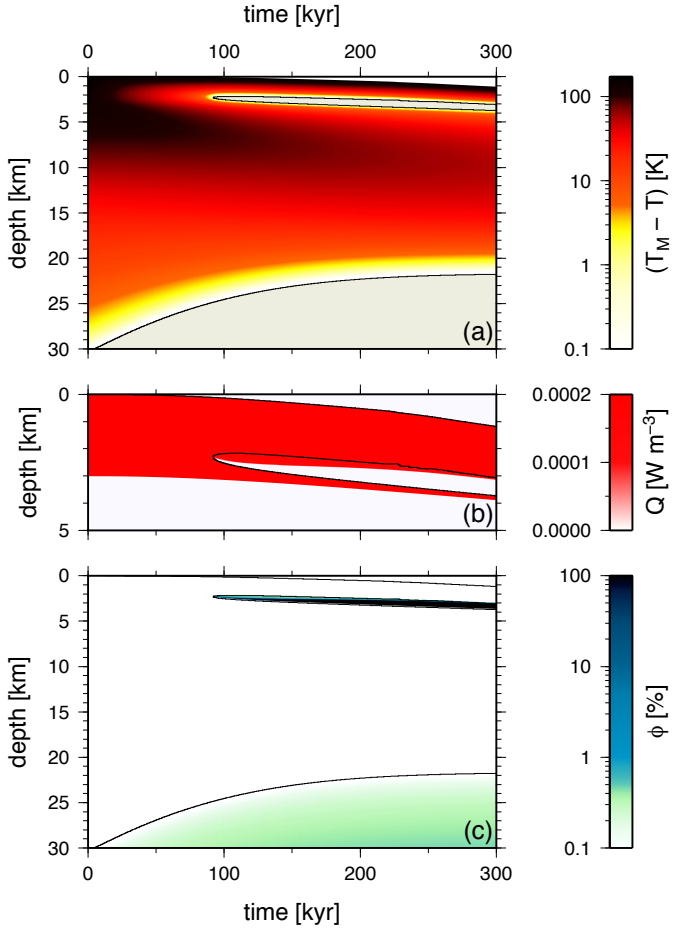

Figure 7.6: Strike-slip fault set-up, H_s=2×10^{-4} W m^{-3}, d_s=3 km and γ_s=45. (a) Space-time evolution of $T_M - T$. The shaded regions (corresponding to the colored regions in panel c) mark the partially molten material at the melting temperature (temperate ice). (b) Space-time evolution of the heating rate in the top 5 km. (c) Space-time evolution of porosity. As in Figure 7.3, the black lines represent the boundary between the temperate ice and the cold ice. The reduction of the domain thickness is apparent in the right upper corners of all panels.

ocean without creating waves. After approximately 90 kyr, melting begins also at a depth of about 2 km where the melting temperature is reached due to the enhanced shear heating. Since the ice below is cold ($T \ll T_M$, Figure 7.6, panel a) and assumed free of fractures, no water propagates downward. Even though the heating in the subsurface temperate ice region decreases rapidly due to the increasing porosity (one order of magnitude reduction per 5% of porosity increase, Figure 7.6, panel b), the liquid water is trapped there and its amount gradually grows (Figure 7.6, panel c). As the initial temperature in the upper half of the ice shell is rather low and the volumetric heating (eq. 7.2) is not very efficient there, the cold impermeable zone separating the subsurface water lens from the bottom temperate zone is preserved throughout the simulation (300 kyr). A closer inspection of the upper right corner of panel b of Figure 7.6 reveals that at the end of simulation the thickness of the domain is reduced by ∼1 km, which is mostly due to matrix melting in the shallow region.

The time evolution of water column height is depicted in panel a of Figure 7.7 (red color, full line). With its maximum reaching almost 600 m, the amount of water produced in the strike-slip fault model is much larger than in the previous hot plume model. Panel b of Figure 7.7 shows the maximum value of porosity within the shear zone ($d \leq d_s$). Once melting starts, it grows rapidly - after approximately 50 kyr it exceeds 95% and stays above this value during the rest of the simulation. As discussed in Section 7.3, our one-dimensional calculations cannot take into account possible initiation of gravitational (Rayleigh-Taylor-like) instabilities due to accumulation of dense liquids above ice, or initiation and propagation of water-filled cracks. Consequently, the amounts of water predicted here should be considered as upper limits.

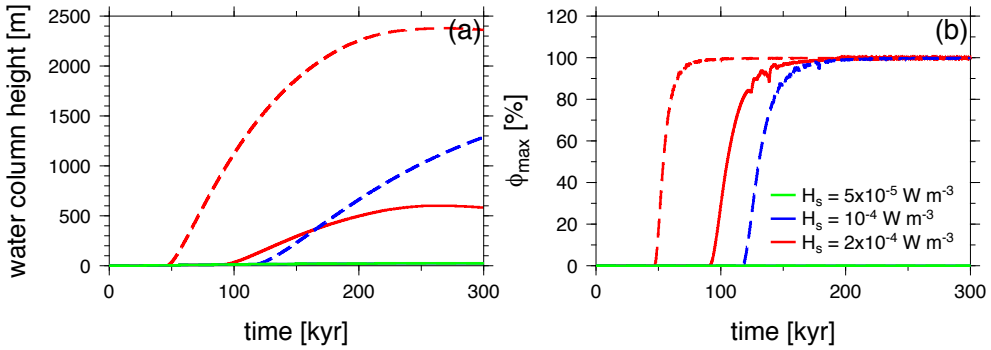

Figure 7.7: Strike-slip fault set-up, results for various combinations of H_s (distingished by colors) and d_s (full lines: d_s=3 km, dashed lines: d_s=5 km). (a) Time evolution of the water column height. (b) Time evolution of porosity maximum within the shear zone ($d \leq d_s$).

Figure 7.7 also illustrates the role of the shear heating amplitude, H_s, and the shear zone depth, d_s. For small shear-heating amplitude (H_s=5×10^{-5} W m^{-3}), no melt is produced at shallow depths (at least during 300 kyr) independently of the shear zone depth d_s. For moderate amplitude of heating (H_s=10^{-4} W m^{-3}) and deeper shear zone (d_s=5 km), a liquid water lens is created and remains stable for at least 100 kyr, but no water is produced for the same amplitude of heating and a more shallow shear zone (d_s=3 km). Increasing further the heating amplitude (H_s=2×10^{-4} W m^{-3}) enables melting also for a more realistic shear zone depth d_s=3 km (cf. *Nimmo & Gaidos*, 2002). The slight oscillations in panel b of Figure 7.7 are caused by the coupling between the temperature and porosity evolution. As the temperature just below the partially molten layer increases, the ice becomes temperate and hence water-permeable. Therefore, the molten water from above can flow downwards in the form of waves, since, in this case, porosity decreases in the direction of flow. Consequently, the maximum value of porosity is temporarily reduced due to redistribution of the liquid water over a wider layer of temperate ice.

Our numerical simulations indicate (not shown in Figure 7.7) that the above results are not affected by varying the value of the porosity weakening parameter γ_s (eq. 7.4). This parameter can slightly change the total amount of molten water but has a negligible effect on the maximum porosity in the shear zone and no effect on the thermal evolution of the cold ice layer below, and thus does not

influence the time scale of the extraction of liquid water from shallow depths.

7.3 Discussion

All our calculations assume a pure water system. The observations of colored hydrated materials within disrupted surface areas suggest that the ice shell may contain a significant fraction of contaminants (e.g. *McCord et al.*, 1998; *Kargel et al.*, 2000; *Zolotov & Kargel*, 2009). Low-eutectic constituents such as chloride salts, which are expected within the internal ocean (*Zolotov & Kargel*, 2009), could lower the melting point by several tens of Kelvins (*Kargel et al.*, 2000; *Pappalardo & Barr*, 2004). If these contaminants were uniformly distributed within the ice shell, the reduction of melting point would be uniform and the results should not be significantly different. The presence of contaminants would have a larger impact if they were located only in the upper part of the ice shell. In this case, concentrated brines might form at shallow depths and accumulate at the base of this enriched crust if the underlying ice is cold and contaminant-free, as suggested by *Schmidt et al.* (2011). In this context, the volume of the accumulated salty water above a hot plume may be larger than in the case of a pure water system. However, for reasonable salt contents (1–2 wt %), the volume fraction of brines should probably not exceed 5–10%. Further modeling efforts are, however, needed to quantify more precisely the role of low-eutectic constituents.

Our model is clearly limited by its 1d geometry. Only the vertical matrix deformation associated with compaction is included, and no lateral variations in water production and matrix properties can be treated. The inclusion of lateral variations may change the results by focusing the water extraction into the warmest part of the ice shell (in the center of a hot plume). Moreover, in our 1d approach, we cannot take into account the ice flow associated with buoyancy variations. In the hot plume case, for instance, we cannot consider the effect of the upwelling ice velocity. According to the simulations of *Tobie et al.* (2003), the velocities in hot plumes are of the order of 3×10^{-8} m s^{-1} for Rayleigh numbers of about 5×10^{6}, before melting initiates. For a moderate value of permeability constant (k_0=10^{-9} m^2), the velocity of downward percolating water is at least 4 times larger than the upwelling velocity. Both velocities are comparable only for the lower bound value (k_0=10^{-10} m^2, cf. Figure 2.3). In this context, the upwelling velocity may inhibit melt extraction. However, as shown in *Tobie et al.* (2003), the upwelling velocities are strongly reduced when meltwater is not efficiently extracted, leading eventually to downwelling of the molten plumes even when water fraction reaches values as low as 1–2%. The extension into 2d or 3d geometry will be needed to properly describe the lateral flows and the development of convective instabilities.

Similarly, a 2d/3d approach is necessary to describe the destabilization of large volume of water accumulated below a shear zone or at the base of a salt-rich crust above a hot plume. The accumulation of dense liquids above an impermeable cold ice layer should lead to the development of gravitational (Rayleigh-Taylor-like) instabilities, which cannot be properly described in our 1d approach. According to the analytical description of *Whitehead & Luther* (1975), the time required to destabilize a dense water reservoir above an ice layer is longer than 10 kyr only for

ice viscosities larger than 10^{22} Pa s. Such high viscosity values are possible only for temperatures lower than 160 K, which implies that large volumes of water can be present at shallow depths only in the case of a cold conductive layer subjected to very intense localized heating.

Furthermore, our model neglects the effect of hydrofracturing, possibly relevant in the strike-slip fault set-up. On the Earth, crevasse hydrofracturing has been shown to allow a very rapid drainage of supraglacial lakes towards the glacier base (cf. *Krawczynski et al.*, 2009; *Irvine-Fynn et al.*, 2011). As discussed in Chapter 2, differences in physical settings make direct comparison between Earth's and Europa's hydrological system questionable. On Europa, the best candidate environment for nucleation and propagation of water-filled cracks would be in cold ice regions beneath a large volume of accumulated water (similar to what we obtain in the strike-slip fault set-up). A strong effect counterbalancing this mechanism would however be the fast freezing of water in such a cold environment (typically several tens of Kelvins below the melting point in our results for the strike-slip fault set-up). The corresponding closure rate depends on the crack geometry and water supply rate and its inclusion would require additional effort (cf. *Michaut & Manga*, 2014).

Both gravitational instabilities and hydrofracturing processes may become predominant only once a sufficient volume of water is accumulated. Further modeling is needed to evaluate the critical volume for which these processes dominate in Europa's ice shell conditions and to understand how they differ from those on the Earth. In any case, once activated, these processes would reduce the amount of accumulated water, and therefore the volumes reported here should be considered as upper limits.

7.4 Summary

In this chapter, we investigated the conditions under which water can be generated and transported by downward two-phase flow within Europa's ice shell. A two-phase mixture model was developed in a 1d framework, distinguishing two possible states: temperate (partially molten ice, with some amount of interstitial water) and cold (purely solid ice below the melting point).

We considered two distinct geophysical contexts possibly leading to melting at shallow depths within Europa's ice shell. Our simulations show that water produced in the head of a tidally-heated hot plume is rapidly extracted (within less than a few hundred kiloyears) and no water accumulates at shallow depths - the maximum porosity never exceeds 1%. In contrast, in the context of a fault subjected to tidally-induced strike-slip motions, a large fraction of water can accumulate just below the fault, as long as the underlying ice layer remains cold, conductive and free of fractures. Our models indicate that complete melting is soon achieved in a layer a few kilometers below the surface for a shear heating rate of at least 10^{-4} W m^{-3}. Our calculations further suggest that the fault must be active during at least 100 kyr and associated with a periodic strike-slip motions with the shear velocities of about 10^{-7}–10^{-6} m s^{-1} (cf. *Nimmo & Gaidos*, 2002) in order to initiate significant melting. The water production and accumulation below the shear zone might explain the formation of water sills advocated by *Dombard et al.* (2013) as a necessary ingredient to produce the morphology of

Europa's ubiquitous double ridges.

Overall, despite some simplifications in the water transport description, our simulations showed that accumulation of a significant water volume above warm ice plumes is very unlikely, whereas it may be temporarily possible below recently active double ridges subjected to large strike-slip motions. Transient water accumulation ($\leq$100 kyr) and drainage may play a key role in the dynamics of Europa's ice shell and may be revealed by future exploration missions (*Grasset et al.*, 2013; *Pappalardo et al.*, 2013). Future modeling will help to understand the consequences of water accumulation and transport in terms of mass and heat transfer through the ice shell, as well as their surface expression.

8. Meltwater production and gravitational stability of water lenses in the ice shell of Europa

In the previous chapter we have investigated the possibility of ice melting at shallow depths within Europa's shell for two geodynamic contexts. We have studied the stability of a potentially newly-emerged meltwater lense in one dimension, considering constant ice viscosity. As discussed in Section 7.3, this approach is limited by its one-dimensional character and can account neither for the lateral ice flows nor for the destabilization of larger water lenses due to formation of gravitational instability. Also the temperature evolution cannot be properly described in one dimension. Finally, as already discussed, ice viscosity is highly nonlinear and, for conditions within Europa's ice shell, probably far from constant. That is why in this chapter we perform a study similar to that in Chapter 7 - while we considered only one-dimensional geometry and constant ice viscosity in the previous chapter, we work in two dimensions and consider temperature-, porosity- and stress-dependent ice viscosity in this chapter. On the other hand, a porous (two-phase) flow is neglected in this chapter, contrary to Chapter 7 - these two chapters thus complement each other.

To investigate meltwater production in Europa's ice shell, we solve the system of equations (4.74) together with boundary conditions (4.75)–(4.77) and (4.80)–(4.82). This system (obtained by setting the ice permeability to zero) represents the impermeable limit of two-phase equations and can be considered as a first step towards a more complex system that would fully couple the two-phase flow with the solid-state thermal convection[1]. In this impermeable approximation, water is locked within the ice matrix and cannot percolate through microporous veins, but is rather advected with the ice. When compared with the results of a one-dimensional study from Chapter 7, the two-dimensional approach should provide a better assessment of the effect of gravity on the water accumulated in a partially molten lense by enabling the transport of this material through the formation of gravitational (Rayleigh-Taylor-like) instability which is not possible in one dimension (cf. discussion in Section 7.3 and compare results of Sections 5.2.2 and 6.3.2). A two-dimensional model also allows to describe the temperature evolution in the ice shell more properly. Given that water transport by porous flow is faster than water advection by the (convecting) ice matrix (cf. water and ice velocities in Figure 6.2), the time scales of gravitational stability of partially molten material provided in this chapter can be considered as maximum estimates.

We use numerical method described in detail in Section 4.3 (cf. Algorithms 2 and 3). If not mentioned otherwise, we consider physical parameters from Table 3.1. For numerical reasons, a non-zero value of background porosity ϕ^{off} must be prescribed (cf. Section 4.3.1). In Section 6.2.4, we found that in the case of porous flow, the background porosity slightly affects the water extraction time scales. However, in the case of the impermeable limit of governing equations, porosity is only advected together with the ice matrix. Its effect on the trans-

[1]Such a model will be considered in the future study.

port velocity is thus only due to density difference and not due to its effect on permeability, i.e. only the difference between the actual porosity value and the background value matters, while the absolute value of porosity does not matter (if it is kept reasonably small, i.e. not exceeding a few percents). Based on experimental measurements (cf. *Golden et al.*, 1998), ice with porosity of 5% can still be regarded as impermeable for water (and therefore 'cold' in the glaciologic terminology, cf. Chapter 2) - we therefore set the background value as ϕ^{off}=5% and keep it unchanged throughout this chapter. However, to further verify its negligible role, we compared the results of the reference simulation from Section 8.2 with d=0.7 mm computed for two different values of background porosity, ϕ^{off}=1 and 5% (results for ϕ^{off}=1% are not shown in the manuscript) and we found qualitatively very similar results. Likewise, the SUPG parameter is not varied in our study. Motivation for this decision is the study performed in Section 6.2.1 which showed small difference between results for various non-zero values of parameter τ. We choose τ=0.5 and keep it throughout this chapter.

We start by comparing our results with these of *Tobie et al.* (2003) for a case of melt production and transport within a hot plume that develops in a tidally-heated convecting shell with temperature- and porosity-dependent viscosity (Section 8.1). In the next section we perform a similar study but considering composite ice rheology (Section 8.2). Finally, in Section 8.3 we explore the possibility of melting at the base of a strike-slip fault and investigate the gravitational stability of the newly formed molten lense. In each of these sections, we provide a short description of the particular model set-up corresponding to considered geophysical context and then we continue with the results. A short discussion and summary are given in Section 8.4. All computations in Sections 8.1 and 8.2 are performed in a domain with aspect ratio (width to height) 2, on a mesh consisting of 200×100 elements, and due to large viscosity contrast across the shell (at least 10^6) are in the conductive lid regime. In Section 8.3, the aspect ratio is 1 and the mesh consists of 100×100 elements.

8.1 Hot plume: comparison with *Tobie et al.* (2003)

As mentioned in Chapter 1, several geophysical contexts were suggested that might initiate partial melting within Europa's ice shell. One of them is melting in the hot plumes triggered by the enhanced tidal heating due to thermally-reduced viscosity suggested by *Sotin et al.* (2002) and further studied by *Tobie et al.* (2003). Here we extend their study by considering compressible mixture of two incompressible phases (cf. remark in Section 4.3.1). We compare our results with those reported by *Tobie et al.* (2003) and investigate also the effect of mixture compressibility.

8.1.1 Model set-up

For the purpose of comparison with *Tobie et al.* (2003), we take $[\boldsymbol{r}]$=20 km and $[L]$=3×10^5 J kg^{-1} instead of values from Table 3.1. Also, we consider Frank-Kamenetskii (cf. *Tobie et al.*, 2003) approximation of temperature-dependent

viscosity (instead of the Arrhenius law, eq. 1.3):

$$\mu_{\rm m} = \mu_{\rm m}^{\rm bot} \exp\left(-\gamma_{\rm T} \frac{T - T_{\rm M}}{\Delta T}\right) , \tag{8.1}$$

with $\mu_{\rm m}^{\rm bot}$ the reference (bottom) viscosity at the melting point and

$$\gamma_{\rm T} = \frac{E_{\rm a} \Delta T}{R T_{\rm M}^2} , \tag{8.2}$$

where $E_{\rm a}$=50 kJ mol^{-1} is the activation energy, $T_{\rm M}$=270 K is the melting temperature (taken constant troughout the domain) and ΔT=170 K is the temperature difference across the shell. For parameters relevant for Europa, this leads to viscosity contrast of $\sim 1.2 \times 10^6$. Porosity weakening is also included in a form slightly modified from eq. (1.5) to cancel out the effect of background porosity:

$$\mu_{\rm m}^{\rm soft} = \begin{cases} \exp(-\gamma_{\rm m}(\phi - \phi^{\rm off})) & \phi > \phi^{\rm off} \\ 1 & \phi \leq \phi^{\rm off} \end{cases} , \tag{8.3}$$

with $\gamma_{\rm m}$=45 corresponding to one order of magnitude viscosity decrease induced by porosity ϕ=5% (cf. *De La Chapelle et al.*, 1999; *Tobie et al.*, 2003). The tidal heating is taken from *Tobie et al.* (2003) as well:

$$Q_{\rm t} = \frac{2 H_{\rm max}}{\frac{\mu_{\rm m}}{\mu_{\rm m}^{\rm max}} + \frac{\mu_{\rm m}^{\rm max}}{\mu_{\rm m}}} , \tag{8.4}$$

with $H_{\rm max}$ the maximum volumetric dissipation rate that occurs at viscosity $\mu_{\rm m}^{\rm max}$, chosen here in accordance with *Tobie et al.* (2003) as $\mu_{\rm m}^{\rm max}$=1.5×10^{14} Pa s.

8.1.2 Results

For the reference simulation, we consider that $\mu_{\rm m}^{\rm bot}$=$\mu_{\rm m}^{\rm max}$=1.5×10^{14} Pa s. The bottom Rayleigh number, defined as

$$\mathrm{Ra}_{\rm bot} = \frac{\alpha \rho_{\rm m}^2 c_{\rm m} g \Delta T [\boldsymbol{r}]^3}{k_{\rm m}^T \mu_{\rm m}^{\rm bot}} , \tag{8.5}$$

is then equal to 1.5×10^6. The maximal tidal heating rate is chosen again in accord with *Tobie et al.* (2003) as $H_{\rm max}$=2.7×10^{-6} W m^{-3}.

Figure 8.1 shows time evolution of ice velocity and porosity from $t\sim$963 kyr (shortly after the melting starts) to $t\sim$1219 kyr. Melting starts at the bottom boundary and occurs also at the top of the ascending plume (cf. panels a–d). After approximately 100 kyr, the amount of melt accumulated at the top of the plume is large enough to inhibit the ascent of warmer material (panel e) and to initiate its collapse. Even though the porosity difference between the molten region and the background value is only a few percents ($\leq$3%), the majority of surplus water is very quickly (within $\lesssim$200 kyr) transported towards the bottom boundary with the collapsing ice (panels g–j). The molten material accumulates at the bottom boundary since water is in our impermeable limit transported only within ice and the bottom boundary is locked for the vertical ice movement (cf.

eq. 4.77). Figure 8.2 shows the temperature and heating rate at t∼963 kyr (corresponding to panels a, b in Figure 8.1) - the maximum heating is concentrated

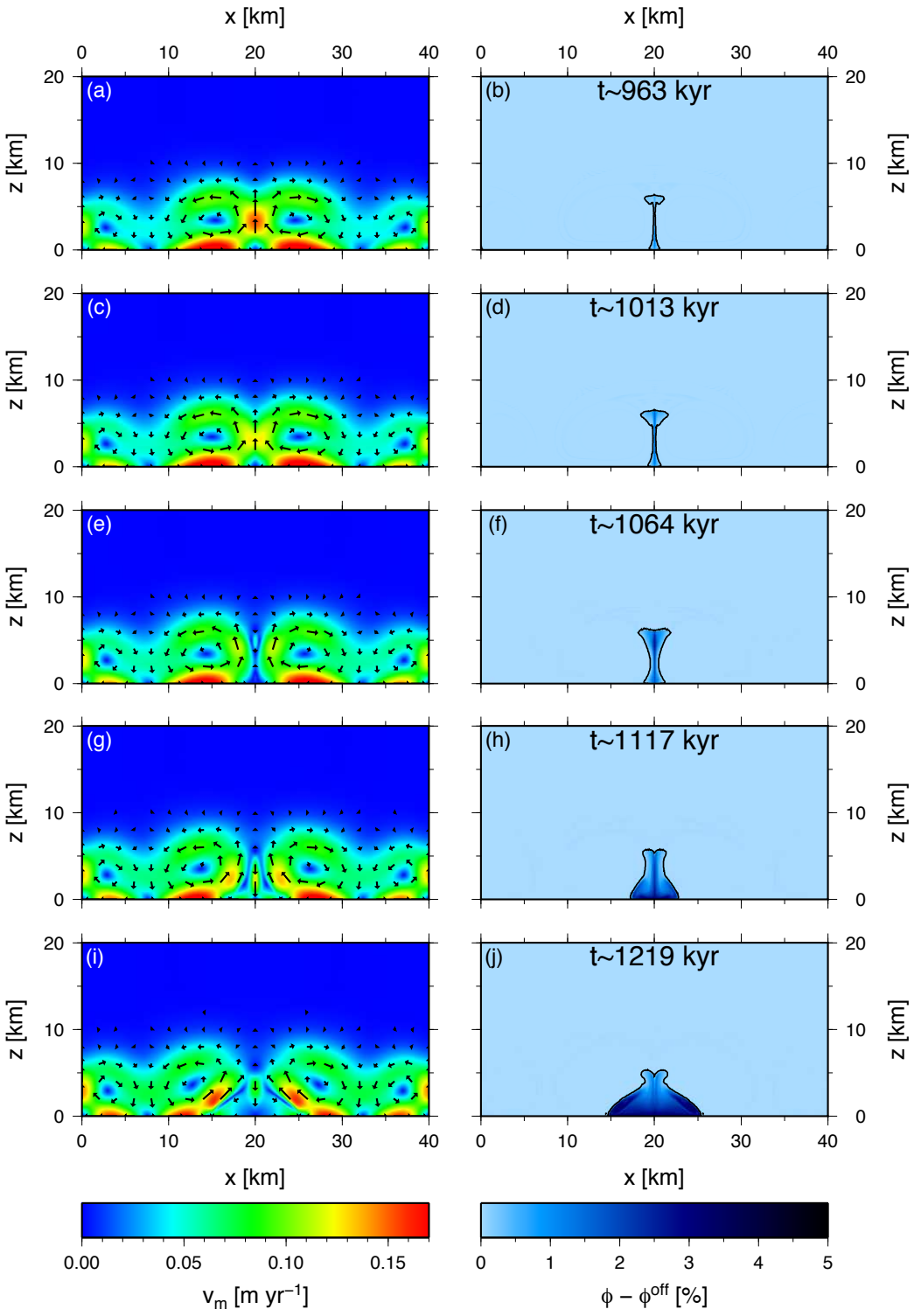

Figure 8.1: Snapshots of ice velocity (left column) and porosity (right column) computed with $H_{\max}$=2.7×10^{-6} W m^{-3}, $\mu_{\mathrm{m}}^{\max}$=1.5×10^{14} Pa s and $\mu_{\mathrm{m}}^{\mathrm{bot}}$=1.5×10^{14} Pa s. Time increases from top to bottom. Black contours in porosity fields bound porosity larger than the background value (ϕ>ϕ^{off}).

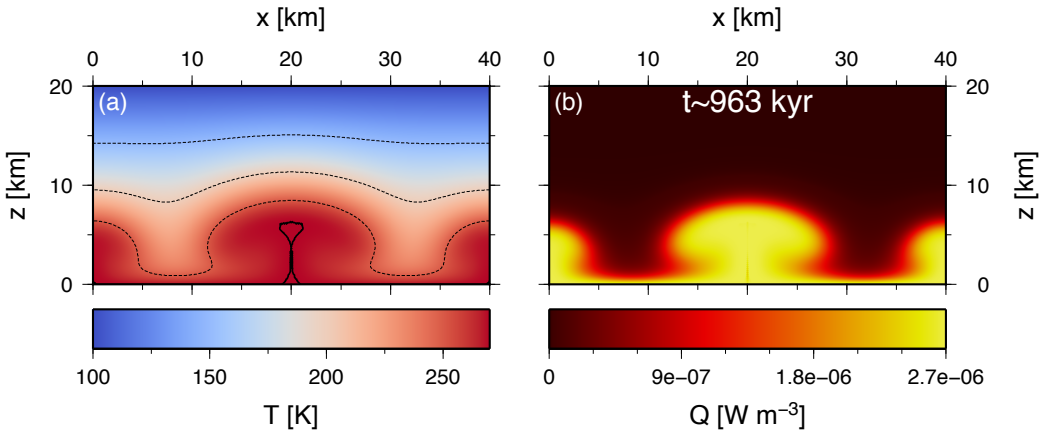

Figure 8.2: Temperature (left) and heating rate (right) at the same time as panels a, b in Figure 8.1. The temperature isocontours are spaced by 50 K and the thick black contour marks the melting temperature.

within the hot plume, in agreement with the findings of *Tobie et al.* (2003).

In order to verify our results, we check the conservation of mass and energy - we integrate in time (from $t{=}0$ to $t{=}\tau$) and space (over the whole domain Ω) equations (4.74a) and (4.74d) with the terms r_f and $-\frac{[\phi]}{\mathcal{T}}r_\mathrm{f}$, respectively, added on their right-hand sides (to account for the effect of phase change). Taking into account the appropriate boundary conditions, this leads to:

$$\int_\Omega \phi \,\mathrm{d}x\,(t{=}\tau) = \int_\Omega \phi \,\mathrm{d}x\,(t{=}0) + \int_0^\tau \int_{\Gamma_\mathrm{T}} \frac{\mathcal{V}}{[\phi]}(1{-}[\phi]\phi)\boldsymbol{v}_\mathrm{m}\cdot\boldsymbol{n}\,\mathrm{d}s\,\mathrm{d}t + \int_0^\tau \int_\Omega r_\mathrm{f}\,\mathrm{d}x\,\mathrm{d}t \tag{8.6}$$

and

$$\begin{aligned}\int_\Omega T\,\mathrm{d}x\,(t{=}\tau) \;&=\; \int_\Omega T\,\mathrm{d}x\,(t{=}0) - \int_0^\tau\int_\Omega \mathcal{V}\boldsymbol{v}_\mathrm{m}\cdot\nabla T\,\mathrm{d}x\,\mathrm{d}t \\ &+\; \int_0^\tau\int_{\Gamma_\mathrm{B}\cup\Gamma_\mathrm{T}} \mathcal{V}\nabla T\cdot\boldsymbol{n}\,\mathrm{d}s\,\mathrm{d}t + \int_0^\tau\int_\Omega \frac{[\phi]}{\mathcal{T}}(Q_\mathrm{T}{-}r_\mathrm{f})\,\mathrm{d}x\,\mathrm{d}t\ ,\end{aligned} \tag{8.7}$$

respectively. Figure 8.3 depicts the left- and right-hand sides of eqs (8.6) and (8.7) and shows that the balances are well conserved.

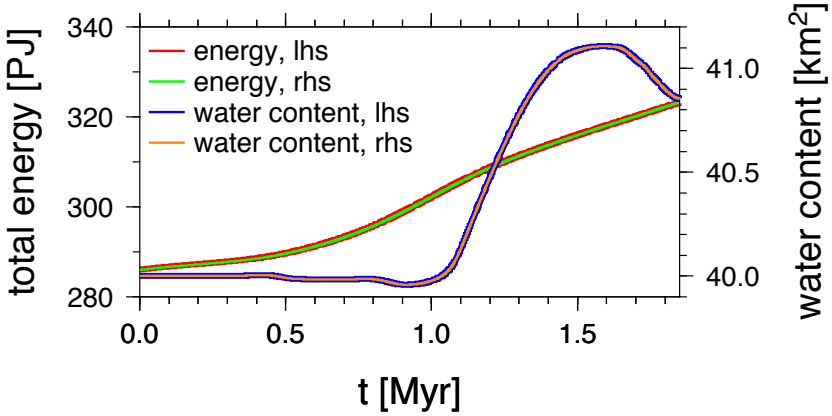

Figure 8.3: Conservation of mass and energy for the reference simulation.

The role of delayed tidal heating introduction and of mixture compressibility

While we included tidal heating from the very beginning of the simulation, *Tobie et al.* (2003) computed a quasi steady-state without heating and included it only after convection in the shell was well developed (personal communication). To even more assimilate our results with these of *Tobie et al.* (2003), we proceed in the same manner: after reaching a quasi steady-state without tidal heating, we add the heating and consider two possibilities - an incompressible mixture (by setting the right-hand side of eq. 4.74b zero), that should closely correspond to the approach of *Tobie et al.* (2003), and a compressible mixture (our formulation).

The difference between compressible and incompressible mixture formulation is however, for this case, negligible, as can be seen from Figure 8.4, that shows the time evolution of the total amount of water within the domain (left-hand side of eq. 8.6) for these two cases - the only difference is that in the case of incompressible mixture (green line) a slightly larger amount of water is generated.

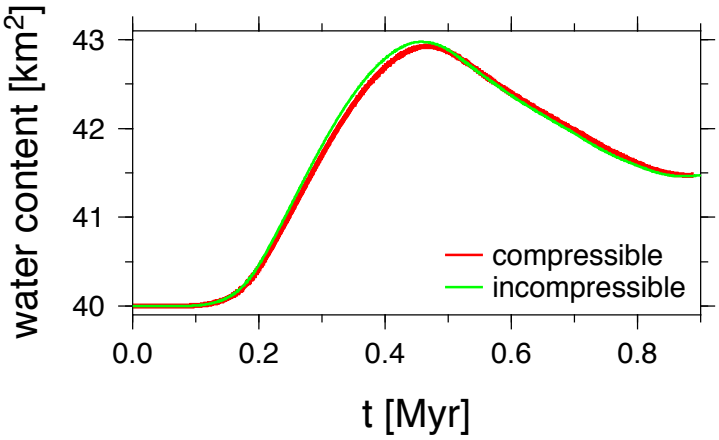

Figure 8.4: Time evolution of water contents for simulations with heating only added after reaching a quasi steady-state. Two different mixture formulations are considered: compressible (red) and incompressible (green, cf. text).

Comparing the water content from these two simulations with the water content from our reference simulation (with heating considered from the beginning of simulation), we observe that more water is produced when a quasi steady-state is reached first - this can be seen also from Figure 8.5 that shows time evolution of porosity (to be compared with the right column of Figure 8.1). Here, as in the reference case, melting occurs at the bottom boundary as well as at the top of the hot plume (panels a, b)[2]. After approximately 60 kyr, the amount of meltwater is large enough to stop the upwelling of warm ice (panel c) and the majority of generated meltwater collapses down with sinking ice after another ∼60 kyr. The overall evolution closely resembles that of the reference simulation (Figure 8.1), only it happens approximately two times faster (time frame of 123 kyr instead of

[2]Note that the plume is now a few kilometers higher since melting did not inhibit the formation of the plume before a quasi steady-state was reached, contrary to the reference case, where the onset of melting before reaching a fully developped plume slightly slowed down its formation.

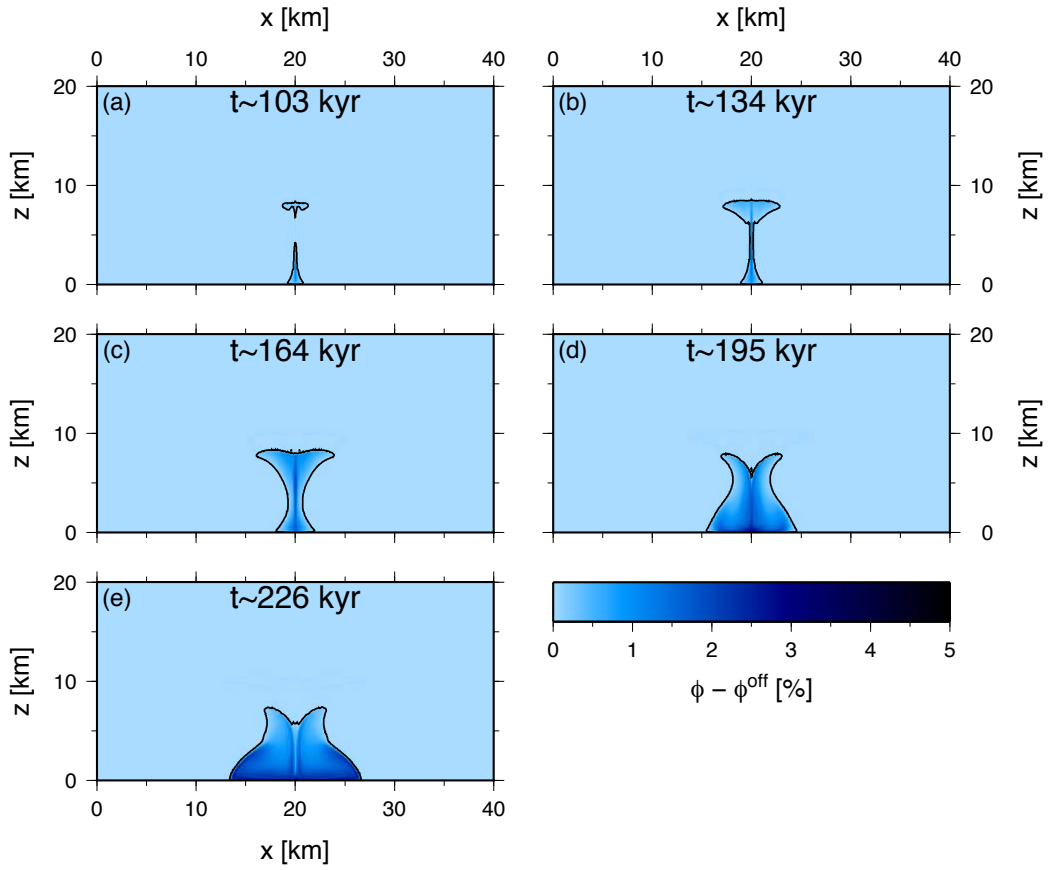

Figure 8.5: Snapshots of porosity for the simulation when heating is introduced after reaching a quasi steady-state and considering compressible mixture (cf. text). Computed with $H_{\max}$=2.7×10^{-6} W m^{-3}, $\mu_{\rm m}^{\max}$=1.5×10^{14} Pa s and $\mu_{\rm m}^{\rm bot}$=1.5×10^{14} Pa s. Time increases from top to bottom and from left to right. Black contours in porosity fiels bound porosity larger than the background value (ϕ>$\phi^{\rm off}$).

256 kyr). This is due to the fact that in the latter case (steady-state+heating), a larger region is at (or close to) the melting point and therefore more melt is produced (which in turn quickens the whole process). Overall, the difference between these two approaches (inclusion of heating from the very beginning or its introduction only after a quasi steady-state is reached) is rather quantitavive than qualitative and, since we do not see a reason to delay the introduction of heating, in what follows, the tidal heating will be included from the very beginning of all the simulations.

The role of bottom viscosity and of tidal heating amplitude

Until now, we have assumed that the melting point viscosity $\mu_{\rm m}^{\rm bot}$ is equal to the viscosity that maximizes the heating ($\mu_{\rm m}^{\max}$=1.5×10^{14}). When four times smaller viscosity is considered, $\mu_{\rm m}^{\rm bot}$=$\mu_{\rm m}^{\max}$/4=3.75×10^{13} Pa s (corresponding to Ra$_{\rm bot}$=6×10^6) while keeping the same heating rate $H_{\max}$=2.7×10^{-6} W m^{-3}, the melting temperature is not reached (even after 600 kyr of simulation), since the maximum heating occurs in the cold downwellings (cf. *Tobie et al.*, 2003). To reach the melting temperature and start melting the ice, a larger value of the

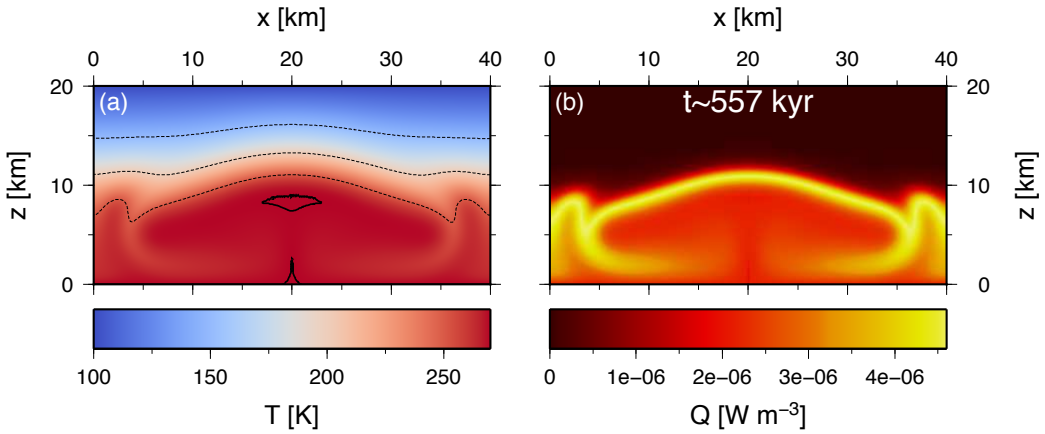

Figure 8.6: The same as in Figure 8.2 but for $\mu_{\rm m}^{\rm bot}$=3.75×10^{13} Pa s and $H_{\rm max}$=4.6×10^{-6} W m^{-3}.

maximal heating rate is necessary. Following *Tobie et al.* (2003), we choose $H_{\rm max}$=4.6×10^{-6} W m^{-3}, for which temperature and heating rate are depicted in Figure 8.6 shortly after the onset of melting. Even though the maximal tidal heating still occurs within the cold downwellings, the heating rate within the plume interior is large enough to reach the melting temperature. As in the pre-

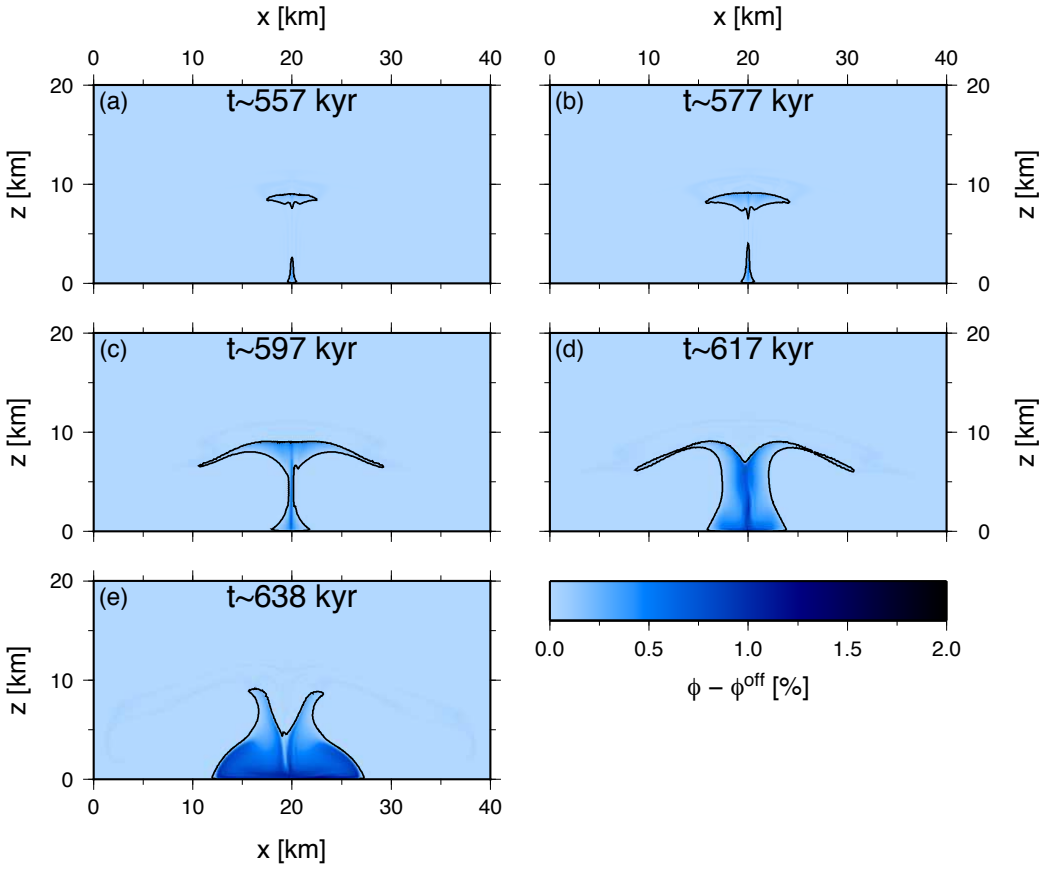

Figure 8.7: The same as in Figure 8.5 but for $\mu_{\rm m}^{\rm bot}$=3.75×10^{13} Pa s and $H_{\rm max}$=4.6×10^{-6} W m^{-3} introduced at the beginning of the simulation.

vious cases, melting first occurs at the bottom boundary and at the top of the ascending plume (cf. Figure 8.7, panels a, b) and, due to larger heating at the top of the plume (cf. Figure 8.6), the partially molten area extends also laterally (Figure 8.7, panel c). However, after approximately 60 kyr, the surplus water content (with respect to the background value ϕ^{off}=5%) starts to collapse down as in the previous cases (Figure 8.7, panel d) and after another ∼20 kyr, the majority of melt is concentrated at the bottom boundary (Figure 8.7, panel e).

Overall, our results agree qualitatively with the results of *Tobie et al.* (2003) and suggest that accumulation of a partially molten material elsewhere than on the bottom boundary is in the current setting (temperature- and porosity-dependent viscosity and uniform melting temperature) almost impossible.

8.2 Hot plume: the effect of stress-dependent viscosity

In this section we investigate the effect of stress-dependent rheology on the process of melting and water transport within a convecting ice shell. The ice viscosity now depends on temperature, stress, and porosity (cf. eqs 1.1, 1.2, and 1.5).

8.2.1 Model set-up

Due to high computational demands, we can no longer use the Taylor-Hood element spaces. Instead, we use linear elements for all mechanical quantities (porosity ϕ, dynamic pressure Π, and ice velocity $\boldsymbol{v}_{\text{m}}$, cf. Sections 6.2.3 and 6.4.1) and regularize the dynamic pressure Π by taking

$$\frac{\mathcal{V}}{[\phi]}\nabla\cdot\boldsymbol{v}_{\text{m}} = -\frac{\mathcal{R}}{1+\mathcal{R}}r_{\text{f}} + \varepsilon_\pi\nabla^2\Pi \tag{8.8}$$

with ε_π=10^{-6} instead of eq. (4.74b). Considering further (only for the purpose of regularization)

$$\nabla\Pi\cdot\boldsymbol{n} = 0 \tag{8.9}$$

at the bottom and side boundaries, Γ_{B} and Γ_{S}, respectively (in order to avoid surface integrals arising from the regularization term), and bearing in mind that ω=0 at the top boundary (due to eq. 4.81), the weak form of eq. (8.8) can be written as

$$\int_\Omega \frac{\mathcal{V}}{[\phi]}(\nabla\cdot\boldsymbol{v}_{\text{m}})\,\omega\,\mathrm{d}x + \int_\Omega \frac{\mathcal{R}}{1+\mathcal{R}}r_{\text{f}}\,\omega\,\mathrm{d}x + \int_\Omega \varepsilon_\pi\nabla\Pi\cdot\nabla\omega\,\mathrm{d}x = 0 \qquad \forall\omega{\in}W \tag{8.10}$$

and will be used instead of eq. (4.86)[3]. Since we no longer attempt to compare our results with these of *Tobie et al.* (2003), we again take values of parameters from Table 3.1, namely $[L]$=3.33×10^5 J kg^{-1} (cf. *Lide*, 2004) and $[\boldsymbol{r}]$=30 km, which is necessary for the onset of convection with medium to larger grain sizes ($d\gtrsim$0.5 mm) while keeping reasonable values of tidal heating (cf. *Han & Showman*,

[3]In the temperate ice setting with composite rheology and linear elements (Sections 6.4.1 and 6.4.3), no regularization is necessary since the term $\sim\nabla^2\Pi$ (or $\sim\nabla\Pi\cdot\nabla\omega$ in the weak form) is already present in the formulation (cf. eq. 4.63).

2011). We consider grain sizes from the range of 0.1–5.0 mm, that are plausible for Europa and allow convection to occur for Europa-like ice shell thicknesses (∼30 km) and realistic values of tidal heating rates (cf. *Tobie et al.*, 2003; *Han & Showman*, 2011). We use parameters for the deformation mechanisms from Table 1.1 (cf. *Goldsby & Kohlstedt*, 2001; *Durham et al.*, 2001). Tidal heating is considered in the same form as in Section 8.1 - we keep $\mu_{\rm m}^{\rm max}$=1.5×10^{14} Pa s and vary $H_{\rm max}$ from 3 to 8×10^{-6} W m^{-3}. Heating is introduced from the very start of all our simulations.

In the previous section, we have confirmed the important role of the ratio of the bottom (reference) viscosity $\mu_{\rm m}^{\rm bot}$ and the viscosity that maximizes the tidal heating, $\mu_{\rm m}^{\rm max}$, reported by *Tobie et al.* (2003). In this section, for the purpose of comparison, we define $\mu_{\rm m}^{\rm bot}$ as a viscosity corresponding to diffusion creep at the bottom boundary (T=$T_{\rm M}$) for a material in rest (zero dynamic pressure Π, no deformation).

For all simulations in this section, the viscosity contrast is approximately 10^{10} (no viscosity cut-off is applied) as a result of combined effect of strengthening towards the top boundary due to temperature decrease and weakening due to presence of melt within the partially molten areas. The implementation of viscosity cut-off (that would roughly approximate the brittle ice rheology, cf. *Han & Showman*, 2005) could substantially modify our results and will be comprised in the future study. The prevailing mechanisms are diffusion creep (acting within approximately the bottom half of the domain), dislocation creep (towards the cold top boundary) and grain boundary sliding (in a layer within these two mechanisms).

8.2.2 Results

For our reference simulation, we choose $H_{\rm max}$=3×10^{-6} W m^{-3} and d=0.7 mm - the bottom viscosity is then $\mu_{\rm m}^{\rm bot}$=1.56×10^{14} Pa s leading to Ra$_{\rm bot}$=4.8×10^{6} and $\mu_{\rm m}^{\rm bot}$∼$\mu_{\rm m}^{\rm max}$. Based on the results of Section 8.1, this choice should lead to maximal tidal heating within the hot plumes, which is indeed the case as can be seen from Figure 8.8 that shows the temperature and heating shortly after the

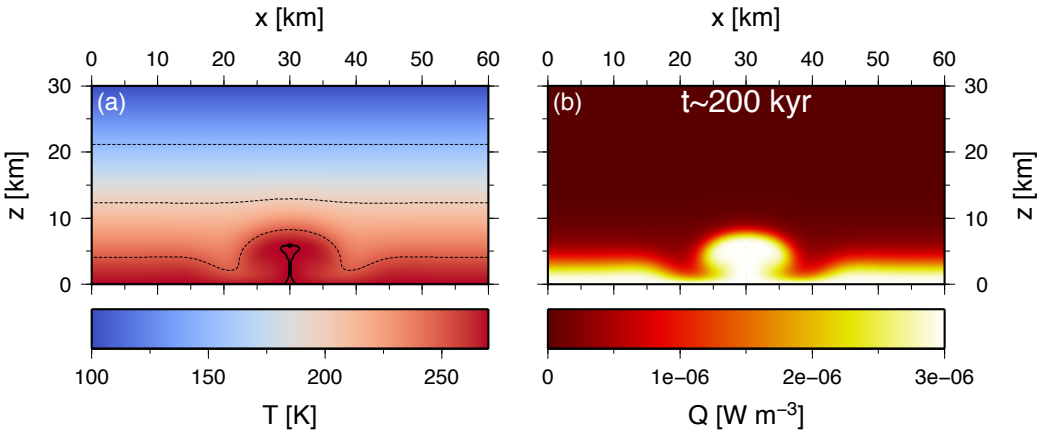

Figure 8.8: The same as in Figure 8.2 but for $H_{\rm max}$=3×10^{-6} W m^{-3} and composite ice rheology with d=0.7 mm.

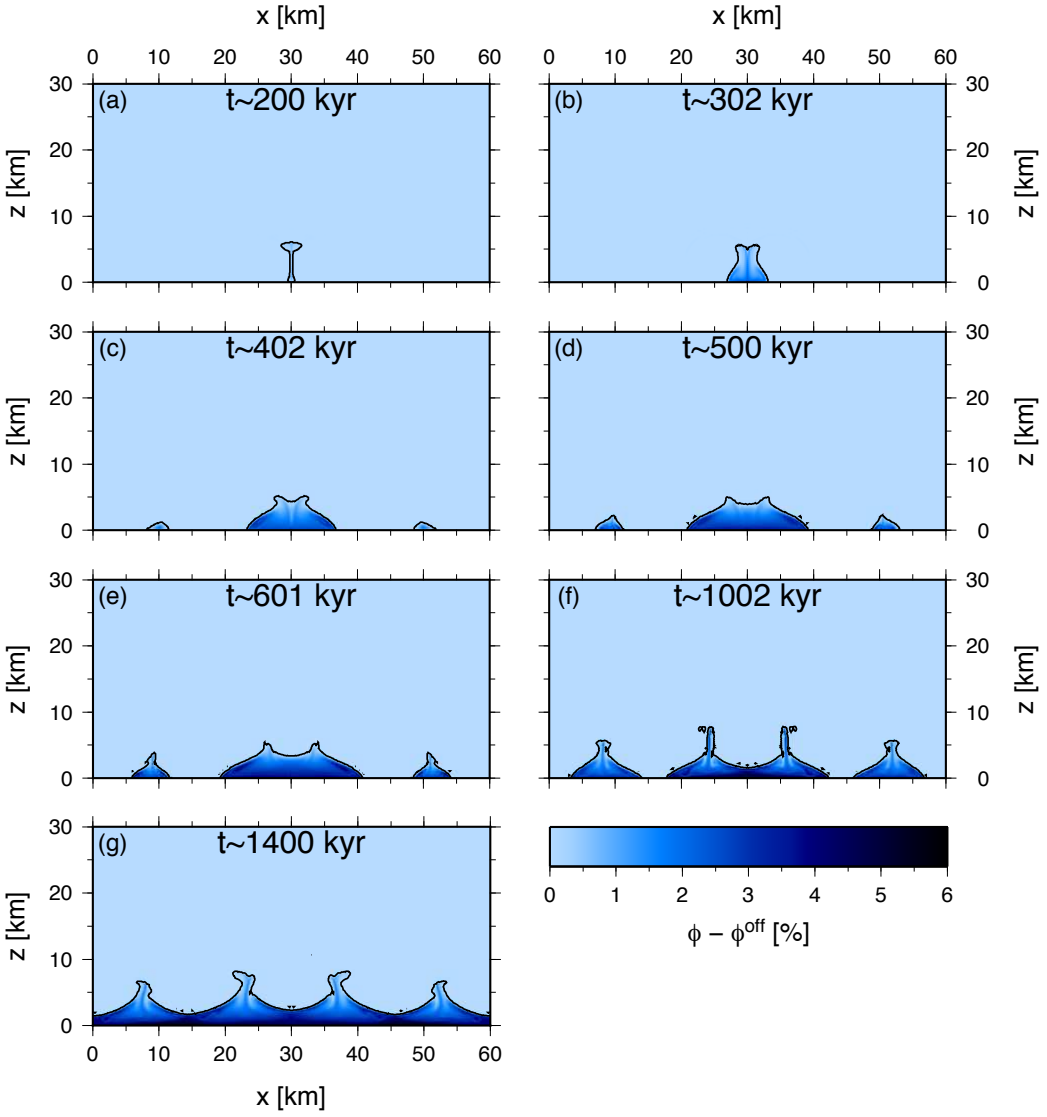

Figure 8.9: The same as in Figure 8.5 but for $H_{\max}$=3×10^{-6} W m^{-3} and composite ice rheology with d=0.7 mm.

onset of melting (t∼200 kyr).

Time evolution of porosity ϕ is depicted in Figure 8.9 - as in the previous cases, melting starts within a central hot plume which is rather quickly (during ∼200 kyr) destabilized due to negative melt buoyancy (panels a–c). Melting then continues within two side plumes (panels d–e) and also within two central plumes that originated from the former central plume destabilized by melt (panel f). After approximately 1200 kyr from the onset of melting, a partially molten region covers the whole bottom boundary (panel g) with the surplus (w.r.t. the background value ϕ^{off}) maxima of about 6%. The maximum height occupied by some amount of partial material (ϕ>ϕ^{off}) is however <10 km.

Time evolution of the total meltwater content within the ice shell is shown in Figure 8.10 (red color) and indicates that once melting starts (at t∼200 kyr), the water content rises until the end of simulation (t=1.5 Myr). Nonetheless, as shown in Figure 8.9, all the melt is accumulated within few kilometers from the

bottom boundary. If permeability of ice at the bottom boundary differed from zero, all the meltwater would flow from the ice shell into the underlying ocean (cf. results for temperate ice in Chapter 6). This free outflow of water would be possible once thermal convection is coupled with the two-phase flow (since the bottom boundary, kept at the melting temperature and therefore temperate, would be always water-permeable) and will be thus comprised in the next step of this work.

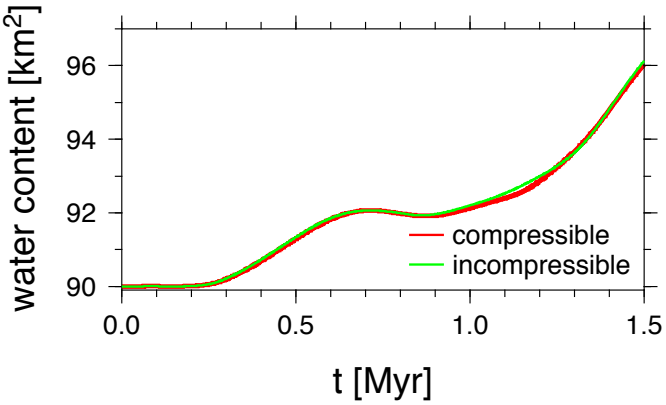

Figure 8.10: The same as in Figure 8.4 but for $H_{\max}=3\times10^{-6}$ W m^{-3} and composite ice rheology with d=0.7 mm.

In the previous section we have found that the effect of compressibility is rather negligible. Green line in Figure 8.10 corresponds to the solution computed with the same set of parameters as above but for the incompressible limit of governing equations. Again, the only difference between compressible and incompressible solutions is a slight overestimation of the amount of melt in the case of the latter, while the overall time evolution is comparable for both cases[4].

The role of grain size

To investigate the effect of grain size on the process of ice melting and subsequent water transport, we compute a couple of simulations with grain sizes ranging between 0.1 and 5 mm. At first, we consider a grain size slightly larger than in the above reference simulation, d=1 mm - the corresponding value of bottom viscosity is then $\mu_{\mathrm{m}}^{\mathrm{bot}}=3.19\times10^{14}$ Pa s leading to $\mathrm{Ra}_{\mathrm{bot}}=2.3\times10^{6}$ and $\mu_{\mathrm{m}}^{\mathrm{bot}}\sim2\mu_{\mathrm{m}}^{\mathrm{max}}$. For this choice of grain size, heating still occurs well within the plume. Since the bottom viscosity is rather high, the flow velocities are quite small and only relatively small hot plume develops. However, as maximum heating occurs within the plume interior, melting temperature is reached within ∼200 kyr from the beginning of the simulation and melting starts at the bottom boundary. Time evolution of porosity is depicted in Figure 8.11 and illustrates that melting occurs only within a few kilometers from the bottom boundary (since the onset of melting

[4]Free surface is prescribed at the top boundary in order to enable compaction/dilation of computational domain once melting/freezing starts. Yet, we do not consider the accompanying changes of the domain shape in our current model. The proper evolution of free surface boundary with the associated domain shape changes might be implemented in one of the next steps towards a more realistic model.

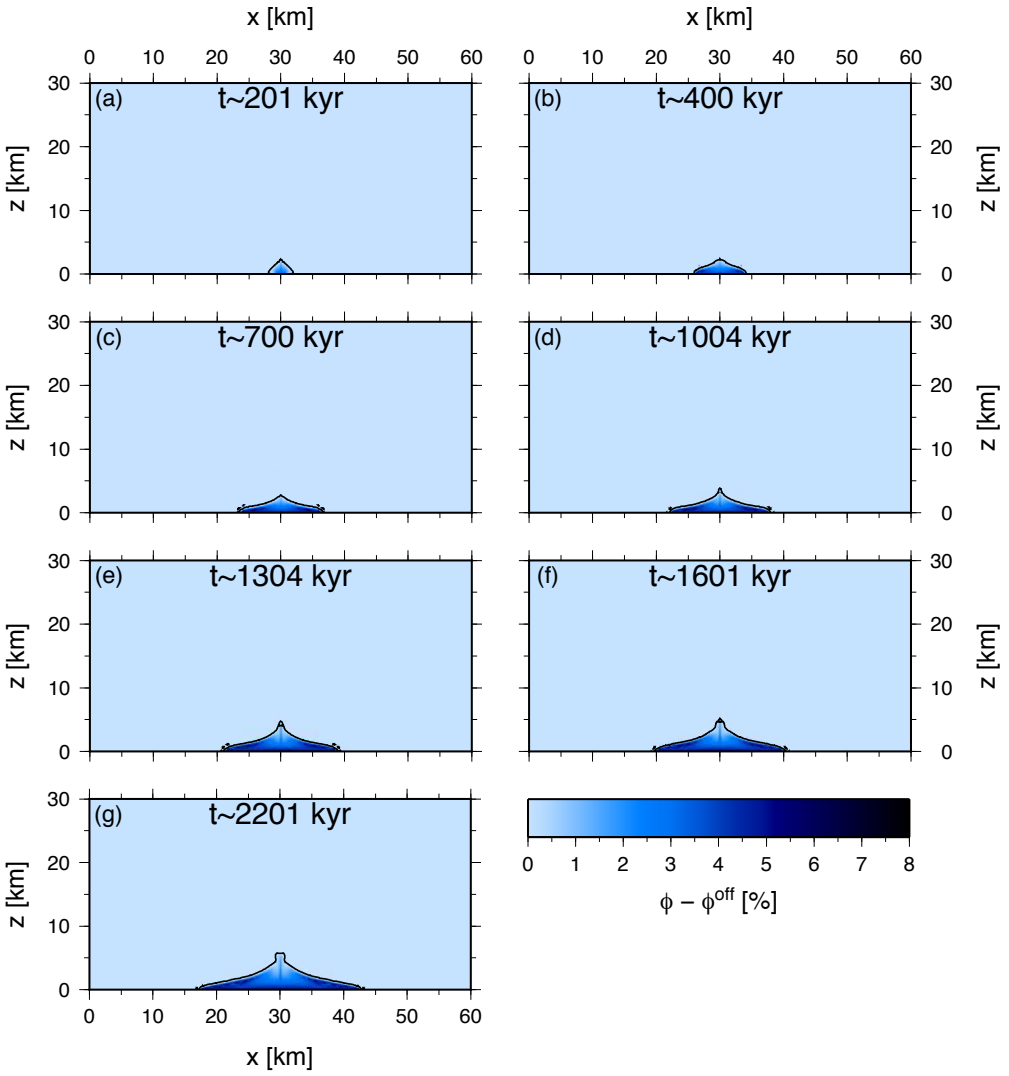

Figure 8.11: The same as in Figure 8.5 but for $H_{\rm max}$=3×10^{-6} W m^{-3} and composite ice rheology with d=1 mm.

occured long before the plume was fully developed). When choosing even larger grain size, d=5 mm, the bottom viscosity is $\mu_{\rm m}^{\rm bot}$=8×10^{15} Pa s leading to Rayleigh number Ra$_{\rm bot}$=9.4×10^4, which is too small to allow convection.

We considered also smaller values of grain sizes. For d=0.5 mm, the bottom viscosity is $\mu_{\rm m}^{\rm bot}$=8×10^{13} Pa s leading to Ra$_{\rm bot}$=9.4×10^6 and $\mu_{\rm m}^{\rm bot}\sim\frac{1}{2}\mu_{\rm m}^{\rm max}$. For this choice of parameters, the results of previous section suggest that the maximal heating will occur at the plume boundary, which can be seen from Figure 8.12. However, in this case, heating is strong also within the plume and thus the overall evolution does not differ significantly from that computed for d=0.7 mm.

For d=0.1 mm, which can be considered as a lower limit for Europan grain size, the bottom viscosity is $\mu_{\rm m}^{\rm bot}$=3.19×10^{12} Pa s leading to Ra$_{\rm bot}$=2.3×10^8 and $\mu_{\rm m}^{\rm bot}\sim\frac{1}{47}\mu_{\rm m}^{\rm max}$. This is indeed extremely small value and based on our previous results, we can expect heating to occur outside hot plumes - this is shown in Figure 8.13 that depicts temperature and heating at t∼500 kyr for the extremely large value of volumetric heating, $H_{\rm max}$=8×10^{-6} W m^{-3} (that can be considered

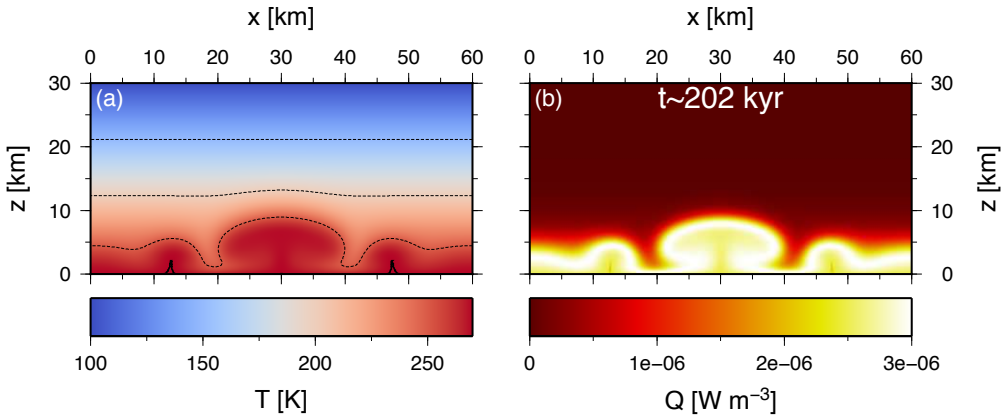

Figure 8.12: The same as in Figure 8.2 but for $H_{\max}=3\times10^{-6}$ W m^{-3} and composite ice rheology with d=0.5 mm.

as an upper limit, cf. *Tobie et al.*, 2003). Nevertheless, even for this large heating, the melting temperature is not reached anywhere within the ice shell, indicating that for the current setting (grain size as small as d=0.1 mm and the heating maximizing viscosity of $\mu_{\rm m}^{\max}=1.5\times10^{14}$ Pa s) no melt would be produced.

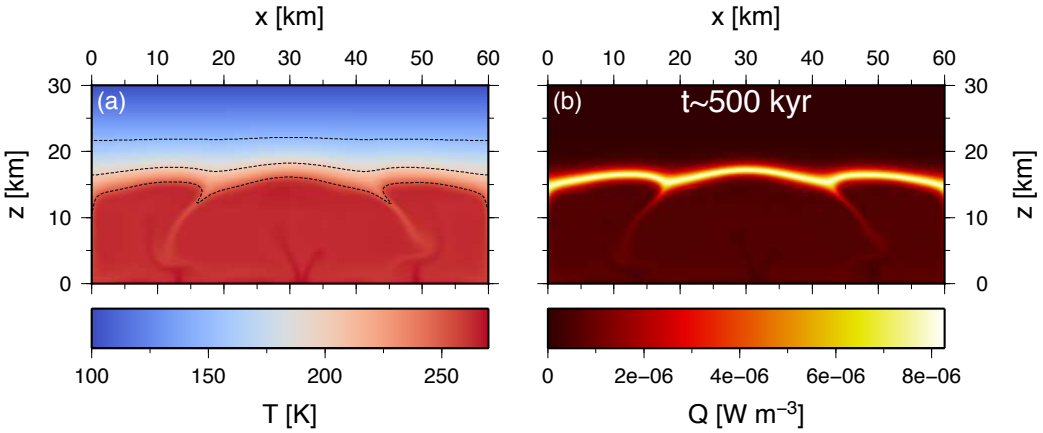

Figure 8.13: The same as in Figure 8.2 but for $H_{\max}=8\times10^{-6}$ W m^{-3} and composite ice rheology with d=0.1 mm.

8.3 Strike-slip fault

In the previous sections, we have investigated whether melting can occur at the top and/or within tidally heated hot plumes. Another source of heat that could initiate partial melting within Europa's ice shell is shear heating at tidally-activated strike-slip faults, first suggested by *Gaidos & Nimmo* (2000) and further studied by *Nimmo & Gaidos* (2002). Our simulations performed in one dimension indicated that large fraction of liquid water may accumulate at the base of a tidally-heated fault (cf. Section 7.2.2). The one-dimensional description of the problem, however, was ignoring the possible gravitational destabilization of the accumulated water due to formation of Rayleigh-Taylor-like instability. Here, we

neglect the porous flow (since we consider the impermeable limit of the governing equations, cf. the beginning of this chapter) and we study the gravitational stability of a potential meltwater lense, thus complementing our resuts from the one-dimensional study. Moreover, in two dimensions, the heat source is strongly localized and better described than in one dimension.

8.3.1 Model set-up

The simulation domain consists of a square of 20 km×20 km. All other parameters are taken from Table 3.1. To describe heating produced by shear motions at the fault, we follow the approach of *Han & Showman* (2008) and prescribe a heat source of the form

$$Q_{\mathrm{s}} = H_{\mathrm{s}} \exp\left[-\left(\frac{x-x_0}{\sigma_{\mathrm{x}}}\right)^2 - \left(\frac{z-z_0}{\sigma_{\mathrm{z}}}\right)^2 \right] \Gamma_{\mathrm{s}}(\phi) \ , \tag{8.11}$$

where we added a reduction of shear heating due to reduction of the friction coefficient after the onset of melting, $\Gamma_{\mathrm{s}}(\phi)$ (cf. Section 7.1.2). For lack of better knowledge, we parameterize it (as in one dimension) in the same way as the weakening of viscosity (eq. 8.3):

$$\Gamma_{\mathrm{s}} = \begin{cases} \exp(-\gamma_{\mathrm{s}}(\phi-\phi^{\mathrm{off}})) & \phi>\phi^{\mathrm{off}} \\ 1 & \phi\leq\phi^{\mathrm{off}} \end{cases} \ , \tag{8.12}$$

with the fixed weakening parameter, $\gamma_{\mathrm{s}}=\gamma_{\mathrm{m}}=45$ (based on the results of section 7.2.2). Two values of shear heating amplitude will be used, $H_{\mathrm{s}}=10^{-4}$ and $H_{\mathrm{s}}=2\times10^{-4}$ W m^{-3} (cf. *Nimmo & Gaidos*, 2002; *Han & Showman*, 2008). The heat source is placed near the top boundary (z_0=19.8 km) in the middle (x_0=10 km) and is approximately 1 km wide (with $\sigma_{\mathrm{x}}\sim$0.63 km and whole Gaussian peak within the computational domain) and 2 km high (with $\sigma_{\mathrm{z}}\sim$2 km and only half of the peak within the computational domain). Geometry of the heat source is fixed in all simulations.

The volumetric tidal heating of the form given by eq. (8.4) is also considered in some simulations with amplitudes of 2×10^{-6} and 5×10^{-6} W m^{-3}, respectively. The initial temperature profile is conductive (without any disturbance) and only temperature (Frank-Kamenetskii approximation) and porosity dependence of viscosity is considered (as in Section 8.1, cf. eqs 8.1–8.3). The bottom (reference) viscosity corresponding to melting-point temperature is set as in Section 8.1 to $\mu_{\mathrm{m}}^{\mathrm{bot}}=1.5\times10^{14}$ Pa s. The viscosity contrast in this setting is approximately six orders of magnitude before melting starts (due to viscosity temperature dependence) and can reach more than 10^8 when melting occurs (due to softening effect of the melt, cf. Figure 8.14, panel d).

8.3.2 Results

The role of shear heating amplitude

At first, we investigate the effect of shear heating amplitude H_{s}. Based on results of *Nimmo & Gaidos* (2002), we choose two values, $H_{\mathrm{s}}=10^{-4}$ and $H_{\mathrm{s}}=2\times10^{-4}$ W m^{-3}. Initially, we do not consider any volumetric tidal heating, i.e. $Q=Q_{\mathrm{s}}$.

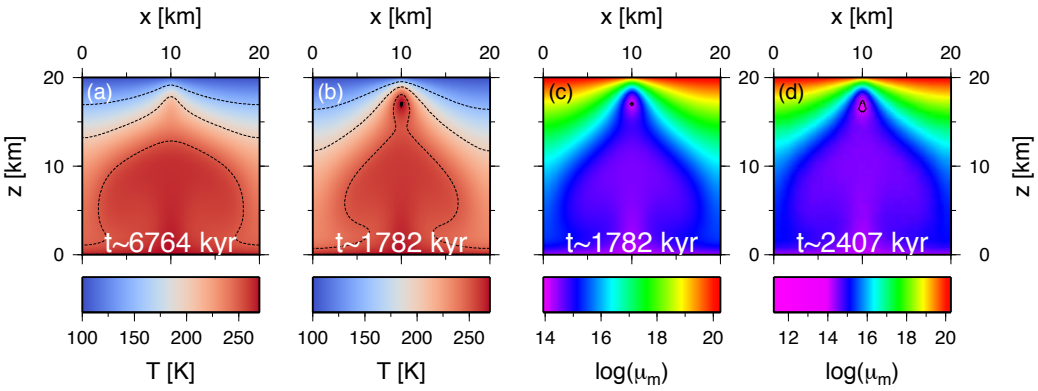

Figure 8.14: Temperature for simulations with H_s=10^{-4} W m^{-3} (panel a) and H_s=2×10^{-4} W m^{-3} (panel b). Viscosity for simulation with H_s=2×10^{-4} W m^{-3} at the onset of melting (panel c) and approximately 600 kyr after the onset of melting (panel d). The temperature isocontours are spaced by 50 K and the thick black contour marks the melting temperature (panel b) or the viscosity at the melting point (μ_m^{bot}=1.5×10^{14} Pa s, panels c, d), respectively. No volumetric heating is considered in these simulations.

The first two panels of Figure 8.14 show temperature for these two cases, respectively. We observe that in the case with weaker shear heating amplitude, H_s=10^{-4} W m^{-3}, the melting temperature is not reached even after ∼6700 kyr from the start of the simulation (panel a). On the other hand, in simulation with larger shear heating, H_s=2×10^{-4} W m^{-3}, the melting temperature is reached after ∼1800 kyr at just ∼3 km below the surface (panel b). The subsequent evolution of porosity is depicted in Figure 8.15 and suggests that (for this model setting) a partially molten lense with surplus porosity (w.r.t. ϕ^{off}) of about 10–15% can form approximately 3 km below the surface and stay there for at least 600 kyr. The stability of this partially molten region is due to viscosity increase of approximately one order (from ∼10^{14} to ∼10^{15} Pa s) just below (cf. panels c, d in Figure 8.14).

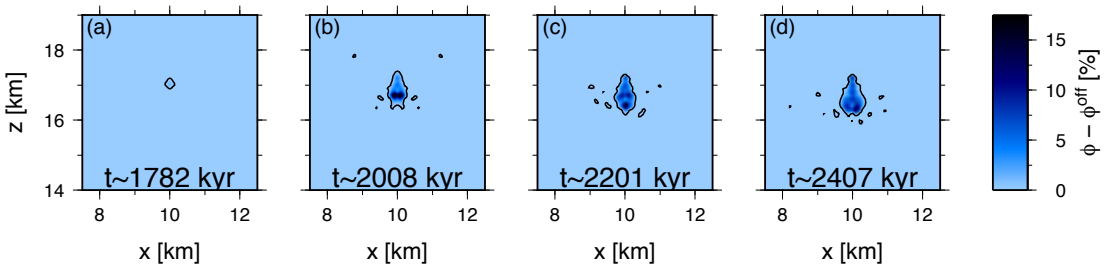

Figure 8.15: Time evolution of porosity for simulation with H_s=2×10^{-4} W m^{-3} and no volumetric heating. Only cut-out detail ($x\in\langle7.5, 12.5\rangle$ and $z\in\langle14, 19\rangle$) is shown for better clarity. Time increases from left to right. Black contours in porosity fields bound porosity larger than the background value ($\phi>\phi^{off}$).

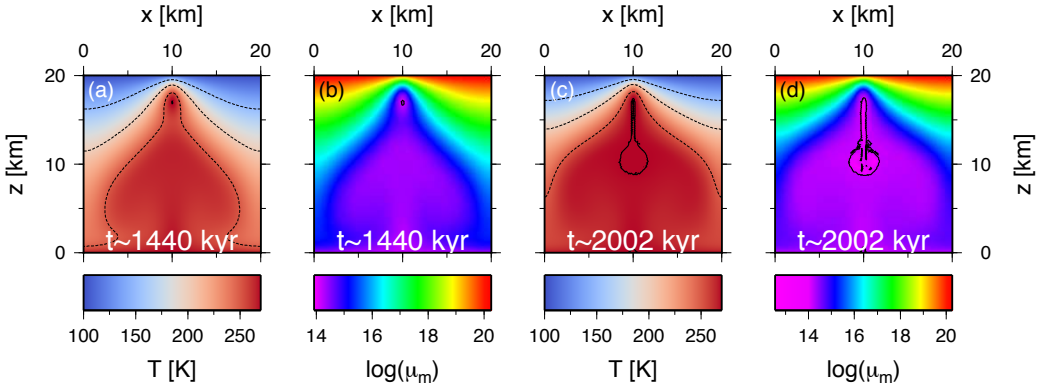

Figure 8.16: Temperature and viscosity at the onset of melting (panels a, b) and at the end of our simulation (panels c, d) computed for $H_{\rm max}$=2×10^{-6} W m^{-3} and $H_{\rm s}$=2×10^{-4} W m^{-3}. The temperature isocontours are spaced by 50 K and the thick black contour marks the melting temperature (panels a, c) or the viscosity at the melting point ($\mu_{\rm m}^{\rm bot}$=1.5×10^{14} Pa s, panels b, d), respectively.

The role of volumetric heating amplitude

We now study the effect of the addition of volumetric heating to shear heating, i.e. we consider Q=$Q_{\rm s}$+$Q_{\rm t}$ in the energy balance (eq. 4.74d). In the following simulations, the shear heating amplitude is fixed to $H_{\rm s}$=2×10^{-4} W m^{-3}, while two values of volumetric heating amplitude are considered, $H_{\rm max}$=2×10^{-6} and $H_{\rm max}$=5×10^{-6} W m^{-3}. Figure 8.16 shows the temperature and the corresponding viscosity for $H_{\rm max}$=2×10^{-6} W m^{-3} at the onset of melting (panels a, b) and at the end of our simulation (panels c, d). Melting temperature is reached after about

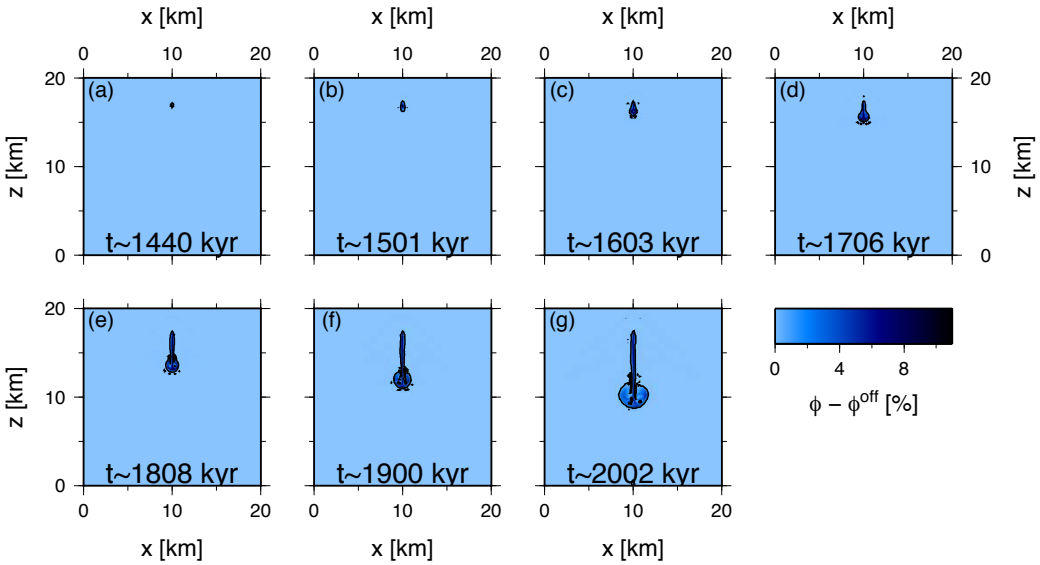

Figure 8.17: Time evolution of porosity computed for $H_{\rm max}$=2×10^{-6} W m^{-3} and $H_{\rm s}$=2×10^{-4} W m^{-3}. Time increases from left to right and from top to bottom. Black contours in porosity fields bound porosity larger than the background value (ϕ>$\phi^{\rm off}$).

1440 kyr at depth of approximately 3 km from the surface, as in the previous case. Contrary to the previous case, the internal temperature increases due to the run-away effect of volumetric heating - once the temperature increases, the corresponding viscosity decreases leading to stronger heating (since $\mu_{\rm m}^{\rm bot}=\mu_{\rm m}^{\rm max}$, cf. Section 8.1) and so on. Therefore, at the end of simulation (at $t\sim$2002 kyr), the temperature of the large part of the computational domain is well above 250 K with corresponding viscosities of the order of 10^{14} Pa s (Figure 8.16, panels c and d). The corresponding porosity evolution is shown in more detail in Figure 8.17. We observe the creation of a partially molten lense of a few percents during approximately 160 kyr (panels a–c) and its relatively rapid destabilization due to its negative buoyancy within less than 200 kyr (panels d, e) with the subsequent water transport towards the bottom boundary (panels f, g).

Results for the same simulation only with $H_{\rm max}=5\times10^{-6}$ W m^{-3} are shown in Figures 8.18 and 8.19. For this intermediate value of volumetric heating, the melting temperature is first reached at the bottom boundary and within the ascending hot plume promoted by the shear-heating-weakened zone in the top middle of the domain. When melting temperature is finally reached also at the fault location (at $t\sim$1252 kyr, cf. Figure 8.18, panel a), a large part of the underlying material is already partially molten (panel a in Figure 8.19) with the corresponding viscosity of the order of 10^{13} Pa s or even less (Figure 8.18, panel b). Within approximately 100 kyr, the top partially molten lense begins to collapse down (panel c in Figure 8.19) and only 50 kyr after it reaches the top of the partially molten plume (panel d). The subsequent transport of water molten at the fault towards the bottom boundary occurs on an already well established pathway through a partially molten plume with viscosities $\lesssim10^{13}$ Pa s (Figure 8.19, panels e–g, and Figure 8.18, panel d).

8.4 Summary and discussion

In this chapter we have investigated the possibility of the onset of melting within the ice shell of Europa in two geodynamical contexts and two-dimensional geometry. In the case of tidally-heated hot plumes, melting temperature is easily reached for the majority of appropriate physical parameters, but melting mostly occurs within the lower half of the ice shell. Even if some melt is produced at

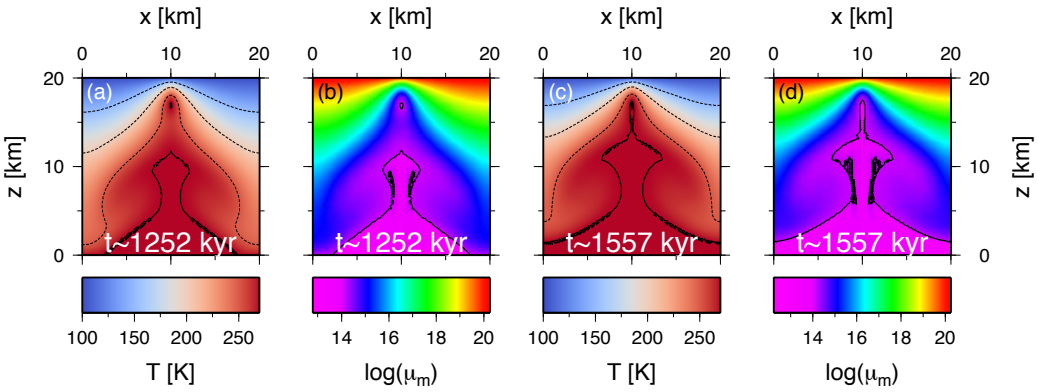

Figure 8.18: The same as in Figure 8.16 but for $H_{\rm max}=5\times10^{-6}$ W m^{-3}.

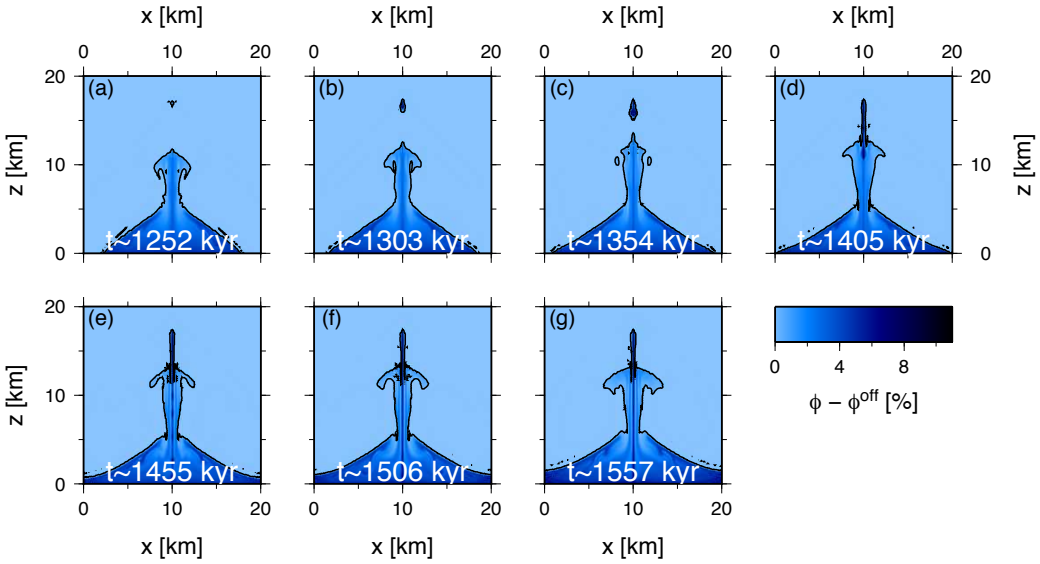

Figure 8.19: The same as in Figure 8.17 but for $H_{\max}=5\times10^{-6}$ W m^{-3}.

the top of hot plume, it is still located at least 10 km below the surface due to the presence of a thick conductive lid at the top of computational domain. Moreover, even small amounts of melt ($\sim$ few percents above the background value ϕ^{off}) cause relatively quick destabilization of the ascending hot plumes and their collapse towards the bottom boundary within approximately 100–200 kyr. Our results thus agree with the results of *Tobie et al.* (2003) and indicate that accumulation of partial melt close to the surface is not likely in this context.

This is in agreement with our results from the one-dimensional study (Section 7.2.1). While in the previous chapter all the liquid water produced in the hot plume was very quickly (within $\lesssim$ few hundreds of kiloyears) drained towards the underlying ocean by a porous flow through the partially molten temperate ice, in this chapter the liquid water was advected downwards with the collapsing ice due to formation of gravitational (Rayleigh-Taylor-like) instability. These two studies are complementary in the sense that one adresses the water transport by porous flow and the other by the development of gravitational instability. Their results agree in that the accumulation of partially molten material is not possible within the convecting ice shell of Europa and that all the produced water is rather rapidly transported towards the underlying ocean. A more complex model that would couple two-phase flow with solid-state thermal convection and would thus address both these aspects (now investigated separately) together will be considered in the future study. However, in the case of hot plumes, it will probably not have a big effect, since both approaches (porous flow and gravitational instability) produce qualitatively similar results.

In the case of the strike-slip fault, melting temperature might be reached very close to the surface ($\sim$3 km) for large amplitudes of shear heating of at least $H_{\text{s}}=2\times10^{-4}$ W m^{-3}. Our results indicate that if the layer below the fault is not internally heated, a small lense of partially molten material can be stable for at least 600 kyr. On the other hand, if the underlying layer is tidally heated, this lense is quickly destabilized (with the destabilization rates depending on the heating amplitude).

The results of our one-dimensional study performed in the previous chapter (Section 7.2.2) indicated that a large fraction of water might accumulate a few kilometers below the surface and remain stable as long as 200 kyr. However, by considering only one dimension, we have naturally neglected the effect of possible gravitational destabilization of this lense due to the development of Rayleigh-Taylor-like instability. In two dimensions, while neglecting porous flow, we show that this effect might destabilize the partially molten lense of only few percents within several tens to few hundreds of kiloyears if the ice viscosity is sufficiently decreased due to internal heating. As already mentioned, a fully coupled model of two-phase and convective flows, adressing both transport mechanisms together, will be the subject of further study. Nevertheless, we do not expect it will significantly change our current results since the porous flow can only occur within an area of partially molten (temperate) ice. The inclusion of water transport by porous flow into the current model will thus probably speed up the process of water extraction in the simulations with internal heating, where the melting temperature is reached within the ice shell (cf. Figures 8.16 and 8.18) but should not affect the stability of a partialy molten lense when the internal heating is omitted.

All our simulations neglect the possible drainage of water through the process of hydrofracturing. As have already been mentioned in Section 2.1, we do not consider this transport mechanism to be responsible for water drainage within Europa's ice shell. If the fractures developed after all, they might drain the accumulated water rather quickly through the formation of a macroscopic system of crevasses - in this sense, the partially molten lense's lifetimes provided in this chapter might be considered as upper estimates.

As already mentioned in Chapter 1, the presence of a possibly significant fraction of contaminants within the ice shell was suggested based on the observations (e.g. *McCord et al.*, 1998; *Kargel et al.*, 2000; *Zolotov & Kargel*, 2009). Low-eutectic constituents such as chloride salts could lower the melting point by several tens of Kelvins (*Kargel et al.*, 2000; *Pappalardo & Barr*, 2004) and their presence might have a large impact if they were located only in the upper part of the ice shell underlaid by cold and contaminant-free ice. Apart from the effects on the melting temperature of ice, the presence of salts would also influence its buoyancy, leading to a coupled thermo-compositional (two-phase) convection problem. The importance of compositional effects on surface topography is advocated by scaling arguments in *Pappalardo & Barr* (2004), and an attempt to numerically simulate the phenomenon has first been done by *Han & Showman* (2005). However, in their model, the advection of salts is assumed to be solely due to ice flow and the potentially important salt transport by two-phase drainage of highly concentrated brines is neglected.

The future development of a current model will naturally involve the relaxation of the zero permeability assumption, thus permitting to arrive at the fully coupled model of solid-state thermal convection and the porous (two-phase) flow. The implementation of viscosity cut-off to approximate brittle ice rheology as well as the extension of the problem to two-phase thermo-chemical convection by computing the salinity evolution and implementing the effect of salt on the melting temperature and buoyancy, might be considered in the future study. Even though we argued for its negligible effect, the independent study of hydrofrac-

turing should be performed in order to verify this assumption. If it, after all, indicates the significance of this transport process, its suitable parameterization should be implemented into the existing model.

Conclusions and perspectives

In this work, we have investigated the conditions under which water can be generated and transported within the ice shell of Europa. For this purpose, we have adapted the theory of two-phase flow to the conditions of Europa's ice shell and we have developped numerical tools in 1d and 2d geometry to quantify the water accumulation and transport for different melting scenarios.

Using the current knowledge about Europa and the analogy with water transport in terrestrial glaciers, we identified the main geodynamical contexts under which water may be generated on Europa and we related them with the expected transport mechanisms. Due to its eccentric orbit around Jupiter, the tidal dissipation has a strong impact on the thermal structure of Europa's ice shell. Assuming that the ice shell is in the convective regime, the thermally-reduced viscosity in the ascending hot plumes may significantly increase the heating rates and lead to runaway melting as suggested by *Sotin et al.* (2002). In this case, melting would occur within the convective portion of the ice shell. According to the findings of *Nimmo & Gaidos* (2002), shear motions along tidally-activated strike-slip faults result in a very localized and strong heat source located only a few kilometers below Europa's cold surface, which might eventually lead to shallow melting within the topmost, brittle part of the shell. Given the anticipated conditions in these two geodynamical contexts, we do not expect crevasse hydrofracturing, a dominant mechanism within the Earth's glaciers responsible for annual water drainage, to be widely present within Europa's ice shell. Instead, we argue that microporous flow of liquid water, similar to magma percolation within the Earth's mantle and mathematically described by two-phase mixture equations, could be responsible for draining the potential water reservoirs together with a possible formation of gravitational (Rayleigh-Taylor-like) instabilities.

Following the approach of *Drew* (1983), *Drew & Passman* (1999), *Bercovici et al.* (2001) and *Šrámek et al.* (2007), we proposed a detailed derivation of two-phase equations for the particular case of mixture of water ice and liquid water. First, we considered the general single-phase balance laws and the corresponding jump conditions and we performed averaging in order to obtain the multi-phase equations. Then, restricting ourselves to two-phase water-ice mixture, we formulated the governing equations together with the appropriate constitutive relations. Finally, we performed a scale analysis that allowed us to neglect terms of minor importance (such as the inertial terms in the equations of motion or the deformational work of both phases in the balance of energy) and we introduced the zero $\mathscr{C}$ approximation, an analogue of the zero compaction length approximation that neglects the mechanical coupling between the viscous matrix deformation and the flow of a less viscous fluid through the compacting matrix. The numerical tools developed and used throughout this thesis are based on finite volume and finite element methods. Since, in the zero $\mathscr{C}$ approximation (and for a suitably chosen initial condition) the system of two-phase equations results in a discontinuous solution containing shocks, a TVD method was chosen in order to assure solution stability. If the mechanical coupling is restored into the system of governing equations, the solution exhibits (again, for a suitably chosen initial profile) the formation of wave trains.

In the third part of this thesis, we performed parametric studies of water transport through the temperate ice shell in one and two dimensions. In this setting, the temperature of the shell is constant in time and equal to the (pressure) melting temperature, and the energy balance serves only to compute the rate of melt production. We investigated the role of several material parameters on the liquid water transport and found that the key role in this process is played by the ice permeability (i.e. the ability of ice to transmit liquid water). Permeability affects both, the local and global characteristics of water transport by controlling the time scale of the process as well as strongly influencing the wavelength. A similar effect on the local scale (in terms of wavelength) was also found for the ice viscosity - the smaller the viscosity, the smaller the wavelength. Yet, viscosity has almost negligible effect on the time scale of the process. Moreover, we have found that the very complex ice rheology (in general depending on temperature, grain size, deformation, water content, etc.) can be in numerical simulations of two-phase flow in our planetary setting approximated by a constant viscosity from the range of 10^{13} to 5×10^{15} Pa s. We also investigated the role of surface tension that could not have been neglected solely based on the scale analysis - its effect however was found to be completely negligible and we thus decided to omit surface tension in the following work. Finally, the mechanical coupling between the two phases, represented by the parameter $\mathscr{C}$, was found to be important, especially when the local character of flow is of interest. While the results of studies in one and two dimensions do not differ substantially for the majority of investigated parameters, a considerable difference was found for simulations with large percolation threshold ($\phi_c \gtrsim 3\%$), that is used as an approximation of the observed permeability drop for very small porosities. While in one dimension, the partially molten material remained at its initial position, since permeability of the ice below was effectively zero, in two dimensions, the partially molten area collapsed downwards (even though the underlying ice was effectively impermeable) due to formation of the gravitational instability. Overall, the results of this parametric study indicate that partially molten reservoirs are not gravitationally stable in the temperate ice shells and that the liquid water is rather quickly (within less than a few tens of kiloyears) delivered to the underlying water ocean.

In the last two chapters, we concentrated on the investigation of the onset of melting and the subsequent water evolution within the ice shell of Europa in the two melting scenarios. We performed a one-dimensional study where the transport of meltwater was enabled in the temperate parts of the ice shell by porous (two-phase) flow and a two-dimensional study where we only considered the impermeable limit of two-phase equations. In the latter case, all the liquid water is locked within the ice and advected with it (i.e. the relative velocity between ice and water is equal to zero). These studies are complementary in the assumed transport mechanism (porous flow vs. gravitational instability) and can be both considered as the first steps towards a more complicated model that would couple these two approaches.

In the case of tidally-heated hot plumes, we found that melting could initiate within an ascending hot plume even for relatively small amplitude of tidal heating of 3×10^{-6} W m^{-3} if the melting point viscosity is close to 1.5×10^{14} Pa s which corresponds to moderate values of grain size (d=0.5–1 mm). For larger value of grain size, d=5 mm, convection does not initiate (shell thickness of 30 km is

considered) and for the smallest grain size used (d=0.1 mm) convection develops but the maximum heating occurs just above the plumes and thus melting temperature is not reached during the simulation. If initiated, melting occurs at the bottom boundary as well as at the top of hot plumes several kilometers below the surface. In the one-dimensional simulations with porous flow, the ice below the partially molten area soon reaches the melting temperature and thus enables very efficient microporous transport of water towards the underlying ocean. In the two-dimensional simulations without porous flow, the partially molten material from the plumes is not gravitationally stable and even small melt fractions of a few percents are very quickly destabilized and within less than a few hundreds of kiloyears collapse down towards the bottom boundary. Our two-dimensional results thus qualitatively agree with those computed in one dimension even though different transport mechanisms (gravitational instability and porous flow, respectively) were considered. These results indicate that the accumulation of partial melt or even liquid water within few kilometers of Europa's surface is very unlikely in this context, at least if the ice shell is free of melting-temperature-lowering contaminants. The efficient water drainage suggested by our results might play an important role in the dynamics of Europa's ice shell and even assure the connection between Europa's shallow subsurface and the deep ocean.

In the case of tidally-activated strike-slip fault, we found that melting could initiate approximately 3 km below the surface for a local heat source of at least 2×10^{-4} W m^{-3}, leading to accumulation of a substantial amount of water. The newly created partially molten domain with maxima of $\sim$10–20% can remain stable this close to the surface for at least 600 kyr if the underlying ice shell is not tidally heated from within. For volumetric tidal heating with amplitudes from the range of 2–5×10^{-6} W m^{-3}, the results of our studies differ. While in one dimension we found that a large amount of water might accumulate and remain stable only a few kilometers below the surface for several hundreds of kiloyears even for the interior heating as high as 5×10^{-6} W m^{-3}, the results of two-dimensional simulations show that the partially molten reservoir is not gravitationally stable and collapses down within $\lesssim$200 kyr even for smaller amplitude of volumetric heating (2×10^{-6} W m^{-3}), contrary to our one-dimensional results. Overall, our simulations suggest that a partially molten lense or even a liquid water reservoir might form below recently active strike-slip faults and remain (gravitationally) stable for at least several hundreds of kiloyears if the underlying ice is free of fractures and not tidally heated from within (and thus sufficiently cold and viscous). These lenses might coincide with the sills advocated by *Dombard et al.* (2013) as a necessary ingredient to produce the morphology of Europa's ubiquitous double ridges.

Even though the numerical tool developed during this thesis and used in the last chapter is unique in the sense that it, for the first time, uses the two-phase formalism to address ice melting and subsequent meltwater evolution within the shell of icy satellite, several improvements are already intended in order to improve the description of physical processes within the icy shells. First of all, naturally, the relaxation of the zero permeability assumption will allow to enable the transport of liquid water also by micropores through those parts of the shell that will reach the melting temperature, resulting in a fully coupled model of the two-phase flow with the classic solid-state thermal convection. In addi-

tion, although we argued for its negligible effect, the independent study of the water transport by hydrofracturing should be performed in order to verify this assumption. If it, after all, indicates significance of this transport process, we will attempt to implement its suitable parameterization into the existing model.

Europa's scarred surface represents an evidence of the brittle behavior. Moreover, as recently proposed by *Kattenhorn & Prockter* (2014), subduction might be responsible for recycling its surface material into the shell interior which would make Europa the only solar system body other than the Earth to exhibit a system of plate tectonics. The implementation of viscosity cut-off as a rough approximation of the brittle rheology might substantially modify our current results and will be considered in the next step. Similarly, the presence of salty contaminants that would lower the melting temperature might have effect on the melt generation and potential water accumulation. The extension of the current model to two-phase thermo-chemical convection by adding the salinity evolution and implementing the effect of salt on the melting temperature and buoyancy might be considered.

In this thesis, we concentrated only on Europa. However, the developed numerical tool may be, after appropriate adjustments, used to investigate meltwater generation and its following evolution also within the ice shells of other satellites. The observational evidence of water at the south pole of Enceladus (e.g. *Porco et al.*, 2006; *Spencer et al.*, 2006) makes this tiny moon one of the most exciting target for further exploration. Investigation of the possibility to form its suggested regional ocean (e.g. *Tobie et al.*, 2008) as well as study of shallow depth melting potentially connected with the erupting jets (e.g. *Porco et al.*, 2006; *Postberg et al.*, 2011) will be among the primary objectives of the future work. The tidally-induced melting processes may have been common also on other icy satellites in the past, when subjected to intense tidal interactions. For instance, on Ganymede, some bright surface features indicate the existence of past cryovolcanic activities, potentially implying meltwater (*Showman et al.*, 2004). Neptune's moon Triton (*Prockter et al.*, 2005), as well as Uranus' moons Ariel and Miranda (*Tittemore*, 1990; *Tittemore & Wisdom*, 1990) may have also experienced analogous processes. Although initially developped for Europa, our numerical tool may be applied to many icy moons and could potentially address major questions regarding the past activities of these objects. Finally, the formalism we developped may be adapted in order to investigate the melt production and transport within the deep layers of high-pressure ices in the interiors of large satellites such as Ganymede or Titan, thus enabling to address the chemical transport between the rocky interior and the internal ocean.

Résumé

Cette thèse traite de la modélisation de la dynamique interne des satellites de glace avec une phase liquide, avec comme objet d'étude plus particulier le cas d'Europe, satellite de Jupiter. Deux approches sont proposées successivement: premièrement une analyse théorique (décrite dans les deux premières parties), puis un traitement numérique du problème en une puis deux dimensions (la deuxième partie de ce manuscrit).

Dans le premier chapitre, nous fournissons une brève description des connaissances actuelles sur Europe, le plus petit des satellites galiléens. Les trois premiers satellites, Io, Europe, et Ganymède, constituent le premier exemple de résonance de Laplace laquelle empêche la circularisation de leurs orbites et maintient des excentricités non nulles. Ce mouvement excentrique d'Europe autour de Jupiter produit la déformation viscoélastique de marée qui conduit à un chauffage considérable de la glace. Ce chauffage joue ainsi un rôle important dans l'évolution d'Europe qui est composée d'un noyau de fer, d'un manteau rocheux, et d'une couche de l'eau, laquelle correspond probablement à la superposition d'une coquille de glace extérieure et d'un océan interne. Contrairement à ses voisins glacés, la surface d'Europe montre une absence des cratères d'impact indiquant un âge jeune (environ de 40–90 millions d'années), mais elle est couverte par un grand nombre des formation géologiques sans équivalents dans notre Système Solaire; ces structures incluent entre autres des terrains chaotiques, des rides cycloïdales, des lenticulaes, des rides doubles, etc. Sur la base d'études morphologiques récentes, nous avons identifié deux types de formations de surface pendant la création desquelles l'eau liquide aurait pu être présente: les terrains chaotiques et les rides doubles. Puisqu'une source de chaleur est nécessaire pour la production d'eau liquide dans la coquille de glace, nous avons associé ces formations de surface à des sources de chauffage suggérées dans la littérature - le chauffage de marée dans un panache chaud attribuable à la viscosité réduite a été associé avec la formation des terrains chaotiques et le chauffage dû aux mouvements de cisaillement à la base des failles décrochantes avec la formation des rides doubles.

Dans le chapitre suivant, nous récapitulons les moyens de transport de l'eau liquide à travers l'exemple des glaciers terrestres et nous définissons les états différents de la glace - la glace tempérée, qui est à la température de fusion et contient jusqu'à quelques pourcents d'eau liquide aux joints de grains, et la glace froide, au-dessous de la température de fusion qui ne contient pas d'eau interstitielle. Un glacier qui est composé en même temps de régions tempérées et froides est appelé polythermique. Nous évoquons ensuite les mécanismes en mesure de transporter l'eau liquide produite au sein de la coquille de glace vers l'océan interne. Les conditions thermodynamiques et mécaniques caractéristiques de la coquille d'Europe ou d'un autre satellite de glace ne semblent pas propices pour accueillir les crevasses formées par fracturation hydraulique qui représentent le mécanisme de drainage dominant dans les glaciers terrestres. La percolation microporeuse de l'eau liquide, similaire à la percolation du magma dans le manteau terrestre, pourrait en revanche être prépondérante. La formation d'instabilités gravitationnelles, de type Rayleigh-Taylor, pourrait être adjointe à ce mécanisme.

Le troisième chapitre contient un exposé détaillé des équations pour un écoulement biphasé du mélange constitué de glace et d'eau liquide. Nous commençons par la dérivation des équations générales pour un matériau monophasé et des conditions aux limites appropriées. Nous effectuons ensuite une moyenne pour obtenir des équations polyphasées. Nous poursuivons avec la formulation des équations gouvernant l'écoulement biphasé du mélange constitué de glace et d'eau liquide complementée par les équations constitutives appropriées. Ce chapitre se termine par une analyse d'échelle, laquelle permet de négliger les termes d'importance mineure (tels que les termes d'inertie dans les équations du mouvement ou le travail de déformation des deux phases dans le bilan de l'énergie). Nous introduisons aussi "l'approximation de $\mathscr{C}$ nul" (ou approximation de longueur de compaction nulle) qui néglige le couplage mécanique entre l'écoulement et la déformation de la matrice visqueuse et l'écoulement de la phase moins visqueuse à traverse de cette matrice.

Les méthodes numériques utilisées pendant cette thèse sont décrites dans le Chapitre 4. La première partie de ce chapitre est dédiée à la description d'un code de calcul en une dimension et avec des paramètres matériels constants, qui a été écrit en FORTRAN90. Ce code est basé sur la méthode des volumes finis et permet de calculer le transport d'eau à travers une couche de glace tempérée ou polythermique. Il permet aussi de calculer l'évolution de la couche de glace tempérée dans une approximation de $\mathscr{C}$ nul - en utilisant cette approximation, la solution des équations biphasées n'est pas continue, mais produit des chocs. Pour obtenir une solution stable, nous avons choisi la méthode de la diminution de la variation totale (TVD). Dans un cas où le couplage mécanique est pris en compte dans le système d'équations, la solution produit des trains d'ondes. Des tests approfondis ont été effectués afin de vérifier l'implémentation numérique. Dans la deuxième partie de ce chapitre, nous décrivons un code qui utilise FEniCS, logiciel libre par éléments finis. Nous avons développé deux versions de ce code - l'une pour calculer le transport de l'eau interstitielle à travers une couche de glace tempérée en une ou deux dimensions et avec des paramètres matériels variables, et l'autre pour calculer la quantité de fusion de la glace et le transport qui s'ensuit par formation d'instabilités de Rayleigh-Taylor (nous négligeons le transport microporeux dans ce code) en deux dimensions. Un ensemble de tests détaillés est proposé pour ces deux codes.

Dans le Chapitre 5 nous effectuons une étude paramétrique du transport d'eau liquide à travers une couche de glace tempérée en une dimension. Dans ce cas, la température de la couche de glace est égale à la température de fusion et reste constante dans le temps - le bilan de l'énergie sert seulement à calculer le taux de production d'eau liquide. Nous avons étudié le rôle des différents paramètres matériels - nous avons trouvé qu'un rôle clé dans ce processus est joué par la perméabilité de la glace (i.e. la capacité de la glace à transporter l'eau liquide). La perméabilité affecte à la fois les caractéristiques locales et globales de transport de l'eau en contrôlant l'échelle de temps du processus ainsi qu'en influençant fortement la longueur d'onde. Un effet similaire à l'échelle locale (en termes de longueur d'onde), a également été constaté pour la viscosité de la glace - plus la viscosité est petite, plus petite est la longueur d'onde. En revanche, la viscosité n'influence pas l'échelle de temps associée au processus. De plus, nous montrons que la rhéologie composite de la glace (en général fonction de la température, de

la taille des grains, du mécanisme de fluage, de la teneur en eau, etc.) peut être approximée dans le cadre des simulations numériques de l'écoulement biphasé et pour le contexte planétaire que nous considérons, par une viscosité constante de la gamme de 10^{12} à 5×10^{15} Pa s. Nous avons également étudié le rôle de la tension de surface qui ne peut pas être négligé sur des arguments d'échelle - son effet a cependant été trouvé tout à fait négligeable et nous avons donc décidé de l'omettre dans les travaux suivants. Le chauffage volumétrique ainsi que la valeur de porosité de fond (background porosity) influence aussi les temps de transport. Enfin, le couplage mécanique entre les deux phases, représenté par le paramètre $\mathscr{C}$ a une influence importante, en particulier en ce qui concerne le caractère local de l'écoulement.

Une étude paramétrique similaire à celle effectuée dans le Chapitre 5 mais en considérant une géométrie à deux dimensions est décrite dans le Chapitre 6. Sur la base des résultats de l'étude en une dimension, nous nous concentrons sur le rôle de la perméabilité et de la viscosité en deux dimensions. Nos résultats ne diffèrent pas trop de ceux obtenus en une dimension. À nouveau, l'échelle de temps est principalement contrôlée par la perméabilité de la glace, tandis que la viscosité a un effet négligeable sur la vitesse de propagation des trains d'ondes. La viscosité et la perméeabilité affectent la longueur d'onde de la même manière, c'est à dire qu'une plus grande viscosité et/ou perméabilité résulte en une plus grande longueur d'onde. De plus, nous avons trouvé que la viscosité composite de la glace, fonction de la température, du mécanisme de fluage, etc., peut être approximée par une viscosité constante dans la gamme 10^{13}–5×10^{15} Pa s. La différence principale entre les études en une et deux dimensions a été trouvée pour les simulations avec un seuil de percolation qui mime la fermeture des micropores observées dans la nature et laquelle résulte en une perméabilité effective égale à zéro. Nous avons observé la plus grande différence pour les grandes valeurs de ce seuil de percolation ($\phi_c \gtrsim 3\%$) - alors qu'en une dimension, la matière partiellement fondue reste à sa position initiale, car la perméabilité de la glace sous-jacente est zéro, en deux dimensions, la zone partiellement fondue s'effondre vers le bas (même si la glace sous-jacente est effectivement imperméable) par la formation d'instabilités gravitationnelles de type Rayleigh-Taylor. En général, les résultats de notre étude en deux dimensions suggèrent que les réservoirs partiellement fondus ne sont pas gravitationnellement stables dans la couche de glace tempérée même pour des perméabilités très petites.

Dans les deux derniers chapitres de cette thèse, nous nous sommes concentrés sur l'investigation du début de la fusion et de l'évolution subséquente de l'eau au sein de la couche de glace d'Europe. En prenant en compte les résultats de l'étude paramétrique du Chapitre 5 et les scénarios de fusion décrits brièvement dans le Chapitre 1, nous avons commencé par une étude en une dimension avec des paramètres matériels constants (Chapitre 7). Dans ce cadre, le transport de l'eau liquide a été facilité dans les régions tempérées de la coquille glaciale par l'écoulement biphasé. Nous avons considéré deux contextes géodynamiques différents. Dans le cas d'un panache chaud chauffé par les marées, l'accumulation d'eau liquide près de la surface d'Europe est peu probable - même si la fusion est produite dans la tête du panache chaud, plusieurs kilomètres sous la surface, la glace sous-jacente atteint vite la température de fusion et permet le transport de l'eau vers l'océan interne par écoulement en milieu poreux. À l'inverse, dans

le cas d'une faille décrochante activée par les marées, nous montrons qu'une quantité d'eau substantielle peut s'accumuler si l'amplitude du chauffage est assez forte ($\gtrsim 10^{-4}$ W m^{-3}). Celle-ci peut rester stable quelques kilomètres sous la surface pendant plusieurs centaines de milliers d'années. Cependant, ces résultats sont fortement influencés par leur caractère unidimensionnel et pourraient être considérablement modifiés si les flux latéraux étaient pris en compte.

C'est pourquoi, dans le dernier chapitre (8), nous avons effectué une étude complémentaire en deux dimensions. Dans une première étape vers un modèle plus complexe, nous avons considéré la limite imperméable d'équations biphasées - dans ce cas, toute l'eau liquide est piégée dans la glace et advecté avec elle (c'est à dire, la vitesse relative entre la glace et l'eau est égale à zéro). Comme dans le Chapitre 7, nous avons étudié deux contextes géodynamiques distincts - la fusion au sein d'un panache chaud et la fusion à la base d'une faille décrochante. Dans le premier cas, nous montrons que la fusion pourrait apparaître dans un panache chaud ascendant pour des valeurs modérées de la taille des grains, d=0.5–1 mm même dans le cas d'une amplitude faible du chauffage de marée. La fusion a lieu principalement à la limite inférieure et au sommet du panache chaud, cependant, la matière partiellement fondue contenue dans les panaches n'est pas gravitationnellement stable et s'effondre très rapidement (en moins de quelques dizaines à quelques centaines de milliers d'années), vers la limite inférieure, où elle s'accumule. Pour des tailles des grains plus grandes, d=5 mm, la convection ne démarre pas (une épaisseur de coquille de 30 km est considérée). Pour la plus petite taille de grains considérée (d=0.1 mm), la convection apparaît mais la température de fusion n'est pas atteinte (au moins pendant des 500 milliers d'années). Nos résultats en deux dimensions correspondent donc à celles calculées dans une dimension même si les mécanismes de transport différents (instabilités Rayleigh-Taylor ou l'écoulement biphasé) ont été pris en compte, et indiquent que l'accumulation d'un réservoir substantiel d'eau liquide à faible profondeur n'est pas très probable. Dans le cas d'une faille décrochante, la fusion pourrait s'initier environ 3 km sous la surface d'Europe pour un chauffage d'au moins 2×10^{-4} W m^{-3}. Le domaine partiellement fondu (avec un maximum de $\sim$10–20%) peut rester stable aussi près de la surface pendant au moins 600 milliers d'années si la couche de glace sous-jacente n'est pas chauffée de l'intérieur. Pour un chauffage volumétrique avec des amplitudes dans la gamme de 2–5$\times10^{-6}$ W m^{-3}, le réservoir partiellement fondu n'est pas gravitationnellement stable et s'effondre en $\lesssim$200 de milliers d'années, contrairement à nos résultats unidimensionnels.

En général, nous avons trouvé que l'accumulation de fusion partielle au-dessus des panaches chauds est très peu probable, au moins s'il n'y a pas de contaminants qui abaissent la température de fusion dans la couche de glace. Même de petites fractions d'eau de quelques pourcents sont destabilisées en moins de quelques centaines de milliers d'années par la combinaison de l'écoulement biphasé et l'instabilité de Rayleigh-Taylor. Ce drainage de l'eau peut jouer un rôle important dans la dynamique de la couche de glace d'Europe, et même assurer la connexion entre subsurface peu profonde d'Europe et l'océan profond. En revanche, une lentille partiellement fondue ou même un réservoir d'eau liquide pourrait se former au-dessous des failles décrochantes récemment actives et rester gravitationnellement stable pendant au moins plusieurs centaines de milliers d'années si la glace

sous-jacente ne contient pas de fractures et n'est pas chauffée de l'intérieur par des marées (et reste donc suffisamment froide et visqueuse). Ces lentilles peuvent coincider avec les seuils préconisés par *Dombard et al.* (2013) comme un ingrédient nécessaire pour produire la morphologie de ride doubles d'Europe.

Même si l'outil numérique développé au cours de cette thèse n'a été appliqué que sur Europe, nous projetons d'élargir son domaine d'application à des études futures des processus de transport dans les autres satellites de glace, tels que Encelade, Ganymède, ou Titan. Plusieurs améliorations sont projetées. Premièrement, la relaxation de l'hypothèse de perméabilité zéro permettra de transporter de l'eau liquide aussi par l'écoulement poreux à travers les parties de la couche de glace qui atteignent la température de fusion, résultant donc en un modèle entièrement couplé de l'écoulement biphasé avec la convection thermique classique. L'implémentation d'une viscosité approximant la rhéologie cassante, pourrait aussi modifier sensiblement nos résultats actuels et sera prise en compte dans les travaux suivants. De la même façon, la présence de contaminants salés qui abaissent la température de fusion, peut avoir un effet sur la production et l'accumulation de matière fondue. L'extension du modèle existant à la convection thermo-chimique-biphasé en ajoutant de l'évolution de la salinité et en incorporant de l'effet du sel sur la température de fusion et la flottabilité peut être considérée. Enfin, même si nous avons argumenté pour son effet négligeable, une étude indépendante de la fracturation hydraulique devrait être effectuée - si, après tout, elle indique l'importance de ce moyen de transport, une paramétrisation adéquate sera mis en œuvre dans le modèle existant.

Bibliography

Alexander, C., R. Carlson, G. Consolmagno, R. Greeley, and D. Morrison (2009), The exploration history of Europa, in *Europa* (eds. R. T. Pappalardo, W. B. McKinnon, and K. Khurana), The University of Arizona Press, Tucson, 3–26.

Anderson, J. D., G. Schubert, R. A. Jacobson, E. L. Lau, W. B. Moore, and W. L. Sjogren (1998), Europa's Differentiated Internal Structure: Inferences from Four Galileo Encounters, *Science*, **281**(5385), 2019–2022, doi:10.1126/science.281.5385.2019.

Arnold, D. N., F. Brezzi, and M. Fortin (1984), A stable finite element for the Stokes equations, *Calcolo*, **21**(4), 337–344, doi:10.1007/BF02576171.

Aschwanden, A., and H. Blatter (2009), Mathematical modeling and numerical simulation of polythermal glaciers, *J. Geophys. Res.*, **114**(F01027), doi:10.1029/2008JF001028.

Aydin, A. (2006), Failure modes of the lineaments on Jupiter's moon, Europa: Implications for the evolution of its icy crust, *J. Struct. Geol.*, **28**(12), 2222–2236, doi:10.1016/j.jsg.2006.08.003.

Barr, A. C., R. T. Pappalardo, and S. Zhong (2004), Convective instability in ice I with non-Newtonian rheology: Application to the icy Galilean satellites, *J. Geophys. Res.*, **109**(E12), doi:10.1029/2004JE002296.

Barr, A. C., and R. T. Pappalardo (2005), Onset of convection in the icy Galilean satellites: Influence of rheology, *J. Geophys. Res.*, **110**(E12), doi:10.1029/2004JE002371.

Barr, A. C., and W. B. McKinnon (2007), Convection in ice I shells and mantles with self-consistent grain size, *J. Geophys. Res.*, **112**(E2), doi:10.1029/2006JE002781.

Barr, A. C., and A. P. Showman (2009), Heat transfer in Europa's icy shell, in *Europa* (eds. R. T. Pappalardo, W. B. McKinnon, and K. Khurana), The University of Arizona Press, Tucson, 405–430.

Běhounková, M., G. Tobie, G. Choblet, and O. Čadek (2010), Coupling mantle convection and tidal dissipation: Applications to Enceladus and Earth-like planets, *J. Geophys. Res.*, **115**(E09011), doi:10.1029/2009JE003564.

Běhounková, M., G. Tobie, G. Choblet, and O. Čadek (2012), Tidally-induced melting events as the origin of south-pole activity on Enceladus, *Icarus*, **219**(2), 655–664, doi:10.1016/j.icarus.2012.03.024.

Běhounková, M., G. Tobie, G. Choblet, and O. Čadek (2013), Impact of tidal heating on the onset of convection in Enceladus's ice shell, *Icarus*, **226**(1), 898–904, doi:10.1016/j.icarus.2013.06.033.

Bercovici, D., Y. Ricard, and G. Schubert (2001), A two-phase model for compaction and damage: 1. General Theory, *J. Geophys. Res.*, **106**(B5), 8887–8906, doi:10.1029/2000JB900430.

Bercovici, D., and Y. Ricard (2003), Energetics of a two-phase model of lithospheric damage, shear localization and plate-boundary formation, *Geophys. J. Int.*, **152**, 581–596.

van den Berg, A. P., P. E. van Keken, and D. A. Yuen (1993), The effects of a composite non-Newtonian and Newronian rheology on mantle convection, *Geophys. J. Int.*, **115**(1), 62–78, doi:10.1111/j.1365-246X.1993.tb05588.x.

Bierhaus, E. B., K. Zahnle, and C. R. Chapman (2009), Europa's crater distributions and surface ages, in *Europa* (eds. R. T. Pappalardo, W. B. McKinnon, and K. Khurana), The University of Arizona Press, Tucson, 161–180.

Billings, S. E., and S. A. Kattenhorn (2003), Comparison between terrestrial explosion crater morphology in floating ice and Europan chaos, *Lunar Planet. Sci., XXXIV*, **1955**.

Billings, S. E., and S. A. Kattenhorn (2005), The great thickness debate: Ice shell thickness models for Europa and comparisons with estimates based on flexure at ridges, *Icarus*, **177**(2), 397–412, doi:10.1016/j.icarus.2005.03.013.

Birchwood, R. A., and D. L. Turcotte (1994), A unified approach to geopressuring, low-permeability zone formation, and secondary porosity generation in sedimentary basins, *J. Geophys. Res.*, **99**(B10), 20051–20058, doi:10.1029/93JB02388.

Blankenbach, B., F. Busse, U. Christensen, L. Cserepes, D. Gunkel, U. Hansen, H. Harder, G. Jarvis, M. Koch, G. Marquart, D. Moore, P. Olson, H. Schmeling, and T. Schnaubelt (1989), A benchmark comparison for mantle convection codes, *Geophys. J. Int.*, **98**(1), 23–38, doi:10.1111/j.1365-246X.1989.tb05511.x.

Blatter, H., and K. Hutter (1991), Polythermal conditions in Arctic glaciers, *J. Glaciol.*, **37**(126).

Brooks, A. N., and T. J. R. Hughes (1982), Streamline upwind/Petrov-Galerkin formulations for convection dominated flows with particular emphasis on the incompressible Navier-Stokes equations, *Comput. Methods Appl. Mech. Eng.*, **32**(1-3), 199–259, doi:10.1016/0045-7825(82)90071-8.

Brown, M. E., and K. P. Hand (2013), Salts and radiation products on the surface of Europa, *Astron. J.*, **145**(4), 110, doi:10.1088/0004-6256/145/4/110.

Buratti, B., and J. Veverka (1983), Voyager photometry of Europa, *Icarus*, **55**(1), 93–110, doi:10.1016/0019-1035(83)90053-2.

Carlson, R. W., R. E. Johnson, and M. S. Anderson (1999), Sulfuric acid on Europa and the radiolytic sulfur cycle, *Science*, **286**(5437), 97–99, doi:10.1126/science.286.5437.97.

Carlson, R. W., W. M. Calvin, J. B. Dalton, G. B. Hansen, R. L. Hudson, R. E. Johnson, T. B. McCord, and M. H. Moore (2009), Europa's surface composition, in *Europa* (eds. R. T. Pappalardo, W. B. McKinnon, and K. Khurana), The University of Arizona Press, Tucson, 283–327.

Carr, M. H., M. J. S. Belton, C. R. Chapman, M. E. Davies, P. Geissler, R. Greenberg, A. S. McEwen, B. R. Tufts, R. Greeley, R. Sullivan, J. W. Head, R. T. Pappalardo, K. P. Klaasen, T. V. Johnson, J. Kaufman, D. Senske, J. Moore, G. Neukum, G. Schubert, J. A. Burns, P. Thomas, and J. Veverka (1998), Evidence for a subsurface ocean on Europa, *Nature*, **391**(6665), 363–365, doi:10.1038/34857.

Chizhov, V. E. (1993), Thermodynamic properties and thermal equation of state of high-pressure ice phases, *Prikladanay Mekhanika i Tekhnicheskaya Fizika*, **2**, 113–123.

Collins, G. C., J. W. Head, R. T. Pappalardo, and N. A. Spaun (2000), Evaluation of models for the formation of chaotic terrain on Europa, *J. Geophys. Res. Planets*, **105**(E1), 1709–1716, doi:10.1029/1999JE001143.

Collins, G., and F. Nimmo (2009), Chaotic terrain on Europa, in *Europa* (eds. R. T. Pappalardo, W. B. McKinnon, and K. Khurana), The University of Arizona Press, Tucson, 259–281.

Connolly, J. A. D., and Y. Y. Podladchikov (2007), Decompaction weakening and channeling instability in ductile porous media: Implications for asthenospheric melt segregation, *J. Geophys. Res.*, **112**(B10205), doi:10.1029/2005JB004213.

Consolmagno, G. J., and J. S. Lewis (1976), Structural and thermal models of icy Galilean satellites, in *Jupiter* (ed. T. A. Gehrels), The University of Arizona Press, Tucson, 1035–1051.

Crawford, G. D., and D. J. Stevenson (1988), Gas-driven water volcanism and the resurfacing of Europa, *Icarus*, **73**(1), 66–79, doi:10.1016/0019-1035(88)90085-1.

Culha, C., A. G. Hayes, M. Manga, and A. M. Thomas (2014), Double ridges on Europa accommodate some of the missing surface contraction, *J. Geophys. Res. Planets*, **119**(3), 395–403, doi:10.1002/2013JE004526.

de Groot, S. R., and P. Mazur, *Non-equilibrium Thermodynamics*, Dover Publications, New York, 1984.

De La Chapelle, S., H. Milsch, O. Castelnau, and P. Duval (1999), Compressive creep of ice containing a liquid intergranular phase: rate-controlling processes in the dislocation creep regime, *Geophys. Res. Lett.*, **26**(2), 251–254, doi:10.1029/1998GL900289.

Doggett, T., R. Greeley, P. Figueredo, and K. Tanaka (2009), Geologic stratigraphy and evolution of Europa's surface, in *Europa* (eds. R. T. Pappalardo, W. B. McKinnon, and K. Khurana), The University of Arizona Press, Tucson, 137–159.

Dombard, A. J., G. W. Patterson, A. P. Lederer, and L. M. Prockter (2013), Flanking fractures and the formation of double ridges on Europa, *Icarus*, **223**(1), 74–81, doi:10.1016/j.icarus.2012.11.021.

Drew, D. A. (1971), Averaged field equations for two-phase media, *Stud. Appl. Math.*, **50**(2), 133–166.

Drew, D. A. (1983), Mathematical modeling of two-phase flow, *Ann. Rev. Fluid Mech.*, **15**, 261–291, doi:10.1146/annurev.fl.15.010183.001401.

Drew, D. A., and S. L. Passman, *Theory of Multicomponent Fluids*, Appl. Math. Sci., **135**, Springer-Verlag, New York, 1999.

Durham, W. B., L. A. Stern, and S. H. Kirby (2001), Rheology of ice I at low stress and elevated confining pressure, *J. Geophys. Res.*, **106**(6), 11031–11042, doi:10.1029/2000JB900446.

Duval, P. (1977), The role of the water content on the creep rate of polycrystalline ice, in *Isotopes and Impurities in Snow and Ice*, pp. 29–33.

Eicken, H., H. R. Krouse, D. Kadko, and D. K. Perovich (2002), Tracer studies of pathways and rates of meltwater transport through Arctic summer sea ice, *J. Geophys. Res.*, **107**(C10), 8046, doi:10.1029/2000JC000583.

Evans, L. C., *Partial Differential Equations*, Graduate studies in mathematics, **19**, Amer. Math. Soc, 1998.

Ferziger, J. H., and M. Perić, *Computational methods for fluid dynamics*, Springer-Verlag, Berlin Heidelberg New York, 2002.

Figueredo, P. H., F. C. Chuang, J. Rathbun, R. L. Kirk, and R. Greeley (2002), Geology and origin of Europa's 'Mitten' feature (Murias Chaos), *J. Geophys. Res. Planets*, **107**(E5), doi:10.1029/2001JE001591.

Fountain, A. G., and J. S. Walder (1998), Water flow through temperate glaciers, *Rev. Geophys.*, **36**(3), 299–328, doi:10.1029/97RG03579.

Fowler, A. C. (1984), On the transport of moisture in polythermal glaciers, *Geophys. Atrophys. Fluid Dynamics*, **28**, 99–140.

Freeman, J., L. Moresi, and D. A. May (2006), Thermal convection with a water ice I rheology: Implications for icy satellite evolution, *Icarus*, **180**(1), 251–264, doi:10.1016/j.icarus.2005.07.014.

Freitag, J. (1999), The hydraulic properties of Arctic sea ice: Implications for the small-scale particle transport [in German], *Ber. Polarforsch.*, **325**, 150.

Freitag, J., and H. Eicken (2003), Meltwater circulation and permeability of Arctic summer sea ice derived from hydrological field experiments, *J. Glaciol*, **49**(166), 349–358, doi:10.3189/172756503781830601.

Gaidos, E. J., and F. Nimmo (2000), Tectonics and water on Europa, *Nature*, **405**(6787), 637, doi:10.1038/35015170.

Ghods, A., and J. Arkani-Hamed (2000), Melt migration beneath mid-ocean ridges, *Geophys. J. Int.*, **140**, 687–697.

Golden, K. M., S. F. Ackley, and V. I. Lytle (1998), The Percolation Phase Transition in Sea Ice, *Science*, **282**(5397), 2238–2241, doi: 10.1126/science.282.5397.2238.

Golden, K. M., A. L. Heaton, H. Eicken, and V. I. Lytle (2006), Void bounds for fluid transport in sea ice, *Mech. Mater.*, **38**(8–10), 801–817, doi:10.1016/j.mechmat.2005.06.015.

Golden, K. M., H. Eicken, A. L. Heaton, J. Miner, D. J. Pringle, and J. Zhu (2007), Thermal evolution of permeability and microstructure in sea ice, *Geophys. Res. Lett.*, **34**(16), L16501, doi:10.1029/2007GL030447.

Goldsby, D. L., and D. L. Kohlstedt (2001), Superplastic deformation of ice: Experimental observations, *J. Geophys. Res.*, **106**(B6), 11017–11030, doi:10.1029/2000JB900336.

Golombek, M. P., and W. B. Banerdt (1990), Constraints on the subsurface structure of Europa, *Icarus*, **83**(2), 441–452, doi:10.1016/0019-1035(90)90078-N.

Grasset, O., M. K. Dougherty, A. Coustenis, E. J. Bunce, C. Erd, D. Titov, M. Blanc, A. Coates, P. Drossart, L. N. Fletcher, H. Hussmann, R. Jaumann, N. Krupp, J.-P. Lebreton, O. Prieto-Ballesteros, P. Tortora, F. Tosi, and T. Van Hoolst (2013), JUpiter ICy moons Explorer (JUICE): An ESA mission to orbit Ganymede and to characterise the Jupiter system, *Planet. Space Sci.*, **78**, 1–21, doi:10.1016/j.pss.2012.12.002.

Greenberg, R. (1987), Galilean satellites: Evolutionary paths in deep resonance, *Icarus*, **70**(2), 334–347, doi:10.1016/0019-1035(87)90139-4.

Greenberg, R., P. Geissler, G. Hoppa, B. R. Tufts, D. D. Durda, R. T. Pappalardo, J. W. Head, R. Greeley, R. Sullivan, and M. H. Carr (1998), Tectonic processes on Europa: Tidal stresses, mechanical response, and visible features, *Icarus*, **135**(1), 64–78, doi:10.1006/icar.1998.5986.

Greenberg, R. G. V. Hoppa, B. R. Tufts, P. Geissler, and J. Riley (1999), Chaos on Europa, *Icarus*, **141**(2), 263–286, doi:10.1006/icar.1999.6187.

Greenberg, R. (2004), The evil twin of Agenor: tectonic convergence on Europa, *Icarus*, **167**(2), 313–319, doi:10.1016/j.icarus.2003.09.025.

Greene, T. F., J. R. Vermilion, R. W. Shorthill, and R. N. Clark (1975), Spectral reflectivity of select areas on Europa, *Icarus*, **25**(3), 405–415, doi:10.1016/0019-1035(75)90005-6.

Greve, R. (1997), A continuum-mechanical formulation for shallow polythermal ice sheets, *Phil. Trans. R. Soc. Lond. A*, **355**(1726), 921–974, doi:10.1098/rsta.1997.0050.

Gusmeroli, A., T. Murray, P. Jansson, R. Pettersson, A. Aschwanden, and A. D. Booth (2010), Vertical distribution of water within the polythermal Storglaciären, Sweden, *J. Geophys. Res.*, **115**(F04002), doi:10.1029/2009JF001539.

Han, L., and A. P. Showman (2005), Thermo-compositional convection in Europa's icy shell with salinity, *Geophys. Res. Lett.*, **32**(20), L20201, doi:10.1029/2005GL023979.

Han, L., and A. P. Showman (2008), Implications of shear heating and fracture zones for ridge formation on Europa, *Geophys. Res. Lett.*, **35**(3), L03202, doi: 10.1029/2007GL031957.

Han, L., and A. P. Showman (2010), Coupled convection and tidal dissipation in Europa's ice shell, *Icarus*, **207**(2), 834–844, doi:10.1016/j.icarus.2009.12.028.

Han, L., and A. P. Showman (2011), Coupled convection and tidal dissipation in Europa's ice shell using non-Newtonian grain-size-sensitive (GSS) creep rheology, *Icarus*, **212**(1), 262–267, doi:10.1016/j.icarus.2010.11.034.

Hand, K. P., C. F. Chyba, J. C. Priscu, R. W. Carlson, and K. H. Nealson (2009), Astrobiology and the potential for life on Europa, in *Europa* (eds. R. T. Pappalardo, W. B. McKinnon, and K. Khurana), The University of Arizona Press, Tucson, 589–629.

Hansen, U., and A. Ebel (1988), Time-dependent thermal convection - a possible explanation for a multiscale flow in the Earth's mantle, *Geophys. J. Int.*, **94**(2), 181–191, doi:10.1111/j.1365-246X.1988.tb05895.x.

Hansen, C. J., L. Esposito, A. I. F. Stewart, J. Colwell, A. Hendrix, W. Pryor, D. Shemansky, and R. West (2006), Enceladus' water vapor plume, *Science*, **311**(5766), 1422–1425, doi:10.1126/science.1121254.

Head, J. W., and R. T. Pappalardo (1999), Brine mobilization during lithospheric heating on Europa: Implications for formation of chaos terrain, lenticula texture, and color variations, *J. Geophys. Res. Planets*, **104**(E11), 27143–27155, doi:10.1029/1999JE001062.

Head, J. W., R. T. Pappalardo, and R. Sullivan (1999), Europa: Morphological characteristics of ridges and triple bands from Galileo data (E4 and E6) and assessment of a linear diapirism model, *J. Geophys. Res. Planets*, **104**(E10), 24223–24236, doi:10.1029/1998JE001011.

Hock, R. (2005), Glacier melt: a review of processes and their modelling, *Prog. Phys. Geog.*, **29**(3), 362–391, doi:10.1191/0309133305pp453ra.

Hoppa, G. V., B. R. Tufts, R. Greenberg, and P. E. Geissler (1999a), Formation of Cycloidal Features on Europa, *Science*, **285**(5435), 1899–1902, doi:10.1126/science.285.5435.1899.

Hoppa, G. V., B. R. Tufts, R. Greenberg, and P. Geissler (1999b), Strike-slip faults on Europa: Global shear patterns driven by tidal stress, *Icarus*, **141**(2), 287–298, doi:10.1006/icar.1999.6185.

Hoppa, G., R. Greenberg, B. R. Tufts, P. Geissler, C. Phillips, and M. Milazzo (2000), Distribution of strike-slip faults on Europa, *J. Geophys. Res. Planets*, **105**(E9), 22617–22627, doi:10.1029/1999JE001156.

Hussmann, H., T. Spohn, and K. Wieczerkowski (2002), Thermal Equilibrium States of Europas Ice Shell: Implications for Internal Ocean Thickness and Surface Heat Flow, *Icarus*, **156**(1), 143–151, doi:10.1006/icar.2001.6776.

Hussmann, H., and T. Spohn (2004), Thermal-orbital evolution of Io and Europa, *Icarus*, **171** (2), 391–410, doi:10.1016/j.icarus.2004.05.020.

Hutter, K. (1982), A mathematical model of polythermal glaciers and ice sheets, *Geophys. Astrophys. Fluid Dyn.*, **21**, 201–224.

Hutter, K. (1993), Thermo-mechanically coupled ice-sheet response - cold, polythermal, temperate, *J. Glaciol.*, **39**(131), 65–86.

Hutter, K., and K. D. Jöhnk, *Continuum methods of physical modeling: continuum mechanics, dimensional analysis, turbulence*, Springer-Verlag, Heidelberg, 2004.

Irvine-Fynn, T. D. L., A. J. Hodson, B. J. Moorman, G. Vatne, and A. L. Hubbard (2011), Polythermal Glacier Hydrology: A review, *Rev. Geophys.*, **49**(RG4002), doi:10.1029/2010RG000350.

Jeffreys, H. (1923), The constitution of the four outer planets, *Mon. Not. R. Astron. Soc.*, **83**(6), 350–354, doi: 10.1093/mnras/83.6.350a.

Jou, D., J. Casas-Vázquez, and G. Lebon, *Extended irreversible thermodynamics (4th ed.)*, Springer, New York Dordrecht Heidelberg London, 2010.

Kadel, S.D., S. A. Fagents, R. Greeley, and Galileo SSI Team (1998), Trough-bounding ridge pairs on Europa: Considerations for an endogenic model of formation, *Lunar Planet. Sci. XXIX*, **1078**.

Kalousová, K., O. Souček, G. Tobie, G. Choblet, and O. Čadek (2014), Ice melting and downward transport of meltwater by two-phase flow in Europa's ice shell, *J. Geophys. Res. Planets*, **119**(3), 532–549, doi:10.1002/2013JE004563.

Kargel, J. S., J. Z. Kaye, J. W. Head, G. M. Marion, R. Sassen, J. K. Crowley, O. P. Ballesteros, S. A. Grant, and D. L. Hogenboom (2000), Europa's Crust and Ocean: Origin, Composition, and the Prospects for Life, *Icarus*, **148**(1), 226–265, doi:10.1006/icar.2000.6471.

Kattenhorn, S. A. (2004), Strike-slip fault evolution on Europa: evidence from tailcrack geometries, *Icarus*, **172**(2), 582–602, doi:10.1016/j.icarus.2004.07.005.

Kattenhorn, S. A., and T. Hurford (2009), Tectonics of Europa, in *Europa* (eds. R. T. Pappalardo, W. B. McKinnon, and K. Khurana), The University of Arizona Press, Tucson, 199–236.

Kattenhorn, S. A., and L. M. Prockter (2014), Evidence for subduction in the ice shell of Europa, *Nature Geosci.*, doi:10.1038/ngeo2245.

Katz, R. F. (2010), Porosity-driven convection and asymmetry beneath mid-ocean ridges, *Geochem. Geophys. Geosyst.*, **11**, Q0AC07, doi:10.1029/2010GC003282.

Kawamura, T., M. Ishikawa, T. Takatsuka, S. Kojima, and K. Shirasawa (2006), Measurements of permeability of sea ice, *Proceedings of the 18th IAHR International Symposium on Ice*, 105–112.

Khurana, K. K., M. G. Kivelson, D. J. Stevenson, G. Schubert, C. T. Russell, R. J. Walker, and C. Polanskey (1998), Induced magnetic fields as evidence for subsurface oceans in Europa and Callisto, *Nature*, **395**(6704), 777–780, doi:10.1038/27394.

Kivelson, M. G., K. K. Khurana, C. T. Russell, R. J. Walker, J. Warnecke, F. V. Coroniti, C. Polanskey, D. J. Southwood, and G. Schubert (1996), Discovery of Ganymede's magnetic field by the Galileo spacecraft, *Nature*, **384**(6609), 537–541, doi:10.1038/384537a0.

Kivelson, M. G., K. K. Khurana, C. T. Russell, M. Volwerk, R. J. Walker, and C. Zimmer (2000), Galileo Magnetometer Measurements: A Stronger Case for a Subsurface Ocean at Europa, *Science*, **289**(5483), 1340–1343, doi:10.1126/science.289.5483.1340.

Krawczynski, M. J., M. D. Behn, S. B. Das, and I. Joughin (2009), Constraints on the lake volume required for hydro-fracture through ice sheets, *Geophys. Res. Lett.*, **36**(L10501), doi:10.1029/2008GL036765.

Lee, S., R. T. Pappalardo, and N. C. Makris (2005), Mechanics of tidally driven fractures in Europa's ice shell, *Icarus*, **177**(2), 367–379, doi:10.1016/j.icarus.2005.07.003.

Lennie, T., D. McKenzie, D. Moore, and N. Weiss (1988), The breakdown of steady convection, J. Fluid Mech., **188**, 47–85, doi:10.1017/S0022112088000631.

Lewis, J. S. (1971), Satellites of outer planets: Their physical and chemical nature, *Icarus*, **15**(2), 174-185, doi:10.1016/0019-1035(71)90072-8.

Lide, D. R. (Editor in chief), *CRC Handbook of Chemistry and Physics*, 85th Edition, CRC Press LLC, 2004.

Lliboutry, L. (1971), Permeability, brine content and temperature of temperate ice, *J. Glaciol.*, **10**(58), 15–29.

Lliboutry, L. (1996), Temperate ice permeability, stability of water veins and percolation of internal meltwater, *J. Glaciol.*, **42**(141), 201–211.

Logg, A., K. A. Mardal, and G. N. Wells (editors), *Automated Solution of Differential Equations by the Finite Element Method, The FEniCS Book*, Lecture Notes in Computational Science and Engineering, **84**, Springer-Verlag, Berlin Heidelberg, 2012, doi:10.1007/978-3-642-23099-8.

Lopes-Gautier, R., A. S. McEwen, W. B. Smythe, P. E. Geissler, L. Kamp, A. G. Davies, J. R. Spencer, L. Keszthelyi, R. Carlson, F. E. Leader, R. Mehlman, and L. Soderblom (1999), Active volcanism on Io: Global distribution and variations in activity, *Icarus*, **140**(2), 243–264, doi:10.1006/icar.1999.6129.

Mader, H. (1992a), Observations of the water-vein system in polycrystalline ice, *J. Glaciol.*, **38**(130), 333–347.

Mader, H. (1992b), The thermal behaviour of the water vein system in polycrystalline ice, *J. Glaciol.*, **38**(130), 359–374.

Manga, M., and C.-Y. Wang (2007), Pressurized oceans and the eruption of liquid water on Europa and Enceladus, *Geophys. Res. Lett.*, **34**(L07202), doi:10.1029/2007GL029297.

Martinec, Z. (2011), Continuum mechanics (lecture notes), `http://geo.mff.cuni.cz/vyuka/Martinec-ContinuumMechanics.pdf`.

McCord, T.B., G. B. Hansen, F. P. Fanale, R. W. Carlson, D. L. Matson, T. V. Johnson, W. D. Smythe, J. K. Crowley, P. D. Martin, A. Ocampo, C. A. Hibbitts, J. C. Granahan, and the NIMS Team (1998), Salts on Europa's surface detected by Galileo's Near Infrared Mapping Spectrometer, *Science*, **280**(5367), 1242–1245, doi:10.1126/science.280.5367.1242.

McEwen, A. S., L. Keszthelyi, P. Geissler, D. P. Simonelli, M. H. Carr, T. V. Johnson, K. P. Klaasen, H. H. Breneman, T. J. Jones, J. M. Kaufman, K. P. Magee, D. A. Senske, M. J. S. Belton, and G. Schubert (1998), Active volcanism on Io as seen by Galileo SSI, *Icarus*, **135**(1), 181–219, doi:10.1006/icar.1998.5972.

McKenzie, D. (1984), The generation and compaction of partially molten rock, *J. Petrol.*, **25**(3), 713–765.

McKenzie, D. (1989), Some remarks on the movement of small melt fractions in the mantle, *Earth Planet. Sci. Lett.*, **95**(1-2), 53–72, doi:10.1016/0012-821X(89)90167-2.

McKinnon, W. B. (1999), Convective instability in Europa's floating ice shell, *Gephys. Res. Lett.*, **26**(7), 951–954, doi:10.1029/1999GL900125.

Mével, L, and E. Mercier (2005), Resorption process in Astypalaea Linea extensive region (Europa), *Planet. Space Sci.*, **53**(7), 771–779, doi:10.1016/j.pss.2004.12.005.

Mével, L, and E. Mercier (2007), Large-scale doming on Europa: A model of formation of Thera Macula, *Planet. Space Sci.*, **55**(7–8), 915–927, doi:10.1016/j.pss.2006.12.001.

Michaut, C., and M. Manga (2014), Domes, pits and small chaos on Europa produced by water sills, *J. Geophys. Res. Planets*, **119**(3), 550–573, doi:10.1002/2013JE004558.

Mitri, G., and A. P. Showman (2005), Convective-conductive transitions and sensitivity of a convecting ice shell to perturbations in heat flux and tidal-heating rate: Implications for Europa, *Icarus*, **177**(2), 447–460, doi:10.1016/j.icarus.2005.03.019.

Mitri, G., and A. P. Showman (2008), A model for the temperature-dependence of tidal dissipation in convective plumes on icy satellites: Implications for Europa and Enceladus, *Icarus*, **195**(2), 758–764, doi:10.1016/j.icarus.2008.01.010.

Moore, W. B. (2006), Thermal equilibrium in Europa's ice shell, *Icarus*, **180**(1), 141–146, doi:10.1016/j.icarus.2005.09.005.

Müller, I. (1968), A thermodynamic theory of mixtures of fluids, *Arch. Rat. Mech. Anal.*, **28**(1), 139, doi:10.1007/BF00281561.

Müller, I., *Thermodynamics*, Boston, MA, etc., Pitman Advanced Publishing Program, 1985.

Nienow, P., and B. Hubbard (2006), Surface and Englacial Drainage of Glaciers and Ice Sheets, in *Encyclopedia of Hydrological Sciences* (ed. M. Anderson), John Wiley and Sons, London, 14:166, doi:10.1002/0470848944.hsa172.

Nimmo, F., and E. Gaidos (2002), Strike-slip motion and double ridge formation on Europa, *J. Geophys. Res.*, **107**(E4), 5021, doi:10.1029/2000JE001476.

Nimmo, F., B. Giese, and R. T. Pappalardo (2003), Estimates of Europa's ice shell thickness from elastically-supported topography, *Geophys. Res. Lett.*, **30**(5), doi:10.1029/2002GL016660.

Nimmo, F., and B. Giese (2005), Thermal and topographic tests of Europa chaos formation models from Galileo E15 observations, *Icarus*, **177**(2), 327–340, doi:10.1016/j.icarus.2004.10.034.

Nimmo, F., and M. Manga (2009), Geodynamics of Europa's icy shell, in *Europa* (eds. R. T. Pappalardo, W. B. McKinnon, and K. Khurana), The University of Arizona Press, Tucson, 381–404.

Nye, J. F., and F. C. Frank (1973), Hydrology of the intergranular veins in a temperate glacier, *Association of Scientific Hydrology Publication* 95 (Symposium at Cambridge 1969 - *Hydrology of Glaciers*, 157–161.

Nye, J. F. (1989), The geometry of water veins and nodes in polycrystalline ice, *J. Glaciol.*, **35**(119), 17–22, doi:10.3189/002214389793701437.

Ojakangas, G. W., and D. J. Stevenson (1989), Thermal State of an Ice Shell on Europa, *Icarus*, **81**(2), 220–241, doi:10.1016/0019-1035(89)90052-3.

Oksanen, P., and J. Keinonen (1982), The mechanism of friction of ice, *Wear*, **78**(3), 315–324, doi:10.1016/0043-1648(82)90242-3.

Olson, P., and U. Christensen (1986), Solitary wave propagation in a fluid conduit within a viscous matrix, *J. Geophys. REs.*, **91**(B6), 6367–6374, doi:10.1029/JB091iB06p06367.

Pappalardo, R. T., J. W. Head, R. Greeley, R. J. Sullivan, C. Pilcher, G. Schubert, W. B. Moore, M. H. Carr, J. M. Moore, M. J. S. Belton, and D. L. Goldsby (1998), Geological evidence for solid-state convection in Europa's ice shell, *Nature*, **391**(6665), 365–368, doi:10.1038/34862.

Pappalardo, R. T., M. J. S. Belton, H. H. Breneman, M. H. Carr, C. R. Chapman, G. C. Collins, T. Denk, S. Fagents, P. E. Geissler, B. Giese, R. Greeley, R. Greenberg, J. W. Head, P. Helfenstein, G. Hoppa, S. D. Kadel, K. P. Klaasen, J. E. Klemaszewski, K. Magee, A. S. McEwen, J. M. Moore, W. B. Moore, G. Neukum, C. B. Phillips, L. M. Prockter, G. Schubert, D. A. Senske, R. J. Sullivan, B. R. Tufts, E. P. Turtle, R. Wagner, and K. K. Williams (1999), Does Europa have a subsurface ocean? Evaluation of the geological evidence, *J. Geophys. Res.*, **104**(El0), 24015–24055, doi:10.1029/1998JE000628.

Pappalardo, R. T., and A. C. Barr (2004), The origin of domes on Europa: The role of thermally induced compositional diapirism, *Geophys. Res. Lett.*, **31**(L01701), doi:10.1029/2003GL019202.

Pappalardo, R. T., D. Senske, L. Prockter, S. Vance, G. W. Patterson, B. Goldstein, T. Magner, B. Cooke, E. Adams, G. Garner, B. Buffington, and the Europa Study Team (2013), Science from the Europa Clipper Mission Concept: Exploring the Habitability of Europa, *European Planetary Science Congress*, London (UK), EPSC Abstracts Vol. **8**, EPSC2013-886, 2013.

Paterson, W. S. B., *The Physics of Glaciers*, Oxford, Pergamon Press, 1981.

Peale, S. J., P. Cassen, and R. T. Reynolds (1979), Melting of Io by tidal dissipation, *Science*, **203**(4383), 892–894, doi:10.1126/science.203.4383.892.

Peale, S. J. (1999), Origin and evolution of the natural satellites, *Annu. Rev. Astron. Astrophys.*, **37**(37), 533–602, doi:10.1146/annurev.astro.37.1.533.

Petrich, C., P. J. Langhorne, and Z. F. Sun (2006), Modelling the interrelationships between permeability, effective porosity and total porosity in sea ice, *Cold Reg. Sci. Tech.*, **44**(2), 131–144, doi:10.1016/j.coldregions.2005.10.001.

Petrich, C., and H. Eicken (2009), Growth, structure and properties of sea ice, in *Sea ice* (eds. D. N. Thomas, and G. S. Dieckmann), Wiley-Blackwell, 23–77.

Pettersson, R., P. Jansson, and H. Blatter (2004), Spatial variability in water content at the cold-temperate transition surface of the polythermal Storglaciären, Sweden, *J. Geophys. Res.*, **109**, F02009, doi:10.1029/2003JF000110.

Pilcher, C. B., S. T. Ridgway, and T. B. McCord (1972), Galilean satellites: identification of water frost, *Science*, **178**(4065), 1087–1089, doi:10.1126/science.178.4065.1087.

Porco, C. C., P. Helfenstein, P. C. Thomas, A. P. Ingersoll, J. Wisdom, R. West, G. Neukum, T. Denk, R. Wagner, T. Roatsch, S. Kieffer, E. Turtle, A. McEwen, T. V. Johnson, J. Rathbun, J. Veverka, D. Wilson, J. Perry, J. Spitale, A. Brahic, J. A. Burns, A. D. DelGenio, L. Dones, C. D. Murray, and S. Squyres (2006), Cassini observes the active South Pole of Enceladus, *Science*, **311**(5766), 1393–1401, doi:10.1126/science.1123013.

Postberg, F., J. Schmidt, J. Hillier, S. Kempf, and R. Srama (2011), A salt-water reservoir as the source of a compositionally stratified plume on Enceladus, *Nature*, **474**(7353), 620–622, doi:10.1038/nature10175.

Press, W. H., S. A. Teukolsky, W. T. Vetterling, and B. P. Flannery, *Numerical Recipes in Fortran: The Art of Scientific Computing* (Vol. 1 of Fortran Numerical Recipes), Cambridge University Press, 1992.

Prockter, L. M., and R. T. Pappalardo (2000), Folds on Europa: Implications for crustal cycling and accommodation of extension, *Science*, **289**(5481), 941–943, doi:10.1126/science.289.5481.941.

Prockter, L. M., F. Nimmo, and R. T. Pappalardo (2005), A shear heating origin for ridges on Triton, *Geophys. Res. Lett.*, **32**(14), L14202, doi:10.1029/2005GL022832.

Quarteroni, A., and A. Valli, *Numerical approximation of partial differential equations*, Springer series in computational mathematics, **23**, Springer-Verlag, Berlin Heidelberg, 1994, doi:10.1007/978-3-540-85268-1.

Rabinowicz, M., Y. Ricard, and M. Grégoire (2002), Compaction in a mantle with a very small melt concentration: Implications for the generation of carbonatitic and carbonate-bearing high alkaline mafic melt impregnations, *Earth Planet. Sci. Lett.*, **203**(1), 1205–1220, doi:10.1016/S0012-821X(02)00836-1.

Rathbun, J. A., G. S. Musser, and S. W. Squyres (1998), Ice diapirs on Europa: Implications for liquid water, *Geophys. Res. Lett.*, **25**(22), 4157–4160, doi:10.1029/1998GL900135.

Rhebergen S., G. Wells, R. F. Katz, and A. Wathen (2013), An optimal preconditioner for models of coupled magma/mantle dynamics, submitted to *SIAM Journal on Scientific Computing*.

Ricard, Y., D. Bercovici, and G. Schubert (2001), A two-phase model for compaction and damage: 2. Applications to compaction, deformation, and the role of interfacial surface tension, *J. Geophys. Res.*, **106**(B5), 8907–8924, doi:10.1029/2000JB900431.

Ricard, Y. (2007), Physics of mantle convection, in *Treatise on Geophysics - Mantle dynamics* (eds. G. Schubert and D. Bercovici), Elsevier, 31–87.

Ricard, Y., O. Šrámek, and F. Dubuffet (2009), A multi-phase model of runaway core-mantle segregation in planetary embryos, *Earth Planet. Sci. Lett.*, **284**(1–2), 144–150, doi:10.1016/j.epsl.2009.04.021.

Roth, L., J. Saur, K. D. Retherford, D. F. Strobel, P. D. Feldman, M. A. McGrath, and F. Nimmo (2014), Transient water vapor at Europa's south pole, *Science*, **343**(171), doi:10.1126/science.1247051.

Rudolph, M. L., and M. Manga (2009), Fracture penetration in planetary ice shells, *Icarus*, **199** (2), 536–541, doi:10.1016/j.icarus.2008.10.010.

Schmeling, H. (2006), A model of episodic melt extraction for plumes, *J. Geophys. Res.*, **111** (B03202), doi:10.1029/2004JB003423.

Schmidt, B. E., D. D. Blankenship, G. W. Patterson, and P. M. Schenk (2011), Active formation of chaos terrain over shallow subsurface water on Europa, *Nature*, **479**(7374), 502–505, doi:10.1038/nature10608.

Schubert, G., F. Sohl, and H. Hussmann (2009), Interior of Europa, in *Europa* (eds. R. T. Pappalardo, W. B. McKinnon, and K. Khurana), The University of Arizona Press, Tucson, 353–367.

Scott, D. R., and D. J. Stevenson (1984), Magma solitons, *Geophys. Res. Lett.*, **11**, 1161–1164.

Scott, D. R., and D. J. Stevenson (1986), Magma ascent by porous flow, *J. Geophys. Res.*, **91**, 9283–9296.

Scott, D. R., D. J. Stevenson, and J. A. Whitehead (1986), Observations of solitary waves in a viscously deformable pipe, *Nature*, **319**, 759–761.

Scott, D. R., and D. J. Stevenson (1989), A self-consistent model of melting, magma migration and buoyancy-driven circulation beneath mid-ocean ridges, *J. Geophys. Res.*, **94**(B3), 2973–2988, doi:10.1029/JB094iB03p02973.

Sharp, D. H. (1984), An overview of Rayleigh-Taylor instability, *Physica D*, **12**(1–3), 3–18, doi:10.1016/0167-2789(84)90510-4.

Showman, A. P. and R. Malhotra (1997), Tidal evolution into the Laplace resonance and the resurfacing of Ganymede, *Icarus*, **127**(1), 93–111, doi:10.1006/icar.1996.5669.

Showman, A. P., I. Mosqueira, and J. W. Head (2004), On the resurfacing of Ganymede by liquid-water volcanism, *Icarus*, **172**(2), 625–640, doi:10.1016/j.icarus.2004.07.011.

Showman, A. P., and L. J. Han (2005), Effects of plasticity on convection in an ice shell: Implications for Europa, *Icarus*, **177**(2), 425–437, doi:10.1016/j.icarus.2005.02.020.

Shu, C.-W. (1998), Essentially non-oscillatory and weighted essentially non-oscillatory schemes for hyperbolic conservation laws, in *Advanced Numerical Approximation of Nonlinear Hyperbolic Equations* (ed. A. Quarteroni), Lecture Notes in Mathematics, Springer-Verlag, Berlin Heidelberg, **1697**, 325–432.

Simon, F., and G. Glatzel (1929), Bemerkungen zur Schmelzdruckkurve, *Z. Annorg. Allg. Chem.*, **178**(1), 309–316, doi:10.1002/zaac.19291780123.

Smith, B. A., L. A. Soderblom, T. V. Johnson, A. P. Ingersoll, S. A. Collins, E. M. Shoemaker, G. E. Hunt, H. Masursky, M. H. Carr, M. E. Davies, A. F. Cook, J. Boyce, G. E. Danielson, T. Owen, C. Sagan, R. F. Beebe, J. Veverka, R. G. Strom, J. F. McCauley, D. Morrison, G. A. Briggs, and V. E. Suomi (1979a), The Jupiter System Through the Eyes of Voyager 1, *Science*, **204**(4396), 951–957+960–972, doi:10.2307/1748136.

Smith, B. A., L. A. Soderblom, R. Beebe, J. Boyce, G. Briggs, M. Carr, S. A. Collins, A. F. Cook, G. E. Danielson, M. E. Davies, G. E. Hunt, A. Ingersoll, T. V. Johnson, H. Masursky, J. McCauley, D. Morrison, T. Owen, C. Sagan, E. M. Shoemaker, R. Strom, V. E. Suomi, and J. Veverka (1979b), The Galilean Satellites and Jupiter: Voyager 2 Imaging Science Results, *Science*, **206**(4421), 927–950, doi:10.2307/1749285.

Sotin, C., J. W. Head, and G. Tobie (2002), Europa: Tidal heating of upwelling thermal plumes and the origin of lenticulae and chaos melting, *Gephys. Res. Lett.*, **29**(8), 1233, doi:10.1029/2001GL013844.

Sotin, C., G. Tobie, J. Wahr, and W. B. McKinnon (2009), Tides and tidal heating on Europa, in *Europa* (eds. R. T. Pappalardo, W. B. McKinnon, and K. Khurana), The University of Arizona Press, Tucson, 85–117.

Souček, O., K. Kalousová, and O. Čadek (2014), Water transport in planetary ice layers by two-phase flow - a parametric study, *Geophys. Atrophys. Fluid Dynamics*, doi:10.1080/03091929.2014.969251.

Spaun, N. A., J. W. Head, G. C. Collins, L. M. Prockter, and R. T. Pappalardo (1998), Conamara Chaos Region, Europa: Reconstruction of mobile polygonal ice blocks, *Geophys. Res. Lett.*, **25**(23), 4277–4280, doi:10.1029/1998GL900176.

Spaun, N. A., J. W. Head, R. T. Pappalardo, and the Galileo SSI Team (1999), Chaos and lenticulae on Europa: Structure, morphology, and comparative analysis, *Lunar Planet. Sci., XXX*, **1276**.

Spencer, J. R., J. C. Pearl, M. Segura, F. M. Flasar, A. Mamoutkine, P. Romani, B. J. Buratti, A. R. Hendrix, L. J. Spilker, and R. M. C. Lopes (2006), Cassini encounters Enceladus: Background and the discovery of a south polar hot spot, *Science*, **311**(5766), 1401–1405, doi:10.1126/science.1121661.

Spiegelman, M., and D. McKenzie (1987), Simple 2-D models for melt extraction at mid-ocean ridges and island arcs, *Earth Planet. Sci. Lett.*, **83**(1–4), 137–152, doi:10.1016/0012-821X(87)90057-4.

Spiegelman, M. (1993a), Flow in deformable porous media I: Simple analysis, *J. Fluid. Mech.*, **247**, 17–38, doi:10.1017/S0022112093000369.

Spiegelman, M. (1993b), Flow in deformable porous media II: Numerical analysis - the relationship between shock waves and solitary waves, *J. Fluid. Mech.*, **247**, 39–63, doi:10.1017/S0022112093000370.

Straub, J. (1994), The role of surface tension for two-phase heat and mass transfer in the absence of gravity, *Exp. Therm. Fluid Sci.*, **9**(3), 253–273, doi:10.1016/0894-1777(94)90028-0.

Sullivan, R. J., R. Greeley, J. E. Klemaszewski, M. Kraft, J. Moreau, K. K. Williams, M. J. S. Belton, M. H. Carr, C. R. Chapman, B. E. Clark, P. E. Geisler, R. J. Greenberg, R. Tufts, J. W. Head, R. T. Pappalardo, and J. M. Moore (1997), Ridge formation on Europa: examples from Galileo high resolution images (abstract), *Geol. Soc. Am. Annual Convention*, **29**(6), A-312.

Sullivan, R., R. Greeley, K. Homan, J. Klemaszewski, M. J. S. Belton, M. H. Carr, C. R. Chapman, R. Tufts, J. W. Head, R. Pappalardo, J. Moore, P. Thomas, and Galileo Imaging Team (1998), Episodic plate separation and fracture infill on the surface of Europa, *Nature*, **391**(6665), 371–373, doi:10.1038/34874.

Šrámek, O., Y. Ricard, and D. Bercovici (2007), Simultaneous melting and compaction in deformable two-phase media, *Geophys. J. Int.*, **168**(3), 964–982, doi:10.1111/j.1365-246X.2006.03269.x.

Šrámek, O., Y. Ricard, and F. Dubuffet (2010), A multiphase model of core formation, *Geophys. J. Int.*, **181**(1), 198–220, doi:10.1111/j.1365-246X.2010.04528.x.

Taylor, C., and P. Hood (1973), A numerical solution of the Navier-Stokes equations using the finite element technique, *Comput. Fluids*, **1**(1), 73–100, doi:10.1016/0045-7930(73)90027-3.

Thomson, R. E., and J. R. Delaney (2001), Evidence for a weakly stratified Europan ocean sustained by seafloor heat flux, *J. Geophys. Res. Planets*, **106**(E6), 12355–12365, doi:10.1029/2000JE001332.

Tittemore, W. C. (1990), Tidal heating of Ariel, *Icarus*, **87**(1), 110–139, doi:10.1016/0019-1035(90)90024-4.

Tittemore, W. C., and J. Wisdom (1990), Tidal evolution of the Uranian satellites: III. Evolution through the Miranda-Umbriel 3:1, Miranda-Ariel 5:3, and Ariel-Umbriel 2:1 mean-motion commensurabilities, *Icarus*, **85**(2), 394–443, doi:10.1016/0019-1035(90)90125-S.

Tiscareno, M. S., and P. E. Geissler (2003), Can redistribution of material by sputtering explain the hemispheric dichotomy of Europa?, *Icarus*, **161**(1), 90–101, doi:10.1016/S0019-1035(02)00023-4.

Tobie, G., G. Choblet, and C. Sotin (2003), Tidally heated convection: Constraints on Europa's ice shell thickness, *J. Geophys. Res.*, **108**(E11), 5124, doi:10.1029/2003JE002099.

Tobie, G., O. Čadek, and C. Sotin (2008), Solid tidal friction above a liquid water reservoir as the origin of the south pole hotspot on Enceladus, *Icarus*, **196**(2), 642–652, doi:10..1016/j.icarus.2008.03.008.

Truesdell, C., *Rational Thermodynamics (2nd ed.)*, Springer-Verlag, New York, 1984.

Van Oss, C. J., R. F. Giese, R. Wentzek, J. Norris, and E. M. Chuvilin (1992), Surface tension parameters of ice obtained from contact angle data and from positive and negative particle adhesion to advancing freezing fronts, *J. Adhesion Sci. Technol.*, **6**(4), 503–516, doi:10.1163/156856192X00827.

Vynnytska, L., M. E. Rognes, and S. R. Clark (2013), Benchmarking FEniCS for mantle convection simulations, *Comput. Geosci.*, **50**(SI), 95–105, doi:10.1016/j.cageo.2012.05.012.

Waite, J. H., M. R. Combi, W. H. Ip, T. E. Cravens, R. L. McNutt, W. Kasprzak, R. Yelle, J. Luhmann, H. Niemann, D. Gell, B. Magee, G. Fletcher, J. Lunine, and W. L. Tseng (2006), Cassini ion and neutral mass spectrometer: Enceladus plume composition and structure, *Science*, **311**(5766), 1419–1422, doi:10.1126/science.1121290.

Walford, M. E. R., D. W. Roberts, and I. Hill (1987), Optical measurements of water lenses in ice, *J. Glaciol.*, **33**(114), 159–161.

Walford, M. E. R., and J. F. Nye (1991), Measuring the dihedral angle of water at a grain-boundary in ice by an optical diffraction method, *J. Glaciol.*, **37**(125), 107–112.

Weertman, J. (1971), Theory of water-filled crevasses in glaciers applied to vertical magma transport beneath oceanic ridges, *J. Geophys. Res.*, **76**(5), 1171–1183, doi:10.1029/JB076i005p01171.

Weertman, J. (1973), Can a water-filled crevasse reach the bottom surface of a glacier, *IAHS Publ.*, **95**, 139-145.

Weertman, J., *Dislocation Based Fracture Mechanics*, World Sci., River Edge, N. J, 1996.

Whitehead, J. A., and D. S. Luther (1975), Dynamics of Laboratory Diapir and Plume Models, *J. Geophys. Res.*, **80**(5), 705–717, doi:10.1029/JB080i005p00705.

Williams, K. K., and R. Greeley (1998), Estimates of ice thickness in the Conamara Chaos region of Europa, *Geophys. Res. Lett.*, **25**(23), 4273–4276, doi:10.1029/1998GL900144.

Zahnle, K., L. Dones, and H. F. Levison (1998), Cratering rates on the Galilean satellites, *Icarus*, **136**(2), 202–222, doi:10.1006/icar.1998.6015.

Zimmer, C., K. K. Khurana, and M. G. Kivelson (2000), Subsurface oceans on Europa and Callisto: Constraints from Galileo magnetometer observations, *Icarus*, **147**(2), 329–347, doi:10.1006/icar.2000.6456.

Zolotov, M. Y., and J. S. Kargel (2009), On the Composition of Europa's Icy Shell, Ocean and Underlying Rocks, in *Europa* (eds. R. T. Pappalardo, W. B. McKinnon, and K. Khurana), The University of Arizona Press, Tucson, 431–457.

Dynamique des satellites de glace avec une phase liquide

Europe, le plus petit satellite de Jupiter, a une surface jeune avec une pléthore de terrains uniques qui indiquent une activité endogène récente. Des modèles morphologiques et des observations spectrales suggèrent la présence d'un océan interne ainsi que de poches d'eau liquide peu profondes dans la coquille de glace extérieure. Cette présence d'eau dans un environnement chimiquement riche et d'une source d'énergie à long terme assurée par chauffage de marée font d'Europe l'un des meilleurs candidats pour l'habitabilité, pour lesquels l'échange de matière entre la surface et l'océan est critique. Dans cette thèse, nous étudions la fusion interne de la coquille de glace et l'évolution ultérieure de l'eau en utilisant un formalisme biphasé développé pour ce contexte. Les résultats d'une étude paramétrique pour une coquille de glace tempérée indiquent que l'échelle de temps de transport de l'eau par écoulement poreux est régie par la perméabilité de la glace, tandis que la viscosité de la glace affecte la longueur d'onde de la solution. Nous considérons alors une couche de glace polythermique avec deux scénarios de fusion: (i) Dans le cas d'un panache chaud chauffé par les marées, la fusion se produit principalement dans sa partie inférieure et toute l'eau est immédiatement transportée vers l'océan sous-jacent. (ii) Au contraire, des mouvements de cisaillement sur une faille décrochante activée par les marées peuvent induire une fusion superficielle (environ trois kilomètres sous la surface). Cette poche d'eau liquide peut rester gravitationnellement stable pendant au moins 600 milliers d'années si la couche de glace sous-jacente n'est pas chauffée par les marées solides.

Mots clés : Europe, chauffage de marée, fusion de la glace, mélange glace/eau liquide, écoulement biphasé.

Dynamics of icy satellites with a liquid phase

Jupiter's smallest moon Europa has a very young surface with a plethora of unique terrains that indicate recent endogenic activity. Morphological models and spectral observations suggest that it possesses an internal ocean as well as shallow pockets of liquid water within its outer ice shell. Presence of water in a chemically rich environment and a longterm energy source ensured by tidal heating, make Europa one of the best candidates for habitability, for which the material exchange between the surface and the ocean is critical. In this thesis, we investigate internal melting and subsequent meltwater evolution within Europa's ice shell by using a two-phase formalism developed for this context. Results of a parametric study for a temperate ice shell indicate that the time scale of water transport by porous flow is governed by the ice permeability, while the ice viscosity affects the solution wavelength. We then consider a polythermal ice shell with two melting scenarios: (i) In a tidally-heated convecting ice shell, melting occurs mainly in its lower half and all the meltwater is immediately transported to the underlying ocean. (ii) Contrarily, shear motions on a tidally-activated fault can induce melting as shallow as three kilometers below the surface. This meltwater pocket can remain gravitationally stable for at least 600 kyr if the underlying ice layer is not volumetrically heated.

Keywords : Europe, tidal heating, ice melting, ice/liquid water mixture, two-phase flow.